EVALUATION OF THE EFFECT OF REINFORCEMENT CORROSION ON THE AXIAL AND FLEXURAL PERFORMANCE OF RC COLUMNS

By

Maha Dabas

Thesis submitted in partial fulfillment of the requirements for the degree of
Doctorate in Philosophy
in Civil Engineering

Department of Civil Engineering
Faculty of Engineering
University of Ottawa

Abstract

The heavy use of de-icing salts in the winter to accommodate heavy traffic has been the most detrimental cause of chloride-induced corrosion in Canadian reinforced concrete (RC) bridge infrastructure. In addition, the rise of greenhouse emissions and subsequent increase in the mean surface temperature have increased the potential risk of carbonation-induced corrosion. It is believed that the synergistic effect of multiple deteriorating mechanisms will accelerate the incidence of reinforcement corrosion in Canadian infrastructure. Over time, premature deterioration of RC bridges due to reinforcement corrosion leads to concrete cover cracking and spalling, loss of bond between reinforcement and concrete, and reduction in the structural capacity and ductility of the structure.

There is limited research work that has examined the effect of corrosion on the structural performance of RC columns. This research has evaluated the axial and flexural capacity of corroded RC columns exposed to different levels and patterns of reinforcement corrosion. An experimental testing campaign of ten RC columns was conducted in two stages. During the first stage, eight columns were subjected to an accelerated corrosion regime by impressing a constant current for 137 days. In the second stage, all ten columns were subjected to an axial quasi-static load until failure. Five columns were loaded concentrically, while the remaining five were loaded eccentrically. The structural performance (residual strength, ductility, resilience, stiffness, toughness, and failure mode) of the columns were analyzed from load-displacement curves of the entire and mid-span length of the columns. The experimental results show that corrosion of the ties directly affects the column's post-peak response even at low corrosion levels. Columns with corroded ties had a brittle failure, and the residual ductility and toughness were significantly reduced. On the other hand, longitudinal reinforcement corrosion primarily affects the residual strength of the columns, which is prominent at a medium level of corrosion. At high levels of both longitudinal and transverse reinforcement corrosion, the residual strength, ductility, and axial stiffness are significantly reduced. This is accompanied by a significant deterioration of the cover and local buckling of the longitudinal rebars, which is attributed to a significant reduction in the confinement pressure of the core concrete.

A three-dimensional non-linear finite element model (3D-NLFEM) of the columns was developed using the finite element package DIANA (v.10.4) and validated with the experimental results. The effect of reinforcement corrosion on the structural response of columns was modelled as a change in the mechanical and geometrical properties of concrete and steel materials. This was achieved by integrating constitutive and deteriorating models into the 3D-NLFEM. The model accounts for the bond-slip behaviour between longitudinal bars and concrete (for eccentrically loaded columns), the confinement of the concrete core and strength reduction of the concrete cover, and the buckling potential of longitudinal reinforcement. The validated model was used to conduct a parametric analysis to investigate the effect of several influencing variables such as damage level and patterns and to explore scenarios beyond those tested in a laboratory setting.

Finally, an analytical model based on sectional analysis was developed and compared with both the experimental and FEM results. The proposed analytical approach was developed by integrating deteriorating models and incorporating data collected from field investigation. Based on this evaluation, a practical analytical approach is proposed to estimate the nominal residual capacity of corroded columns considering the reduction in confinement effects, bond loss and potential buckling. The results from the experimental, numerical, and analytical studies correlate well.

This work's outcome will contribute to a better understanding of the axial and flexural performance in terms of the ultimate capacity, post peak response and failure mode of RC columns affected by the reinforcement corrosion and static loading. Moreover, it provides a simplified analytical tool for practicing engineers to predict the axial and flexural capacity of deteriorated bridges vulnerable to reinforcement corrosion and increased traffic volume.

To my beloved Father and Kids

Acknowledgements

I would like to express my sincere gratitude to my supervisor Prof. Beatriz Martin-Perez for her supervision, support and guidance throughout my graduate studies. Also, I would like to extend my appreciation to my co-supervisor, Dr. Husham Almansour, for his suggestions and encouragement and for providing technical resources.

My sincere gratitude and appreciation go to Dr. Bessam Kadhom, Ajay Mundi, Andisheh Zahedi, Cassandra Trottier, Derick Asirvatham, Luan Antunes and Diego de Souza for their help during the specimens' construction and testing. I would like to thank all the technical officers at the mechanical and structural laboratories at the University of Ottawa. Also, I would like to thank Roger Smith, a technical officer at the National Research Council of Canada, for sharing his knowledge and providing technical guidance during the accelerated corrosion test.

I would also like to acknowledge the financial assistance of the National Research Council of Canada (NRC), the Queen Elizabeth II graduate scholarship in science and technology and the University of Ottawa excellence scholarship.

My deepest gratitude and appreciation go to my father, a compassionate doctor, a dedicated father, and a truly good human being who greatly influenced me. I am forever grateful to my kind mother, siblings, husband and kids for their endless love and support. Special thanks go to my husband and life partner for his continuous encouragement and faith in me throughout my academic years and my kids for strength and motivation. I could not achieve this without them all.

Table of Contents

Table of Figures

List of Tables

Notation List

τ_{ties}	maximum residual bond stress (MPa)
ε_c	concrete strain
ε_s	steel strain
ε_t	the average smeared tensile strain in cracked concrete
ε_o	strain at the maximum compressive stress (0.002 normal strength and weight concrete)
ε_{01}	peak confined concrete strain
ε_{cu}	ultimate strain of the corroded reinforcement
α_c	peak concrete strain
α_u	ultimate concrete strain
δ	degradation coefficient
η_s	mass loss (%)
η_{cr}	cross-sectional loss initiating cracks
K	parameter (0.0575)
k	coefficient based on bar roughness and diameter (0.1 for ribbed bars)
k_c, n_0	parameters in Thornfedlt model for concrete response in compression
β	empirical constants
μ	empirical constants
x_{corr}	area of the bar (m^2)
i_{corr}	current rate in ($\mu A/cm^2$)
t	time in years
I_{corr}	applied current (A)
F	Faraday's constant (96,500 A·s),

z	ionic charge (2 for $Fe \rightarrow Fe^{2+} + 2e^{-}$)
M	atomic weight of metal (56 g/mol for Fe)
x_i	penetration depth in the rebar diameter after time *t* in mm
L	length of the reinforcing bar
c	concrete cover
d	steel bar diameter
a_c	extended corbel width
d_c	extended corbel depth
s	tie spacing
A_s	steel cross-sectional area
ΔA_s	steel cross-section area loss
A_g	gross concrete area
A_{sc}	corroded steel cross-sectional area
$m_{reference}$	reference mass loss,
$m_{residual\ mass}$	corroded mass
m_s	percentage mass loss
M_{corr}	mass of the corroded reinforcement
M_0	original mass of the reinforcement
$\alpha_y, \alpha_u, \alpha_e$	experimental constants representing the reduction in yield strength, ultimate strength and steel elongation, respectively
r_0	radius of the noncorroded bar
Q_{corr}	cross-section loss expressed as a percentage of the original cross-section
α	pit concentration factor (2-8)
P_x	penetration depth
$P_{u,corroded}$	ultimate strength of the corroded column,
P_u	ultimate capacity of noncorroded column
P_{cr}	critical load
P_c^{corr}	ultimate load capacity of the corroded columns
P_{ur}	residual strength

κ_r	residual column stiffness
μ_r	residual column ductility
μ	column ductility
Δ_y	yield displacement
L_e	effective length
f_c	peak concrete compressive stress
f	concrete stress
f_{core}	core concrete compressive stress
f_t	tensile stress of the concrete
f_u	ultimate stress of the steel
f_y	yield stress of the reinforcement
f_{cr}	critical buckling stress of corroded reinforcement
f_{cy}	yield stress of the corroded reinforcement
$f_{cr-cover}$	reduced concrete compressive strength due to cracking
f_{le}	concrete lateral pressure
k_2	reduction parameter to account for the non-uniform nature of the average pressure
f_l	average pressure of the concrete
b_c	core width center-to-centre of the tie perimeter
r	radius of gyration about the axis of buckling,
EI	flexural rigidity of the column
r_b	slenderness ratio
I_s	moment of inertia of the primary reinforcement
k_t	stiffness of the stirrup,
A_t	remaining cross-section area,
l_{st}	length of the stirrup,
E_t	modulus of elasticity of the stirrup
ξ_{st}	confinement index
ω_{st}	degradation coefficient of the transverse reinforcement
ω_c	degradation coefficient of the concrete cover

$w_{max.cr}$	maximum crack width
$\bar{t}_{eff}$	effective loss of cover length is estimated as follows
$\bar{b}_{eff}, \bar{h}_{eff}$	effective concrete cross-section affected by corroded ties and longitudinal bars
G_f	fracture energy
G_{ft}	tensile fracture energy
G_c	compressive fracture energy
t	plate thickness
M_r	moment resistance
Δu_t	total relative displacement
s_{slip}	steel slip
F_{rsi}	reinforcement resistance of layer *i*,
d_1	depth to the first layer of the reinforcement
d_2	depth second layer of the reinforcement
C_r	concrete load capacity
f'_{CD}	compressive strength after FTC exposure
f'_{c0}	compressive strength before FTC exposure
N	number of FT cycles
E_{CD}	modulus of elasticity after FTC exposure
E_{C0}	modulus of elasticity before FTC exposure
N	number of FTC

Chapter 1 Introduction

1.1 Overview

De-icing salts used during the long winter season to accommodate heavy traffic have been the most detrimental cause of reinforcement corrosion in Canadian reinforced concrete (RC) infrastructure. The synergistic effect of chloride-induced reinforcement corrosion with other deteriorating mechanisms, such as frost damage and alkali-aggregate reaction, can accelerate the incidence of reinforcement corrosion in RC infrastructure. Furthermore, the rise of greenhouse emissions (CO_2) and subsequent increase in the mean surface temperature (Government of Canada 2019) have increased the potential risk of carbonation-induced corrosion in addition to that caused by chloride-based salts. Over time, premature deterioration of RC bridges due to reinforcement corrosion leads to concrete cover cracking and spalling, loss of bond between reinforcement and concrete, and reduction in the structural capacity and ductility of the structure. The cost of repairing and maintaining aging bridges must increase from $14 to $22 billion annually to complete all necessary repairs to enhance their current conditions (ASCE 2021). Champlain Bridge in Montreal city in QC, built in 1962, was recently decommissioned in 2019 due to extensive deterioration of its elements; chloride-induced reinforcement corrosion due to deicing exposure was one of the main deterioration mechanisms observed (The Jacques Cartier and Champlain Bridges Incorporated (JCCBI). 2018).

The average service life of a bridge is 50 years (Canada Infrastructure Report Card (2019). Moreover, with regular maintenance, the average useful life can extend up to 70 years (Statistics Canada 2018). However, there is an increase in demand due to growth in traffic volume, higher loads and environmental deteriorating conditions. Statistics Canada (2018) and the Canada Infrastructure Report Card (2019) estimated that 40% of Canadian highway bridges are 80 years old. Moreover, 40% of these bridges have deteriorated and are in very/poor to fair condition (Canada Infrastructure Report Card 2019).

To assess the condition and extent of damage of the deteriorated structures, engineers rely on qualitative and quantitative testing procedures that include visual inspection and material surveys. The Ontario Inspection Manual (OSIM) (Ontario Ministry of Transportation 2008) describes

procedures that involve only visual inspections. In OSIM, damage associated with reinforcement corrosion is classified as follows:

- Light: rust stain on the concrete surface,
- Medium: exposed reinforcement with uniform light rust. Loss of reinforcing steel section less than 10%,
- Severe: exposed reinforcement with heavy rusting and localized pitting. Loss of reinforcing steel section between 10% and 20%,
- Very severe: exposed reinforcement with very heavy rusting and pitting, loss of reinforcing steel section over 20%.

Moreover, from collaborative work between Canada Infrastructure and Canada Statistics, the latter released a comprehensive report on the health of Canada's infrastructure, including bridges (Statistics Canada 2018). The report is based on the contribution of 1,500 government organizations and outlines the condition of bridges into six ratings based on their physical condition as follows (Statistics Canada 2018; Canada Infrastructure Report Card 2019):

- Very good: well, maintained in good condition, new or recently renovated,
- Good: within the middle of its service life, and adequate
- Fair: shows signs of deterioration and deficiencies, and requires attention,
- Poor: near its end service life,
- Very poor: unfit for sustained service and at or beyond its service life,
- Unknown: not enough data to conclude.

The survey identified in 2016 that 31% of publicly owned bridges are in Ontario and 21% are in Alberta, while Quebec has 17% of the country's bridges. In Canada, 80% of highway and expressway bridges were built between 1940 and 1999. In 2016, the distribution, in percentage, of bridges that were built before 1970's is as follows: 54% in Manitoba, 51% in Alberta, 49% in Ontario and 47% in Nova Scotia (Statistics Canada 2018).

The Canada Infrastructure Report Card (2019) released a report based on collaborative work with different contributing organizations. This report was established from a voluntary and federally administered Canadian Core Public Infrastructure Survey (CCPIS) that aligns with that published in 2018 by Statistics Canada (2018). However, it included more responses (surveys) from more

participating organizations. Survey results indicate that 80% of bridges are more than 20 years old. Moreover, 40% of Canada's bridges have deteriorated (very/poor to fair conditions).

The cost associated with inspection (visual or NDT such as ground penetration radar or half-cell potential mapping), routine maintenance (proper drainage, washing concrete surfaces), repair (patch concrete cover), and design has increased over the years. It was estimated that the cost of replacing infrastructure in a fair to poor condition is a minimum of $155 billion (ASCE 2021). This cost is expected to increase significantly with the impact of climate change on existing structures that are not designed to withstand expected extreme conditions (Cannon et al. 2020). The increase in the annual mean temperature due to continuous greenhouse emissions will result in shorter times for corrosion to initiate and subsequent higher corrosion rates.
The commentary of the Canadian Highway Bridge Design Code, CSA S6:19 in Section C14.4.4 (CSA 2019), highlights the need to evaluate deteriorated members in aged bridges by a designated professional. This evaluation should include:

- Three-dimensional analysis that captures material and geometrical properties of structures,
- Detailed inspection assessment of potential stress concentrations,
- Inspection of longitudinal reinforcement quantities and anchorage to ensure adequacy and to prevent bond failure,
- Inspection of locations of disturbed regions for potential inadequate detailing.

However, there is a lack of a systematic methodology for practicing engineers to assess the structural performance of deteriorated RC members. Therefore, the engineering community requires practical evaluating procedures to evaluate the axial and flexural performance (ductility) and residual capacity of corroded structures. Based on such assessment approaches, designers can accurately estimate corroded columns' residual axial and flexural response to develop adaptive measures to retrofit existing infrastructures, e.g., using FRP sheets. Moreover, an understanding of the problematic effects of corrosion on the degradation of the columns' axial and flexural response prompts designers to improve the resiliency of Canadian newly constructed infrastructure, e.g., improve the quality of concrete (low water-to-cement ratio, adequate air content) and improve concrete strength by use of fibres, as an example.

1.2 Research Objectives

The main objective of this study is to evaluate the effects of different levels and patterns of reinforcement corrosion on the structural performance of concentrically and eccentrically loaded RC columns. This study also proposes a practical, theoretical evaluation procedure of the nominal capacity of deteriorated RC columns. This was achieved by the following:

1. Experimental investigation was conducted on RC columns subjected to an accelerated corrosion regime followed by a loading test under a quasi-static load applied eccentrically and concentrically,
2. Finite element analyses were carried out for both corroded and non-corroded columns, and calibration analyses were conducted to simulate exact material and loading conditions,
3. The finite element models (FEM) were validated with the experimental results,
4. Parametric studies using FEMs were conducted to investigate additional corrosion scenarios beyond those tested experimentally,
5. A simplified assessment approach is proposed for the practicing engineering community to estimate the nominal capacity of corroded RC columns.

1.3 Research Significance

This work's outcome will contribute to a better understanding of the axial and flexural performance in terms of ultimate capacity, post-peak response, ductility, and failure mode, of RC columns affected by reinforcement corrosion and static loading. Moreover, it provides a simplified analytical tool for practicing engineers to predict the axial and flexural capacity of deteriorated bridge piers vulnerable to reinforcement corrosion and increased traffic volume. The accuracy of the proposed model is verified with experimental and numerical findings, yielding agreeable results.

1.4 Thesis Format and Organization

The format of this thesis is a combination of technical papers and supplementary chapters that provide additional details. Although care has been placed to avoid unnecessary repetition, sections in the thesis might describe the same stages of the research, particularly those related to the experimental component of this work.

Chapter 1 presents a brief overview of the problem statement and introduces the research objectives and thesis structure.

Chapter 2 presents a comprehensive review of the state-of-the-art on the mechanism of reinforcement corrosion, the effect of reinforcement corrosion on the material properties of concrete and steel, and the effect of reinforcement corrosion on the structural performance of RC columns. Section 2.8 has been published as a paper at the CSCE 2021 Annual Conference (Dabas, M., Martin-Pérez, B., and Almansour, H. (2021). "Effects of different patterns of reinforcement corrosion on concrete cover and residual strength in aged bridge piers: state-of-the-art-review." *CSCE 2021 Annual Conference*, online, May 26-29, 2021, MAT810.).

Chapter 3 presents a detailed explanation of the experimental program.

Chapter 4 is prepared as a scientific journal paper that presents the effect of reinforcement corrosion on the structural performance of concentrically-loaded RC columns. Chapter 5, written in paper format, analyses the effect of reinforcement corrosion on the structural performance of eccentrically-loaded RC columns.

Chapter 6 presents the methodology used to develop the finite element models of corroded RC columns. The finite element models are calibrated through sensitivity analysis of the chosen material models and are further validated with experimental results reported in the literature and in this thesis.

Chapter 7 is prepared as a scientific journal paper describing the development of an analytical approach for evaluating the residual strength of affected RC columns. Finally, Chapter 8 presents the conclusions of this thesis contributions and recommendations for future work.

Additional information is presented in the appendices. Appendix A includes a full review paper on the combined effect of multiple deteriorating mechanisms (freeze/thaw cycles and reinforcement corrosion) on the structural performance of RC columns. Appendix B presents detailed design calculations of the base plate used for the loading set-up and the column corbel design and stress-strain relationship adopted for the compressive longitudinal bars.

1.5 References

ASCE. (2021). Report Card for America's Infrastructure- Bridges. USA.

Canada Infrastructure Report Card. (2019). Canada Infrastructure Report Card 2019-Monitoring the State of Canada's Core Public Infrastructure. Canadian Infrastructure, Canada.

Cannon, A. J., Jeong, D. Il, Zhang, X., and Zwiers, F. W. (2020). Climate-Resilient Buildings and Core Public Infrastructure: An Assessment of the Impact of Climate Change on Climatic Design Data in Canada. Government of Canada, Environment and Climate Change CANADA, Canada.

Clinkard, J. (2018). "Despite being well into middle age, Canadian bridges get a C+ based on their condition." Canada Construct Connect, Toronto, 3.

CSA. (2019). "CSA-S6.1:19 Commentary on CSA S6:19, Canadian Highway Bridge Design Code." Toronto, ON, Canada.

Government of Canada. (2019). Canada's Changing Climate Report. (D. S. Bush, E. and Lemmen, ed.), Environment and Climate Change CANADA, Ottawa.

Ontario Ministry of Transportation. (2008). Ontario Structure Inspection Manual (OSIM). Ministry of Transportation, St. Catharines, Ontario, Canada.

Statistics Canada. (2018). Canada's Core Public Infrastructure Survey: Roads, bridges and tunnels, 2016. The Daily Statistics Canada's official release bulletin, Canada.

The Jacques Cartier and Champlain Bridges Incorporated (JCCBI). (2018). "Pont Champlain, Services de consultant , Inspections annuelles des sections 5 , 6 et 7 et services d ' assistance pour inspections sur demande (2015-2018) – Contrat 62450 Rapport d ' inspection 2018 – Volume 1 : Inspection annuelle des sections 5 et 7." N/Réf: P-159000038 | M04024D | MTR-00229620, Quebec, Canada, <https://jacquescartierchamplain.ca/en/the-corporation/reports-and-publications/reports-and-studies/#deconstruction> (Mar. 27, 2022).

Chapter 2 Literature Review

2.1 Introduction

Reinforcement corrosion is the primary cause of the deterioration of ageing infrastructure in Canada. De-icing salts used during the winter to accommodate heavy traffic has been the most detrimental cause of chloride-induced corrosion. In addition, the rise of greenhouse emissions (CO_2) and subsequent increase in the mean surface temperature (Government of Canada 2019) have increased the potential risk of carbonation-induced corrosion. It is believed that the synergistic effect of multiple deteriorating mechanisms will accelerate the incidence of reinforcement corrosion in Canadian infrastructure. Over time, premature deterioration of RC bridges due to reinforcement corrosion leads to concrete cover cracking and spalling, loss of bond between reinforcement and concrete, and reduction in the structural capacity and ductility of the structure. This chapter presents a comprehensive literature review of the following:

i) Mechanism and process of chloride-induced reinforcement corrosion,
ii) Effect of reinforcement corrosion on the mechanical properties of concrete and steel materials,
iii) Effect of reinforcement corrosion on the structural performance of RC columns.

Section 2.9 reviews the effect of reinforcement corrosion on the structural response of RC columns and has been published as a conference paper at the 2021 CSCE Annual Conference (Dabas, M., Martín-Pérez, B., and Almansour, H. (2021). "Effects of different patterns of reinforcement corrosion on the concrete cover and residual strength in aged bridge piers: state-of-the-art-review." *CSCE 2021 Annual Conference*, online). In addition, Appendix A presents a state-of-the-art on the effect of frost damage and corrosion on RC columns' structural performance based on a published journal in the ASCE Journal of Performance of Constructed Facilities (Dabas, M., Martín-Pérez, B., and Almansour, H. (2021). "Combined effects of freeze/thaw and corrosion on the performance of RC structures: a state-of-the-art review." *Journal of Performance of Constructed Facilities*, **35**(5), 03121002).

2.2 Reinforcement Corrosion Mechanism

Reinforcement corrosion is an electrochemical mechanism that involves the flow of charges (electrons and ions) (Fig. 2.1). Two electrochemical reactions (anodic and cathodic) occur at different points along the reinforcement or between different reinforcing bars in the presence of the electrolyte (concrete pore solution). Corrosion of the reinforcement (anodic dissolution) is initiated when there is a potential difference across the electrolyte and the metal surface due to non-uniformity within the micro-environment or the concentrations of ions. The anodic reaction involves the oxidation of iron (Fe) and the release of electrons (e^-) and ferrous ions (Andrade 2007).

$$Fe \rightarrow Fe^{+2} + 2e^- \ \textit{(anodic reaction)} \qquad \textit{Eq. 2.1}$$

The electrons travel through the metallic conductor (reinforcement) to the cathode, where they are consumed in the presence of oxygen and water to produce hydroxides (OH^-) (cathodic reaction) (Broomfield 2007):

$$4e^- + H_2O + O_2 \rightarrow 4OH^- \ \textit{(cathodic reaction)} \qquad \textit{Eq. 2.2}$$

Hydroxide ions generated from the cathodic reactions combine with the ferrous ions to form ferrous hydroxide:

$$Fe + OH^- \rightarrow Fe(OH)_2 \ \textit{(Ferrous Hydroxide)} \qquad \textit{Eq. 2.3}$$

Ferrous hydroxide can be further oxidized into other oxides, such as ferric hydroxide. Insoluble rust products have lower density and occupy more volume than that of the consumed steel. They can swell six to ten times the original steel volume when hydrated (Broomfield 2007; Andrade 2007; Andrade 2019). With sufficient oxygen and water levels (favourable conditions), iron is oxidized into different rust products with different expansive volumes. For example, ferric hydroxide is four times larger in volume than the intact iron. When ferric hydroxide is hydrated, it forms reddish-brown rust that occupies 6.5 times the volume of the original steel material (Weizhong et al. 2010 translated by Kivell 2012).

$$4Fe(OH)_2 + O_2 + 2H_2O \rightarrow 4Fe(OH)_3 \ \textit{(Ferric Hydroxide)} \qquad \textit{Eq. 2.4}$$

$$2Fe(OH)_3 \rightarrow Fe_2.O_3.H_2O + 2H_2O \quad (Brown\ red\ rust) \qquad Eq.\ 2.5$$

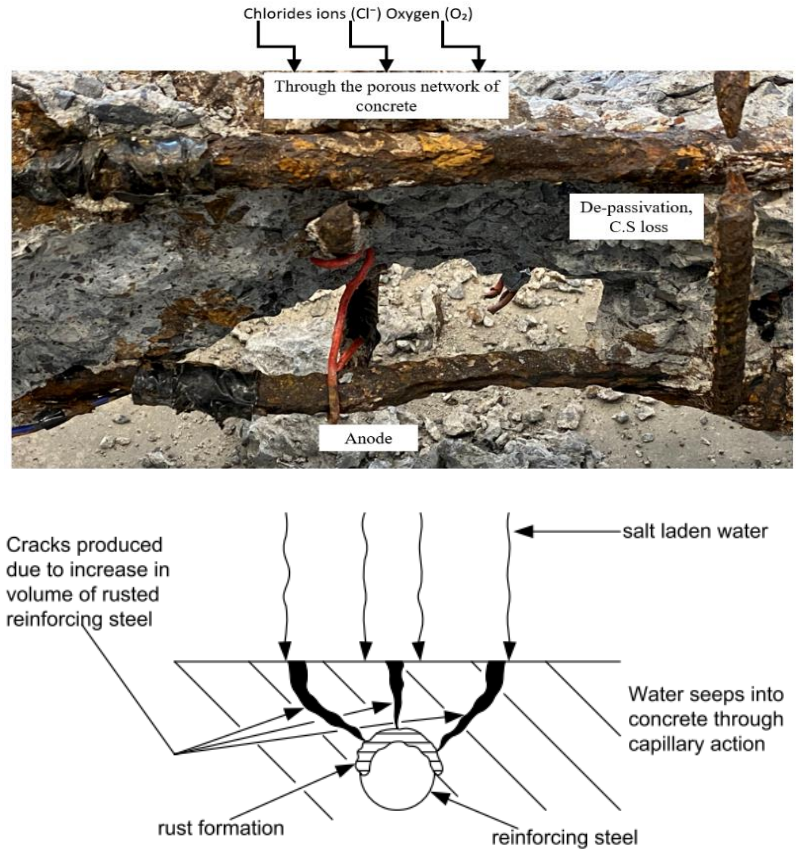

Fig. 2.1: Top: Chloride-induced reinforcement corrosion in concrete, Bottom: schematic (reproduced from Ontario Ministry of Transportation 2008)

According to Tuutti (1981) the service life of RC structures exposed to reinforcement corrosion is idealized into an initiation period and a propagation period. The initiation period is defined as the time required for chloride ions at the reinforcement to reach a critical level to destroy the passive layer. On the other hand, the time during which corrosion-induced damage accumulates is referred to as the propagation period. The process of reinforcement corrosion is described in detail in section 2.3.

2.3 Chloride-Induced Reinforcement Corrosion

The leading cause of chloride contamination is either unintended chloride addition to the fresh concrete mix for old highway bridges or de-icing sprinkled atop or splashed against the surface of

the concrete structure during the winter. Also, bridge piers in the marine environment sustain severe corrosion-induced damages along the splash and tidal zones due to the high concentration of sea salt and high humidity.

De-icings (Chloride-based salts) penetrate the concrete cover and attack the passive layer on the reinforcement. Chloride-induced corrosion initiates when the chloride content reaches a threshold (critical) level at the steel depth (Broomfield 2007). This level is usually reported in terms of the total chloride content in the concrete and is expressed by the percent of cement weight or by the molar ratio of chloride-to-hydroxide ions in the concrete pore solution. The total chloride content refers to both free chloride and bound chloride ions. Free chloride ions are water-soluble and dissolved in the concrete pore solution, and they are the primary cause of corrosion in the reinforcement. They are responsible for depassivating the rebar when their concentrations reach a threshold value (Bertolini et al. 2014).

Free chloride ions move through concrete pores by ionic diffusion due to concentration gradients according to Fick's laws. Chloride ions can become chemically bound to cement hydrates, such as C_3A, or physically bound to the concrete pore walls by reacting with aluminates or by absorption (Broomfield 2007). Typically, chloride bound to the C_3A as a Freidel's salt at a given total chloride concentration does not trigger steel corrosion (Broomfield 2007; Khan et al. 2017). However, when the pH level of the concrete pore solution is reduced by any deteriorating mechanism, such as carbonation, bound chloride ions can be released, and they will contribute to maintaining the disintegration of the protective film on the rebar (Reddy et al. 2002; Bertolini et al. 2014). Therefore, the amount of chloride concentration influencing steel corrosion (threshold level) is due to the contribution of the total chloride content relative to the weight of the cement (Glass and Buenfeld 1997, 2000; Reddy et al. 2002).

Depending on the ratio of surface area and location of the cathode to anode, steel corrosion can be either localized (macrocell) or uniform (microcell) (Elsener 2002). Microcell corrosion occurs when either cathode and anode reactions are directly adjacent to each other or the concentration of the chloride ions is very high. Macrocell corrosion occurs when the cathode-to-anode surface ratio is high, subsequently leading to localized (pitting) steel corrosion. Localized reinforcement corrosion is found to be 5 to 8 times more damaging to the steel cross-section than uniform steel corrosion along the bar length. This form of corrosion is of great concern to engineers, and it is

attributed to rapid corrosion rates of 1 mm/year in bridge decks (Elsener 2002). Chloride attacks cause local pits (active anode zone that is depassivated) (Bertolini et al. 2014).

On the other hand, uniform corrosion is typically associated with the carbonation of the concrete cover. Fig. 2.2 illustrates a schematic of the attack morphology associated with either kind of reinforcement corrosion chlorides-induced corrosion or carbonation of the concrete cover(CONTECVET 2001; Andrade 2007).

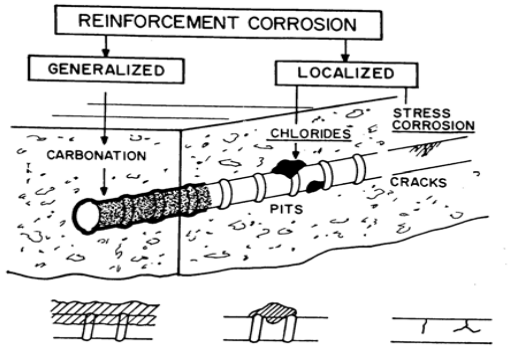

Fig. 2.2: Schematic representation of the attack morphology of reinforcement corrosion due to carbonation or chloride-induced corrosion (reproduced from CONTECVET 2001)

2.3.1 Initiation Period

A thin passivating film is spontaneously formed on the interface between reinforcement and concrete due to the alkaline nature of the concrete (pH≥13) (Tuutti 1981). Alkalinity is attributed to the high concentrations of soluble calcium, sodium and potassium oxides that fill the microscopic pores of the concrete. These oxides produce very alkaline hydroxides (pH value of 12-13) when mixed with water (Broomfield 1997). The passive layer inherently protects the reinforcement from corrosion. However, it is destroyed when the threshold value of chloride concentration (coming from either de-icing salt or marine environments) on the reinforcement surface is reached in the presence of sufficient oxygen and moisture. Chloride ions react with iron compounds in the passive layer to create FeCl.

$$Fe^{+2} + 2Cl^{-1} \rightarrow FeCl_2 \ (Cathodic\ reaction) \qquad Eq.\ 2.6$$

$$Fe^{+2} + 2Cl^{-1} + 2H_2O \rightarrow Fe(OH)_2 + HCL \qquad Eq.\ 2.7$$

Chloride threshold is defined as the amount of chloride required to cause depassivation of the reinforcement (or drop in corrosion potential). A threshold value of chloride content that exceeds 2% of the cement mass is believed to cause significant corrosion damage (Bertolini et al. 2014).

Experimental work by different authors has established a relation between the cumulative probability of corrosion onset and the amount of chlorides by weight of cement (%), as shown in Fig. 2.3 (Bertolini et al. 2014).

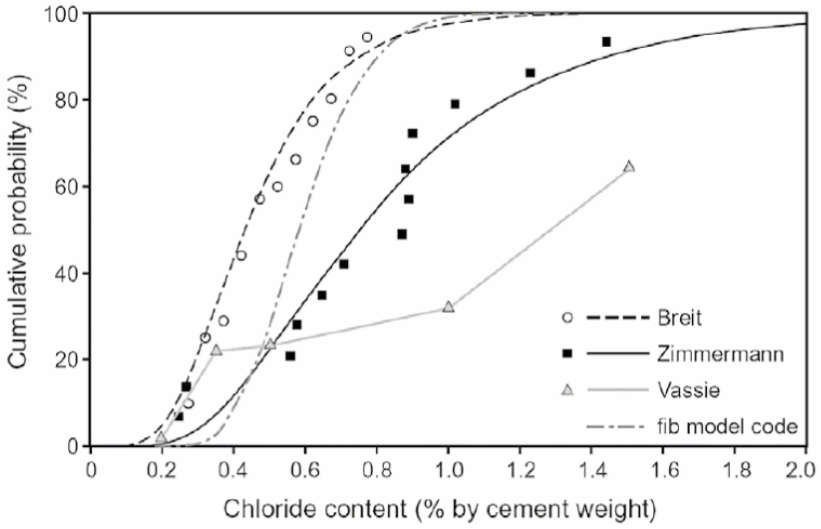

Fig. 2.3: The cumulative probability of corrosion initiation based on chloride content (% weight of cement) (reproduced from Bertulini 2013)

Once the threshold value is reached, reinforcement corrosion is initiated. Thus, the initiation period of chloride-induced corrosion refers to the time required for chlorides concentrations to reach a threshold value at the reinforcement surface. The time needed for corrosion to initiate depends on the rate of chloride penetration through the concrete cover to accumulate over a threshold value (Bertolini 2008).

The accumulation of chloride ions at which steel corrosion is initiated depends on several parameters (Alonso et al. 2000), as follows:

- Exposure
- Concrete cover
- Cement type
- Reinforcement condition
- Transport mechanism
- Carbonation
- Temperature
- Oxygen level
- Cl^-/OH^-
- Water-to-cement

A brief summary of the effect of each of those parameters follows.

Exposure: cyclic exposure to wetting and drying leads to continuous moisture movements through the concrete pore network (Crumpton et al. 1989). In effect, harmful materials penetrate deep into the concrete (Moukwa 1990), which significantly influences concrete durability and longevity. It is established that wet and dry cycles promote chloride ingress in concrete (Hong 1998). As water evaporates during the drying cycle, the concentration of salt ions increases, and oxygen diffuses faster through the partially-saturated concrete pore network. Moreover, the duration of the dry or wet cycle plays a significant role in promoting chlorides ingress. For example, a longer drying cycle will allow chloride ions to penetrate deeper into the core of the concrete during the subsequent wetting periods (Neville 1995).

Transport mechanism: chloride ions dissolved in water ingress through the concrete cover by multiple transport mechanisms such as diffusion and capillary suction (Bertolini 2008). During wetting (precipitations or splashing) cycles, chlorides penetrate through the concrete cover by capillary suction followed by diffusion mechanisms. During the dry cycles, water evaporates from the concrete leading to chlorides accumulation near the concrete surface. As described by Fick's second law, diffusion occurs when there is a concentration gradient between the chloride's solution and the contact surface of fully saturated concrete.

For partially saturated concrete, chlorides ingress is governed by capillary suction (Bertolini 2008). Interestingly, in-situ concrete structures are between partial and fully saturated states depending on the exposure circumstances. Also, structures experience multidirectional diffusion of chlorides

that affect corners and edges, leading to faster deterioration. On the other hand, if the concrete is in contact with freshwater, chlorides will diffuse out of the concrete (a process termed leaching) (Kamaitis 2002).

Cl^-/OH^- ratio: the concentration level of OH^- depends on the level of water saturation of the concrete pores and the cement composition. The hydration of C_3S and C_2S in cement consumes water and yields $Ca(OH)_2$; subsequently, the concentration of OH^- increases. In addition, the concentration of free chloride ions might decrease as a result of physical or chemical binding to the cement hydrates. An increase in the concentration of OH^- and the decrease in free chloride ions delay the onset of reinforcement corrosion. This is because the concentration of chlorides must reach a specific value (threshold value) for corrosion to occur. Otherwise, the hydroxide ions maintain an alkaline environment that protects and repairs the passive layer (Tuutti 1981).

Temperature: temperature fluctuations and cyclic precipitations promote the ingress of chloride ions through the concrete cover by diffusion, capillary suction, and/or permeation (Bertolini 2004). An increase in temperature increases the kinetics of the electrochemical reactions because it improves fluid flow and the movement of ions. High temperatures lead to the drying of the concrete cover and allow for oxygen to penetrate through the cover and dissolve in the pore solution. Accordingly, sufficient amount of oxygen creates favourable conditions to promote reinforcement corrosion (Otieno 2019). Moreover, higher temperatures increase the solubility of different substances such as oxygen and enhance molecules' transport within the pore system (Tuutti 1981). The effect of temperature is observed in warmer regions where it is found that corrosion-induced damages are prominent within a few years compared to decades in colder ones (Tuutti 1981).

Cement type: the type of cement affects the availability of free chloride ions in the concrete's pore solution. A significant amount of C_3A in cement increases the amount of bound chlorides (Broomfield 2007). The latter is not usually a direct contributor to corrosion initiation.

Concrete cover: cracks openings allow chloride ions to ingress through the concrete. This is in the presence of other factors such as moisture and oxygen. It is found that longitudinal cracks are more significant compared to transverse cracks. On the other hand, deeper concrete covers provide physical protection by increasing the path for chloride ions to reach the reinforcement, increasing the time to the onset of corrosion (Broomfield 2007).

Carbonation: carbonation is a reaction between carbon dioxide from the atmosphere with the concrete calcium hydroxides. Initially, carbon dioxide is dissolved in water to form carbonic acid. Then, carbonic acid reacts with calcium hydroxide (pore solution) to produce calcium carbonate. This, in effect, neutralizes the alkalis in the pore solution. For the pH level to be reduced, all the calcium hydroxides have to react with carbon dioxide (Broomfield 2007). Carbonation decreases the level of pH (from 13 to 8) causing a general and uniform type of corrosion (Andrade 2007). Moreover, neutralization leads to the release of bound chlorides, further promoting the disintegration of the protective layer covering the rebar (Glass and Buenfeld 2000; Reddy et al. 2002).

Reinforcement: the condition of the reinforcement, chemical composition and microstructure is believed to affect the level of reinforcement corrosion (Alonso et al. 2000).

2.3.2 Propagation Period

During the propagation period, concrete deteriorates due to the build-up of rust products (Apostolopoulos 2012). The build-up of rust products creates expansive tensile stresses against the concrete cover that eventually exceed the concrete cover's tensile capacity, leading to cracks and spalling. As a result, cracks facilitate the external ingress of chloride ions into the concrete matrix. Moreover, with a sufficient amount of oxygen and moisture at the cathode, the rate of corrosion propagation is increased.

Several conditions affect the propagation period of the reinforcement corrosion process, such as concrete resistivity, water, and oxygen levels. Concrete resistivity is a useful material property to detect and monitor the potential risk of corrosion in RC structures. This property has a linear relation with the corrosion level such that concrete with low resistivity leads to higher reinforcement section loss (CONTECVET 2001). Concrete resistivity of equal to or higher than 1,000 Ω. m indicates a very low corrosion steel section loss of <1%, while a resistivity of 500-1,000 Ω. m indicates a low corrosion section loss of 1-5%. A concrete resistivity of more than 100-500 Ω. m indicates a med ium corrosion section loss of 5-10%, while a concrete resistivity of less than 100 Ω. m indicates a high corrosion section loss of >10% (CONTECVET 2001).

In other words, it describes the electrical resistance concrete provides to the flow of current (charge) through its electrolyte (Yoon and Chang 2020). On the other hand, concrete resistivity is

an indicative of the saturation level of the concrete and the connectivity of its pore network. Thus, when the electrical resistivity of the concrete is high, the ingress or mobility of chloride ions is hindered.

2.4 Concrete Electrical Resistivity

In general, concrete electrical resistivity is affected by the following parameters:

- Curing time,
- Water-cement-ratio,
- Temperature,
- Carbonation,
- Saturation level,
- Chlorides concentration.

Curing time: the electrical resistivity of concrete without chlorides generally increases with time due to cement hydration and the attainment of a denser pore structure.

Water-cement ratio: concrete with a low water-to-cement ratio has a high electrical resistivity. This is attributed to a denser microstructure with less porosity (Fig. 2.4).

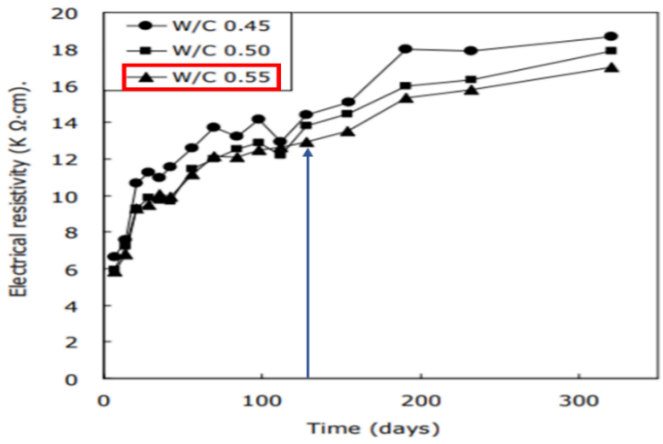

Fig. 2.4: Relation between concrete resistivity and time (days) for concretes different w/c ratios without chlorides (reproduced from Yoon and Chang 2020)

Temperature: An increase in temperature increases the kinetics of the electrochemical reactions because it enhances the movement of ions, thus, the electrical resistivity of the concrete decreases.

Carbonation: the mechanism of carbonation is detailed in section 2.3.1. The decrease in pH due to concrete carbonation leads to the release of bound chlorides, which promotes the disintegration of the protective layer covering the rebar (Glass and Buenfeld 2000; Reddy et al. 2002).

Chloride concentration: An important parameter during the initiation period because it reduces the electrical resistivity of concrete (Broomfield 1997). Electrical resistivity describes or measures how susceptible the concrete material is to the flow of electrical current in the pore solution of the concrete. And since resistivity has a reciprocal relationship with conductivity, a conductive (less resistive) concrete permits the movement of electrical charges that are carried by chloride ions in the electrolyte solution. It is found that the higher the concentration of chloride ions, the more conductive the electrolyte solution is (Yoon and Chang 2020).

For concrete with chloride ions with a concentration level higher than 2% by weight of cement, a water-to-cement ratio of 0.55, and wet and dry conditioning of saltwater, it is found that concrete resistivity is reduced by 50-60% at approximately 325 days (Presuel-Moreno et al. 2010). On the other hand, Yoon and Chang (2020) reported a 65-71% reduction in electrical resistivity for concrete containing 2% chloride ions by weight of cement compared to chloride-free concrete (Fig. 2.5 and Fig. 2.6).

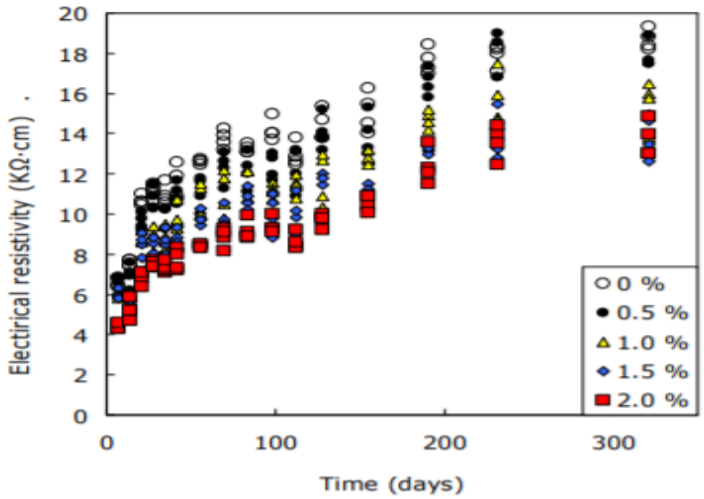

Fig. 2.5: Relation between electrical resistivity and time (for w/c=0.55 and different concentrations of chlorides by weight of cement) (reproduced from Yoon and Chang 2020)

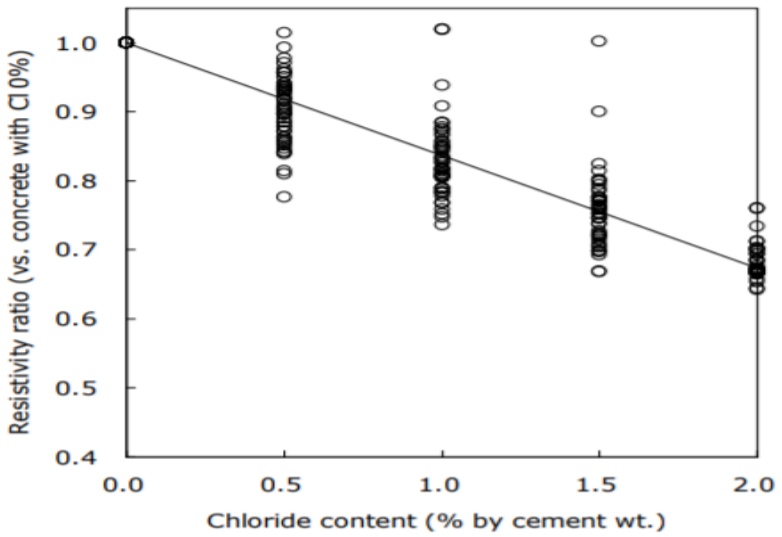

Fig. 2.6:Relation between concrete resistivity and a chloride content (%) (reproduced from Yoon and Chang 2020)

2.5 Corrosion Rate

The theoretical estimation of steel mass loss (m_s), as a function of time, is calculated using Faraday's law (CONTECVET 2001):

$$m_s = \frac{MI_{corr}t}{zF} \qquad \textit{Eq. 2.8}$$

where m_s is the mass of steel consumed due to corrosion (g), I_{corr} is the applied current (A), t is the time (s), F is Faraday's constant (96,500 A·s), z is the ionic charge (2) and M is the atomic weight of metal (56 g/mol for Fe).

Corrosion level, also referred to as the percentage of mass loss (m_s), is the ratio of the mass loss to the original mass of the non-corroded reinforcement, i.e.,

$$ms(\%) = \left(\frac{M_0 - M_{cor}}{M_0}\right).100 \qquad \textit{Eq. 2.9}$$

where M_0 is the original mass of the reinforcement in g, and M_{corr} is the mass of the corroded reinforcement.

The percentage of mass loss can also be expressed as the percentage of rebar section loss per unit length:

$$Ms(\%) = \left(1 - \frac{(r_0 - P_x)^2}{r_0^2}\right).100 \qquad \textit{Eq. 2.10}$$

where r_0 is the uncorroded radius, and P_x is the attack penetration or reduction in bar radius

The corrosion current density (or corrosion rate) i_{corr} is defined as the current per surface area of corroding reinforcement, and it is calculated from:

$$i_{corr} = I_{corr}/\pi dL \qquad \textit{Eq. 2.11}$$

where i_{corr} is the corrosion current density, I_{corr} is the applied current, d is the bar diameter, and L is the length of the corroding reinforcing bar (cm). When the corrosion density (i_{corr}) is > $0.1\frac{\mu A}{cm^2}$, the steel is considered corroding.

The penetration depth (P_x) in the rebar diameter after time *t* is calculated (CONTECVET 2001) as:

$$P_x = 0.0116 \cdot i_{corr} \cdot t \qquad \textit{Eq. 2.12}$$

where P_x is the average value of the reduction in the bar radius in mm, i_{corr} is the current density in μA/cm^2, and *t* is the time in years. Also, 0.0116 is a conversion factor from $\frac{1\mu A}{cm^2} = \frac{0.0116\ mm}{year}$.

An average current density of 1μA/cm^2 is equivalent to 11.6 μm/year (CONTECVET 2001), i.e.,

$$\frac{1\mu A}{cm^2} = \frac{0.0091g}{cm^2} x \frac{cm^3}{7.87g} x\ 10\frac{mm}{cm} = \frac{0.0116mm}{year} \qquad \textit{Eq. 2.13}$$

$$\therefore \frac{1\mu A}{cm^2} = \frac{11.6\ \mu m}{year}$$

Reduction in the cross-section area ($A_{corroded}$) of the rebar is expressed as a function of the penetration attack (CONTECVET 2001):

$$A_{corroded} = \pi(r_0 - P_x)^2 \qquad \textit{Eq. 2.14}$$

where r_0 is the uncorroded radius, and P_x is the attack penetration

2.6 Accelerated Reinforcement Corrosion: Constant Current Method

The process of reinforcement corrosion in RC structures that are in service takes years. Corrosion initiation can take few years or decades (depending on exposure conditions) and decades for cracks to propagate (Tuutti 1981; Angst 2018). It is very challenging for researchers to track and obtain sufficient information from field cases. Therefore, several accelerated corrosion techniques have been utilized to simulate reinforcement corrosion in a laboratory environment and to induce it faster.

Among available techniques is the impressed current (electrolytic cell). It is conducted by directly applying a predetermined constant current from a DC power supply to the reinforcement. The theoretical current is estimated according to Faraday's law for a target mass loss. In the set-up of this test, the positive terminal of the DC power supply is connected to the embedded reinforcement (anode). In contrast, the negative terminal is connected to the stainless-steel sheets (cathode). The current is impressed from the cathode through the electrolyte solution of the concrete to the embedded reinforcement with or without the aid of chloride ions.

Among the challenges of accelerated corrosion testing is the need to closely resemble the corrosion kinetics of in-service structures and produce meaningful durability and structural deteriorations (Caré and Raharinaivo 2007). This could be achieved by controlling the degree of corrosion (damage) and simulating the same conditions and characteristics occurring in the field.
Regardless, numerous studies reported in the literature have showed that experimental testing using accelerated reinforcement corrosion provides a convenient and controlled method of investigation of the effect of corrosion on the structural performance of RC members.
Corrosion current densities found in the field are about 0.1 to 10 $\frac{\mu A}{cm^2}$, depending on the severity of the corrosion environment (Alonso et al. 1998; Cairns et al. 2005). In experimental work, this is often increased to accelerate the corrosion process. The effect of increasing the intensity level of the current on reinforcement corrosion is controversial. The average impressed current applied experimentally is in the range of 15 to 3000 $\frac{\mu A}{cm^2}$ (Maaddawy and Soudki 2003). Maaddawy and Soudki (2003) briefly summarized some experimental tests utilizing different current densities. The following review will focus on investigating the effectiveness of introducing wet and drying

cycles, the addition of salt, different techniques of accelerated corrosion, and the impact of varying current density (15 to 500 $\frac{\mu A}{cm^2}$) with and without chlorides addition.

Andrade (2020) indicates that to produce realistic experimental results, corrosion should be accelerated using a constant current and the current density should be limited to 100-200 $\frac{\mu A}{cm^2}$. Moreover, higher current densities produce small concrete cracks compared to current densities of 100-200 $\frac{\mu A}{cm^2}$.

Several exposure conditions influence and promote the process of accelerated corrosion. Immersing specimens in saline solution was found to accelerate corrosion compared to pure water to prevent salt leaching (Caré and Raharinaivo 2007). Moreover, a saline solution reduces concrete resistivity and increases the electrolyte conductivity to carry the current (CONTECVET 2001).

Specimens immersed in a NaCl solution had visible cracks after 20 days with an applied current density of 100 $\frac{\mu A}{cm^2}$. When the current density increased to 500 $\frac{\mu A}{cm^2}$ visible cracks appeared after 4 days. On the other hand, no cracks were observed for specimens immersed in water without chloride ions for the same low and high current densities. Caré and Raharinaivo (2007) found that the transverse expansion of the tested specimens (40 mm in diameter, 100 mm in length) with w/c of 0.5, measured by a micrometre, depends primarily on both chloride content and current density. It was observed that specimen's expansion is 30 μm for a current density of 100$\frac{\mu A}{cm^2}$ while it is 13 μm for a current density of 500$\frac{\mu A}{cm^2}$. Moreover, Wang and Liang (2008), Wang et al. (2012) and Otieno (2019) found that exposure to wet and dry cycles enhances chlorides ingress and increases the rate of corrosion.

Altoubat et al. (2016) conducted experimental work to evaluate damage effects induced by accelerated corrosion using constant voltage and constant current techniques. Six small-scale (666-mm long, 208-mm in diameter) columns were statically tested after being wrapped in GFRP (glass fibre reinforced polymer). Four out of the columns were exposed to accelerated corrosion (one pair corroded using a constant voltage while another pair corroded using a constant current). The specimens were immersed in 3% NaCl solution and exposed to wet and dry cycles. The authors found that the constant current resulted in more damage (longitudinal cracks, maximum crack widths and reinforcement circumference expansion) than a constant voltage technique.

Furthermore, the authors found that there was more reduction in the load-carrying capacity for specimens corroded using a constant current than constant voltage compared with control specimens. Based on the authors' findings, this could be attributed to a constant rate of mass loss produced from the constant current technique, as shown in Fig. 2.7.

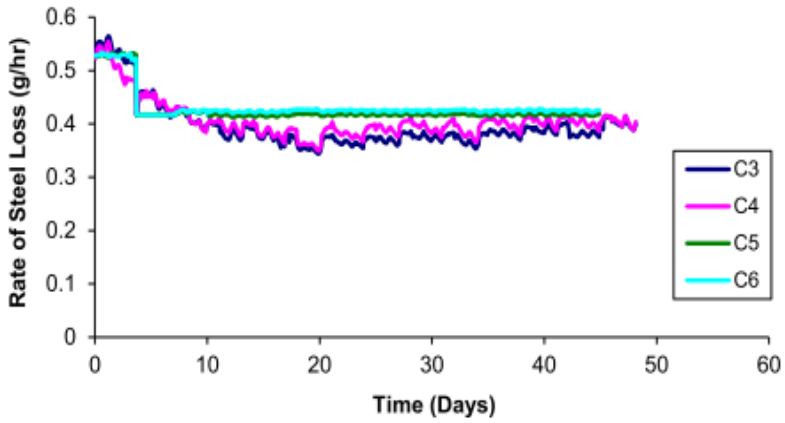

Fig. 2.7: Rate of mass loss for specimens C3/C4 corroded using constant voltage technique and C5/C6 corroded using a constant current technique (reproduced from Altoubat et al. 2016)

Alonso et al. (1998) and Maaddawy and Soudki (2003) investigated the effect of different levels of current density on reinforcement corrosion. Alonso et al. (1998) conducted accelerated corrosion on RC prisms (100×150×380 mm) mixed with 3% $CaCl_2$ by weight of cement by applying a current density of 100 $\frac{\mu A}{cm^2}$. The authors tested different specimens with different concrete covers (10, 15, 20, 30, 50 and 70 mm), bar diameter (3, 8, 10, 12 and 16 mm), corrosion rates (15 to 116 $\frac{\mu A}{cm^2}$) and w/c ratios (0.5, 0.62 and 0.65). Several factors affect crack evolution, such as concrete cover to bar diameter ratio, current density, concrete porosity, and reinforcement (Alonso et al. 1998). The authors estimated that there is a linear relationship between crack width and attack penetration during the propagation period for a current density in the range of 100-200 $\frac{\mu A}{cm^2}$ (Fig. 2.8). Also, it was observed that there is a delay in crack growth for higher concrete porosity (high w/c ratio) because expansive rust products quickly fill the voids without exerting pressure against them (Fig. 2.8). The authors found that crack widths increase faster with a lower corrosion rate of 15.04 $\frac{\mu A}{cm^2}$ compared to 115.86 $\frac{\mu A}{cm^2}$. A lower current density (15 $\frac{\mu A}{cm^2}$) produced a lower radius loss (80 microns) and resulted in higher crack widths (0.7 mm) (Fig. 2.9).

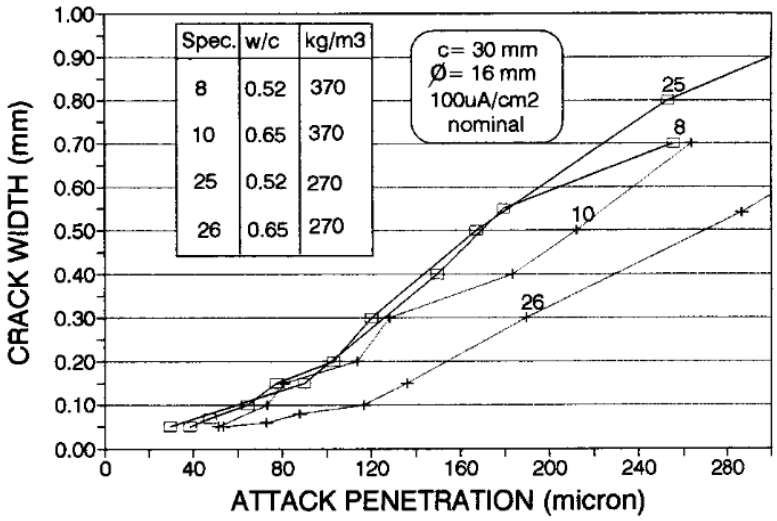

*Fig. 2.8:*Crack width vs radius loss for different w/c ratios (reproduced from *Alonso et al. 1998)*

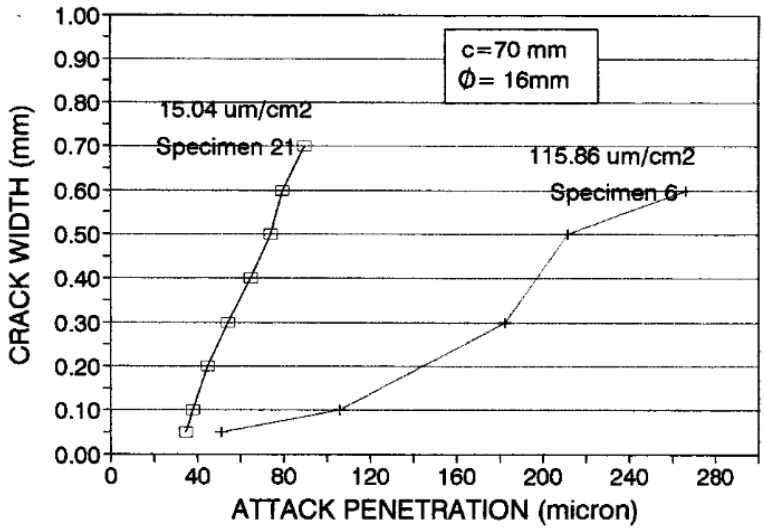

Fig. 2.9: Crack width vs radius loss for different corrosion rates (reproduced from Alonso et al. 1998)

Maaddawy and Soudki (2003) tested prisms (150×250×300 mm) with w/c of 0.58 reinforced with No.10 rebar. Specimens were subjected to accelerated corrosion by impressing current densities in the range of 100-500 $\frac{\mu A}{cm^2}$. Sodium chloride (NaCl), 5% by weight of cement, was added to the concrete mix to depassivate the reinforcement. The objectives of the test were to determine the effect of different levels of corrosion on crack width and patterns, percentage of mass loss and concrete strain due to expansive stresses. For an impressed current density up to 200 $\frac{\mu A}{cm^2}$, the corrosion products partly diffuse into the concrete pores reducing the pressure developed along the steel against the concrete pores and resultant concrete strain (Mangat and Elgarf 1999). On the

other hand, corrosion products accumulate around the steel for higher levels of corrosion (mass loss above 0.8%) and higher levels of current densities (from 200 to 500 $\frac{\mu A}{cm^2}$). Increasing the current density from 200 to 500 $\frac{\mu A}{cm^2}$ resulted in a 43% increase in the maximum crack width at the same mass loss of 7.2%.

Moreover, the authors concluded that the current density level does not affect the percentage of mass loss or crack pattern (distribution such as longitudinal cracks) (Maaddawy and Soudki 2003). Also, the measured percent for mass loss using a gravimetric weight loss agrees with Faraday's prediction of mass loss for current densities between 100 to 500 $\frac{\mu A}{cm^2}$. On the other hand, current densities higher than 200 $\frac{\mu A}{cm^2}$ result in higher concrete strain and crack width values for the same percentage of mass loss (Fig. 2.10).

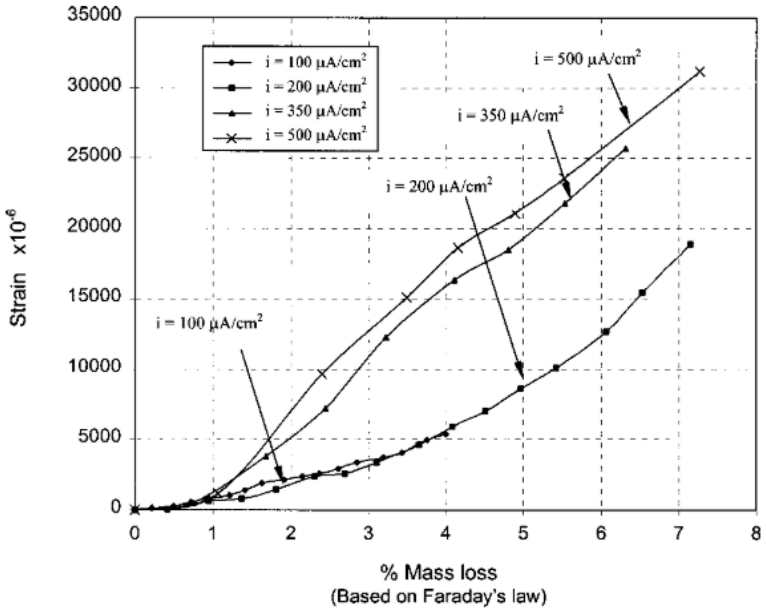

Fig. 2.10: Effect of different levels of current density on concrete strain (reproduced from Maaddawy and Soudki 2003)

The main findings of the abovementioned literature (Alonso et al. 1998; Mangat and Elgarf 1999; Maaddawy and Soudki 2003; Caré and Raharinaivo 2007; Altoubat et al. 2016) are summarized below:

- Wetting and drying cycles provide favourable conditions (moisture, oxygen and fresh supply of chlorides) to accelerate the rate of corrosion,

- Reinforcement corrosion using a constant current is a more effective technique than constant voltage one to produce consistent mass loss compared with theoretically estimated mass loss,
- There is a delay in crack growth for higher concrete porosity (high w/c ratio) because expansive rust products quickly fill the voids before exerting pressure against the concrete,
- One study found that crack width increases faster with a lower corrosion rate, while another reported that current densities higher than 200 $\frac{\mu A}{cm^2}$ result in higher concrete strain and crack width values for the same percentage of mass loss. Therefore, further investigation is required,
- Low current densities allow for dissipation of the corrosion products through the concrete pores reducing exerted pressure against the concrete,
- The current densities utilized in accelerated corrosion testings exceed those found in in-service structures. The target value of current density to employ when testing is controversial. However, one study recommended maintaining the value of current density between 100 to 500 $\frac{\mu A}{cm^2}$ while others recommend maintaining it below 200 $\frac{\mu A}{cm^2}$.
- It is found that the measured percent for mass loss using a gravimetric weight loss agrees with Faraday's prediction of mass loss for current densities between 100 to 500 $\frac{\mu A}{cm^2}$,
- Increasing current density affects the crack size (width) and concrete strain. In one study, increasing the current density from 200 to 500 $\frac{\mu A}{cm^2}$ resulted in a 43% increase in the maximum crack width at the same mass loss of 7.2%,
- On the other hand, the increase in current density does not affect mass loss, level of corrosion. Moreover, higher current densities will result in the same percentage of mass loss produced at a low current density at a shorter period.

2.7 Analytical Models Relating Corrosion Attack and Crack Development

It is expected that concrete cracks when subjected to loads and other mechanisms such as early age shrinkage. In addition, reinforcement steel corrosion leads to the internal expansion of corrosion products, inducing internal cracks that propagate from the reinforcing steel to the external surface. The density and connectivity of these cracks become a significant issue along

with crack width opening as it may lead to further damage (Li and Li 2019). The crack opening width is a significant parameter used by different standard codes as a service limitation for long-term durability problems. For example, ACI 224 (2008) specifies less than 0.18 mm for flexural structures exposed to de-icing salts. Cracking is one of the first signs of RC columns deterioration due to steel corrosion.

The residual life of RC structures can be assessed by determining the level of corrosion from the developed cracks. Crack development depends on the material properties of concrete, strength, stiffness, w/c ratio and cover-to-rebar diameter ratio. The quality of the concrete cover stiffness describes the initial cracking, penetration cracking and ultimate cracking. Corrosion has a significant effect on concrete cracking. Hence, several factors contribute to the degree of concrete cover deterioration, such as cover thickness, size, location and orientation of the reinforcement and concrete cover to longitudinal reinforcement diameter ratio (Tapan 2011).

Vidal et al. (2004) conducted experimental work to analyze crack distribution and the level of longitudinal reinforcement corrosion. The authors assessed two RC beams that naturally corroded for a period of 14 to 17 years. On the other hand, Vidal et al. (2004) proposed an analytical model that relates crack width to steel cross-sectional loss (Fig. 2.11). Two 3-m long RC beams with a cross-section of 150×380 mm were naturally corroded in a NaCl solution with periodic wetting and drying conditioning. The two beams had different reinforcement sizing and accordingly were designated as beams A and B. Concrete had a water-to-cement ratio of 0.5. The authors provided crack maps based on measurements of crack widths and distribution of the mass loss along the reinforcement. The authors found a relation between crack initiation and the ratio of concrete cover to bar diameter.

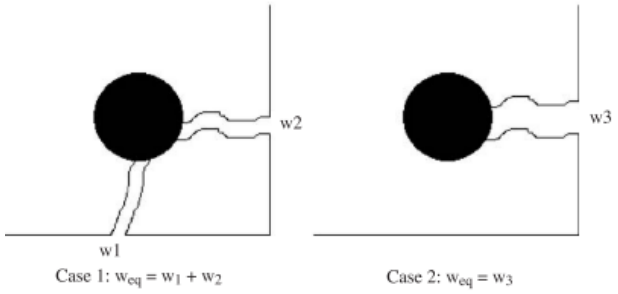

Fig. 2.11: Crack width estimation (reproduced from Vidal et al. 2004)

Vidal et al. (2004) proposed an empirical model to predict localized crack width (w) propagations as follows:

$$w = KA_s(\eta - \eta_{cr}) \qquad \textit{Eq. 2.15}$$

K is a parameter taken as 0.0575, A is the cross-sectional area of noncorroded bar, η is the steel cross-sectional loss ratio, η_{cr} is the steel cross-sectional ratio. It is estimated as follows:

$$\eta_{cr} = 1 - \left[1 - \frac{\alpha}{d}\left(7.53 + 9.32\frac{c}{d}\right) \times 10^{-3}\right]^2 \qquad \textit{Eq. 2.16}$$

where c is the concrete cover, d is bar diameter, and α is the pit factor ($2 \leq \alpha \leq 8$)

2.8 Effect of Reinforcement Corrosion on Material Properties

Corrosion of the reinforcement in concrete structures has several degrading effects on both concrete and steel durability. The level of damage or rate of degradation depends on the extent of reinforcement corrosion. This section examines available literature on the effect of reinforcement corrosion on the mechanical properties of concrete and steel.

2.8.1 Concrete Material

The quality of concrete has a significant effect on the corrosion of reinforcement. Degradations of the concrete material expose the reinforcement to the deteriorating elements (de-icing salts and carbon dioxide), which leads to reinforcement corrosion. Reinforcement corrosion occurs in a constantly changing environment (relative humidity and temperature). Reinforcement corrosion consumes the atoms of the iron (iron oxidation) and replaces them with rust products. Rust products accumulate atop the reinforcement and expand as the corrosion rate increases (Pantazopoulou and Papoulia 2001). The pressure build-up from rust expansion causes internal cracking.

Reinforcement corrosion reduces the compressive strength of the cover due to the formation of cracks that propagate internally from the corroded reinforcement to the external concrete surface. Vecchio and Collins (1986) proposed a model to account for compressive strength reduction based on total crack width and transverse tensile strain. To predict the reduction in the compressive strength as a function of the corrosion rate, Coronelli and Gambarova (2004) suggested integrating

a crack width model by Molina et al. (1993) into the Vecchio and Collins's model. Molina et al. (1993) assumed that the volumetric expansion of oxides relative to the virgin material is 2 and evaluated the corrosion-induced crack width w_{cr} as:

$$w_{cr} = \Sigma u_{icorr} = 2\Pi(v_{rs} - 1)P_x \qquad \textit{Eq. 2.17}$$

where v_{rs} the ratio of volume of corrosion products to that of consumed steel taken as 2, and P_x is the attack penetration estimated according to Eq. 2.12.

Coronelli and Gambarova (2004) used a modified model by Cape (1991), which is that originally proposed by Vecchio and Collins (1986), to estimate the effects of cracks on the reduction of the compressive strength of the concrete cover ($f_{cr-cover}$). This equation is a function of the original compressive strength and the average tensile strains in the transverse direction, causing longitudinal cracks.

$$f_{cr-cover} = \frac{f_c}{1+k(\frac{\varepsilon_t}{\varepsilon_o})} \qquad \textit{Eq. 2.18}$$

where f_c is the normal compressive strength, k is the coefficient based on bar roughness and diameter (Cape 1999 proposed 0.1 for ribbed bars), ε_t is the average smeared tensile strain in cracked concrete, and $\varepsilon_o$is the strain at the maximum compressive stress (0.002 for normal strength and weight concrete) (Coronelli and Gambarova 2004). The average tensile strain is calculated from:

$$\varepsilon_t = \frac{b_f - b}{b} = \frac{\Sigma w_{cr}}{b} = \frac{2\pi n(2P_x)}{b} \qquad \textit{Eq. 2.19}$$

where b is the original cross-section width without cracks, b_f is the increased width of the cracked cross section, Σw_{cr} is the total crack width, n is the number of reinforcing bars across the cross-section width, and P_x is the corrosion attack penetration (Eq. 2.12).

2.8.2 Bond-slip Response

The bond relation defines the interaction (transfer of forces) between concrete and reinforcement. Bond is established from the chemical adhesion between reinforcement and concrete, frictional forces, dependent on the surface roughness and relative slip of the bar from concrete, and

mechanical anchorage (interlocking) of the reinforcement ribs producing an inclined bearing force (ACI 408 2003), as shown in Fig. 2.12.

The chemical adhesion between concrete and rebar is lost quickly when the rebar slips against the surrounding concrete under applied load. The bearing and frictional forces on the ribs are engaged. The frictional forces decrease as the applied loads further increase and a slip occurs. The forces on the bar are balanced by the compressive and shear stresses provided by the concrete contact surfaces (ACI 408 2003). If the concrete cover, bar spacing or transverse reinforcement is insufficient, it can lead to splitting cracks as shown in Fig. 2.12 (b) and (c).

According to ACI 408 (2003), the residual bond strength for non-corroded structures is based on the contribution of the concrete and transverse reinforcement. It is estimated as a function of the ratio of the concrete cover-to rebar diameter, the tensile stress of the concrete, and cross-sectional area, yield strength and spacing of the ties.

$$\tau_{ties} = \tau_{concrete} + \tau_{ties} \qquad \textit{Eq. 2.20}$$

Several factors influence bond response, such as compressive and tensile strength of the concrete, cover size, size and spacing of reinforcement bars, and confinement effects due to transverse reinforcement.

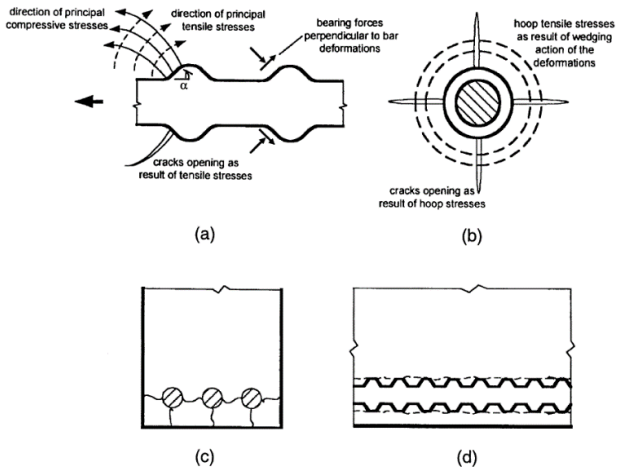

Fig. 2.12: Damage mechanism in bond loss due to pull-out force a) cracks formation b) splitting cracks formations parallel to the bar c) splitting cracks between end bar and concrete cover, d) local concrete crushing (reproduced from ACI 408 2003)

The accumulation of rust products against the surrounding concrete generates tensile stresses leading to radial splitting cracks that propagate through the concrete cover. Accumulation of the rust products reduces the frictional forces (Almusallam et al. 1996). Bond strength reduction initiates due to crushing of the concrete near the ribs. Almusallam et al. (1996) and Coronelli and Gambarova (2004) found that the mode of bond failure in corroded RC is attributed to a splitting mechanism of the cover due to cracking. However, with a significant increase in corrosion of the ribs of a deformed bar, the horizontal component of the bearing force is significantly reduced. Subsequently, the mechanism of bond failure is altered to a slippage mechanism of the bar (Almusallam et al. 1996). Moreover, Almusallam et al. (1996) details the relationship between the development of crack width and reduction in bond strength at different levels of corrosion. Splitting cracks propagate where the concrete cover is small or lateral confinement is insufficient. Furthermore, the confinement strength provided by the transverse reinforcement delays bond deterioration and propagation of cracks (Coronelli 2002 and ACI 408 2003).

Rodriguez et al. (1994) tested cubes reinforced with four rebars. From the experimental work, the authors proposed an expression to define bond strength decay due to corrosion considering the contribution of the transverse reinforcement:

$$\tau_{max} = \tau_{concrete} + \tau_{ties} = 0.6(0.5 + c/d)f_t\,(1 - \beta P_x^u) + kA_t f_y/sd \qquad \textit{Eq. 2.21}$$

where β, u, k are empirical constants (0.16, 0.1 and 0.26-0.4, respectively), f_t is the concrete tensile strength, A_t is the tie cross-sectional area, f_y is the yield strength of the ties, d is the original rebar diameter, s is the tie spacing, c is the thickness of the concrete cover, and P_x is the attack penetration

Expressions that relate the effect of attack penetration on bond degradation can be used according to CONTECVET (2001). The residual bond strength (τ_{max}) in RC with ribbed rebars when no stirrups are present is given by:

$$\tau_{max} = 2.25 - 6.6P_x \qquad \textit{Eq. 2.22}$$

where the attack penetration P_x is determined as a function of the ratio of concrete cover to bar diameter and splitting tensile strength of the concrete as follows:

$$p_x = 83.8 + 7.4\frac{c}{d} - 22.6f_t \qquad \textit{Eq. 2.23}$$

When stirrups are present, the residual bond strength is determined as:

$$\tau_{max} = \frac{4.75-4.64P_x}{(1-0.08P)} \qquad \textit{Eq. 2.24}$$

where P is the external pressure (MPa) that confines the steel bars anchored at the support zones

Several authors (Chung et al. 2004; Bhargava et al. 2008; Kivell 2012; Lin and Zhao 2016; Ma et al. 2017) have defined the steel mass loss at which cracking initiates bond degradation as the critical level. This value has been estimated between 0.5 to 6% of mass loss. The following section provides a brief introduction to each model.

Chung et al. (2004) proposed the following bond degradation model based on experimental and analytical investigations of flexural members. For this model, the bond loss was observed at 2% mass loss.

$$\gamma = f(x) = \begin{cases} 1, & \eta_s < 2.0\% \\ 2.09(\eta_s \times 100)^{-1.09}, & \eta_s \geq 2.0\% \end{cases} \qquad \textit{Eq. 2.25}$$

where γ is the ratio of the corroded bond strength to the non-corroded one, and η_s is the percentage mass loss

Bhargava et al. (2008) proposed a bond degradation model based on results of experimental work conducted by Al-Sulaimani et al. (1990), Rodriguez et al. (1994), Almusallam et al. (1996), Cabrera (1996), Amleh (2000), Auyeung et al. (2000), and Fang et al. (2004). The model is normalized to consider different concrete strengths; however, it does not account for the confinement effect provided by stirrups.

$$\gamma = f(x) = \begin{cases} 1, & \eta_s < 1.5\% \\ 1.192e^{-0.117(\eta_s - 1.5\%)}, & \eta_s \geq 1.5\% \end{cases} \qquad \textit{Eq. 2.26}$$

Kivell (2012) proposed the following equation based on cyclic loads. Bond degradation was observed at 2.4% mass loss.

$$\gamma = f(x) = \begin{cases} 1, & \eta_s < 2.4\% \\ e^{-7.6(\eta_s - 2.4\%)}, & \eta_s \geq 2.4\% \end{cases} \qquad \textit{Eq. 2.27}$$

Non-uniform reinforcement corrosion and erosion of the bar's surface ribs lead to partial or complete loss of bond (Tapan and Aboutaha 2011). The average loss in concrete strain along the exposed length of reinforcement is calculated as follows:

$$\varepsilon_s = \varepsilon_{c.avg} = \frac{\Delta L_{exp}}{L_{exp}} = \frac{1}{L_{exp}} \int_0^{Lexp} \Delta\varepsilon_c . dx \qquad \textit{Eq. 2.28}$$

where ε_s is the strain in the deteriorated reinforcement, $\varepsilon_{c.avg}$ is the average strain in the deteriorated reinforcement, L_{exp} is the exposed length of the corrosion damaged reinforcement, and ε_c is the strain in concrete

Lin and Zhao (2016) developed a comprehensive bond strength model for corroded members. The ratio of the corroded bond strength to the non-corroded one γ is defined using an exponential function from best fit to experimental data. The model considers several influencing parameters that contribute to bond strength degradations for corroded members, such as concrete cover, confinement effects, and current density (Zhao and Lin 2018) using a bond degradation coefficient (ω). In this model, the bond degradation coefficient (ω) is a function of the ratio of the concrete cover to the diameter size of the tensile reinforcement (c/d), confinement effects provided by the transverse reinforcement (ξ_{st}) and current density (i_{corr}).

$$\gamma = f(x) = \begin{cases} 1, & \eta_s < 1.5\% \\ e^{-\omega(\eta_s - 1.5\%)}, & \eta_s \geq 1.5\% \end{cases} \qquad \textit{Eq. 2.29}$$

where γ is the ratio of the corroded bond strength to the non-corroded one, η_s is the mass loss (%), and ω is the degradation coefficient. The overall degradation coefficient of bond strength is determined by taking into account degradations of bond strength due to concrete cover deterioration (ω_c), reduction in confinement (ω_{st}) and the effect of variable impressed current densities (ω_i).

$$\omega = \omega_c \times \omega_{st} \times \omega_i \qquad \textit{Eq. 2.30}$$

The degradation coefficient (ω_c) of the concrete cover is determined from fitting experimental data reported in the literature (Shima et al. 1987; Al-Sulaimani et al. 1990; Cabrera 1996; Almusallam et al. 1996; Amleh 2000; Horrigmoe et al. 2007), observing that degradation is a function of the concrete cover-to-rebar diameter ration *c*/*d*, and it is given by:

$$\omega_c = k_1 + k_2(c/d) \qquad \textit{Eq. 2.31}$$

where parameters k_1, k_2 were empirically fitted to the experimental data as k_1= 13.28, k_2= -0.57. Plizzari et al. (1998) studied the confining effect of transverse reinforcements by conducting pull-out experimental tests. The authors found that stirrups inhibit further propagations of the splitting concrete cracks, thus, reducing bond strength degradation. Moreover, experimental results on corroded beams (Rodriguez 1994; Hanjari et al. 2011) showed higher bond strength values for members reinforced with stirrups compared to beams without stirrups. The degradation coefficient (ω_{st}) of the transverse reinforcement is determined from finding the best fit of the experimental tests data (beam and pull-out tests on members with stirrups) conducted by Al-Sulaimani et al. (1990), Cabrera (1996), Hanjari et al. (2011), Kivell (2012), and Lin and Zhao (2016):

$$\omega_{st} = \frac{1}{k_4\xi_{st}+1} \qquad \textit{Eq. 2.32}$$

where parameter $k_4 = 43.54$ is determined experimentally from the relationship between ω_{st} and the confinement index (ξ_{st}), which is determined by Plizzari et al. (1998) as:

$$\xi_{st} = \frac{A_{st}}{nds} \qquad \textit{Eq. 2.33}$$

where A_{st} is the cross-sectional area of the ties, d is the bar diameter, n is the number of bars, s is tie spacings

Saifullah and Clark (1994) investigated the effect of the corrosion current density i_{corr} (40-4000 $\mu A/cm^2$) on bond strength reduction. The authors found that bond strength is reduced when the current density is higher than 250 $\mu A/cm^2$. Moreover, it was found that bond strength for a current density lower than 200 $\mu A/cm^2$ approaches the value of the bond strength in naturally corroded specimens.

The degradation coefficient ω_i is defined as $\omega_i = k_3 \ln\left(i_{corr}/200\right)+1$ with k_3=1 for current density values lower than 200 μA/cm^2. The degradation coefficient (ω), proposed by Lin and Zhao (2016), is the product of ω_c, ω_s and ω_i, i.e.,

$$\omega = \begin{cases} \frac{k_1+k_2(c/d)}{k_4\xi_{st}+1)} & i_{corr} \le 200\,\mu A/cm^2 \\ \frac{k_1+k_2(c/d)}{k_4\xi_{st}+1)}\left(k_3\, ln\left(\frac{i_{corr}}{200}\right)+1\right) & i_{corr} > 200\,\mu A/cm^2 \end{cases} \qquad \textit{Eq. 2.34}$$

parameters k_1, k_2, k_3, k_4 are based on experimental conditions: current density, the shape of the deformed ribs on the bars and the loading method; thus, they should be adjusted accordingly.

Ma et al. (2017) conducted experimental pull-out tests on plain and deformed reinforcement. The authors proposed a bond degradation model where the critical bond loss initiates at 2.41% of mass loss. The model is expressed in the following equation as a function of corrosion level.

$$\gamma = f(x) = \begin{cases} 1, & \eta_s < 2.41\% \\ 1.68(\eta_s \times 100)^{-0.59}, & \eta_s \geq 2.41\% \end{cases} \qquad \textit{Eq. 2.35}$$

In analyzing the effect of reinforcement corrosion on bond degradation, it is essential to consider the conditions of the experimental tests that control and affect the proposed models' results.

2.8.3 Steel Reinforcement

In the literature, the effect of reinforcement corrosion on the mechanical properties of steel has been modelled by either reducing its cross-sectional area or reducing its mechanical properties (ductility) due to a reduction in cross-sectional area. Reinforcement corrosion due to chlorides penetration leads to severe deterioration in the reinforcement material's mechanical properties, strength, and ductility. Over the years, several authors (Andrade et al. 1991; Zhang et al. 1995; Lee et al. 1996; Palsson and Mirza 2002; Du et al. 2005; Cairns et al. 2005; Lee and Cho 2009; Imperatore et al. 2017) have investigated experimentally the effect of reinforcement corrosion on the degradation of mechanical properties of steel. The tests differ in terms of the following:

- conditions (exposure to wet and dry cycles),
- corrosion type (chloride-induced corrosion or carbonation of the concrete cover),
- diameter size of the corroded reinforcement,
- testing set-up (reinforcement embedded vs. not embedded in concrete),
- corrosion rate and damage level.

A comparison between experimental results of different researchers on the effect of reinforcement corrosion on the mechanical properties of steel is presented in Table 2.1.

Andrade et al. (1991) tested ribbed bare (not embedded in concrete) bars with a diameter size of 12 mm using accelerated corrosion for a percentage of mass loss between 0-11%. The authors established an empirical equation to quantify the reduction in mechanical properties. Zhang et al.

(1995) tested ribbed bars embedded in concrete with a diameter size of 10-25 mm using service carbonation-induced corrosion for a percentage of mass loss between 0- 67%. Results showed a lesser reduction in mechanical properties compared to chloride-induced corrosion. This is typically attributed to the nature of carbonation-induced corrosion, which is characterized by uniform corrosion.

Lee et al. (1996) investigated the effect of different levels of reinforcement corrosion on the structural performance of concrete beams. The tested reinforcement was ribbed bars, with a diameter of 10 mm. The specimens were exposed to an accelerated corrosion regime with chlorides exposure for corrosion levels between 0-25%. The authors established an empirical equation to quantify the reduction in mechanical properties. Cairns et al. (2005) experimentally tested the effect of pitting corrosion on steel mechanical properties by using a hemispherical mill cutter to drill out some sections. From these tests, empirical equations and reduction factors were developed to estimate the reduction in yield and ultimate strength, modulus of elasticity and elongation of the steel.

Palsson and Mirza (2002) tested the mechanical properties of reinforcement extracted from the old Dickson Bridge in Montreal, Québec. The reinforcement was exposed to carbonation and chloride contamination. The authors concluded a severe reduction in toughness and strain values of the reinforcement as a result of corrosion and found that a 20% difference between the smallest and largest cross section leads to a 50% reduction in strain to failure.

Du et al. (2005) carried out tests on ribbed bare bars with variable diameter sizes (8, 16, 32 mm) using accelerated corrosion for corrosion levels between 0-25%. Du et al. (2005) also conducted experiments on exposed and embedded concrete bars exposed to accelerated corrosion to determine their properties. The authors found that corrosion affects both their shape and properties. The erosion of the ribbed face and roundness of the bar's circumference became irregular along the length and circumference due to variable penetration points of corrosion attack. For this reason, the authors believed that estimating the capacity of bars based solely on weight loss is inadequate. In addition, reinforcement corrosion results in a significant and rapid reduction in bars residual yield and ultimate capacity values, as shown in Fig. 2.13 and Fig. 2.14.

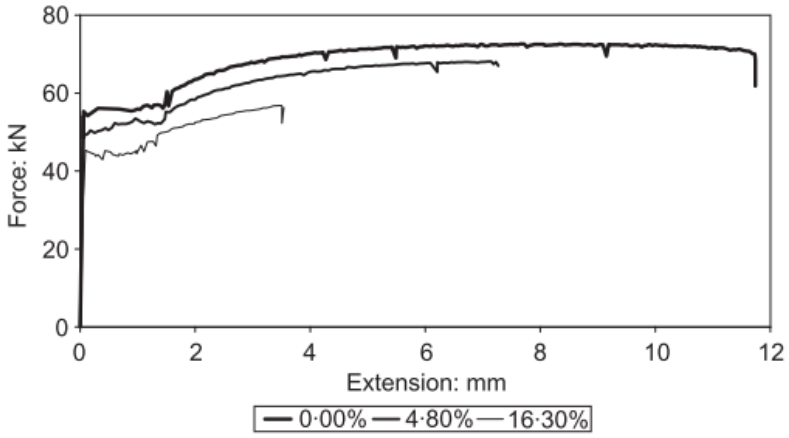

Fig. 2.13: Force-extension curve of corroded bars, at 4.8 and 16.3% mass loss (reproduced from Du et al. 2005)

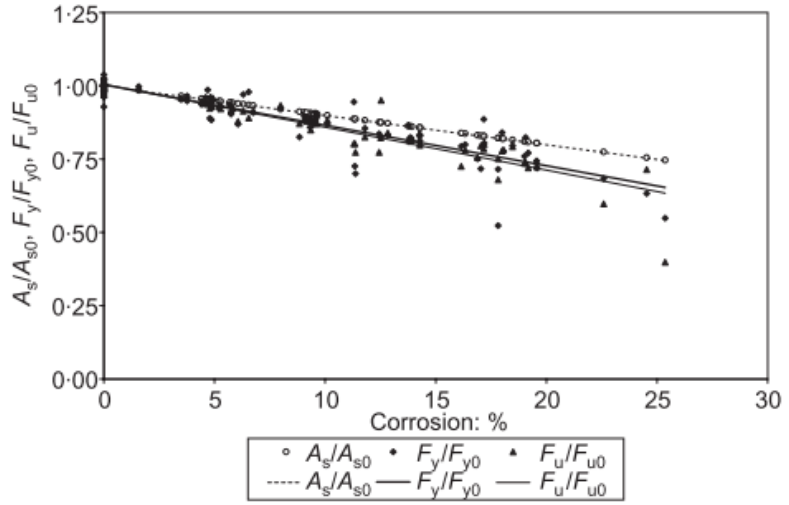

Fig. 2.14: Reduction in mechanical properties of the reinforcement as corrosion level is increased (reproduced from Du et al. 2005)

Lee and Cho (2009) carried out a more recent study that reported experimental work using a direct current in a chloride environment to trigger pitting corrosion. The ingress of chloride ions into the concrete specimens was accelerated by cyclic wetting and drying at high temperatures. The rebars were ribbed. The level of corrosion varied from 0-35%. Relationships were established between corrosion level and yield point, ultimate load, elastic modulus, and elongation ratio. The mechanical properties of corroded reinforcement induced by chloride ions were lower than those induced by the electric method at the same level of corrosion (Lee and Cho 2009).

Imperatore et al. (2017) conducted accelerated corrosion on bare bars at 100 μA to investigate the effect of carbonation-induced corrosion on the residual strength of steel. The authors proposed degradation equations based on the experimental results.

Table 2.1: Comparison between available studies on the effect of reinforcement corrosion on the degradation of steel properties

Authors	Bar Type	Bar Size	Method/Rate	Mass loss (%)	α_y	α_u	α_e
Andrade et al. (1991)	Bare, ribbed	12	10-100 μA/cm²	0-11%	0.015	0.013	0.017
Zhang et al. (1995)	Embedded, plain & ribbed	10-25	Carbonation	0-67%		--	
Lee et al. (1996)	Embedded ribbed	12	Chlorides 1300 μA/cm²	0-25%		0.014	
Palsson and Mirza (2002)	Embedded	Not stated	Carbonation and Chlorides	10-30%		--	
Du et al. (2005)	Bare & embedded	8,16,32	Bare 500-2000, embedded 1000 μA/cm²	0-25%	0.015	0.015	0.04
Cairns et al. (2005)	Embedded, plain, ribbed	16, 20	10-50 μA/cm², Saline conditioned	3%	0.012	0.011	0.03
Lee and Cho (2009)	Embed, ribbed	10,13	Chlorides (density not stated)	0-35%	0.012	0.011	0.02
Imperatore et al. (2017)	Bare	8,12,16,20	Chloride & carbonation 100 μA	0-60%		--	

α_y, α_u, α_e are experimental constants representing the reduction in yield strength, ultimate strength and steel elongation, respectively

Lee and Cho (2009) investigated the effect of chloride-induced reinforcement corrosion on the reduction in the mechanical properties of the reinforcement. The investigation was carried out over different levels of corrosion on embedded and ribbed reinforcement. Reduction in the geometry and mechanical properties of steel reinforcement due to uniform corrosion was accounted for using an empirical model developed by Lee and Cho (2009).

$$f_{cy} = \left(1 - 1.24\left(\frac{m_s}{100}\right)\right) f_y \qquad \textit{Eq. 2.36}$$

$$f_{cu} = \left(1 - 1.07\left(\frac{m_s}{100}\right)\right) f_u \qquad \textit{Eq. 2.37}$$

$$E_{cs} = \left(1 - 0.75\left(\frac{m_s}{100}\right)\right) E_s \qquad \textit{Eq. 2.38}$$

$$\varepsilon_{cu} = \left(1 - 1.95\left(\frac{m_s}{100}\right)\right) \varepsilon_u \qquad \textit{Eq. 2.39}$$

where $m_s$is the percentage mass loss, f_{cy}, f_{cu} are respectively the residual yield and ultimate stress after corrosion, f_y, f_u are respectively the yield and ultimate stresses before corrosion, E_{cs}, E_s are respectively the moduli of elasticity after and before corrosion, and ε_{cu}, ε_u are respectively the elongation before and after corrosion.

Reduction in the mechanical properties of steel reinforcement due to pitting corrosion was accounted for using an empirical model developed by Lee and Cho (2009).

$$f_{cy} = \left(1 - 1.98\left(\frac{m_s}{100}\right)\right) f_y \qquad \textit{Eq. 2.40}$$

$$f_{cu} = \left(1 - 1.57\left(\frac{m_s}{100}\right)\right) f_u \qquad \textit{Eq. 2.41}$$

$$E_{cs} = \left(1 - 1.15\left(\frac{m_s}{100}\right)\right) E_s \qquad \textit{Eq. 2.42}$$

$$\varepsilon_{cu} = \left(1 - 2.59\left(\frac{m_s}{100}\right)\right) \varepsilon_u \qquad \textit{Eq. 2.43}$$

The reduction in the mechanical properties of reinforcement subjected to pitting corrosion, according to Cairns et al. (2005) are determined as follows:

$$f_{cy} = (1 - \alpha_y . Q_{corr}) f_y \qquad \textit{Eq. 2.44}$$

$$f_{cu} = (1 - \alpha_u . Q_{corr}) f_u \qquad \textit{Eq. 2.45}$$

$$\varepsilon_{cu} = (1 - \alpha_1 . Q_{corr}) \varepsilon_u \qquad \textit{Eq. 2.46}$$

where f_y , f_u, ε_u are the yield strength, ultimate strength, and the ultimate strain of corroded bars, respectively, f_y, f_u, ε_u are the yield strength, ultimate strength, and the ultimate strain of non-corroded bars, respectively, Q_{corr} is the cross-section loss expressed as a percentage of the original cross-section, and α_y, α_u and α_1 are empirical coefficients as given in Table 2.1.
coefficients.

2.8.3.1 Corrosion-induced Rebar Buckling

Corrosion-induced cracking of the concrete cover and reduction in the cross-sectional area of confinement reinforcement (either stirrups or ties) can lead to premature buckling of longitudinal reinforcement subjected to compression. In RC columns, corrosion of the ties reduces their confinement effect due to a reduction in bar stiffness and strength. This increases the unsupported length of the longitudinal bars, increasing the potential risk of premature buckling of the reinforcement.

The compressive behaviour of the longitudinal reinforcement is primarily affected by the buckling length (effective unsupported length). Subsequently, it is influenced by the stiffness of the transverse reinforcement laterally restraining the longitudinal bars. Thus, failure of the longitudinal reinforcement is dependent on:

- Spacing between the adjacent transverse reinforcement,
- Axial stiffness of the transverse reinforcement,

Yield strength of longitudinal reinforcement.

Rodriguez et al. (1996), Tapan and Aboutaha (2011), and Li et al. (2020) used several formulations to estimate the critical stress of the corroded reinforcement at which buckling occurs. Rodriguez et al. (1996) used the following formulation to calculate the theoretical Euler load:

$$P_{cr} = \pi E[0.25d]^2 / [0.75s]^2 \qquad \textit{Eq. 2.47}$$

where P_{cr} is the Euler critical load, E is the modulus of elasticity, d is the diameter of the longitudinal bar, s is the spacing of the transverse reinforcement, and 0.75s is considered the effective length of the main bars.

Tapan and Aboutaha (2011) estimated the buckling strength of the corroded reinforcement subjected to axial compression loading according to AISC Spec E2 (AISC 2017).

$$P_{cr} = A_g . f_{cr} \qquad \textit{Eq. 2.48}$$

$$f_{cr} = 0.658^{\lambda_c^2} . f_y \; for \lambda_c \leq 1.5 \qquad \textit{Eq. 2.49}$$

$$f_{cr} = \left(\frac{0.877}{r_c^2}\right) . f_y \; for \lambda_c \geq 1.5 \qquad \textit{Eq. 2.50}$$

where the slenderness (λ_c) is estimated as follows:

$$\lambda_c = \frac{k}{r}.\frac{L}{\pi}.\sqrt{\frac{f_y}{E}} \qquad \textit{Eq. 2.51}$$

where P_{cr} is the buckling load, A_g is the gross area of the bar, f_{cr} is the critical buckling stress of corroded reinforcement, f_y is the yield stress, k is the effective length factor, L is the laterally unbraced and exposed length of the bar, r_c is the governing radius of gyration about the axis of buckling, and E is the steel modulus of elasticity.

Li et al. (2020) examined the coupling effect of sustained loads and reinforcement corrosion on the structural performance of RC columns. The authors observed that columns transition into a brittle failure as the corrosion level increases to a mass loss of 20% along with an increase in the sustained loads (0-60%). The authors proposed a buckling model to investigate the buckling potential of the compressive longitudinal bars due to corrosion (Fig. 2.15). According to elastic theory (Chen and Lui 2018), the buckling capacity of the compressive rebar with elastic support is given as follows.

$$P_{cr} = \frac{0.6\,\pi^2 E.I_s}{L_{corr}^2} + 2\sqrt{C_{eq}E.I_s} \qquad \textit{Eq. 2.52}$$

where $P_{cr}$is the buckling load of the compressive rebar, $I_s$is the moment of inertia of the primary reinforcement, E is the modulus of elasticity of the primary reinforcement, L_{corr} is the corrosion length of the longitudinal reinforcement, and parameter $C_{eq}$is estimated as follows:

$$C_{eq} = \frac{k_t}{s}, k_t = \frac{E_t A_t}{l_{st}} \qquad \textit{Eq. 2.53}$$

where $k_t$is the stiffness of the tie, A_t is the remaining cross-sectional area of the tie, l_{st} is the length of the tie, and $E_t$is the modulus of elasticity of the tie. If the buckling load is larger than the yielding capacity of the reinforcement, then it is unlikely that the reinforcement will buckle. More so if the transverse reinforcement (stiffness and spacing) provides sufficient lateral restraint to the longitudinal reinforcement.

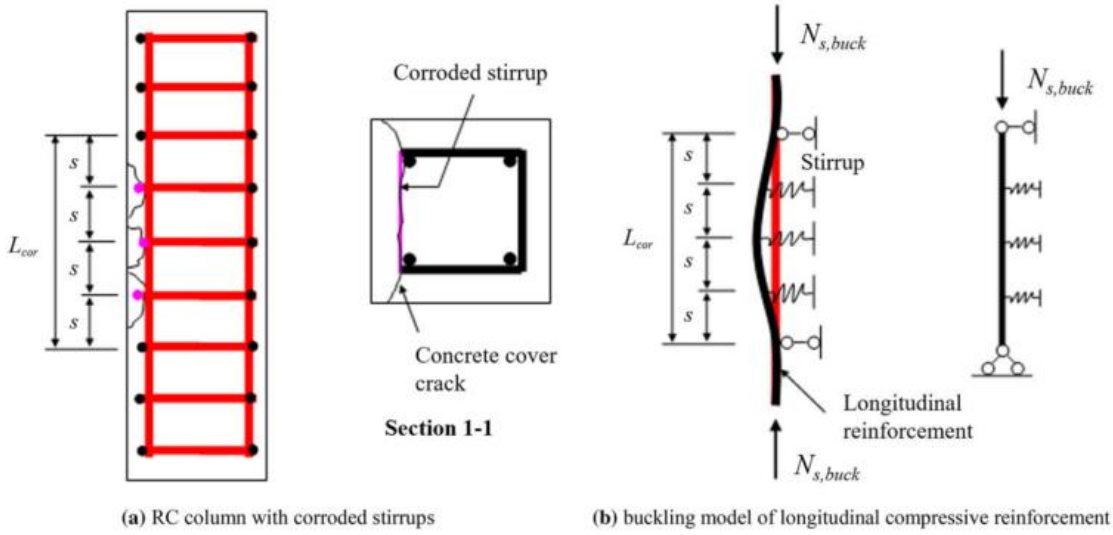

Fig. 2.15: Proposed buckling model of the longitudinal rebar (reproduced from Li et al. 2020)

2.9 Effect of Reinforcement Corrosion on Concrete Cover and Residual Strength of RC Columns

Analytical, numerical and experimental studies have been conducted to investigate the effect of reinforcement corrosion on the structural performance of RC columns. Several factors affect the structural performance of corroded RC columns, such as the extent and pattern of reinforcement corrosion, load eccentricity, and reinforcement details such as tie spacing. This section reviews available research on the effects of different reinforcement corrosion levels and patterns on the degradation of the concrete cover, residual strength, stiffness, ductility and confinement of RC columns subjected to eccentric loads. It also reviews research methods utilized to evaluate the concrete cover loss and residual capacity and confinement. The review is focused only on corroded RC columns with rectangular cross-sections and subjected to an eccentric compressive load. The content of this section has been adapted from a paper originally published in the 2021 CSCE Annual Conference (Dabas, M., Martín-Pérez, B., and Almansour, H. (2021). "Effects of different patterns of reinforcement corrosion on the concrete cover and residual strength in aged bridge piers: State-of-the-Art Review." *CSCE 2021 Annual Conference*, online.)

2.9.1 Experimental Studies

Rodriguez et al. (1996) tested corroded RC columns 2,000-mm long with three different reinforcing details. An axial load was applied concentrically atop the column. The longitudinal rebars were subjected to a current density of 100 $\frac{\mu A}{cm^2}$. A 3% by weight of cement of $CaCl_2$ was added to the concrete mix to accelerate the corrosion process. The experimental results highlighted a reduction in the overall load capacity, mean strain, and the RC columns' compressive stiffness. It was found that the overall capacity of the column is affected by several parameters, mainly an increase in the load eccentricity due to asymmetrical deterioration associated with reinforcement corrosion. This led to premature buckling of the reinforcement and cracking/spalling of the concrete cover. Premature buckling of the rebar, observed after column failure, was attributed to a reduction in stiffness of the concrete cover and failure of the tie. The authors estimated the reduction in the reinforcement capacity using Euler's formula. The effective length of the longitudinal rebar is taken as 0.75s.

Wang and Liang (2008) tested 11 RC columns (1,300-mm). The authors subjected partial length (350 or 700-mm) of the longitudinal bars at the mid-zone of the column to an accelerated corrosion regime using a DC power supply for a specified time. Wet sheets were wrapped around the mid-section of the columns to maintain the corrosion process, which were sprayed several times a day. Subsequently, a compressive load was applied at two eccentricities (50 and 150 mm). A more significant reduction in ultimate capacity was found for the smaller eccentricity with partial corrosion of the longitudinal bars along the compression zone. In contrast, for the larger eccentricity, it was found that a more considerable reduction in ultimate capacity resulted from partial corrosion of the longitudinal bars along the tension zone. In general, partial corrosion of the column generated longitudinal cracks and spalling of the concrete cover along the corroded longitudinal bars, reduced the overall load capacity, generated irregularities (due to asymmetry of corrosion), and reduced the confinement effects due to corrosion of the ties in the mid-section.

Wang et al. (2012) extended previous work (Wang and Liang 2008) to include all tested specimens in this study. The author investigated the effect of extent and location of corrosion on the structural performance of 20 (1,300-mm long) RC columns subjected to loading at small (50 mm) and large (150 mm) eccentricities. For both eccentricity values, 18 columns were either corroded along the tensile, compressive, or tensile and compressive zones for a partial length of 700 mm. For small

eccentricity, a more significant reduction in mass loss in the compression zone resulted in a more significant reduction in the ultimate capacity and stiffness, in addition to higher mid-span deflection. For equally corroded reinforcement on both compression and tension zones, it was observed that there is a higher decrease in the column stiffness compared to columns that were partially corroded along either the tension or compression zones. Also, the reduction in ultimate capacity was more significant when the corrosion level was increased and spread along the compression and tension zones of the column. As the corrosion level was increased on both tension and compression reinforcement and ties, the ultimate capacity and stiffness of the column was reduced, and the response was less ductile. For columns loaded at large eccentricities, a high corrosion level in both compression and tension zones resulted in a reduction in the ultimate capacity of the columns. There was a more significant reduction in ultimate capacity and ductility response for asymmetrical deterioration.

Li et al. (2012) conducted experimental tests on 12 columns (450 mm) subjected to accelerated corrosion using a DC power supply followed by an axial compression test. The testing regime intended to corrode the ties only at various corrosion degrees. The results were assessed in terms of changes in material stress-strain curves, bearing capacity, failure mode, deformation and confinement effects. The current density of the test was set to a range of 200 to 500 $\mu A/cm^2$ for 10 to 50 days. At 80-100% of the peak load, new vertical cracks appeared in addition to spalling of the concrete cover. After the peak, both corrosion-induced and newly formed cracks rapidly propagated, leading to concrete spalling. The test ended when the longitudinal rebars buckled and the ties fractured at the corner side of the column. Reduction in the cross-section area of the ties resulted in a reduction in column stiffness and ultimate bearing capacity. In addition, the mode of failure changed from ductile to brittle failure.

Azad and Al-Osta (2014) conducted extensive experimental work to test 48 specimens to estimate residual strength. The authors tested two groups (24 specimens each) of small-scale (1,350-mm long) RC columns with different cross-sections and reinforcement sizes. The compressive load was applied at three eccentricity values: 30, 60 and 95 mm for one group and 35, 65 and 115 mm for another. To corrode the middle section of the columns, the authors utilized an accelerated corrosion method using a constant current of 250 $\frac{\mu A}{cm^2}$ for 7, 10 and 11.5 days. The authors proposed a reduction factor established from a multi-regression analysis of test data to account for the effects

of corrosion damage. It is a function of member size and diameter reduction, and it accounts for bond degradation, cracks damage and possible variation in yield strength of the reinforcement. The reduction factor was validated with experimental tests from Wang and Liang (2008). The residual strength value was then calculated by multiplying the reduction factor with the undamaged value. In conclusion, for a compression-controlled column (with an eccentricity e over height h ratio of $e/h \leq 0.17$), the entire section remains in compression; hence, the reduced cross-sectional area of the corroded steel has a minimum effect on the ultimate capacity reduction. The ultimate capacity of the column is governed by the reduction of the compressive strength of the concrete cover due to crack growth. The failure of columns with e/h=0.16 occurred on the side that experienced high compressive stresses. For cases with $e/h > 0.16$, transverse cracks appeared on the tension side of the column. It was found that as the corrosion period is increased, the corrosion damage is more extensive. Also, the flexural rigidity of the corroded columns is reduced compared to non-corroded ones.

Tapan et al. (2016) conducted experimental work on 12 (350-mm long) columns to investigate the effect of tie corrosion on confinement strength. The 12-mm diameter longitudinal bars were enveloped by ties with a diameter size of 8 mm spaced at 10 mm. The columns were corroded using an accelerated corrosion regime with a DC power supply with a current output of 6A, while being submerged in 5% NaCl solution to produce different levels of tie section loss (5, 10, 15, 20, 25, 30, 35, 40, 45 and 50%). The RC columns were then subjected to an axial compressive load until failure. The deterioration of the ties had very significant effects on the structural response. The ultimate capacity of the columns was reduced as the rate of the corrosion level was increased. The author found evidence of tie debonding and concrete cover cracking. According to the author, pitting corrosion was not considered for simplicity; hence, section loss was estimated by measuring the average weight loss of the damaged tie. The author found that cross-sectional loss is non-uniform along the tie length. From the experimental results, the author concluded that confinement effects are reduced due to tie corrosion. The author recommended a detailed and full-scale testing program to determine the effect of tie corrosion on the confinement strength, ultimate capacity and failure mode.

Xia et al. (2016) tested 24 (1,500-mm long) RC columns to determine their structural performance and evaluate the relationship between reinforcement cross-sectional loss and maximum crack width of the concrete cover. The specimens were corroded using an accelerated corrosion method

at a current density of 200 μA/cm^2 while exposed to wet and dry conditions. A compressive load was applied at two eccentricity values of 50 and 90 mm for two sets of columns with different tie spacings (200 and 100 mm). The relationship between cross-sectional area loss of steel, maximum crack width of the concrete cover and strength loss of the RC column was analysed. The residual compressive strength of the column was estimated from measured crack widths of the concrete cover. The authors found that increasing the level of corrosion leads to adverse effects on column strength, stiffness, and mechanical properties of both steel and concrete materials. Also, the crack opening increased as the corrosion level increased. The column stiffness and strength decreased as the loading eccentricity, and corrosion level was increased.

Vu et al. (2017) investigated the effect of corroded transverse reinforcement on the stress-strain curve of confined concrete. The authors tested 36 columns with a length of 600 mm and 200 mm, either square or circular cross-sections, with three different transverse reinforcement layouts at different corrosion levels. Transverse reinforcement was subjected to an accelerated corrosion method using a DC power supply with a current density of 500 $\frac{\mu A}{cm^2}$ while immersed in a 5% NaCl solution. Three methods were used to estimate the corrosion degree: mass loss, average cross-section, and residual cross-section loss.

To measure the effect of crack width on the stress-strain relations of confined concrete, the average crack width w_{cr} was defined as the total crack width measured on the four sides of the specimen along the length L of the specimen:

$$w_{cr} = \frac{\sum w_{cri} L_i}{L} \qquad \textit{Eq. 2.54}$$

where L_i is the crack length, and w_{cri} is the width of the crack

The reduction of the concrete compressive strength f_r was estimated according to Eq. 2.68:

$$f_r = \frac{0.9}{\sqrt{1+600\varepsilon_r}} \qquad \textit{Eq. 2.55}$$

where the tensile strain induced by cracks ε_t was estimated as follows:

$$\varepsilon_t = \frac{w_{cr}}{p_o} \qquad \textit{Eq. 2.56}$$

where p_o is the perimeter of the cross section

For corrosion levels of 15-30%, the transverse ties were fractured due to severe pitting. This resulted in a significant reduction in the concrete confinement strength, followed by a buckling of the longitudinal bars. Furthermore, these specimens exhibited a brittle response with a significant reduction in ultimate strength. Specimens with corrosion levels lower than 10% failed by buckling of the longitudinal bars and exhibited a more ductile response. Furthermore, it was found that the ultimate strength, peak stress, and strain values were reduced for low volumetric ratios of transverse reinforcement, and the specimens had a brittle mode of failure. For example, for a square section with a volumetric ratio of 2.51 and 0.97% and corrosion levels of 16.7 and 17.5%, there is a 10% and 22.3% reduction in peak stress, respectively, compared to non-corroded sections.

Furthermore, there is a 13.8% and 31.3% reduction in ultimate strain, respectively, compared to non-corroded sections. From the experimental results, Vu et al. (2017) proposed an analytical stress-strain model based on the model by Mander et al. (1988) for confined concrete that applies to both square and circular cross section with different transverse volumetric ratios. The results of this model were verified with the experimental tests from both square and circular cross sections and three different reinforcement layouts.

2.9.2 Analytical Studies

Rodríguez et al. (2002) calculated the axial force of RC columns tested by Rodriguez et al. (1996) using conventional models. To account for corrosion, the cross-sectional area of the steel was reduced, and the concrete cover was removed on one side or on all sides. The authors developed four axial load-moment curves that consider: non-deteriorated case, removal of two or three ties, and complete removal of concrete on all sides. Experimental data were fitted within the curves and aligned with the curve that considers tie failure. It was found that the structural behaviour of the analysed columns (eccentricity values of 0 and 20 mm) is mainly controlled by: concrete cover degradations, increased load eccentricities due to irregular damage associated with reinforcement corrosion, and the premature buckling of steel.

Tapan and Aboutaha (2008, 2011) investigated the effect of reinforcement corrosion and loss of concrete cover on the structural response of RC columns using interaction diagrams. Six different cases of reinforcement corrosion patterns with different corrosion levels were investigated for a cover-to-diameter (c/d) ratio of 1 (Fig. 2.16). This was established using a modified analytical

approach. The authors proposed a modified procedure to calculate interaction diagrams by considering material degradation in concrete and steel due to section and bond loss and asymmetry. A bilinear stress-strain curve for corroded reinforcement was used, taking into account the strength reduction of the reinforcement. The reduction in yield stress f and cross section A_s of the reinforcement was estimated based on the expressions proposed by Du et al. (2005):

$$f = \left(1 - 0.005 Q_{corr}\right) f_y \qquad \textit{Eq. 2.57}$$

$$A_s = A_{s0}\left(1 - 0.01 Q_{corr}\right) \qquad \textit{Eq. 2.58}$$

Where Q_{corr} is the amount of corrosion (%) given by:

$$Q_{corr} = \frac{0.046 \cdot I_{corr} \cdot t}{d} \qquad \textit{Eq. 2.59}$$

Where f and f_y are the yield strength of corroded and non-corroded steel, respectively, A_{s0} is the initial cross-sectional area of non-corroded steel, A_s is the average cross-sectional area of corroded steel, d is the diameter of non-corroded steel, I_{corr} is the corrosion rate in the reinforcement ($\mu A/cm^2$), and t is the time elapsed since the initiation of corrosion (years)

Tapan and Aboutaha (2011) accounted for the strain change along the corroded region of the longitudinal bar.

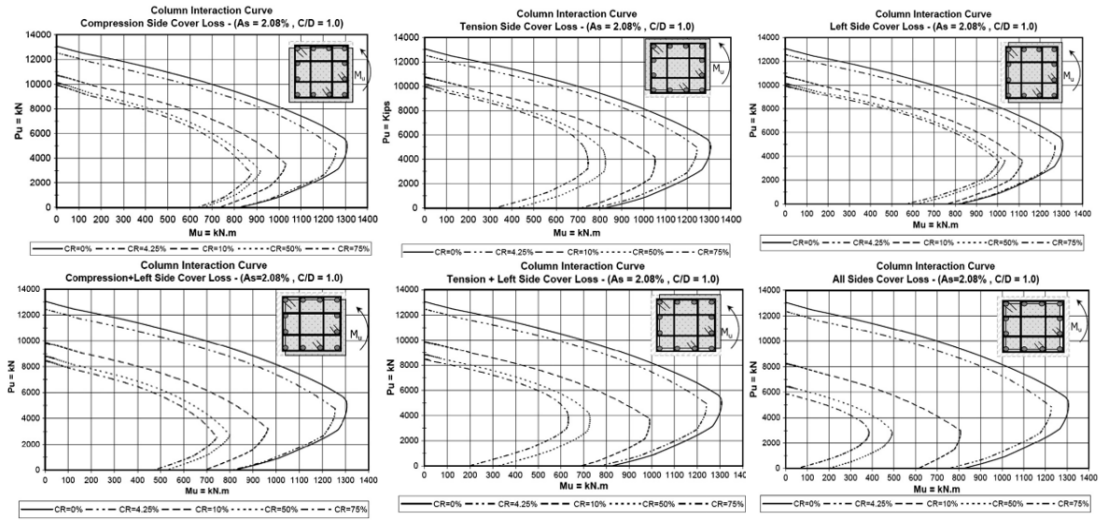

Fig. 2.16: Interaction diagrams for six different cases of corrosion patterns with different corrosion rates (reproduced from Tapan and Aboutaha 2011)

Furthermore, longitudinal bars are more vulnerable to buckling due to the loss of concrete cover; subsequently, the affected bars are exposed. Also, corrosion of the ties increases the unsupported length of the longitudinal bars. Tapan and Aboutaha (2011) estimated the buckling strength of compression members subjected to concentric loading according to AISC Spec E2 (AISC 2017). The loss of concrete cover was estimated based on a numerical model which analyses the effect of volume increase of the corrosive products on the cover cracking (Pantazopoulou and Papoulia 2001; Wang and Liu 2004). Based on the above, Tapan and Aboutaha (2011) concluded that corrosion of the reinforcement reduces the ultimate strength of the column depending on the location and exposed length of the corrosion. The authors reported a 7-17% reduction in ultimate capacity for corroded longitudinal bars on the compression zone, while a 16-41% reduction was found on the tension zone of the corroded longitudinal bars. This is because corrosion of the reinforcement on the compression side reduces the effective depth and leads to a more ultimate reduction in capacity for compression-controlled columns. However, corrosion of the tension reinforcement causes more strength reduction for tension-controlled columns subjected to load eccentricity. It was reported that reinforcement corrosion on all sides of the column causes the most severe reduction in ultimate strength.

Campione et al. (2017) proposed a simple analytical model to estimate the moment-axial force curves for corroded columns. The model considers material deterioration, concrete cover spalling, loss of bond, rebar buckling, and reduction in confinement effects due to tie corrosion. The analytical model estimates only specific points on the interaction diagram, such as pure bending, pure axial load, balanced point, and a point having some pure moment and axial force. In the development of the model, the compressive strength for confined concrete was calculated according to Razvi and Saatcioglu (1999). The reduction in the compressive strength of the concrete cover due to cracks induced by rust expansion was estimated according to a study by Coronelli and Gambarova (2004) who suggested incorporating the crack width model of Molina et al. (1993) into the model developed by Vecchio and Collins (1986).

For compression-controlled columns, it was found that under severe conditions of reinforcement corrosion, there is about 20-30% reduction in the ultimate capacity, which was mainly affected by the significant reduction in the compressive strength of the concrete cover and not by reinforcement mass loss. On the contrary, the ultimate capacity of flexure-controlled columns is

mainly reduced by mass loss of the reinforcement and bond loss, with about a 40% decrease in ultimate strength associated with a 15-20% mass loss of reinforcement. The developed model had a good agreement with experimental and analytical results established from previous research work.

Xin et al. (2018) proposed an analytical model to evaluate the bearing capacity of corroded RC columns under eccentric loads based on Hermite interpolation and Fourier function. The first step of the model estimates the degradation of concrete and steel properties due to reinforcement corrosion. The model accounts for the reduction in bond strength, confinement effects, cross-section reduction of the steel, buckling of the longitudinal bars and concrete cover cracking for three points on the column interaction diagram (axial load point, balanced load point and pure bending point). The interpolation points were determined through piecewise cubic Hermite interpolating polynomials, and curve fitting was conducted through the trigonometric Fourier series model. The cross-section of the RC column was divided into different regions: unconfined concrete, cracked confined concrete, uncracked confined concrete and the area of the longitudinal reinforcement considering the buckling mechanism. The model was verified with data collected from experimental work on 45 RC columns conducted by different researchers. In addition, the interaction diagrams estimated using this method agreed well with the ones estimated using the analytical model proposed by both Tapan and Aboutaha (2011) and Campione et al. (2017).

2.9.3 Numerical Studies

Mohammed et al. (2018) proposed a simplified Nonlinear Finite Element Analysis (NFEA) to assess the residual capacity of corroded aged beam-columns. The NLFEA evaluates the structural performance of corroded slab-on-girder bridge columns under the application of external loads. The NLFEA determines the instantaneous stiffness through the transfer of axial and flexural rigidities from the section level to the member level. The effects of reinforcement corrosion on material degradations of both concrete cover, reinforcement strength reduction and bond loss are incorporated into the model. The model was verified with four cases from previous experimental and analytical work conducted by different researchers.

Dabas et al. (2020) developed a 3D nonlinear Finite Element Model (FEM) using ABAQUS software to determine the structural response of large-scale (2.2 m) corroded RC columns. The columns were subjected to a small eccentric load of 30 mm atop the column. In the numerical

model development, concrete response in compression for unconfined concrete was defined using Hognestad's parabola, while the model proposed by Razvi and Saatcioglu (1999) was used for confined concrete. An elastoplastic model was used to simulate the stress-strain relationship of the steel reinforcement. Reinforcement corrosion was simulated by reducing the reinforcement cross section or by removing corroded ties. In addition, the stiffness of the concrete cover was reduced by 50% to account for severe corrosion-induced cracking.

Furthermore, Euler's equation was used to calculate the critical buckling stress for the longitudinal bars along the exposed length. The 3D numerical model evaluated the RC structural behaviour for two different patterns of corrosion exposure: (i) corrosion of two ties at the mid-section of the column with cover stiffness reduction, (ii) corrosion in the compression rebars and cover stiffness reduction. The numerical model was validated with experimental work reported by Xia et al. (2016). The numerical results of the model indicated that for high-corrosion levels (50% of steel area reduction), the ultimate capacity of the RC column was reduced, and the column had a brittle failure mode. When mid-ties were compromised, the exposed and unsupported length of the longitudinal rebars was increased, and confinement effects were reduced, both leading to buckling of the longitudinal bars (Fig. *2.17*).

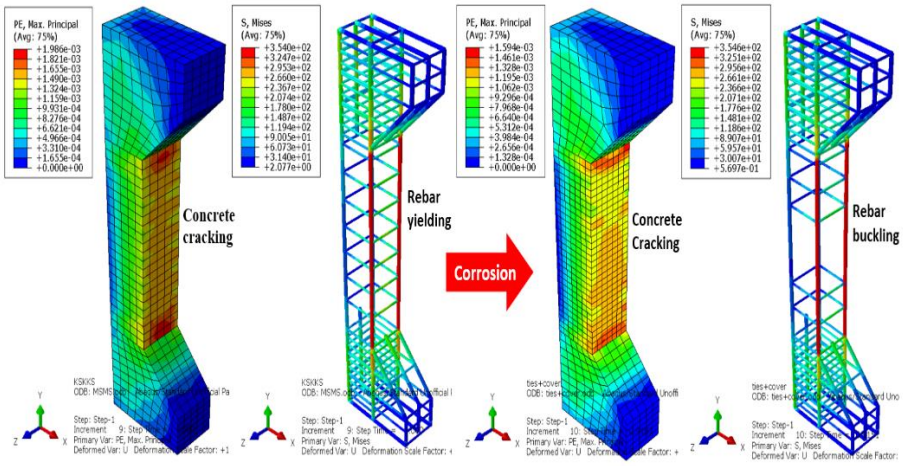

Fig. 2.17: Comparison between failure of non-corroded and corroded columns (Dabas et al. 2020)

2.9.4 Estimation of Concrete Cover Loss

The loss of the concrete cover due to severe cracking and spalling leads to a reduction in concrete strength; subsequently, the ultimate capacity of the RC column is reduced. Xia et al. (2016)

examined the pattern and amount of both tie and longitudinal corrosion on the concrete cover loss. Subsequently, equations were developed to determine the effective cross section of the concrete based on tie spacing and cover depth. Xia et al. (2016) modified the equation proposed by Higgins.C. et al. (2003) to account for various angles of wedge spalling-off (ϕ or β) due to transverse or longitudinal reinforcement corrosion. The authors estimated the effective cross-section of the column (b_{eff} and h_{eff}) damaged by corrosion of the ties according to the followings:

$$b_{eff} = \begin{cases} b - 2\left(c + d_v\right) + \dfrac{s\tan\phi}{2} & s < 2c\cot\phi \\ b - \dfrac{2}{s\tan\phi}\left(c + d_v\right)^2 & s \geq 2c\cot\phi \end{cases} \qquad \textit{Eq. 2.60}$$

$$h_{eff} = \begin{cases} h - 2\left(c + d_v\right) + \dfrac{s\tan\phi}{2} & s < 2c\cot\phi \\ h - \dfrac{2}{s\tan\phi}\left(c + d_v\right)^2 & s \geq 2c\cot\phi \end{cases} \qquad \textit{Eq. 2.61}$$

where b and h are the original width and height of the undamaged column, respectively, s is the tie spacing, c is the concrete cover, d_v is the tie diameter, and ϕ is the angle for corrosion-induced spalling at tie locations (determined from test measurements). The effective concrete cover depth c_{eff} affected by tie corrosion can be obtained as follows:

$$c_{eff} = \begin{cases} \left(c + d_v\right) - \dfrac{s\tan\phi}{2} & s < 2c\cot\phi \\ \dfrac{1}{s\tan\phi}\left(c + d_v\right)^2 & s \geq 2c\cot\phi \end{cases} \qquad \textit{Eq. 2.62}$$

Xia et al. (2016) found that the location and number of corroded reinforcing bars significantly affect the damage of the concrete cross section. The effective concrete cross-section affected by corroded ties and longitudinal bars can be obtained as follows.

$$\bar{b}_{eff} = b_{eff} - (2 + cot\,\beta)\left(c_{eff} + d\right) \qquad \textit{Eq. 2.63}$$

$$\bar{h}_{eff} = h_{eff} - (2 + cot\,\beta)\left(c_{eff} + d\right) \qquad \textit{Eq. 2.64}$$

The effective loss of cover length is estimated as follows.

$$\bar{t}_{eff} = \left(1 + \frac{cot\,\beta}{2}\right)\left(c_{eff} + d\right) \qquad Eq.\ 2.65$$

where d is the diameter of the longitudinal bar, β is the angle of the spalling wedge caused by corrosion of the longitudinal bars, $\bar{b}_{eff} \times \bar{h}_{eff}$ is associated with the instant when the concrete section no longer resists the applied load and $\bar{t}_{eff}$ is the length of cover that is lost.

Xia et al. (2016) proposed an analytical model to estimate the ultimate load capacity for corroded columns, which considers bond degradation and concrete cover loss based on the affected reinforcement, as shown in Fig. 2.18.

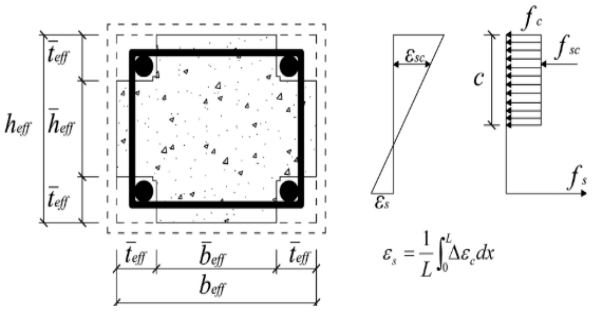

Fig. 2.18: Equivalent cross-section damaged by corroded ties (reproduced from Xia et al. 2016)

2.10 Combined Effects of Multiple Deteriorations Mechanisms on the Performance of RC Columns

Freezing and thawing cycles (FTC) on RC columns are a significant problem for vulnerable infrastructure exposed to extreme climate conditions. This problem is exacerbated by the presence of de-icing that leads to reinforcement corrosion and overall concrete deterioration. Current research has mainly focused on studying the mechanical properties of concrete when exposed to cyclic conditions of freezing and thawing. Few studies have analysed FTC's influence or the dual action of FTC and steel corrosion on the structural performance of RC. A review of available literature on the synergistic effects of one or multiple environmental exposures on RC columns and methodologies for inducing frost damage according to current standards has been published in the ASCE Journal of Performance of Constructed Facilities (Dabas, M., Martín-Pérez, B., and Almansour, H. (2021). "Combined effects of freeze/thaw and corrosion on the performance of RC structures: state-of-the-art review." *Journal of Performance of Constructed Facilities*, **35**(5), 03121002). This review, which is presented in Appendix A, is organized into the following

sections: (1) frost damage mechanism; (2) test methods to evaluate frost damage; (3) effect of FTC on concrete mechanical properties; (4) effect of FTC on the structural performance of RC columns; and (5) effect of dual action of FTC and steel corrosion on RC columns. The paper draws a series of conclusions and recommendations for future work based on the review.

2.11 Gap in the State-of-the-Art

Currently, there is limited research on the structural behaviour, residual strength, material degradations and failure mode of corroded RC columns subject to eccentric load. All recent work is limited to small-scale corroded columns (Wang and Liang 2008; Wang et al. 2012; Azad and Al-Osta 2014; Tapan et al. 2016; Vu et al. 2017). Wang and Liang (2008) and Wang et al. (2012) conducted the most extensive experimental work on the effect of partial length and location of reinforcement corrosion on the structural performance of columns subjected to load at small and large eccentricity levels. Azad and Al-Osta (2014) evaluated the residual strength of corroded columns with different reinforcement layouts. For both Wang et al. (2012) and Azad and Al-Osta (2014), the corrosion level of the experiment is limited to mass losses lower than 10-15%. Moreover, limited information is provided on the post-peak response of the corroded columns. Therefore, it is necessary to investigate the effect of higher corrosion levels on columns as the structural response becomes more critical along with the increase in load eccentricity value. There is a significant need to evaluate the residual strength and post-peak response of corroded columns with different corrosion patterns and degrees while monitoring crack evolution before and after failure. Furthermore, it is essential to investigate the reduction in confinement strength due to tie corrosion in large-scale columns and to understand the post-peak response of corroded columns.

To address this need, experimental work on 2,200-mm columns was conducted to investigate the effect of different steel corrosion patterns due to chloride-induced corrosion under cyclic exposure to wet and dry conditions on the structural performance of RC columns. The columns were tested under both concentric and eccentric loads. Crack evolution was monitored and recorded periodically. Experimental work has been complemented with 3D nonlinear numerical modelling using Diana software to evaluate the post-peak response of corroded columns at various corrosion scenarios. The model takes into account steel and concrete degradations due to corrosion. It considers the confinement effects of the core concrete, buckling of the longitudinal bars and bond-

slip behaviour. Using both experimental and numerical approaches, this study concludes with simplified approach to evaluate and predict the ultimate capacity of RC columns affected by corrosion.

2.12 References

ACI 408. (2003). "Bond and Development of Straight Reinforcing Bars in Tension Reported by ACI Committee 408." ACI 408-03, 1–49.

Al-Sulaimani, G. J., Kaleemullah, M., Basunbul, I. A., and Rasheeduzzafar. (1990). "Influence of corrosion and cracking on bond behaviour and strength of reinforced concrete members." ACI Structural Journal, 87(2), 220–231.

Almusallam, A. A., Al-Gahtani, A. S., Aziz, A. R., and Rasheeduzzafar. (1996). "Effect of reinforcement corrosion on bond strength." Construction and Building Materials, 10(2), 123–129.

Alonso, C., Andrade, C., Castellote, M., and Castro, P. (2000). "Chloride threshold values to depassivate reinforcing bars embedded in a standardized OPC mortar." Cement and Concrete Research, 30(7), 1047–1055.

Alonso, C., Andrade, C., Rodriguez, J., and Diez, J. M. (1998). "Factors controlling cracking of concrete affected by reinforcement corrosion." Materials and Structures/Materiaux et Constructions, 31(211), 435–441.

Altoubat, S., Maalej, M., and Shaikh, F. U. A. (2016). "Laboratory Simulation of Corrosion Damage in Reinforced Concrete." International Journal of Concrete Structures and Materials, Korea Concrete Institute, 10(3), 383–391.

Amleh, L. (2000). Bond Deterioration of reinforcing steel in concrete due to corrosion. Dissertation, A thesis submitted to the Faculty of Graduate Studies and Research in partial fulfilment of the requirements for the degree of Doctor of Philosophy, Department of Civil Engineering and Applied Mechanics McGill University, Montreal, Canada.

Andrade, C. (2007). Corrosion of steel reinforcement-Chapter 6. Environmental Deterioration of Materials, (A. Moncmanová, ed.), WIT Transactions on State of the Art in Science and Engineering.

Andrade, C. (2019). “Propagation of reinforcement corrosion: principles, testing and modelling.” Materials and Structures/Materiaux et Constructions, Springer Netherlands, 52(1), 1–26.

Andrade, C. (2020). “Initial steps of corrosion and oxide characteristics.” Structural Concrete, 21(5), 1710–1719.

Angst, U. M. (2018). “Challenges and opportunities in corrosion of steel in concrete.” Materials and Structures, Springer Netherlands, 51(1), 1–20.

Apostolopoulos, C. (2012). “The Consequences of Chloride-Induced Corrosion on Steel Bar and Reinforced Concrete Structures.” Journal of Applied Mechanical Engineering, 01(04), 1–2.

Azad, A. K., and Al-Osta, M. A. (2014). “Capacity of corrosion-damaged eccentrically loaded reinforced concrete columns.” ACI Materials Journal, 111(6), 711–722.

Bertolini, L. (2008). “Steel corrosion and service life of reinforced concrete structures.” Structure and Infrastructure Engineering, 4(2), 123–137.

Bertolini, L., Elsener, B., Pedeferri, P., Redaelli, E., and Polder, R. (2014). “Corrosion of steel in concrete: prevention, diagnosis, repair.” Corrosion of steel in concrete: prevention, diagnosis, repair, John Wiley & Sons, Ltd, 20.

Bhargava, K., Ghosh, A. K., Mori, Y., and Ramanujam, S. (2008). “Suggested Empirical Models for Corrosion-Induced Bond Degradation in Reinforced Concrete.” Journal of Structural Engineering, 134(2), 221–230.

Boyle, J., Cunningham, M., and Dekens, J. (2013). Climate change adaptation and water resource management: A review of the literature. Energy Economics, Winnipeg, Manitoba, Canada.

Broomfield, J. (1997). Corrosion of steel in concrete: understanding, investigation and repair. Taylor & Francis, London.

Broomfield, J. P. (2007). Corrosion of Steel in Concrete understanding, investigation and repair. Taylor & Francis, London, New York.

Cabrera, J. G. (1996). “Deterioration of Concrete Due to Reinforcement Steel Corrosion.” 9465(95), 47–59.

Cairns, J., Plizzari.G.A., Law, D., and Franzoni.C. (2005). “Mechanical properties of corrosion-damaged reinforcement.” ACI Materials Journal, 102(4), 256–264.

Campione, G., Cannella, F., Cavaleri, L., and Ferrotto, M. F. (2017). “Moment-axial force domain of corroded R.C. columns.” Materials and Structures/Materiaux et Constructions, Springer Netherlands, 50(1), 1–14.

Caré, S., and Raharinaivo, A. (2007). “Influence of impressed current on the initiation of damage in reinforced mortar due to corrosion of embedded steel.” Cement and Concrete Research, 37, 1598–1612.

Chen, W.., and Lui, E. (2018). Stability design of steel frames. CRC Press Taylor & Francis Group, New York,USA.

Chung, L., Cho, S. H., Kim, J. H. J., and Yi, S. T. (2004). “Correction factor suggestion for ACI development length provisions based on flexural testing of RC slabs with various levels of corroded reinforcing bars.” Engineering Structures, 26(8), 1013–1026.

CONTECVET. (2001). A validated Users manual for assessing the residual service life of concrete structures. EC Innovation Programme IN30902I, GEOCISA, Madrid, Spain.

Coronelli, D. (2002). “Corrosion cracking and bond strength modeling for corroded bars in reinforced concrete.” ACI Structural Journal, 99(3), 267–276.

Coronelli, D., and Gambarova, P. (2004). “Structural Assessment of Corroded Reinforced Concrete Beams: Modeling Guidelines.” Journal of Structural Engineering, 130(8), 1214–1224.

Crumpton, C. F., Smith, B. J., and Jayaprakash, G. P. (1989). “Salt weathering of limestone aggregate and concrete without freeze-thaw.” Transportation Research Record, (1250), 8–16.

Dabas, M., Zaghian, S., Martin-Perez, B., and Almansour, H. (2020). “Numerical investigation of the structural performance of aged RC bridge columns subjected to corrosion and service loads.” REHABEND 2020, Granada,Spain, 8.

Du, Y. G., Clarkt, L. A., and Chan, A. H. C. (2005). “Effect of corrosion on ductility of reinforcing bars.” Magazine of Concrete Research, 57(7), 407–419.

Elsener, B. (2002). “Macrocell corrosion of steel in concrete - Implications for corrosion monitoring.” Cement and Concrete Composites, 24(1), 65–72.

Fang, C., Lundgren, K., Chen, L., and Zhu, C. (2004). “Corrosion influence on bond in reinforced concrete.” Cement and Concrete Research, 34(11), 2159–2167.

Glass, G. K., and Buenfeld, N. R. (1997). “The presentation of the chloride threshold level for corrosion of steel in concrete.” Corrosion Science, 39(5), 1001–1013.

Glass, G. K., and Buenfeld, N. R. (2000). “The influence of chloride binding on the chloride induced corrosion risk in reinforced concrete.” Corrosion Science, 42(2), 329–344.

Government of Canada. (2019). Canada’s Changing Climate Report. (D. S. Bush, E. and Lemmen, ed.), Environment and Climate Change CANADA, Ottawa.

Hanjari, K. Z., Coronelli, D., and Lundgren, K. (2011). “Bond capacity of severely corroded bars with corroded stirrups.” Magazine of Concrete Research, 63(12), 953–968.

Higgins.C., Farrow, W. C., Potisuk, T., Miller, T. H., and Yim, S. C. (2003). Shear capacity assessment of corrosion-damaged reinforced concrete beams. Oregon Department of Transportation and Federal Highway Administration.

Hong, K. (1998). “Cyclic Wetting and Drying and its Effects on Chloride Ingress in Concrete.” 123.

Horrigmoe, G., Saether, I., Antonsen, R., and Arntsen, B. (2007). “Laboratory investigations of steel bar corrosion in concrete.” Sustainable Bridges: Sixth Framework Programme, SB 3.10, 137.

Imperatore, S., Rinaldi, Z., and Drago, C. (2017). “Degradation relationships for the mechanical properties of corroded steel rebars.” Construction and Building Materials, Elsevier Ltd, 148(2017), 219–230.

Kamaitis, Z. (2002). “Damage to concrete bridges due to reinforcement corrosion: Part II-design considerations.” Transport, 17(5), 163–170.

Khan, M. U., Ahmad, S., and Al-gahtani, H. J. (2017). “Chloride-Induced Corrosion of Steel in Concrete: An Overview on Chloride Diffusion and Prediction of Corrosion Initiation Time.” International Journal of Corrosion, 2017.

Kivell, A. (2012). “Effects of bond deterioration due to corrosion in reinforced concrete.” Thesis in partial fulfilment of the requirements for the degree of Master of Engineering in Civil Engineering.

Lee, H. S., and Cho, Y. S. (2009). “Evaluation of the mechanical properties of steel reinforcement embedded in concrete specimen as a function of the degree of reinforcement corrosion.” International Journal of Fracture, 157(1–2), 81–88.

Lee, H. S., Tomosawa, F., and Noguchi, T. (1996). “Effect of Rebar Corrosion on the Structural Performance of Single Reinforced Beams.” Durability of Building Materials and Components, E & FN Spon, London, 1(7), 571–580.

Li, K., and Li, L. (2019). “Crack-altered durability properties and performance of structural concretes.” Cement and Concrete Research, 124(January), 1–11.

Li, Q., Huang, L., and Ye, H. (2020). “Mechanical Degradation of Reinforced Concrete Columns Corroded Under Sustained Loads.” International Journal of Civil Engineering, Springer International Publishing, 0123456789.

Li, Q., Niu, D., and Liu, L. (2012). “The experimental study on reinforced concrete short-columns restrained by corroded stirrups.” Advanced Materials Research, 446–449, 1376–1379.

Lin, H., and Zhao, Y. (2016). “Effects of confinements on the bond strength between concrete and corroded steel bars.” Construction and Building Materials, Elsevier Ltd, 118(2016), 127–138.

Ma, Y., Guo, Z., Wang, L., and Zhang, J. (2017). “Experimental investigation of corrosion effect on bond behavior between reinforcing bar and concrete.” Construction and Building Materials, Elsevier Ltd, 152, 240–249.

Maaddawy, T. A. El, and Soudki, K. A. (2003). “Effectiveness of Impressed Current Technique to Simulate Corrosion of Steel Reinforcement in Concrete.” Journal of Materials in Civil Engineering, 15(February), 41–47.

Mangat, P. S., and Elgarf, M. S. (1999). “Flexural strength of concrete beams with corroding reinforcement.” ACI Structural Journal, 96(1), 149–158.

Mohammed, A., Almansour, H., and Martín-Pérez, B. (2018). “Simplified finite element model for evaluation of ultimate capacity of corrosion-damaged reinforced concrete beam-columns.” International Journal of Advanced Structural Engineering, Springer Berlin Heidelberg, (0123456789), 20.

Molina, F. J., Alonso, C., and Andrade, C. (1993). “Cover cracking as a function of rebar corrosion: Part 2-Numerical model.” Materials and Structures, 26(9), 532–548.

Moukwa, M. (1990). “Deterioration of concrete in cold sea waters.” Cement and concrete research, 20(c), 439–446.

Neville, A. (1995). “Chloride Attack of Reinforcement Concrete an Overview.” Materials and Structures.

Ontario Ministry of Transportation. (2008). Ontario Structure Inspection Manual (OSIM). Ministry of Transportation, St.Catharines, Ontario, Canada.

Otieno, M. (2019). “Acceleration of steel corrosion in concrete by cyclic wetting and drying : effect of drying duration and concrete quality.” Materials and Structures, Springer Netherlands, 52(2), 1–14.

Palsson, R., and Mirza, M. S. (2002). “Mechanical response of corroded steel reinforcement of abandoned concrete bridge.” ACI Structural Journal, 99(2), 157–162.

Pantazopoulou, S. J., and Papoulia, K. D. (2001). “Modeling cover-cracking due to reinforcement corrosion in RC structures.” Journal of Engineering Mechanics, 127(4), 342–351.

Plizzari, G. A., Deldossi, M. A., and Massimo, S. (1998). “Transverse reinforcement effects on anchored deformed bars.” Magazine of concrete research, 161–177.

Presuel-Moreno, F., Suares, A., and Liu, Y. (2010). Characterization of New and Old Concrete Structures Using Surface Resistivity Measurements: Final Report. Florida, USA.

Razvi, S., and Saatcioglu, M. (1999). “Confinement model for high strength concrete.” Journal of Structural Engineering, 125(March), 281–289.

Reddy, B., Glass, G. K., Lim, P. J., and Buenfeld, N. R. (2002). “On the corrosion risk presented by chloride bound in concrete.” Cement and Concrete Composites, 24(1), 1–5.

Rodriguez, J., Ortega, L. M., and Casal, J. (1996). “Load bearing capacity of concrete columns with corroded reinforcement.” Corrosion of reinforcement in concrete construction. proceedings of fourth international symposium, Cambridge, 1-4 july 1996. special publication no 183, 220–230.

Shima, H., Chou, L. L., and Okamura, H. (1987). “Micro and macro models for bond in reinforced concrete.” Journal of the Faculty of Engineering, University of Tokyo, Series B.

Tapan, M., and Aboutaha, R. S. (2008). “Strength Evaluation of Deteriorated RC Bridge Columns.” Journal of Bridge Engineering, 13(3), 226–236.

Tapan, M., and Aboutaha, R. S. (2011). “Effect of steel corrosion and loss of concrete cover on strength of deteriorated RC columns.” Construction and Building Materials, 25(5), 2596–2603.

Tapan, M., Ozvan, A., and Akkaya, I. (2016). “Effect of stirrup corrosion on Concrete Confinement Strength.” International Journal of Civil and Environmental Engineering, 10(12), 3.

Tuutti, K. (1981). Corrosion of Steel in Concrete. Swedish Cement and Concrete Research Insititute, Swedish Cement and Concrete, Stockholms.

Vidal, T., Castel, A., and François, R. (2004). “Analyzing crack width to predict corrosion in reinforced concrete.” Cement and Concrete Research, 34(1), 165–174.

Vu, N. S., Yu, B., and Li, B. (2017). “Stress-strain model for confined concrete with corroded transverse reinforcement.” Engineering Structures, 151, 472–487.

Wang, X.-H., Liu, X.-L., and Deng, B.-R. (2012). “Effects of length and location of steel corrosion on the behavior and load capacity of reinforced concrete columns.” Journal of Shanghai Jiaotong University (Science), 17(4), 391–400.

Wang, X. H., and Liang, F. Y. (2008). “Performance of RC columns with partial length corrosion.” Nuclear Engineering and Design, 238(12), 3194–3202.

Xia, J., Jin, W., and Li, L. (2016). “Performance of corroded reinforced concrete columns under the action of eccentric loads.” Journal of Materials in Civil Engineering, ASCE, 28(1), 1–16.

Yoon, I., and Chang, C. (2020). “Effect of Chloride on Electrical Resistivity in Carbonated and Non-Carbonated Concrete.” Applied Sciences, 10(18), 16.

Zhang, P., Lu, M., and Li, X. Y. (1995). “The mechanical behaviour of corroded bar.” Journal of Industrial Buildings, 25(257), 41–44.

Zhao, Y., and Lin, H. (2018). “The bond behaviour between concrete and corroded reinforcement: State of the art.” 6th International Conference on Durability of Concrete Structures, ICDCS 2018, (July), 63–73.

Chapter 3 Experimental Program

3.1 Introduction

The experimental program of this thesis has examined the structural behaviour of RC columns subjected to reinforcement corrosion. The experimental work was conducted at the structural lab of the University of Ottawa. The work scope was achieved in two stages: stage I (exposure to corrosion environment) and stage II (structural testing). Each stage is described as follows (see Fig. 3.1 and Fig. 3.2).

For stage I (exposure to corrosion environment):

- Design RC columns with normal ready-mix concrete,
- Construct formworks and steel reinforcement cages for the RC columns,
- Cast concrete, and
- Expose column specimens to an accelerated corrosion regime.

For stage II (structural testing):

- Assemble loading set-up and prepare instrumentation for data measurements, and
- Apply quasi-static load up to failure.

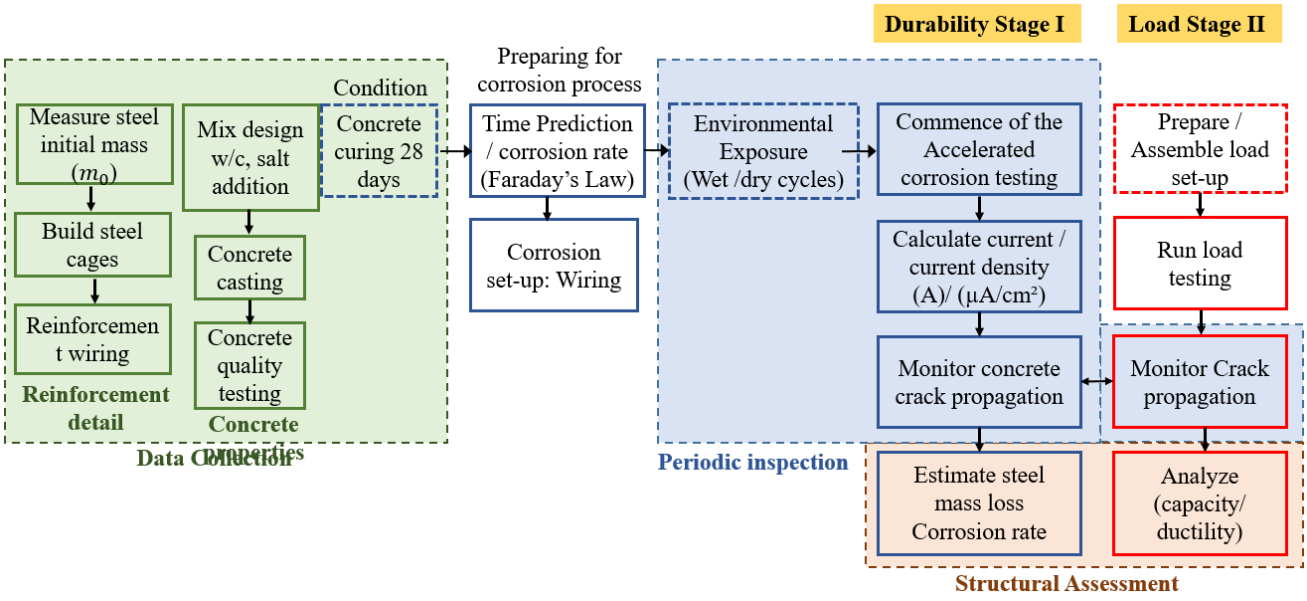

Fig. 3.1: Methodology for the experimental program

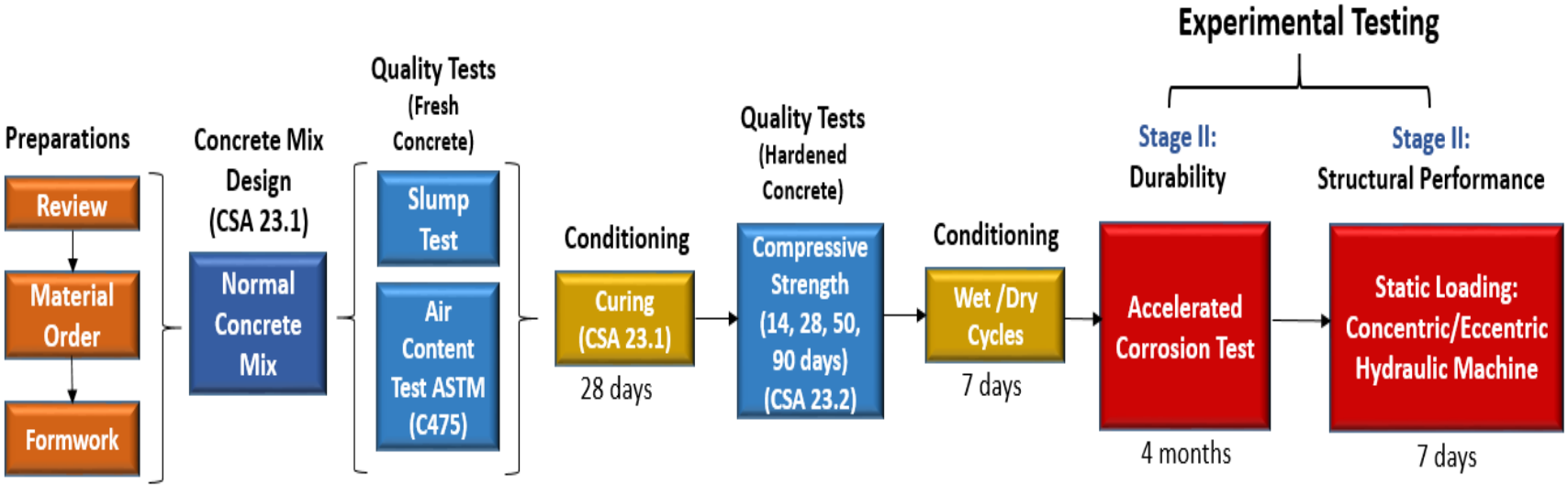

Fig. 3.2: Scope of experimental work

3.2 Description of Test Specimens

A total of ten columns were built and tested to failure in five sets (as shown in Table 3.1): (i) two control specimens subjected to static load only without inducing any reinforcement corrosion (C-C- C and C-E-C); (ii) two columns, in which two ties at the effective zone (mid 1,100-mm region) were corroded, subjected to concentric loading (C-C-T1 and C-C-T2); (iii) two columns, in which two ties at the effective zone were corroded, subjected to eccentric loading (C-E-T1 and C-E-T2); (iv) two columns, whose longitudinal reinforcement was corroded, subjected to eccentric loading (C-E-R1 and C-E-R2); and, (v) two columns, whose both longitudinal and tie reinforcement underwent accelerated corrosion, subjected to concentric loading (C-C-All1 and C-C-All2). Five columns were loaded concentrically (e = 0), while the remaining five were loaded eccentrically at an eccentricity of e = 190 mm. The columns were designed with transverse reinforcement having a spacing of S=150 mm. The patterns of reinforcement corrosion were selected for the following reasons:

1- The axial response of columns subjected to concentric load is governed by the reduction in confinement provided by corroded transverse reinforcement.
2- The flexural response of RC columns eccentrically loaded are dominated by the decrease in cross-sectional area and ductility of corroded longitudinal reinforcement.

Therefore, the goal was to corrode the reinforcement dominating the corresponding behaviour to different corrosion levels to evaluate its effect on the RC column structural response.

Table 3.1: RC column specimens

Specimen	Corrosion	Eccentricity (mm)
C-C-C	No	0
C-C-T1	Ties	0
C-C-T2	Ties	0
C-C-All1	Longitudinal + ties	0
C-C-All2	Longitudinal + ties	0
C-E-C	No	190 mm
C-E-T3	Ties	190 mm
C-E-T4	Ties	190 mm
C-E-R1	Longitudinal reinforcement	190 mm
C-E-R2	Longitudinal reinforcement	190 mm

The RC column is comprised of a 260-mm square cross-section column with an effective span of 1,100 mm connected at the top and base with a hunched beam (Fig. 3.3). The clear concrete cover for all the columns is 30 mm. The columns were designed using 4-20M longitudinal bars with a yield strength of 400 MPa and 10M transverse ties at 150-mm spacing. The columns resistance was determined according to CAN/CSA S6:19 and CAN/CSA23.3 standard requirements and compared to AASHTO ASD (1969). Full calculations of the column design are included in Appendix B. Table 3.2 compares the column resistance estimated according to existing codes in North America, CAN/CSA S6:19 (CSA 2019), CSA A23.3 (CSA 2019), and AASHTO LRFD, compared to standard requirements used in structures constructed pre-1971 AASHTO ASD (1969).

Table 3.2: Comparison between column requirements for bridge design according to AASHTO LRFD, ASD and CAN/CSA S6:19.

Design Standard	Transverse spacing (≤)	P_0 (kN) Concentric	P_0 (kN) Eccentric
CAN/ CSA S6:19 CHBDC & CAN/CSA A23.3	300	1,492	563, e_b=131mm 421, e=166mm 337, e=197mm
AASHTO LRFD (CL5.7.4.4)	--	1,748	
AASHTO ASD (1969)	300	941	310, e_b=131 mm 260, e=166 mm 225, e=197mm

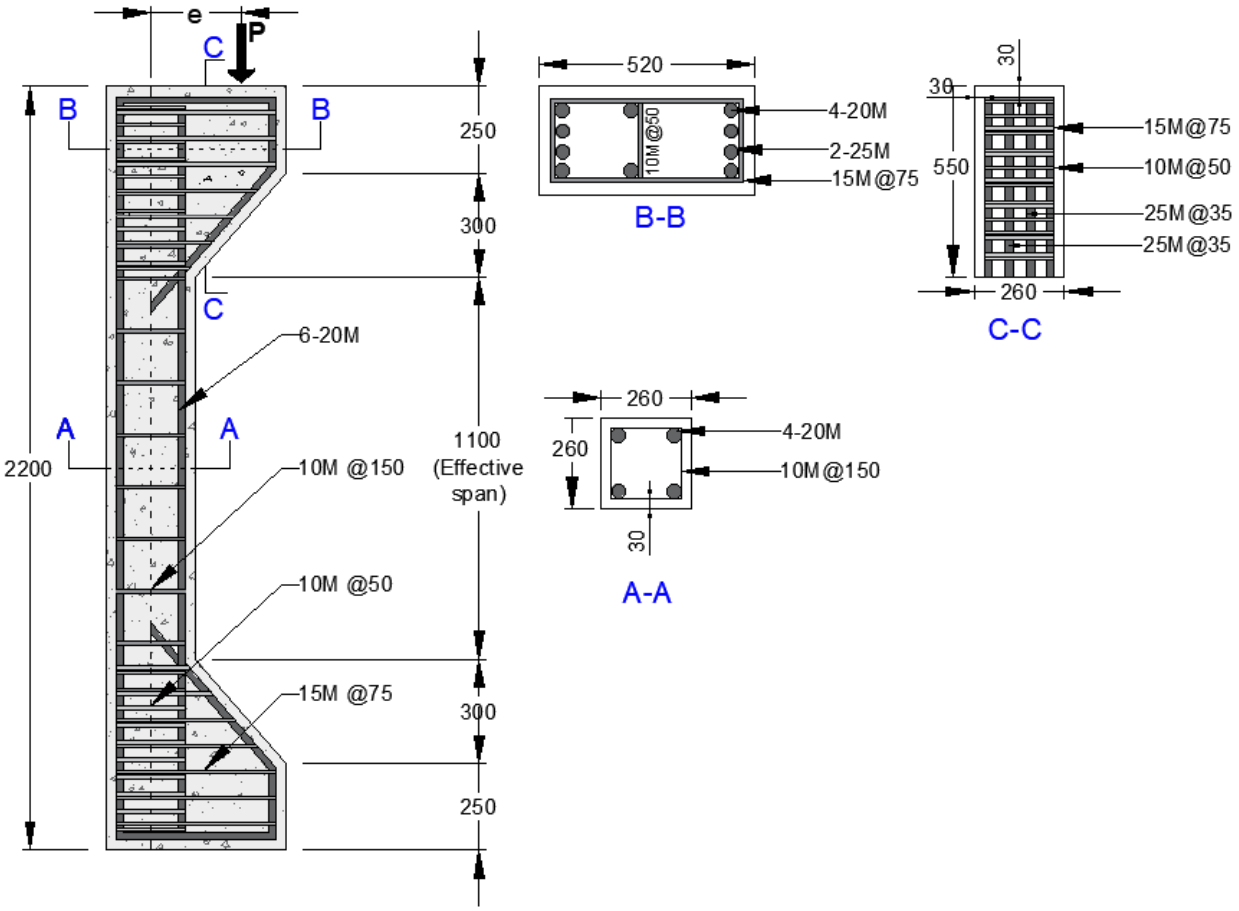

Fig. 3.3: *Geometry and reinforcement details of RC column (dimensions in mm)*

3.3 Design of Corbel Detail

The beam-column connection at the top and base provided both structural support and a base for load application. The connection is also referred to as a "corbel" since the span-to-depth (a_c/d_c), a_c is the extended corbel width and d_c is the extended corbel depth, is less than 1 according to ACI code section 11.8 (ACI 2019). For this case ($a_c/d_c<1$), two design procedures can be used to determine the corbel size and detailing according to the ACI code: the traditional method (section 9.2) and the tie-strut method (section 11.8). The traditional method was used to determine the size of the corbel and required reinforcement detailing, while the second procedure based on the tie-strut method was used for the tentative location of the strain gages along the column span. The tie-and-strut method creates a truss system for load transfer according to clause 8.10.2 from CAN/CSA S6:19 (CSA 2019) and clause 5.8.2 from AASHTO LRFD (Grubb et al. 2015).

Throughout, special design considerations were necessary for detailing the sections to prevent undesirable localized failure due to excessive tensile strains and moments imparted from the corbel to the column. Furthermore, to restrict the damage to the column's effective span, it was essential to provide adequate concrete confinement using both longitudinal and transverse reinforcement, which significantly improves the structural behaviour, increases the section ductility, and enhances the section efficiency. Longitudinal rebars (6-20M) extended from the column span into the corbel sections, with three of them wrapping the corbel; the corbels were further reinforced with 2-25M. The longitudinal rebars were tied with 10M transverse reinforcement at 50 mm centre-to-centre (CC) at the top and base sections, and the corbel sections were tied with 16M ties at 75-mm CC Full calculations of the corbel design are included in Appendix B.

3.4 Construction of Test Specimens

3.4.1 Material Properties

3.4.1.1 Concrete Mix

A ready-mix concrete cast in one-day was used for all tested specimens. General Use (GU) Ordinary Portland Cement (PC) concrete was used with normal exposure conditions and non-air entrainment. Table 3.3 shows the material requirements according to the current CAN/CSA S6:19 CHBDC, with a maximum water-to-cement ratio (w/c) of 0.4. However, for this study, the w/c was increased to 0.55 to increase concrete permeability and porosity, allowing the accelerated corrosion mechanism to occur effectively. The intended compressive strength at 28-days was 30 MPa. The calculated concrete mix proportions are given in Table 3.4. The individual amounts of materials in Table 3.4 were adjusted to produce one column of 0.2 m^3. A volume of 2.65 m^3 was needed to cast ten columns. For those columns subjected to an accelerated corrosion regime, 3.5% of sodium chloride (NaCl) was added to the mixing water to depassivate the protective film on the rebar.

Table 3.3: Concrete mix requirements according to available standards

Code	f_c (28-days) (MPa)	a max (mm)	Slump (mm)	w/c max	AC %
CAN/CSA S6:19	30	28	50±20	0.45	5±1
AASHTO LRFD	28	--	--	0.45	6±1.5

Table 3.4: Calculated concrete mix proportions

Ingredients	Unit mass (kg/m^3)	Mass (kg) to obtain a volume of 0.2 m^3	Mass (kg) to obtain a volume of 0.1225 m^3	Mass (kg)
Coarse aggregate	1,115.8	223.2	136.7	3,871.9
Fine aggregate	790.4	158.1	96.8	2,742.5
Water	192.7	38.6	23.6	668.8
Cement	350.4	70.1	42.9	1,215.9
NaCl	12.3	2.5	1.2	38.6

3.4.1.2 Quality Control Tests

The following tests were done to determine the properties of the materials used, as illustrated in Fig. *3.4*:

- Slump test according to CAN/CSA S6:19 and A23.2-5C:19 (CSA A23.1:19/CSA A23.2:19 2019). Concrete had a good consistency, workability and fluidity. The experimentally measured slump was 120 mm.
- Air content test according to ASTM C231 (ASTM 2017). The air content was 0.5% for the first concrete batch and 1.2% for the second batch. This test was conducted to determine concrete vulnerability to freeze/thaw cycles. The test was not carried out.

- Concrete from each batch was cast into cylinders to measure the compressive strength (CAN/CSA A23.2-9C:19). The reinforcement bars were tested under tension according to ASTM A370 (ASTM 2020).

Fig. 3.4*: Left: air content test, Right: slump test*

3.4.2 Preparations of Specimens

3.4.2.1 Epoxy Coating

In preparation for the accelerated corrosion test, epoxy coating was applied at the top and bottom of the column reinforcement (corbel sections) to eliminate any end corrosion effects, as shown in Fig. 3.5. Furthermore, Epoxy coating was applied on the longitudinal rebars in the effective area for the case where only the ties where corroded. In addition, tapes were placed at the ties/longitudinal rebar connections to prevent localized corrosion.

3.4.2.2 Casting

Plywood sheathing was used for the column formwork, as it provides a smooth and clean finish of the outer surface of the element. Bracings were provided at the mid-section to support the sheathing against buckling, as illustrated in Fig. 3.5. Extra care was taken throughout to ensure that the column reinforcement and formwork assembly was levelled and accurately aligned. The formwork

was slowly stripped after seven days of curing. A special formwork design was adopted according to Hognestad (1951), as shown in Fig. 3.5, which allows consecutive casting of two specimens while providing a shared lateral bracing. The columns were cast horizontally with intermittent compaction periods similar to field practice. In preparation for axial loading, 19-mm steel bolts were fastened to a steel plate atop each column.

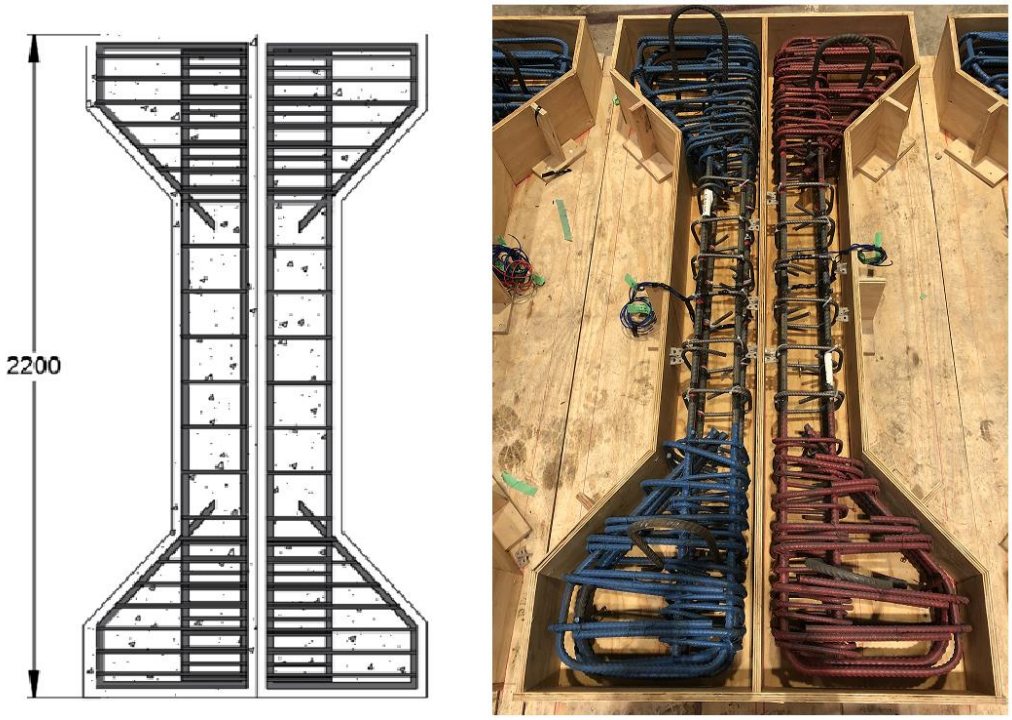

Fig. 3.5: Casting and formwork of concrete columns (dimensions in mm) with epoxy-coated corbel sections

3.4.2.3 Curing

The specimens were cured for 28 days according to CAN/CSA A23.1:19 (CSA 2019), during which moist burlap fabrics wrapped with plastic sheets were placed atop the specimens to ensure adequate humidity. The specimens were sprayed daily to prevent the fabric from drying out.

3.5 Accelerated Corrosion Regime

Reinforcement corrosion-induced damage typically observed in the field was simulated in the experimental laboratory set-up by impressing an accelerated constant current. Fig. 3.6 to Fig. 3.12

summarizes the process of accelerated corrosion testing: specimens' preparation, conditioning, testing, and measurement. To induce an early depassivation of the reinforcement, 3.5% (by weight of cement) of NaCl was incorporated into the mixing water. A constant and direct current was impressed against the reinforcement at a specified rate, predetermined theoretically according to Faradays' law. A constant current was impressed through the specimens using six DC power supplies with an overall voltage and current capacity of 30 V and 3 A, respectively. The advantage of the DC power supply is that it continuously impresses a constant current (predetermined by the user) throughout the specified time by automatically adjusting the non-constant parameter (voltage) to maintain the value of the current. There were four groups of columns connected to the six DC power supplies. Groups 1 and 2 comprised of two columns connected in series, as shown in Fig. 3.6. Thus, one DC power supply was used for two columns. These two groups (1 and 2) were assembled to induce corrosion in 2-ties at 150-mm spacing at the effective corrosion zone. Group 3 was comprised of two columns where each had a separate DC power supply for a total of two DC power supplies. For this group, the intention was to corrode four longitudinal rebars at the effective zone; subsequently, the reinforcing bars were connected in parallel to the DC power supply. Group 4 was comprised of two columns similar to group 3; each column had a separate DC power supply. In this last group, the intention was to corrode all the longitudinal bars and two mid-section ties at the effective zone, with the longitudinal and transverse reinforcement assembled in parallel to their DC supply (Fig. 3.7). For all groups (1, 2, 3 and 4), the electrical circuit was assembled such that the reinforcement acted as the anode while stainless steel sheets located on the external surfaces acted as the cathode. The effective zone was wrapped in a sponge to provide a wet medium for the electrons to pass from the cathode (stainless steel) through the electrolyte (concrete cover) to the anode (reinforcement). The specimens were then subjected to wetting and drying cycles to simulate natural conditions.

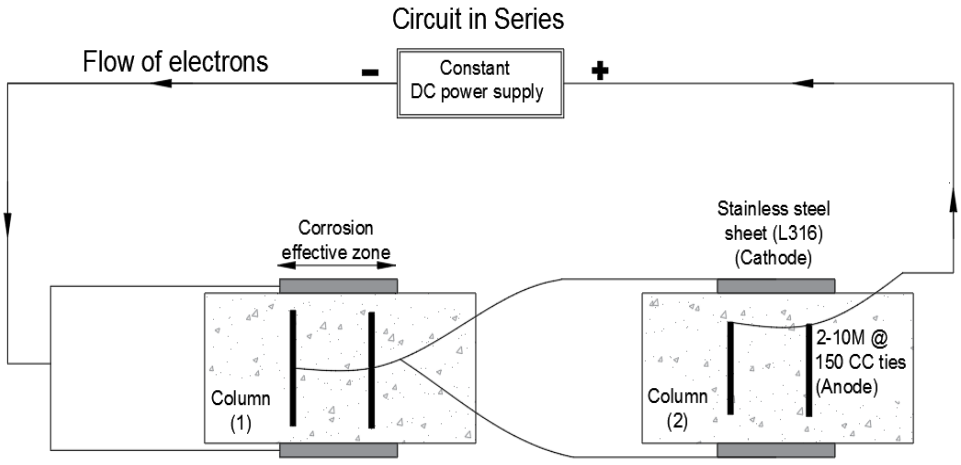

Fig. 3.6: Set-up of the accelerated corrosion process for C-C-T1/T2 and C-E-T3/T4 connected in series

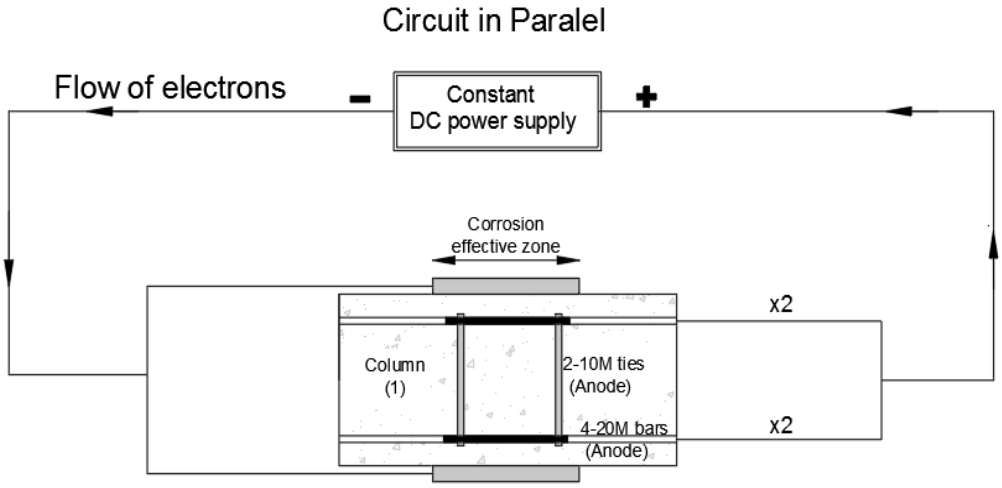

Fig. 3.7: Set-up of the accelerated corrosion process for C-C-All1/All2 and C-E-R1/R2 connected in parallel

The corroded reinforcement was used as the anode, while two or three 250×750-mm stainless steel sheets (316L in grade,18 GA in thickness) were used as the cathode to allow the current induced to complete the electrochemical cell through the concrete that served as an electrolyte, as illustrated in Fig. 3.8 to Fig. 3.12.

Several considerations were taken in the corrosion set-up to accelerate the corrosion process. For instance as the cover depth or spacing between the electrodes (cathode and the anode) had to be small to allow for the transfer of ions from the anode to the cathode to complete the electrical circuit and a sufficient amount of cathode-to-anode surface area, with a ratio of 2:1. Fig. 3.8 shows

a typical schematic of the test set-up, where the power supply impresses a constant current across the anode (+), in this case the transverse reinforcement, while the stainless steel sheets were mounted on the surface of the specimens to act as the cathode (-). Four specimens were connected in series (Group 1 and 2), while the other four were connected in parallel (Group 3 and 4). Specimens were wrapped with thick sponges, periodically wetted in salted water, and dried for better corrosion effects. Electrical connections of electrical wires Gauge 12 (extended outside the columns) connected the reinforcement to be corroded to the DC power supply. Fig. 3.9 illustrates the effective corrosion area along the mid-section of the column. Epoxy coating was applied at the top and bottom of the column reinforcement and on the longitudinal rebars in the effective area to eliminate any end corrosion effects. In addition, tapes were placed at the ties/longitudinal rebar connections to prevent localized corrosion. The corrosion setup in the laboratory is shown in Fig. 3.8 to Fig. 3.12. Fig. 3.13 illustrates the current applied to all column set-ups (Groups 1 to 4) over the duration of the accelerated corrosion regime (5 months). The current density was determined by dividing the impressed current by the surface area of the corroding reinforcement according to Eq. 2.11. For corrosion of the transverse reinforcement (4 columns), the current density was calculated as 525 $\frac{\mu A}{cm^2}$, while for longitudinal reinforcement corrosion (2 columns) and transverse and longitudinal reinforcement corrosion (2 columns), the current density was calculated as 475 $\frac{\mu A}{cm^2}$. These values were pre-estimated assuming that there were no losses, and all the impressed current was used in the corrosion process. Although the current density values used in this experiment were higher than what would be expected in the field (Andrade 2020), it was necessary to achieve the intended steel mass loss in a reasonable amount of time. Maaddawy and Soudki (2003) studied the effectiveness of impressing different levels of current densities. The authors concluded that a current density in the range of (100-500 $\frac{\mu A}{cm^2}$) produces mass losses (based on gravimetric weight loss measurements) agreeable with those estimated theoretically according to Faraday's law.

After actual measurements of the gravimetric mass loss detailed in section 3.6, the actual current densities values considering current loss were recalculated and plotted over time as illustrated in Fig. 3.14: . The actual current density (corrosion rate) for group 1 and 2 (corrosion of the transverse reinforcement) was 90 $\frac{\mu A}{cm^2}$ and 62 $\frac{\mu A}{cm^2}$ respectively. The columns had significant current loss,

which was attributed to the set-up of the experiment connected in series. On the other hand, the actual current density for group 3 (corrosion of the longitudinal reinforcement) and group 4 (corrosion of all the reinforcement) was 398 $\frac{\mu A}{cm^2}$ and 322 $\frac{\mu A}{cm^2}$, respectively.

The primary objective of the experiment was to induce and sustain the reinforcement corrosion rate throughout the accelerated corrosion regime. Thus, favourable conditions for corrosion are achieved by providing an adequate amount of moisture and oxygen at an appropriate temperature level. This is because the chemical conductivity or resistivity of the electrolyte (concrete) depends on the amount of moisture present. In addition, the electrolyte must be sufficiently aerated so that oxygen is available for the cathodic reaction. To that end, the specimens were subjected to repeated wetting and drying cycles. Also, specimens were wrapped in wet burlap and covered in a plastic sheet to maintain a high humidity environment. A three-day wet, four-day dry regime was found to be the most effective regime.

On the first week of the accelerated corrosion test, the potential difference between the cathode and anode was applied at a maximum capacity of the DC power supply (30V), while the passing current was below the pre-determined current (0.38 A for Group 1 and 2; 0.83 A for Group 3, 1 A for Group 4) to cause the desired mass loss at a specific time (Fig. 3.13). Moreover, the columns had a very high resistance reading of over 100 Ω measured using a multimeter on-site, indicating that reinforcement corrosion is highly unlikely (CONTECVET 2001).

Thus, it was necessary to improve the conditions of the experiment by adopting the following:

i) a three-day wet, four-day dry regime
ii) the addition of salt to the water basin (external solution)
iii) refreshing the water basin every two weeks to ensure a fresh supply of saline water. This is because the external solution becomes alkaline due to the cathodic reaction (oxygen reduction producing hydroxides). This, in effect, slows down chlorides mobility (Andrade 2020).

As a result, concrete resistivity and the specimens' electrical resistance were reduced. The electrical resistance of the specimens was calculated based on the voltage and current readings (Fig. 3.15). Moreover, voltage readings were reduced and the current stabilized at the pre-determined values for each group, and the rate of corrosion was increased (Fig. 3.13 to Fig. 3.15). For example, the

voltage reading for group 4 was reduced to 10 V, and a desired constant current of 1 A was maintained throughout the testing period (Fig. 3.13 and Fig. 3.15).

A wetting and drying regime was adopted to enhance and accelerate corrosion of the reinforcement (Otieno 2019). A three-day wet, four-day dry regime was the most effective regime to reduce columns resistivity and increase corrosion rate. A constant current was induced for 137 days combined with wetting and drying cycles (WDCs) to enhance and accelerate corrosion effects. It was observed that crack size, continuity, and formation were increased with the increase of corrosion degree and wetting and drying cycles. Cracks spread along the reinforcement length (transverse for C-C-T1 and longitudinal for C-E-R1). Crack formations for both scenarios remain unchanged after the artificial corrosion regime was stopped.

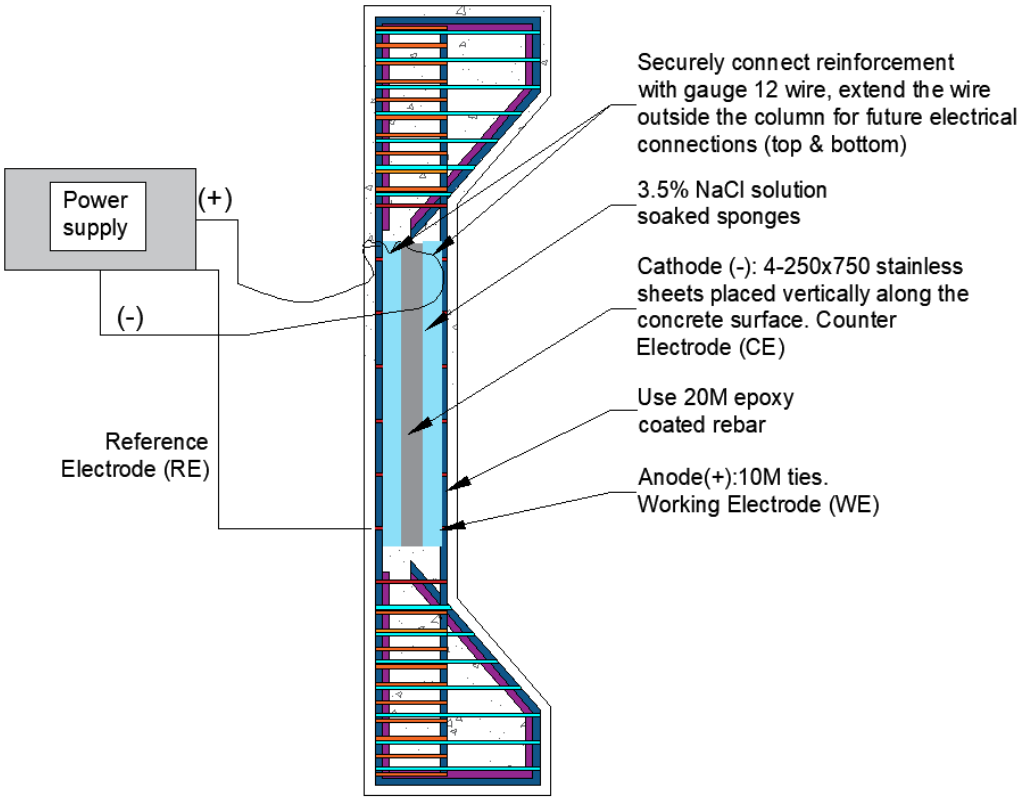

Fig. 3.8: Set-up of the electrolytic cell

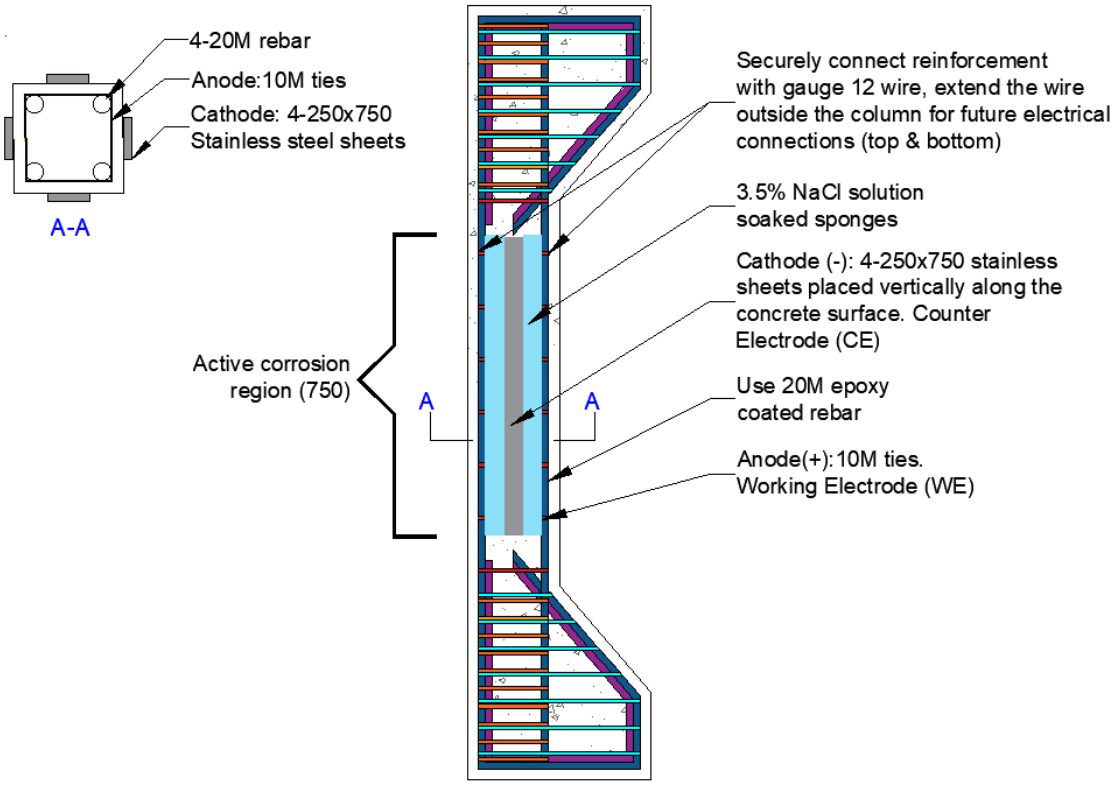

Fig. 3.9: Corrosion set-up (column elevation, dimensions in mm)

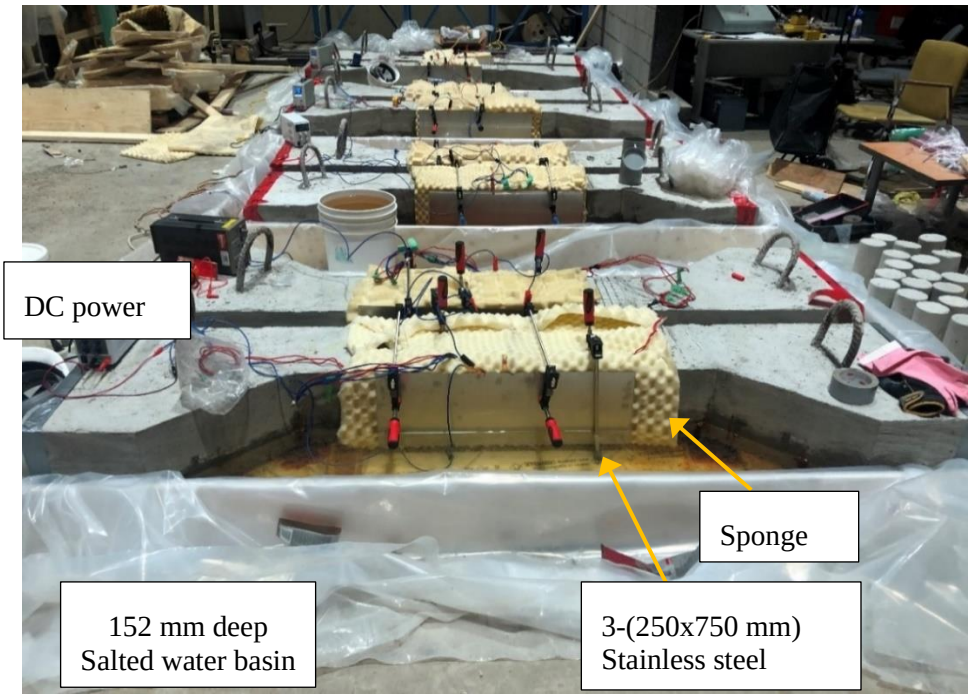

Fig. 3.10: Accelerated corrosion set-up (lab environment)

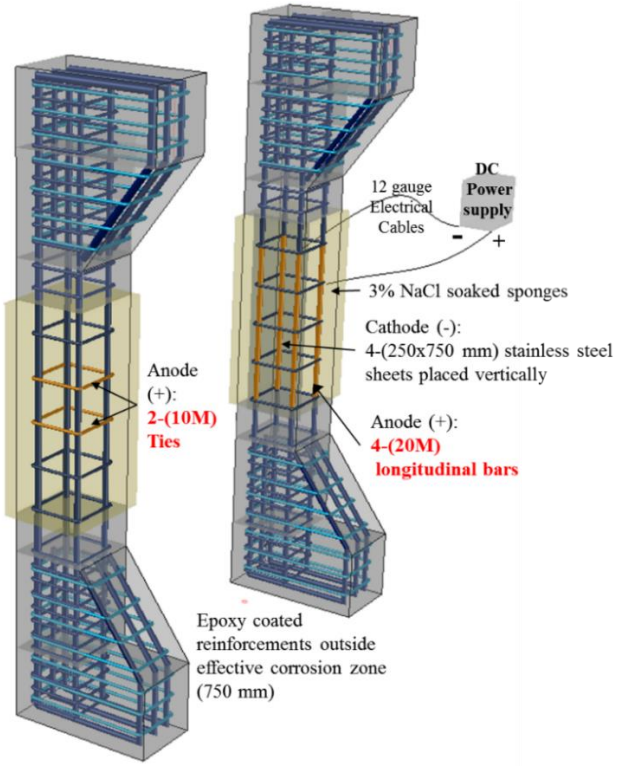

Fig. 3.11: Corrosion set-up for specimens C-E-T3/4 and C-E-R1/2

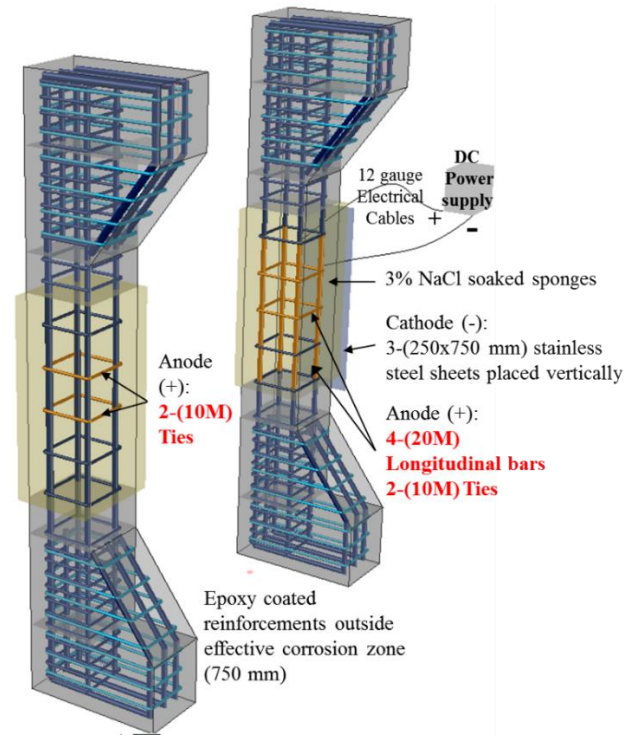

Fig. 3.12: Corrosion set-up for specimens C-C-T1/2 and C-C-All1/2

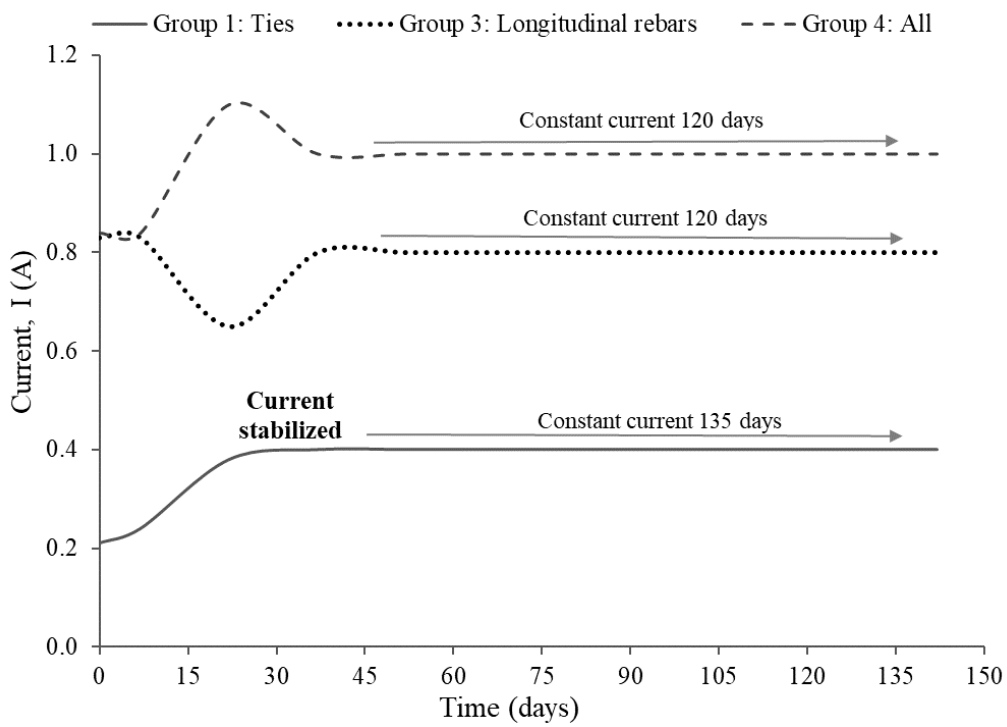

Fig. 3.13: Applied current during the accelerated corrosion regime

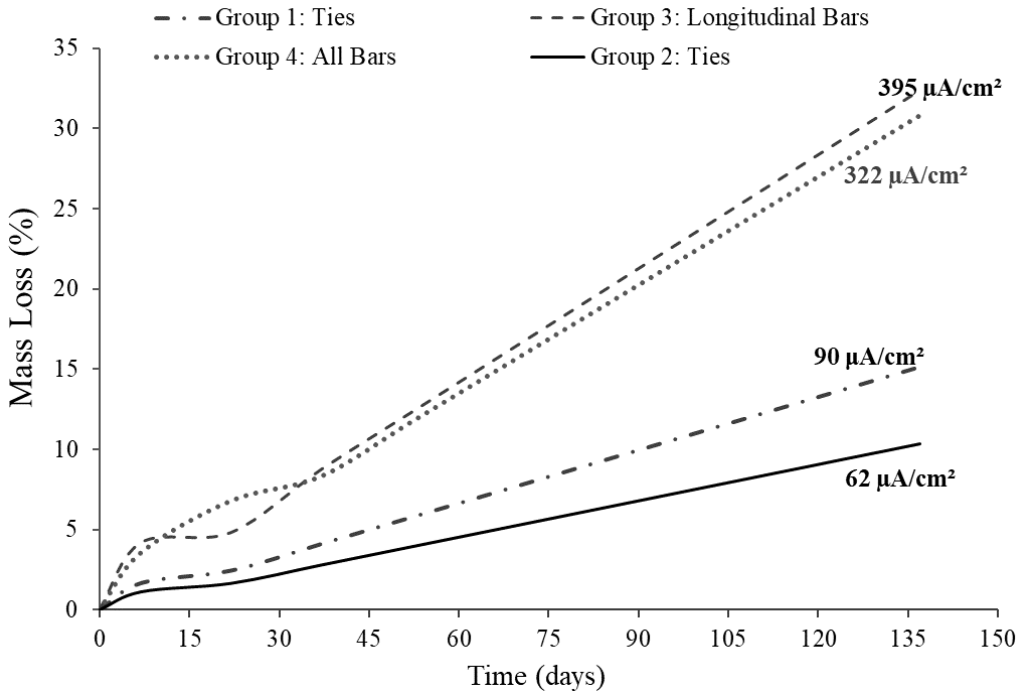

Fig. 3.14: Actual mass loss (%) according to Faraday's law considering current loss with corresponding corrosion rate

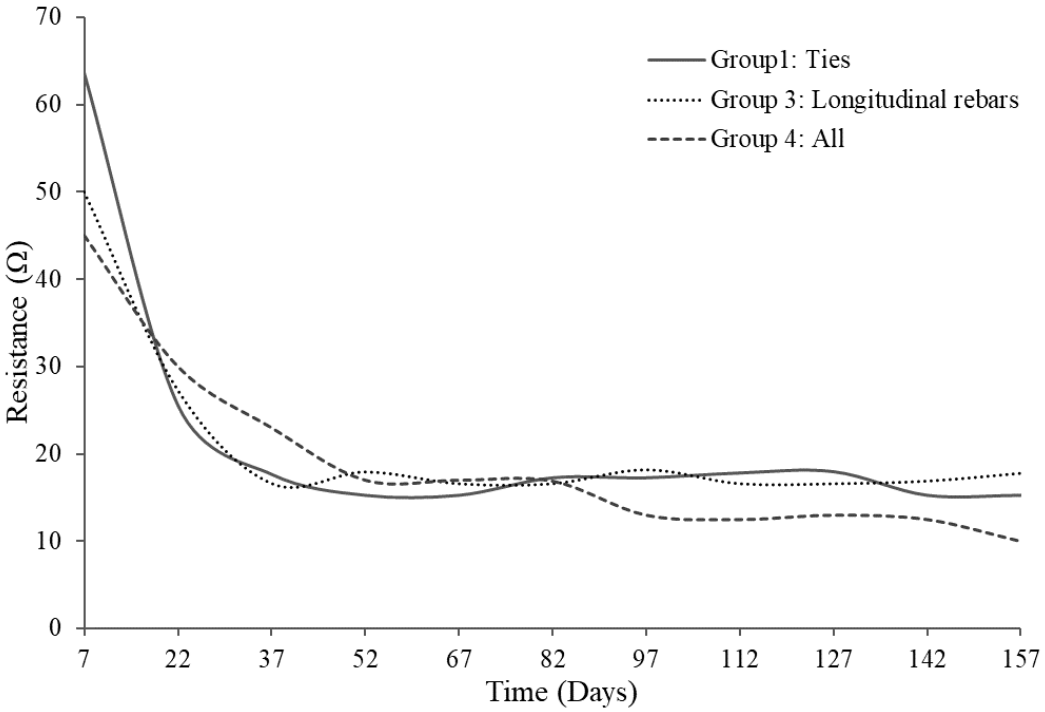

Fig. 3.15*:* Theoretical electrical resistance based on measured current and voltage of the columns

A summary of the accelerated corrosion test requirements and conditions is provided in Table 3.5 along with the total number of specimens used and their size. The accelerated corrosion regime was carried out until it was believed the reinforcement experienced a 30% material loss, as estimated theoretically through Faraday's law, given by Eq. 2.8. For example, to induce a steel mass loss of 30% in the transverse reinforcement, a current density of i_{corr} = 304 $\frac{\mu A}{cm^2}$ needs to be applied over an estimated time of 85 days, as shown in Table 3.6.

A 26×26-mm grid was drawn over the effective zone region of the column to monitor crack initiation, propagation, density and type. The columns were monitored regularly and throughout the test to observe corrosion-induced crack development and propagation and determine its pattern.

Table 3.5: Summary of corrosion test

Accelerated Corrosion	
Specimens	C-C-T1, C-C-T2, C-C-All1, C-C-All2, C-E-T2, C-E-T3, C-E-R1, C-E-R2
No. Specimens	Eight
Size	260×260×750 mm
Test Method	Accelerated corrosion (constant current)
Conditions	Water periodically, Cover with burlap
Temperature	Ambient temperature and constant relative humidity
Cycle Duration	Three-day wet, Four-day dry
Equipment and	Tank, DC power supply, Cable sensors, crack gauge
Material	Wires, stainless steel sheets, 3.5% NaCl solution (concrete)
Failure Criteria	Variable, up to 25% material loss for longitudinal rebars and transverse reinforcement as estimated from Faraday's law

Table 3.6: Mass loss of the transverse reinforcement

Area (cm^2) for a stirrup (1)	0.95
Volume (cm^3)	95
Density of steel (g/cm^3)	7.85
Initial mass (g)	746
Mass loss (%)	30%
Mass loss (g)	74.6
Time (days)	85
Current I (μA)	105,293
i_{curr} ($\mu A/cm^2$)	304

3.6 Gravimetric Reinforcement Mass Loss

The embedded reinforcement at the effective zone was exposed and cleaned after load testing according to ASTM G1 (ASTM G1-03 2017) (Fig. 3.16). The average mass loss was determined

according to ASTM G1. The penetration depth (pit depth) was measured using a calliper after removing the corrosion products.

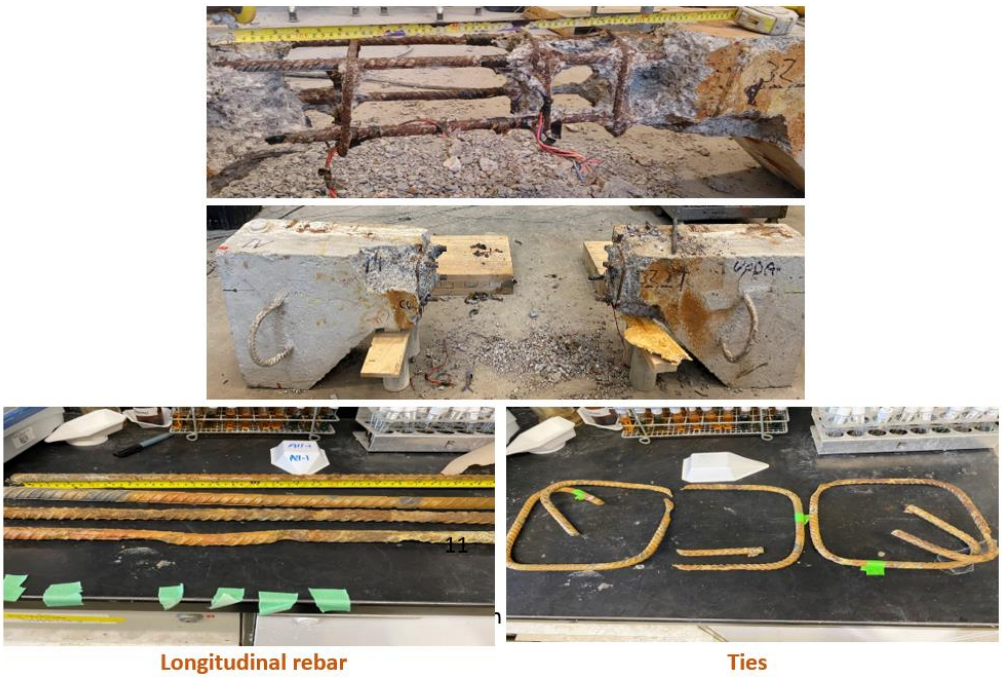

Fig. 3.16: Exposure of reinforcement cage in preparation for ASTM G1 test

3.7 Process and Implications of the Accelerated Corrosion Test

The RC columns were exposed to accelerated corrosion for 125 days after casting. The measured electrical resistance of the columns was found to be very high (higher than 100 Ω). Thus, it is most likely that a passive layer had formed on the reinforcement, and chlorides ions had bonded chemically to the cement hydrates. Similarly, Otieno et al. (2016) found that the reinforcement tends to revert to its passive state when the level of chloride content is less than the chlorides threshold.

Therefore, it was found necessary to provide a fresh supply of chloride ions (chloride solution) to the concrete to depassivate the steel and maintain the growth of active anodic zones (local pits). This is because reinforcement may repassivate at the early stage (initiation period) of reinforcement corrosion in a laboratory setting (Angst et al. 2011). It was found that there was a significant decrease in concrete resistivity with the increase in content level (by weight of cement) of chloride ions (Angst et al. 2011). Thus, sodium chloride was repeatedly added to the water bath

in which the columns were partially immersed to promote the growth of active anodic zones. During the propagation period of reinforcement corrosion, the corrosion rate may slow down in the absence of adequate conditions to sustain corrosion, such as inadequate oxygen supply or pores clogged by rust products.

After 40 days of accelerated corrosion, visible stains produced by corrosion products were reddish-brown. Since their kinetics were not tested, it is presumed that they are FeOOH (lepidocrocite and akageneite.) based on their colour alone (Caré and Raharinaivo 2007). This is similar to the corrosion products observed in the natural environment.

After removing the DC power supply, the corrosion rate was slowed down (and crack width did not increase further).

3.8 Structural Testing

3.8.1 Loading Setup

The columns were simply supported at the top and bottoms edges of the end corbels. The specimens were loaded concentrically and eccentrically using a hydraulic machine (MTS 793). The head of the hydraulic MTS machine applies a static compressive load against the top of the column-beam structure. The ultimate capacity of the machine is 2,500 kN. The overall view of the loading set-up is shown in Fig. 3.17. The column was strategically placed between the moving and stationary heads of the machine using a forklift. Then, the top-loading set-up was assembled on top of the column (Fig. 3.18). A custom-made load set-up was specifically designed for the top and bottom columns to ensure uniform distribution of stresses (Fig. 3.18). The loading set-up was comprised of two assemblies of a 60.3-mm diameter cylinder (COLD ROLLED C12L14 round bar ASTM A108) sandwiched between two 32-mm plates, all sitting atop of a 44-mm (44W HOT ROLLED) steel plate. The complete design of this setup is included in Appendix II. A displacement-controlled method was utilized at a rate of 0.25 mm/min. Cable sensors extended from a steel frame to the RC column to measure the column's lateral displacement and axial deformation, as illustrated in Fig. 3.17.

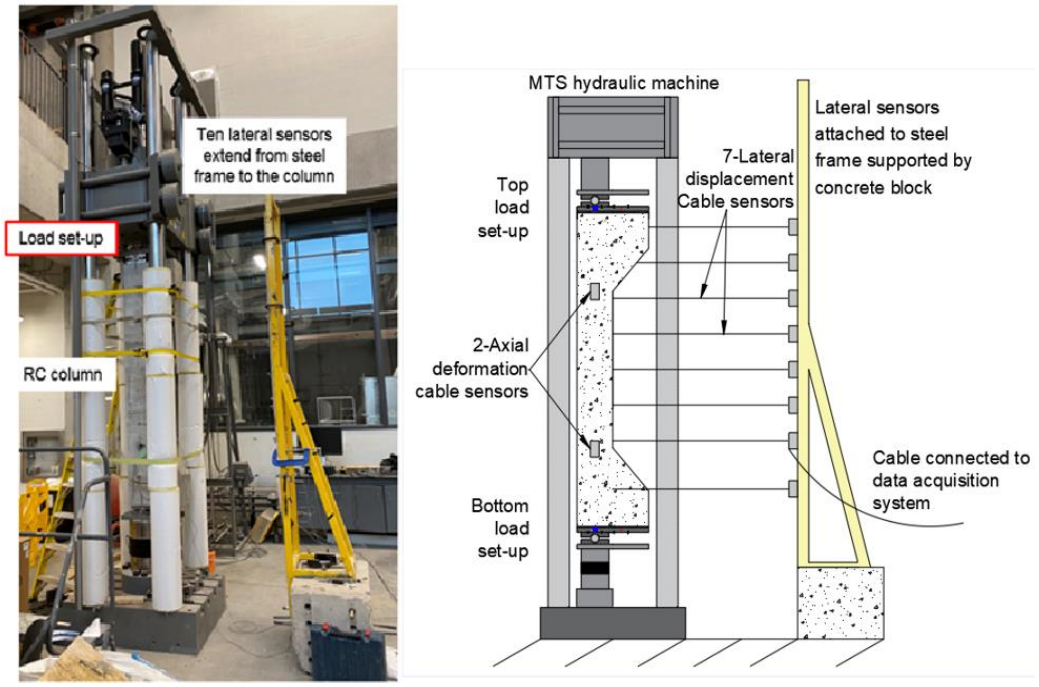

Fig. 3.17: Overall view of the loading set-up

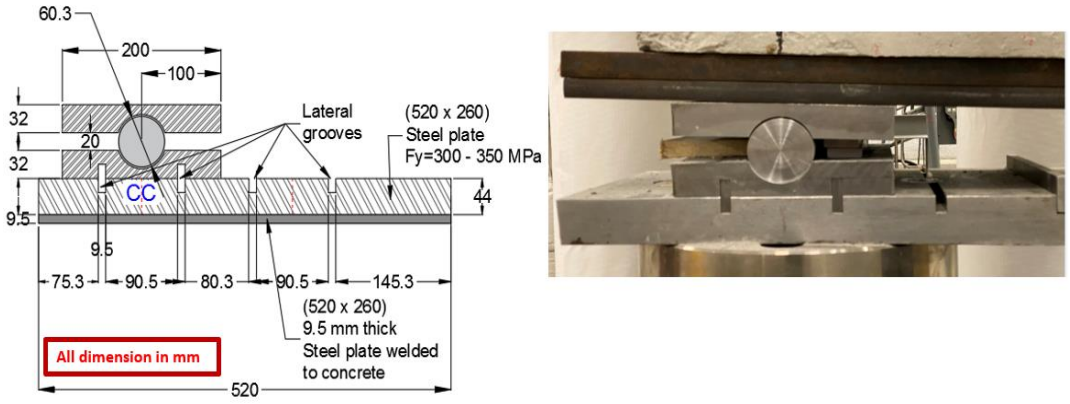

Fig. 3.18: Top & bottom load set-up

A summary of the loading test program is shown in Table 3.7. The total number of columns, size and labels are given along with the test conditions, requirements and failure criteria.

Table 3.7: Summary of quasi-static axial test

Samples	**Columns:** C-C-T1, C-C-T2, C-C-All1, C-C-All2, C-E-R1, C-E-R2, C-E-T3, C-E-T4
Preparations	Assembly of the columns
No. Samples	Ten
Size	Columns: 1,100 mm effective length, 260×260 mm cross section. Top and base corbel: 520×550×260 mm
Test Method	Quasi-Static method: displacement-controlled at a rate of 0.25 mm/min
Loading Protocol	Quasi-static axial load was applied
Load Magnitude	25% post-peak attainment
Preparations & Conditions	The columns surfaces were marked with 26×26 mm grids before the start of the experiments (to clearly observe crack changes)
Temperature	Ambient temperature and constant relative humidity
Equipment	Cable sensors, MTS machine
Failure Criteria	Yielding of the reinforcement, buckling of the reinforcement and crushing of the concrete

3.8.2 Instrumentation

Cracks along the effective zone of the columns were mapped and measured after the static load test. Deteriorations associated with reinforcement corrosion and load application include a combination of staining, longitudinal and transverse cracks, spalling, concrete crushing, and flexural and diagonal cracks.

For this study, the primary devices utilized to assess the condition and determine the structural performance of the specimens after testing were:

- Cable sensors: A simple device to measure linear motion (axial deformation and lateral displacements) of the specimens. The cable wire is drawn relative to a point to measure either deformation or displacement. Cable sensors S1-S7 are used to measure the lateral displacement while S8 and S9 measures the axial displacement as shown in Fig. 3.19. All cable sensors were connected to the MTS data acquisition system to obtain readings for each column.

- Load Cell: An electronic device to measure force, part of the MTS hydraulic machine. Strain gages are embedded within the diaphragm of the load cell to measure the amount of pressure induced by the applied load,
- Crack gauge: a simple tool to measure accurately and precisely the crack width along the concrete surfaces.
- Strain gages along the reinforcement were not used as they are likely to get damaged and disengage due to reinforcement corrosion.

The tie-and-strut method was used to tentatively allocate instrumentations along the height of the column. A schematic of the placement of the required instrumentation is illustrated in Fig. 3.19.

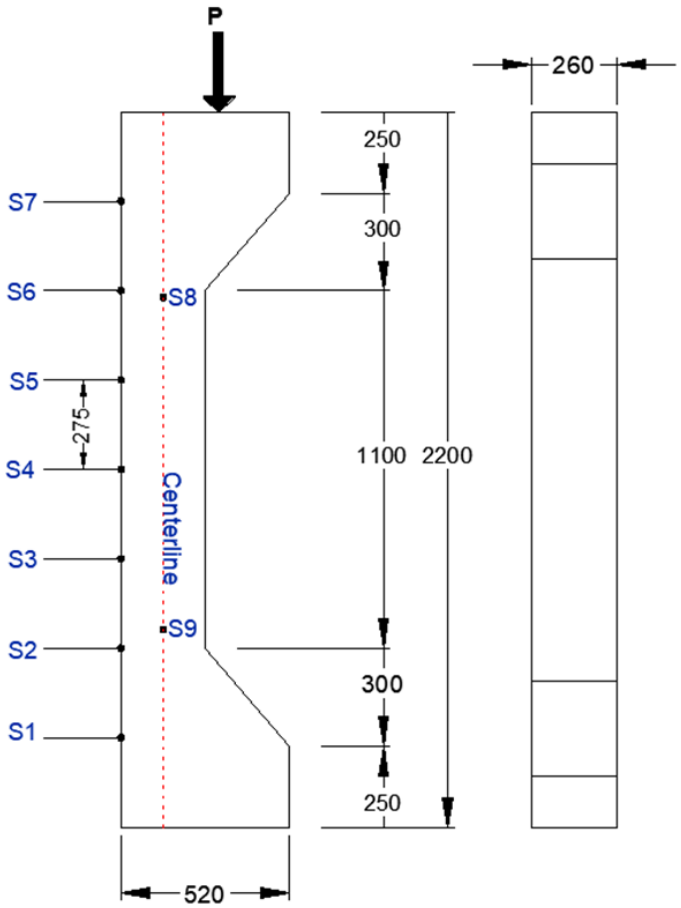

Fig. 3.19: Instrumentation set-up (mm)

3.9 References

ACI 318-19. (2019). Building Code Requirement for Structural Concrete. American Concrete Institute, American Concrete Institute, Farmington Hills, MI, USA.

Andrade, C. (2020) “Initial steps of corrosion and oxide characteristics.” Structural Concrete, 21(5), 1710-1719.

Angst, U., Elsener, B., Larsen, C. K., and Vennesland,. (2011). “Chloride-induced reinforcement corrosion: Rate limiting step of early pitting corrosion.” Electrochimica Acta, Elsevier Ltd, 56(17), 5877–5889.

ASTM A370. (2020). “Standard Test Methods and Definitions for Mechanical Testing of Steel Products.” ASTM International, West Conshohocken, PA.

ASTM C231 / C231M-17a. (2017). Standard Test Method for Air Content of Freshly Mixed Concrete by the Pressure Method. ASTM International, West Conshohocken, PA.

ASTM G1-03. (2017). Standard Practice for Preparing, Cleaning, and Evaluating Corrosion Test. West Conshohocken, PA.

Caré, S., and Raharinaivo, A. (2007). “Influence of impressed current on the initiation of damage in reinforced mortar due to corrosion of embedded steel.” Cement and Concrete Research, 37, 1598–1612.

CONTECVET. (2001). A validated User’s manual for assessing the residual service life of concrete structures. EC Innovation Programme IN30902I, GEOCISA, Madrid, Spain.

CSA-S6.1:19. (2019). Commentary on CSA S6:19, Canadian Highway Bridge Design Code. Canadian Standards Association (CSA Group), Ontario, Canada.

CSA-A23.1:19/CSA A23.2:19. (2019). Concrete materials and methods of concrete construction/Test methods and standard practices for concrete. Canadian Standards Association (CSA Group), Ontario, Canada.

Grubb, M. A., Wilson, K. E., White, C. D., and Nickas, W. N. (2015). Load and Resistance Factor Design (LRFD) for Highway Bridge Superstructures REFERENCE MANUAL.

Maaddawy, T. A. El, and Soudki, K. A. (2003). “Effectiveness of Impressed Current Technique to Simulate Corrosion of Steel Reinforcement in Concrete.” Journal of Materials in Civil Engineering, 15(February), 41–47.

Otieno, M. (2019). “Acceleration of steel corrosion in concrete by cyclic wetting and drying effect of drying duration and concrete quality.” Materials and Structures, Springer Netherlands, 52(2), 1–14.

Otieno, M., Beushausen, H., and Alexander, M. (2016). “Cement and Concrete Research Chloride-induced corrosion of steel in cracked concrete – Part I: Experimental studies under accelerated and natural marine environments.” Cement and Concrete Research, Elsevier Ltd, 79, 373–385.

Chapter 4 Corrosion Effects on the Structural Performance of Columns under Concentric Load

4.1 Abstract

This paper presents the results of an experimental investigation on the effects of different levels and patterns of reinforcement corrosion on the structural performance of reinforced concrete columns under concentric loads. Two sets of two columns each were subjected to an accelerated corrosion regime and tested to failure afterwards. Two of the columns had their transverse reinforcement corroded, whereas the other two had both transverse and longitudinal reinforcement corroded. The results are analysed and compared to a non-corroded column to evaluate the structural performance of the corroded columns. Results show that corrosion of the ties directly affects the post-peak response of the column at low levels of corrosion. The corroded columns had a brittle failure, and the residual ductility and toughness were 70% and 38% of the control specimen, respectively. For columns whose ties and longitudinal reinforcements were corroded, the reduction in residual strength was prominent at a medium level of corrosion. At higher levels of reinforcement corrosion, there was a significant reduction in structural performance, concrete deterioration, and longitudinal rebars buckling due to tie fracture. Based on the results of the experimental investigation, a practical theoretical estimation is proposed to estimate the nominal capacity of corroded columns considering the reduction in confinement effects. The proposed analytical approach agrees well with the experimental results.

Keywords: Reinforcement corrosion, reinforced concrete, bridge columns, concentric load

4.2 Introduction

The condition of ageing highway reinforced concrete (RC) bridges in Canada has worsened over time due to the heavy use of de-icing salts and the growing traffic volume (Lounis 2007). Furthermore, the increase in temperature and precipitation events due to climate change (Government of Canada 2019) will likely contribute to accelerate further existing deterioration in ageing RC infrastructure (Boyle et al. 2013). De-icing salts used in the winter are the predominant cause of reinforcement corrosion in RC. However, the synergistic effect of multiple deteriorating mechanisms, such as frost damage, aggravates the incidence of reinforcement corrosion. For road

bridges in cold climates, columns are vulnerable to being exposed to water mixed with de-icers sprayed regularly by moving traffic (Chauvin and Elstner 2019). It is found that surfaces facing a heavy traffic volume are more exposed to salt-laden water (Gode and Paeglitis 2014). This chloride exposure leads to a reduction in the time to corrosion initiation and subsequently produces higher corrosion rates, thus, reducing the service life of the affected structure. Therefore, it is significant to understand the influence of variable patterns and levels of corrosion on the structural response of RC columns due to variations in exposure to different chloride and moisture levels along their surfaces and elevation (Petersen et al. 2007).

There are very few experimental studies on the structural performance of corroded RC columns (Dabas et al. 2021). Over the past decade, experimental studies have focused on the lateral response of (less than 1,500 mm long) corroded columns under eccentric compression loads (Azad and Al-Osta 2014; Li et al. 2012; Tapan et al. 2016; Vu et al. 2017; Wang et al. 2012; Wang and Liang 2008; Xia et al. 2016). Rodriguez et al. (1996) examined the axial behaviour of (2,000 mm long) corroded columns with three different reinforcing details. The overall load capacity, mean strain and compressive stiffness of the RC columns were reduced as a result of corrosion of the reinforcement. It was also observed that an axial load eccentricity was introduced due to asymmetrical deterioration associated with reinforcement corrosion. Failure was characterized by premature buckling of the longitudinal reinforcing steel due to a reduction in stiffness of the concrete cover and failure of the ties. Wang et al. (2012) and Wang and Liang (2008) examined the ultimate capacity and lateral response of corroded columns (1,300-mm long) under axial loads applied at an eccentricity of 50 mm. Longitudinal bars were partially corroded over a 350-mm or 700-mm length on either the compression, tension or both compression and tension zones at the middle section of the column. A significant reduction in ultimate capacity was found when partial corrosion of the longitudinal bars occurred along the compression zone.

Experimental tests were conducted by Li et al. (2012) on 12 (450 mm) subjected to accelerated corrosion, followed by an axial compression test. The testing regime intended to corrode only the ties at various corrosion degrees. After reaching the peak load, both corrosion-induced and newly formed cracks rapidly propagated, leading to concrete spalling. The test ended when the longitudinal rebars buckled and the ties fractured at the corner side of the columns. The reduction in the cross-section area of the ties resulted in a decrease in the column stiffness and ultimate

bearing capacity. In addition, the mode of failure changed from ductile to brittle failure. Azad and Al-Osta (2014) conducted an extensive experimental study wherein 48 columns were tested to evaluate their residual strength. The authors tested two groups (24 specimens each) of RC columns (1,350-mm long) with different cross sections and reinforcement detailing. The entire section remained in compression for a compression-controlled column with an eccentricity-over-height ratio of $e/h \leq 0.17$. The authors observed that the column's ultimate capacity was governed by the reduction of the compressive strength of the concrete cover due to crack growth.

Experimental work was conducted by Tapan et al. (2016) on 12 (350-mm long) columns to investigate the effect of tie corrosion on confinement strength at different levels of tie section loss (5, 10, 15, 20, 25, 30, 35, 40, 45 and 50%). The ultimate capacity of the columns was reduced as the rate of the corrosion level was increased. The author found evidence of tie debonding and concrete cover cracking. From the experimental results, the author concluded that confinement effects are reduced due to tie corrosion. Xia et al. (2016) tested 24 (1,500-mm long) RC columns to determine their structural performance and evaluate the relationship between reinforcement cross-sectional loss and maximum crack width of the concrete cover. The authors tested two sets of columns with different tie spacings (200 and 100 mm) under a load eccentricity of 50mm. A relationship between cross-sectional area loss of steel, maximum crack width of the concrete cover and strength loss of the RC column was established. The residual compressive strength of the column was estimated from measured crack widths of the concrete cover.

Vu et al. (2017) investigated the effect of corroded transverse reinforcement on the stress-strain curve of confined concrete. The authors tested 36 columns with a length of 600 mm and 200 mm, either square or circular cross-sections, with three different transverse reinforcement layouts at different corrosion levels. As the level of corrosion of the ties increased, pitting corrosion increased. In addition, it was found that tie fracture occurred for severely pitted ties with a mass loss above 15%. This, in effect, reduced ductility due to the reduction in confinement strength. However, more research is needed to understand the structural performance of concentrically loaded columns affected by reinforcement corrosion. This paper presents an experimental study of the effects of variable patterns and levels of reinforcement corrosion on the structural performance (ultimate capacity, ductility, stiffness and mode of failure) of concentrically-loaded columns. Then, a practical approach is presented to estimate the residual capacity of reinforced concrete

columns concentrically loaded and subjected to reinforcement corrosion. The approach is based on the mechanics of RC while accounting for material deterioration (strength, cross-section area and confinement effects) due to reinforcement corrosion by incorporating constitutive models and experimental observations. This approach is applicable for corroded columns subject to static axial loads at small eccentricities (0 to 50 mm) for different sections configurations.

4.3 Experimental Program

In total, five columns were built and tested. One column was a control specimen, and four of them were subjected to an accelerated corrosion regime and wet-dry cycles, as shown in Table 4.1. Two duplicate columns, C-C-T1 and C-C-T2, were exposed to corrosion on two ties at the mid-section of the column, while two duplicate columns, C-C-All1 and C-C-All2, were exposed to corrosion on two-ties and all longitudinal reinforcing bars at the effective corrosion zone (750-mm in the middle of the column). Following the accelerated corrosion process, all columns were subjected to an axial static load applied concentrically up to failure using a hydraulic (MTS) machine.

Table 4.1: Test matrix

w/c	Column label	Accelerated corrosion	Corrosion rate (□A /cm²)	Corrosion set-up	No.	Scenario
	C-C-C	No	0	None	1	Control
0.55	C-C-T1/2	Yes	525	Series	2	Ties
	C-C-All1/2	Yes	475	Parallel	2	All

The RC columns had a 260-mm solid square cross-section confined using tied reinforcement, as shown in Fig. 4.1. The columns were designed using 4-20M longitudinal bars and 10M transverse ties at 150 mm spacing. The columns resistance was determined according to CAN/CSA S6:19 (CSA 2019) and CAN/CSA23.3 (CSA 2019) standard requirements. Corbel sections were designed according to the traditional method specified in the ACI Building Code Section 16.5 (ACI 318 2019).

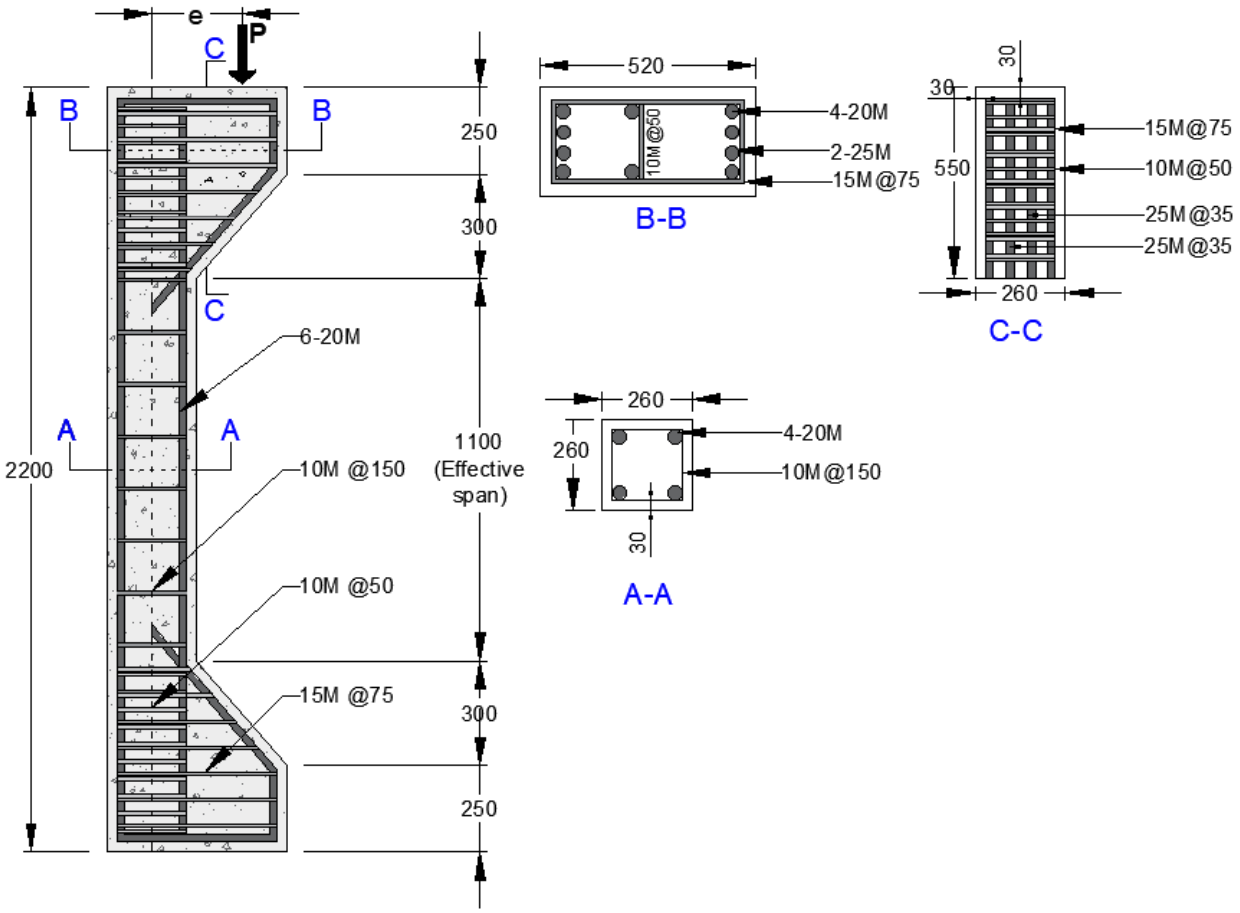

Fig. 4.1: Column details for C-E-C, C-E-T3, C-E-T4, C-E-R1, C-E-R2 (dimensions in mm)

4.4 Fabrications of the Specimens

Ready-mix concrete cast in one day was used for all specimens. General Use (GU) Ordinary Portland Cement (PC) concrete was specified for normal exposure conditions, non-air entrainment, with a maximum coarse aggregate of 14 mm and water-to-cement ratio (w/c) of 0.55; the cement content was 350 kg/m^3, and the coarse-to-fine aggregate ratio was 1.41 (by mass). The intended

compressive strength at 28 days was 30 MPa. For those columns that were subjected to an accelerated corrosion regime, 3.5% of sodium chloride (NaCl) by weight of cement was added to the mixing water to depassivate the protective film on the reinforcement. Three 100 mm in diameter and 200 mm in length cylinders were cast for each column to obtain the compressive strength of the column on the day of the loading test; average values are reported in Table 4.2. All columns were cast horizontally, considering the size and heavy layout of the reinforcement at the corbel sections, to ensure even compaction and prevent the potential development of differential strength along the column length. The specimens were cured for 28 days according to CAN/CSA A23.1:19/ CSA A23.2:19 (CSA 2019), during which moist burlaps fabrics wrapped with plastic sheets were placed atop the specimens to ensure adequate humidity. The specimens were sprayed daily to prevent the fabric from drying out.

Table 4.2: Concrete compressive strength of the RC columns

Column designation	Compressive strength (f_c, MPa) (Test day)
C-C-C	31.9
C-C-T2	33.7
C-C-T1	32.9
C-C-All2	34.0
C-C-All1	32.1

4.5 Steel Reinforcement Properties

Three types of hot-rolled reinforcing steel bars were used in assembling the reinforcement cage of the columns: 25M at the top and bottom corbel sections of the columns; 20M for the longitudinal bars; and 10M for the transverse reinforcement. Standard tensile tests were conducted at the National Council of Canada using an MTS machine (ASTM 2020) on non-corroded steel reinforcement Table 4.3. The yield stress, ultimate strength and maximum elongation of the reinforcements are summarized in Table 4.3. Also, a selected number of corroded longitudinal bars with different levels of corrosion were extracted and tested after the columns were subjected to static loads. The yield and maximum strengths and elongation of the tested corroded reinforcements are summarized in Table 4.3. Fig. 4.2 illustrates the stress-strain curves of the corroded longitudinal reinforcement at low, high, and very high corrosion levels. This figure illustrates a significant reduction in reinforcement ductility (elongation) due to corrosion. The yield and maximum strengths in Table 4.3 were calculated from the minimum measured cross-sectional area of the corroded longitudinal bars.

Table 4.3: Properties of steel reinforcement

Steel No.	Nominal Cross-section (mm^2)	Yield strength (MPa)	Ultimate Strength (MPa)	Elasticity modulus (MPa)	Maximum Strain at failure (mm/mm)
20M(Rebar)	314.2	446.23	598.1	2.0×10^5	0.18
10M (Ties)	100.3	425.01	578.3	2.1×10^5	0.18
Extracted corroded reinforcement after loading test					
20M (Rebar)	$m_s\leq5\%$	446.2	593.1	--	0.21
	$m_s=25\%$	260.7	261.7	--	0.08
	$m_s=30\%$	211.0	211.0	--	0.08

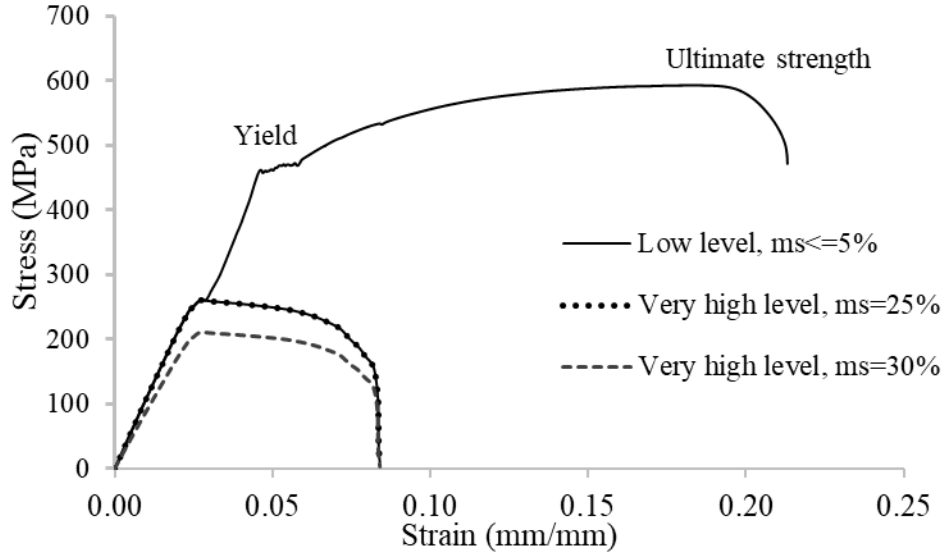

Fig. 4.2: Stress-strain curves of corroded reinforcements after load test for concentrically loaded columns

4.6 Accelerated Corrosion Test

To induce corrosion in the columns reinforcement, a constant and direct current was impressed against the reinforcement at a specified rate predetermined theoretically according to Faradays' law to achieve the desired steel mass loss in a relatively short period. The applied current was maintained constant throughout the corrosion process. Two groups of columns were connected to six DC power supplies. Each group was comprised of two identical columns. Group 1, which comprised columns with only two ties being corroded at the effective corrosion zone, was connected in series, as shown in Fig. 4.3 and Fig. 4.4, using one DC power supply. Columns in Group 2, in which all four longitudinal bars and the two ties in the middle of the effective zone were corroded, were connected in parallel using two DC power supplies, one for each column (Fig. 4.3 and Fig. 4.4). Maaddawy and Soudki (2003) studied the effectiveness of impressing different levels of current densities. The authors concluded that a current density in the range of 100-500 $\frac{\mu A}{cm^2}$ produces mass losses agreeable with those estimated theoretically according to Faraday's law. Thus, the current density calculated according to Faraday's law was pre-calculated to 525 and 475 µA/cm² for Groups 1 (connected in series) and 2 (connected in parallel), respectively. Although the current density values used in this experiment were on the upper limit, it was necessary to

achieve the intended steel mass loss (30%) in a specific period of time. Four 250×750 mm stainless sheets were placed on the outside of each of the faces of the columns along the effective corrosion region to act as cathodes. The effective zone was wrapped with a sponge to provide a wet medium for the electrons to pass from the cathode (stainless steel) through the electrolyte (concrete cover) to the anode (reinforcement being corroded).

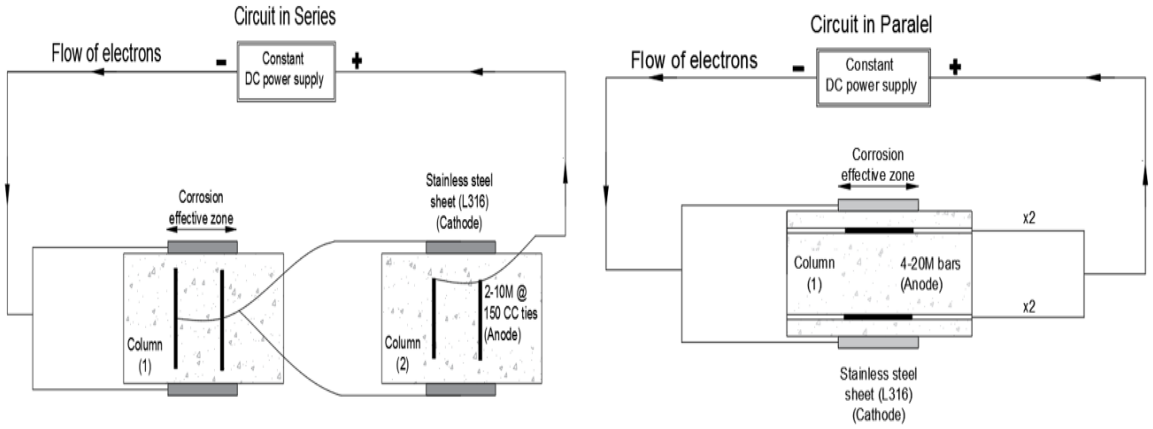

Fig. 4.3: Constant-current accelerated corrosion method: series and parallel connections

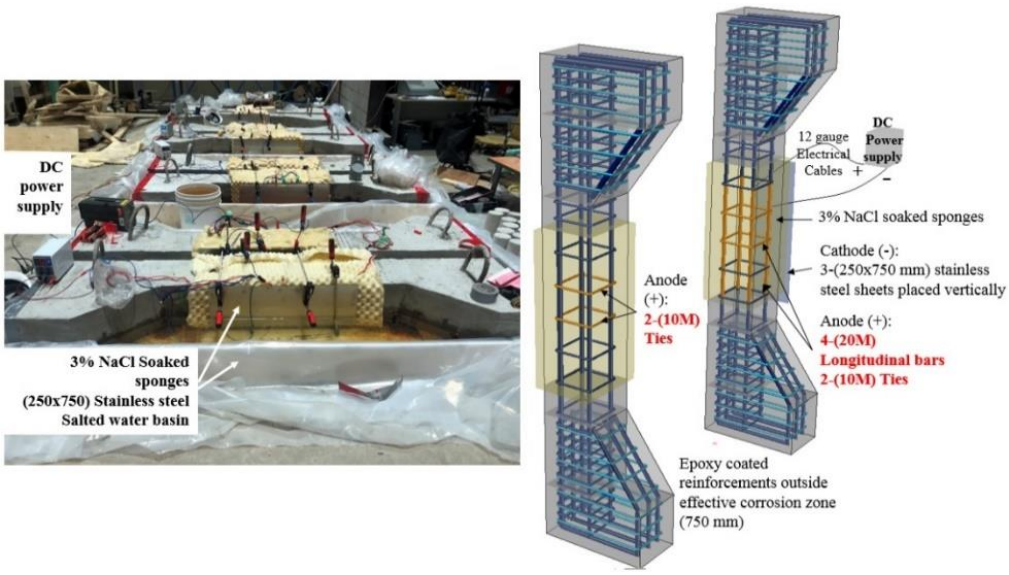

Fig. 4.4: Set-up of the accelerated corrosion method using DC power supply

The specimens were partially immersed in a water pool with 1.5% (by weight of cement) of sodium chloride (NaCl) to reduce the concrete resistivity, prevent leaching and maintain a high humidity environment (Fig. 4.4). Moreover, a cyclic regime of wetting and drying was adopted to enhance

and accelerate the corrosion of the reinforcement (Otieno 2019). A three-day wetting, four-day drying regime was found to be the most effective regime in maintaining concrete resistance at a low level. Epoxy coating was placed at the top and bottom of the column reinforcement and on the longitudinal rebar in the effective corrosion zone for specimens C-C-T1 and C-C-T2 to eliminate any end corrosion effects. In addition, electrical tape was placed at the ties/longitudinal rebar connections to prevent localized corrosion. The accelerated corrosion regime was carried out for 137 days.

4.7 Gravimetric Mass Loss

For those columns whose reinforcement was subjected to accelerated corrosion, reinforcement at the effective corrosion zone was exposed, extracted, and cleaned according to ASTM G1-03 (ASTM 2017) after load testing. The attained corrosion level (average mass loss m_s) is reported as the ratio of the reduced weight to the original weight of the reinforcement. The maximum, minimum, and average mass losses for each column are reported in Fig. 4.5. Results of the gravimetric analysis demonstrate asymmetrical corrosion among the reinforcements for all the columns. However, the measured corrosion levels (based on gravimetric tests) for specimens C-C-All1 and C-C-All2 (connected in parallel) show a good agreement with the corrosion levels calculated according to Faraday's law (4-10% variations). In contrast, for specimens C-C-T1 and C-C-T2 (connected in series), corrosion levels are not agreeable between measured and calculated ones, although it was expected that ties would corrode severely due to a smaller cross-sectional area than the longitudinal bars. This is potentially attributed to lower current (current loss) going through the columns due to the experimental set-up of the accelerated corrosion for columns connected in series compared to those connected in parallel. Thus, based on the achieved mass loss after 137-days, the actual calculated current density of C-C-T1 and C-C-T2 was calculated as 90 $\mu A/cm^2$ and 322 $\mu A/cm^2$, respectively, as explained in Section 3.5.

For all tested columns, reinforcement corrosion was found to occur only in the effective zone (750 mm), specifically for the two mid-section transverse and all the longitudinal reinforcement as intended. In addition, it was observed that reinforcement corrosion was non-uniform along the rebar. It was characterized by multiple localized cavities (pits) at the rebar surface facing the concrete cover, whereas the inner face of the rebar facing the core concrete maintained a prominent

ribbed surface (Fig. 4.5). The diameter of the corroded longitudinal rebars was measured using a Vernier calliper every 100 mm along the length of the bar (700 mm); the variation of cross-sectional loss of the bars for specimen C-C-All1 is plotted in Fig. 4.6. This is consistent with the findings of natural corrosion in the field inflicted by chloride contamination. Based on the experimental results presented in Fig. 4.5, the columns were classified from low to high levels of corrosion according to the average mass loss for both transverse and longitudinal reinforcement (Ontario Ministry of Transportation 2008):

- Intact level (I) for $m_s \leq 1\%$,
- Low level (II) for $m_s < 5\%$,
- Moderate (medium) level (III) for $5 \leq m_s \leq 10\%$,
- High (severe) level (IV) for $10 < m_s \leq 20\%$,
- Very high (very severe) $m_s > 20\%$.

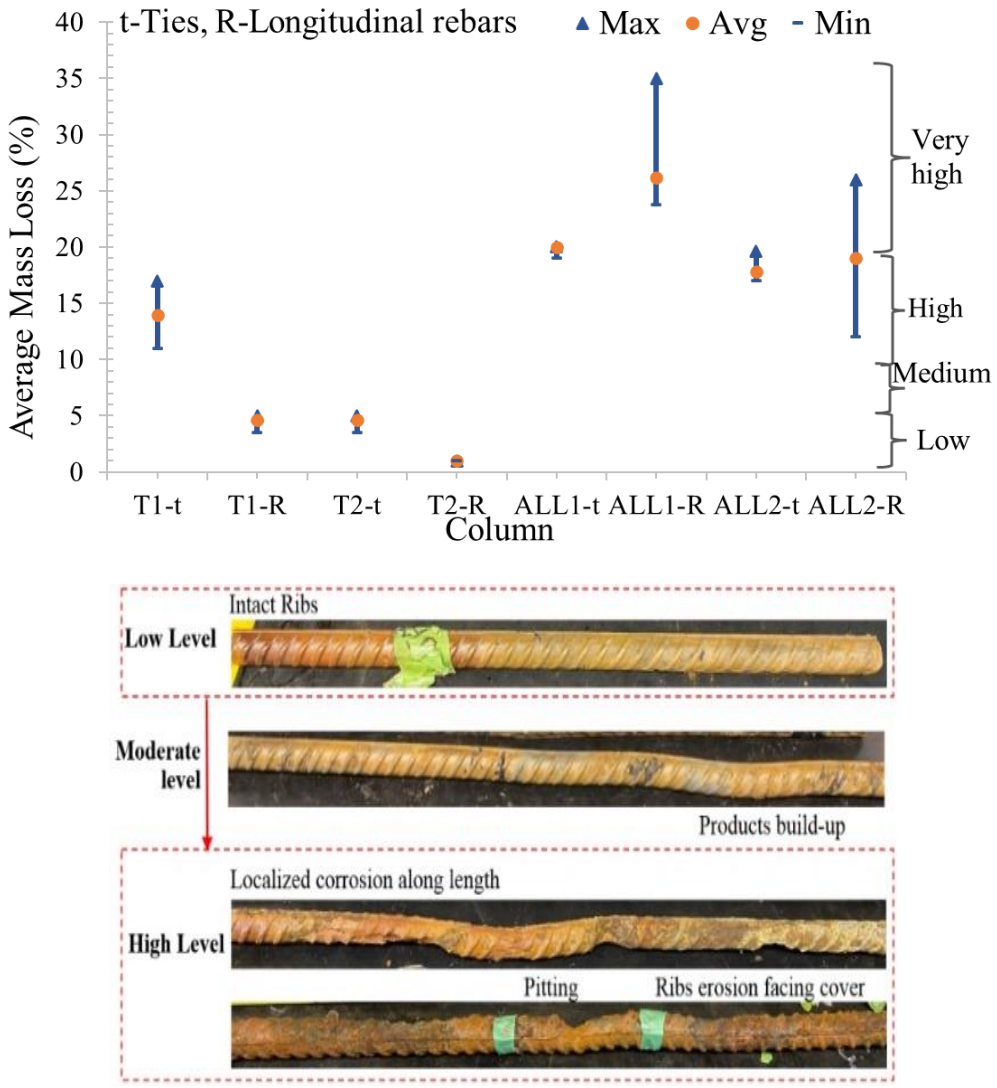

Fig. 4.5: Top: Average mass loss according to ASTM G1,

Bottom: Patterns of reinforcement corrosion at different levels for columns C-C-T1 and C-C-All1

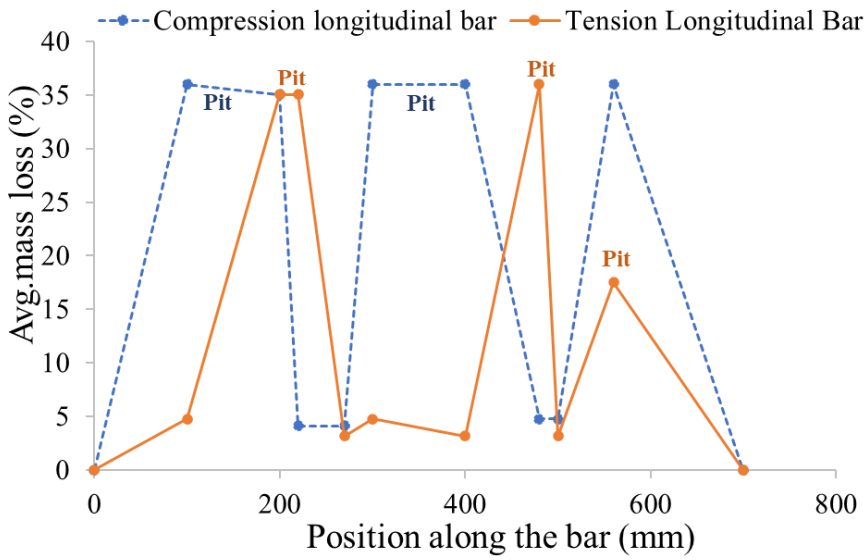

Fig. 4.6: Cross-sectional area loss of the longitudinal bars at the effective zone for C-C-All1

4.8 Loading Test

A quasi-static load was applied at an eccentricity of 190 mm and a 0.25 mm/min rate using a hydraulic testing machine with a maximum capacity of 2,500 kN. A displacement-controlled method was utilized to capture the post-peak behaviour of the columns. The loading was terminated when the post-peak load reached 25% of the column's capacity. The columns were simply supported at the top and bottoms edges, as shown in Fig. 4.7. Seven lateral sensors were attached along the length of the columns to record lateral displacements. All sensors were connected to a data acquisition system to collect and record data.

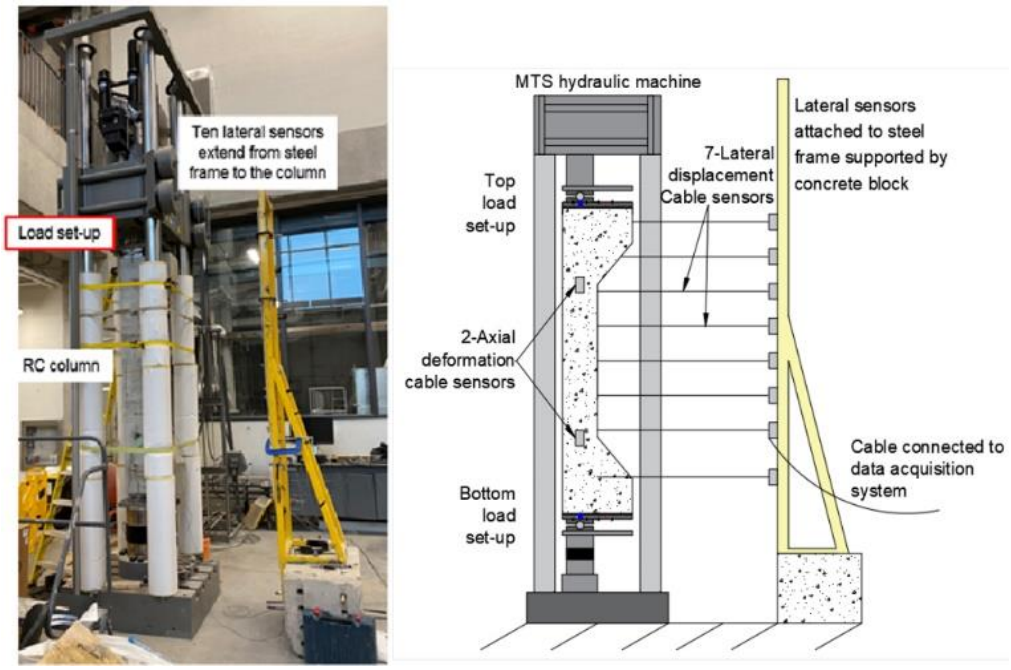

Fig. 4.7: Loading test set-up using MTS hydraulic machine

4.9 Test Results and Discussion

4.9.1 Performance Assessment of the Corroded Columns

4.9.1.1 Development of Concrete Cracks

It was observed that crack size, continuity and formation was increased with higher corrosion levels. Columns C-C-T1 and C-C-T2 suffered from localized stains at tie spacing and transverse cracks that spread along the reinforcements. For C-C-T1, the width of transverse cracks grew from 0.35 mm, measured before the load was applied, to 2mm after column failure. Moreover, the longitudinal bar at the bottom surface of the column, with an unforeseen low level of corrosion due to cross-contamination, led to the development of a longitudinal crack along the longitudinal reinforcement length (Fig. 4.9). This longitudinal crack grew from 0.85 to 3 mm after failure. On the other hand, columns C-C-All1 and C-C-All2 suffered from extensive staining that was widespread over all column's surfaces. Both C-C-All1 and C-C-All2 had longitudinal cracks that grew from 0.85 to 3mm after failure. All columns suffered from corner cover spalling. A summary of crack development is shown in Table 4.4.

Table 4.4: Crack development for all columns

C-C	Corrosion Level	Before load	Afterload	Affected reinforcement/Type of corrosion
		w_{cr}(mm), pattern		
C-C-C	None	None	Concrete crushing	None
C-C-T2	Low	None	2mm, Spalling/widening pre-exiting/ bridging with new cracks/diagonal cracks/ concrete crushing	Uniform corrosion ties
C-C-T1	Medium	0.35, Longitudinal / transverse cracks. Localized stains at tie spacing		Localized pitting / Uniform corrosion along tie length
C-C-All2	High	0.85-0.95, Longitudinal cracks along full effective length, extensive stains on full surface	3mm, Spalling/widening pre-existing cracks/ crack bridging/ concrete crushing	Localized pitting along tie & bars length /Two tie fracture tension side
C-C-All1	Very high			Localized pitting along tie & bars length / Two tie fracture compression side

4.9.1.2 Axial Response

The applied axial load versus axial strain of the entire span and of the effective corrosion zone of the columns is plotted in Fig. 4.8(a) and Fig. 4.8(b), respectively. For corroded columns, a reduction of 6% and 14% in the ultimate axial capacity is observed for specimens C-C-T2 and C-C-T1, respectively, when compared to the control specimen. However, specimen C-C-T2, with a 5% average mass loss in the two mid-ties, displayed the same axial stiffness as the control specimen, whereas specimen C-C-T1 exhibited about 15% reduction in axial stiffness when the mass loss in the ties increased to 14%. Columns subjected to axial compressive loads tend to experience lateral deformation due to the Poisson effect (the ratio of the transverse strain to the axial one increases as the applied loads increase). However, a sufficient amount of transverse reinforcements in non-corroded columns restrain the lateral expansion (transverse strain) of the concrete. However, as the corrosion level of ties increases from C-C-T2 to C-C-T1 (5 to 14%), the confining pressure counteracting the expansion action is reduced due to a reduction in tie stiffness. Thus, the columns' lateral displacement in the overall column is increased due to corrosion. Moreover, the corroded middle section of the column to the lateral displacement is increased.

For specimens C-C-All1 and C-C-All2, whose longitudinal reinforcing bars had also been corroded, the columns' ultimate capacity was further reduced from that of the control specimen by 36% and 44% for C-C-All2 and C-C-All1, respectively (Table 4.5). The axial stiffness of both C-

C-All2 and C-C-All1 decreased by 37 and 46%, respectively Fig. 4.8. The columns did not experience significant axial strain compared to columns C-C-T1 and C-C-T2 due to the longitudinal bars' high level of corrosion (loss of ductility) and subsequent reduction in the ultimate capacity.

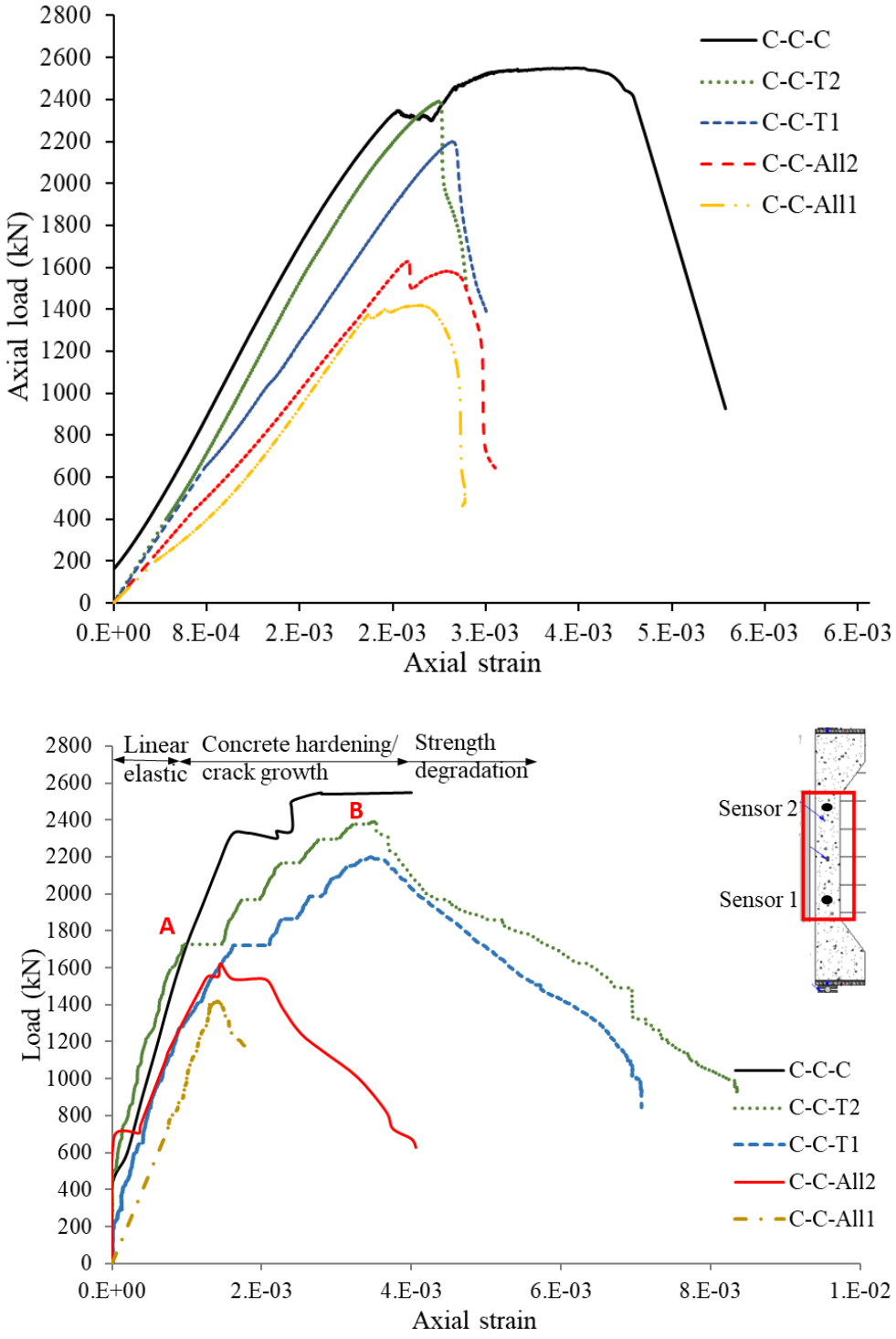

Fig. 4.8: Load-axial strain curve of the columns (a-top) overall length, (b-bottom) middle section

4.9.2 Failure Mode

The control column (C-C-C) followed a compression-controlled failure mechanism, wherein the load-carrying capacity of the column was dependent on the contribution of both steel and concrete materials. Crushing of the concrete cover was observed at peak load. The column displayed a ductile post-peak response owing to the good distribution of ties along the middle region of the column, as illustrated in Fig. 4.8(a).

For specimens C-C-T1 and C-C-T2, the failure pattern was characterized by crushing of the concrete on the compression side and spalling of the concrete cover. A global failure characterized by lateral displacement along the entire length of the columns was evident. This was attributed to the asymmetrical unintended corrosion of the longitudinal rebars as a result of the failure of electrical isolation from the transverse reinforcement. These two specimens exhibited primarily three different types of cracks at failure: significant widening of pre-existing corrosion-induced cracks, development of large diagonal cracks, and development of flexural cracks. Diagonal cracks extended from one side of the column to the outermost side on all surfaces of the column, while flexural cracks developed on the tension side of the column (Fig. 4.11).

Inspection of the extracted reinforcement revealed that the ribs and circumference of the longitudinal reinforcing bars were intact over the spacing between adjacent ties as intended. This was a good indication that corrosion did not occur along the longitudinal reinforcement. However, at the tie-rebar joint at the corner of the column's compression-downward side (bottom casting surface), the ribs and circumference of the longitudinal reinforcement were eroded and reduced. At the affected corner, local buckling of the longitudinal reinforcing bar was evident. At the failure section, there was no evidence of tie fracture, but the corroded tie likely failed to provide sufficient restraint against the applied loads, which led to local rebar buckling. Failure of specimens C-C-T1 and C-C-T2 was initiated by hardening of the concrete cover (increase in column deformation with the increase in load increments). This is evident by the widening of pre-existing cracks and the development of new microcracks at 70% of peak load (point A in Fig. 4.8(b)). This was followed by premature local rebar buckling and concrete crushing at peak load (point B in Fig. 4.8(b)). The columns then experienced a rapid reduction in post-peak strength, as illustrated in Fig. 4.8. These specimens experienced significant lateral displacement along their entire length. This is attributed

to potential accidental eccentricity due to asymmetrical reinforcement corrosion and general column imperfections (see Fig. 4.9 and Fig. 4.11).

Column C-C-All1 exhibited a significant reduction in the mechanical and geometrical properties of both concrete and steel due to induced corrosion. Concrete cover lost its stiffness due to extensive cracking. This was evident from the significant widening of pre-existing cracks along all column surfaces. Moreover, large pieces of concrete cover spalled off at the corners of the column on the downward surface (Fig. 4.10). Furthermore, several cracks propagated through the core of the concrete in between the three adjacent ties. Moreover, two of the adjacent ties were fractured. This section was very brittle and easy to disintegrate with a hammer indicating a significant reduction in the core compressive strength and confinement effects. Moreover, evidence of rust accumulation resulted in the loss of adhesion between the concrete cover and the reinforcement, erosion of the ribs and the formation of multiple localized pits along the rebar length (Fig. 4.6). The ribbed surface of the bar facing the concrete cover was eroded, and the roundness of the bar's circumference was irregular along the length and circumference due to the presence of several pits. Moreover, ties were almost ineffective in resisting lateral pressure as they were very brittle. Longitudinal bars suffered a significant mass loss (m_s>20%), which resulted in considerable strength and ductility degradation. Failure of C-C-All1 was comprised of fracture of the two ties due to pitting corrosion in the middle region of the column on the compression side (Fig. 4.12). Subsequently, the confinement strength was reduced, and the exposed (unsupported) length of the longitudinal bar was increased, leading to local buckling of the longitudinal reinforcement between the two ties at the corner of the downward-compression side of the column (Fig. 4.12). Failure of specimen C-C-All2, which had a high level of corrosion, was characterized by fracture of the two mid-ties on the tension side of the column. Unlike C-C-All1, the core concrete did not exhibit visible cracks and did not disintegrate when hit by a hammer. This strongly indicates that the compressive strength of the concrete core was not significantly reduced.

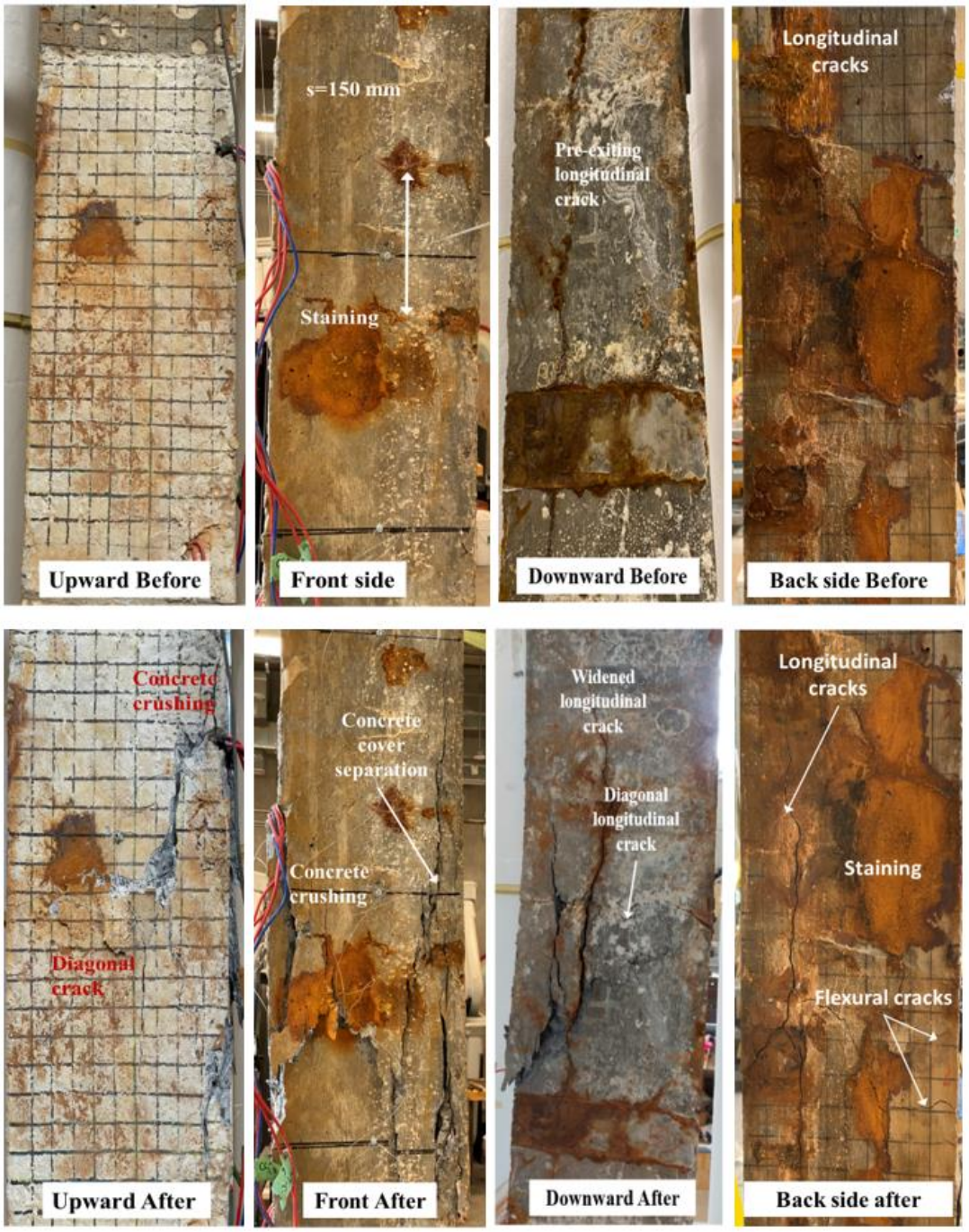

*Fig. 4.9: Top: corrosion-induced damage before loading, Bottom: damage after loading for C-C-*T1

Fig. 4.10: Corrosion-induced damage before loading, Bottom: damage after loading (C-C-All1)

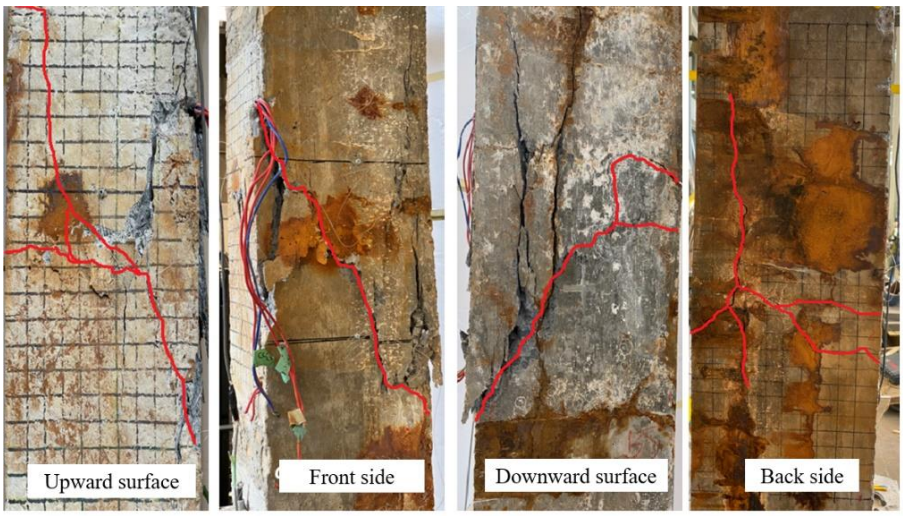

Fig. 4.11: Inclined cracks along column surfaces (C-C-T1)

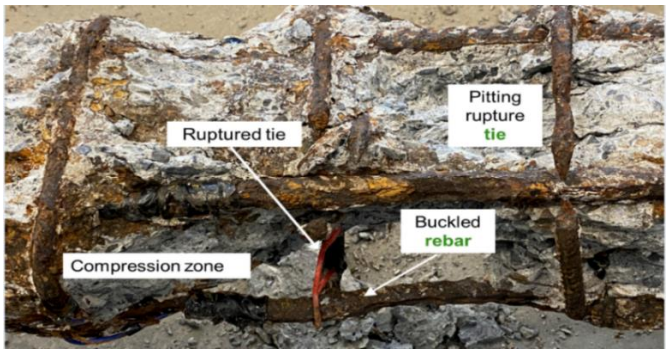

*Fig. 4.12: Profile of the corroded reinforcement cage at the effective zone for C-C-A*ll1

4.9.3 Flexural Response

Fig. 4.13 plots the applied axial load against the lateral displacement of the middle section for all columns. The control specimen C-C-C had a minor lateral displacement up to a peak load of 2,550 kN. Once the peak load was reached, the lateral displacement increased gradually up to failure of the specimen. Fig. 4.13 illustrates an increase in the extent of the lateral displacement for specimens C-C-T1 and C-C-T2 compared to the non-corroded column. This is attributed to potential accidental eccentricities resulting from asymmetrical corrosion of the ties leading to asymmetrical cracking of the concrete cover on the sides of the column. The increase in the lateral displacement is more evident for C-C-T1 than C-C-T2 due to an increase in the corrosion level of the ties. Columns under high axial loads are vulnerable to higher lateral deformation when the

restraining effects provided by the ties are compromised due to corrosion. For specimens C-C-All1 and C-C-All2, the concrete cover extensively deteriorated on all sides of the columns due to corrosion of the ties and the longitudinal bars. Moreover, C-C-All2 had a higher level of corrosion leading to an increase in lateral displacement of the column compared to C-C-All1.

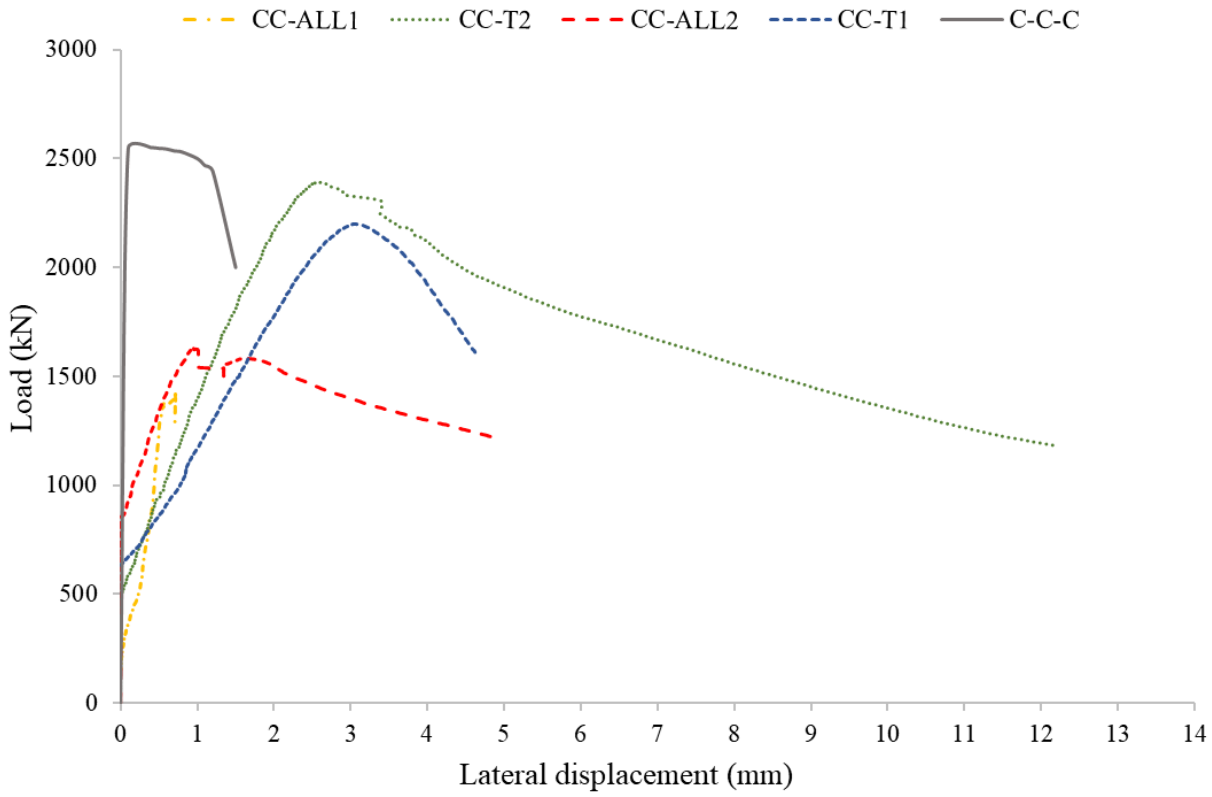

Fig. 4.13: Load-lateral displacement of the middle section for all columns

4.9.4 Residual Strength and Ductility

Results of this experimental work are summarized in Table 4.5. In Table 4.5, the ultimate capacity (F_u) refers to the peak load attained during the test, while the residual strength ratio is the ratio of the corroded column peak load to the uncorroded one. Residual ductility was determined from the area under the load-deformation curves of the columns that were corroded compared to the control specimen. For non-corroded members, ductility (μ) is conventionally estimated as the ratio of the deformation measured post peak at 85% of the ultimate load (Δ_{u85}) to the yield deformation (Δ_y), $\mu = \frac{\Delta_{u85}}{\Delta_y}$. The yield load and corresponding displacement were determined according to the energy

equivalence method and are equal to the turning point of a bilinear curve idealized from the actual load-displacement curve (Fig. 4.13) (Zhou et al. 2020). The axial stiffness is determined by estimating the slope in the elastic region of the load-deformation curve for both control and corroded columns using a linear regression equation considering all points along the ascending line of the load-deformation curve. The residual stiffness ratio is the slope ratio of the corroded column to the control column. Moreover, relationships were established between the average mass loss and the residual strength, axial stiffness and ductility to better understand the effect of reinforcement corrosion on the structural performance of the columns (Fig. 4.14). From the figure, it is observed that the column behaviour is considerably influenced by the level and pattern of reinforcement corrosion. As the level and extent of reinforcement corrosion increased, all the structural performance indices decreased (Fig. 4.14).

At a low level (5%) of tie corrosion, the residual ductility for specimen C-C-T2 decreased to 70% of the uncorroded specimen while the residual strength remained unaffected. Although the stiffness of the ties was affected by this level of corrosion, the compressive strength of the concrete cover and core were still adequate to maintain ultimate column resistance. On the other hand, there was a gradual reduction in residual strength for all specimens as the level of corrosion-induced cracking is increased. As the level of tie corrosion increased for the specimen (C-C-T1) to a medium level (14%), concrete cover cracking increased (Fig. 4.9). The residual strength was 86% of the control specimen. The stiffness of the corroded ties decreased leading to a reduction in the restraining effects, subsequently, a reduction in core confinement strength.

For the columns that were subjected to high levels (20-26%) of all reinforcement corrosion (C-C-All1 and C-C-All2), there is a noticeable reduction in all structural indices (Fig. 4.14). The residual strengths ratio are 64 and 56%, respectively. Moreover, for C-C-All1 and C-C-All2, ductility is 40 and 46%, while stiffness is 69 and 54%, respectively (Fig. 4.14). This was attributed to significant degradation in all reinforcement cross-sectional area and bars' mechanical properties (ductility) due to pitting corrosion (as shown in Fig. 4.6). Moreover, two ties fractured due to pitting which decreased the restraining effects, thus, core strength. Furthermore, rust products created expansive forces that led to significant concrete cover and core deteriorations (cracking) (Fig. 4.10 and Fig. 4.12). Both reduction in steel area and cracking of the concrete cover and core weakened the ultimate load-bearing capacity of the column. Thus, the residual strength of the column is affected

by concrete cover deterioration, reduction in cross-sectional area of the longitudinal reinforcement and accidental eccentricities due to asymmetrical corrosion similar to Rodriguez et al. findings (Rodriguez et al. 1996).

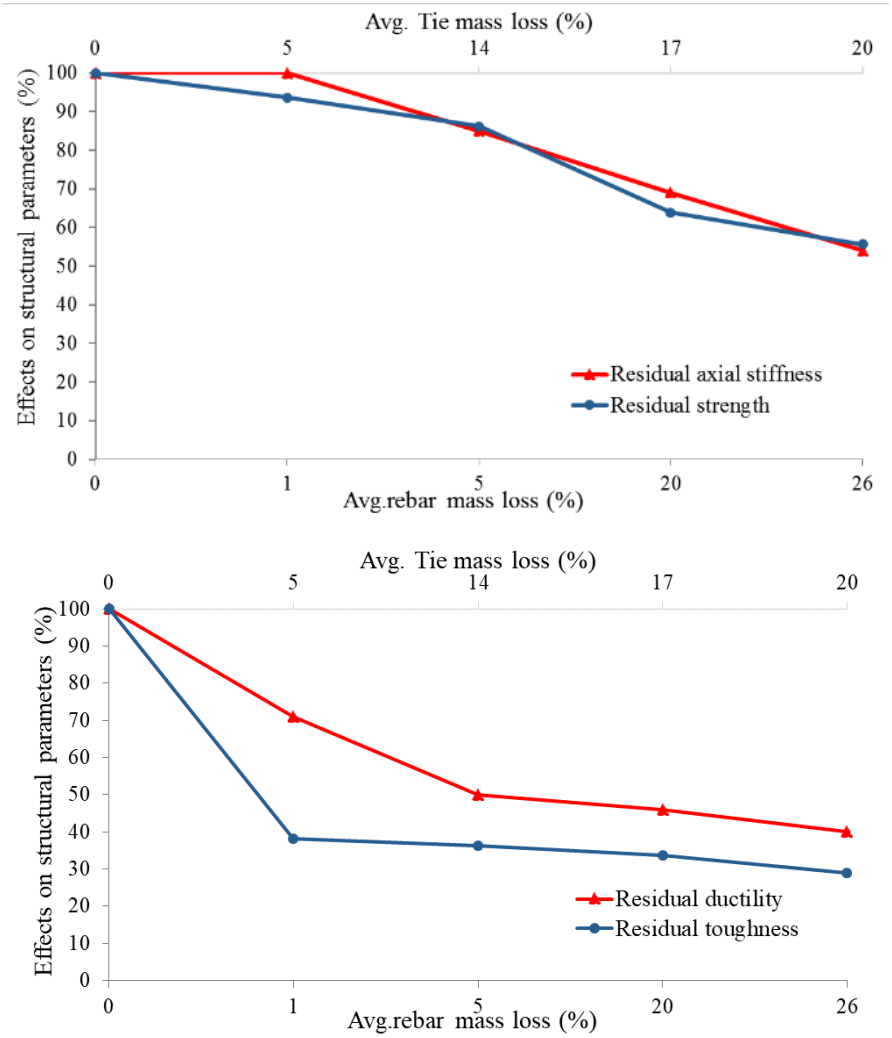

Fig. 4.14: Effects of corrosion on the structural performance of columns

Table 4.5: Experimental results

Column Label	Corrosion level	m_s (%) Tie	m_s (%) Rebar	P_u (kN)	P_{ur} (%)	85% P_u (kN)	μ_r (%)	κ_r (%)	$w_{max.cr}$ before load (mm)	$w_{max.cr}$ afterload (mm)
C-C-C	None	0	0	2,550	100	2,168	100	100	None	Cover Crushing
C-C-T2	Low	5	1	2,389	94	2,031	71	100	Hairline	Spalling corners/ widening pre-existing cracks
C-C-T1	Moderate (medium)	14	5	2,199	86	1,869	50	85	0.35	
C-C-All2	High	17	20	1,630	64	1,386	46	69	0.85	Spalling/widening pre-existing cracks/ crack
C-C-All1	Very high	20	26	1,418	56	1,205	40	54	0.9	

4.10 Failure Mode Comparison

For different reinforcement corrosion levels and patterns, the RC column's response transitions from a ductile for specimen C-C-C to a brittle response for specimens C-C-T1 and C-C-All1 and C-C-All2, as shown in Fig. 4.15. Reduction in ductility was evident at low-level of transverse reinforcement corrosion. Excessive lateral displacement was evident for columns (C-C-T1/2) that had asymmetrical corrosion. On the other hand, at a very high level of all reinforcement corrosion ties were fractured and rebar buckling occurred (C-C-All1).

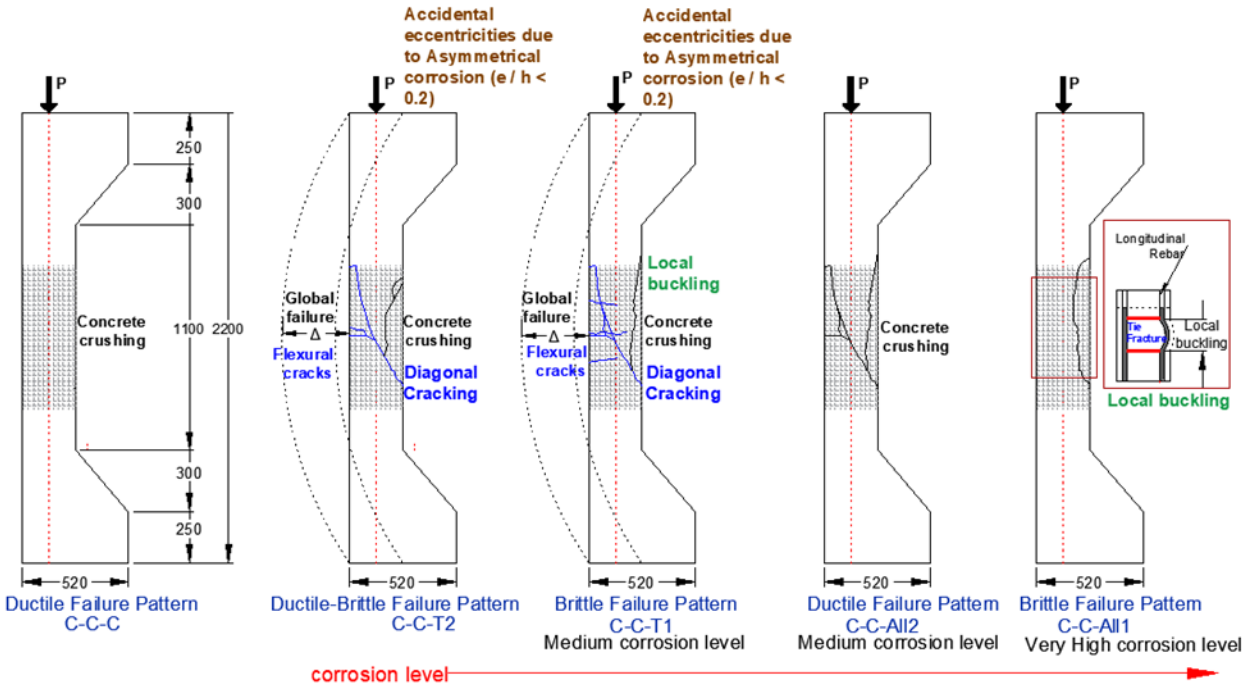

Fig. 4.15: Comparison between all concentrically-loaded columns failure mode

Fig. 4.16 illustrates the lateral displacement measured along the entire column. The intended failure mechanism planned initially was to produce failure at the middle section of the column where it has deteriorated. For specimens C-C-T1, C-C-T2 and C-C-All2, the maximum lateral displacement occurs at 1,375 mm (275 mm above) the mid-height of the entire column. In contrast, for column C-C-All1 the maximum lateral displacement occurs at precisely the middle height (1,100 mm) of the entire column. The columns fail as intended; however, a minor variation in the precise position of the maximum lateral displacement is attributed to asymmetrical reinforcement corrosion.

Moreover, it is attributed to the corroded reinforcement pattern; the transverse reinforcement's corrosion primarily affects the post-peak response of the load-displacement curve of the column. Such as ductility, toughness and flexural response are reduced significantly as the corrosion level is increased. In contrast, for column C-C-All1, all the reinforcements were severely corroded along the middle section.

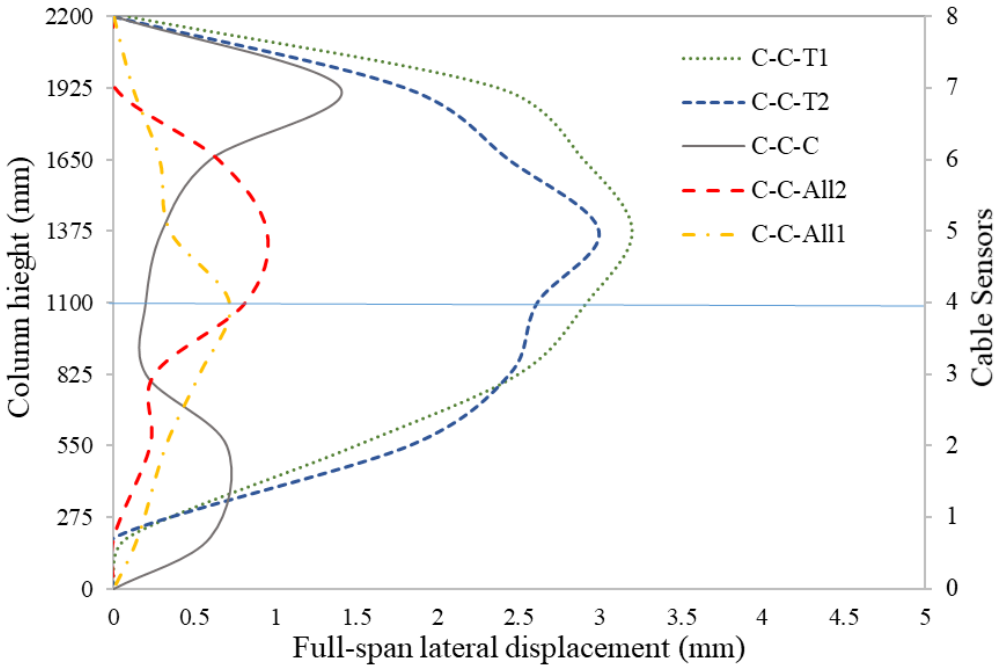

Fig. 4.16: Lateral displacement for all the columns at the middle section of the column

4.11 Analytical Estimation of the Residual Capacity of Corroded Columns

4.11.1 Proposed Analytical Procedure

In engineering design applications, the nominal axial load-carrying capacity of non-corroded RC columns P_c is conventionally estimated according to CAN/ CSA A23.3 (CSA 2019) by summing the strength contributions of both concrete and steel reinforcement. This equation does not account for concrete and steel degradations due to reinforcement corrosion.

$$P_c = \alpha_1 f_c A_g + f_y A_s \qquad Eq.\ 4.1$$

where α is 0.8, f_c f_c' is the concrete compressive strength, A_g is the gross concrete area, f_y is the yield strength of the longitudinal bars, and A_s is the area of the longitudinal bars.

Experimental results of this study indicate that the corroded columns fail prematurely before attaining the ultimate load-bearing capacity. This indicates that the conventional equation for non-corroded columns cannot safely predict (as it overestimates) the actual axial capacity of corroded columns. Therefore, this study presents a practical daily tool for the engineering community to estimate the residual load capacity for RC columns subjected to reinforcement corrosion and small eccentricities (0 to 50 mm). The equation is modified by incorporating existing deterioration models and collected field data about crack width and locations and corrosion level determined through NDT testing into the conventional equation. The modified equation has a broad application to columns with variable reinforcement area sections and different concrete strengths; thus, it is not limited to this experimental study. Moreover, the estimation can be applied to determine the columns' residual capacity at different corrosion levels. The experimental results of this study were used to investigate column response and validate the modified equation. The experimental results demonstrated that the columns' residual capacity is primarily affected by a reduction in concrete cover due to cracking, reduction in core strength due to cracking and loss of restraining effects provided by the corroded ties, and the reduction in the cross-sectional area of reinforcing steel. Therefore, the inherent characteristics of each material affected by corrosion are accounted for by dividing the column's cross-section into three sections: concrete core, concrete cover, and steel reinforcement. The modified ultimate capacity (P_c^{corr}) of the corroded columns subject to concentric loads is only modified to reflect the corrosion effects as follows:

$$P_c^{corr} = \alpha\left(f_{cr-cover}(A_{cover}) + f_{core}(A_{core})\right) + f_y A_{sc} \qquad \textit{Eq. 4.2}$$

where α is a constant assumed to equal 0.8 for the corroded columns, A_{cover} is the cross-sectional area of the concrete cover, A_{core} the cross-sectional area of the concrete core, $f_{cr-cover}$ is the reduced compressive strength of the concrete cover according to Cape (1999), f_{core} is the compressive strength of the concrete core estimated according to Razvi and Saatcioglu (1999), and f_{yc} and A_{sc} are the yield strength and the area of the corroded reinforcement. The reduced concrete area is estimated according to the following.

$$A_{cover} = 2bc + 2hc - 4c^2 \qquad \textit{Eq. 4.3}$$

$$A_{core} = hb - 2bc - 2hc + 4c^2$$

$$A_{cover-reduced} = bc + hc - 2c^2 \quad \textit{for a high level of corrosion}$$

4.11.1.1 Reduction in Core Strength due to Cracking and Loss of Restraining Effects

The experimental results show that the ultimate capacity and ductility of concentrically loaded columns are governed by the strength of the concrete core and the transverse reinforcement. It is found that any damage to the longitudinal reinforcement results in further reduction in ultimate capacity and potential buckling. The core of the concrete that is restrained by the ties is still capable of withstanding incremental loads. For corroded columns, the ineffective area to axial load resistance is enlarged as the contribution of the concrete core is reduced by corrosion of the ties and/or reduction of their stiffness at the crossties. As a result, it was observed in the experiments that reduction in the ultimate capacity became noticeable at a medium level of tie corrosion and became more significant at higher levels of corrosion. This is because, at the medium level, the ties suffered deep pits at the crossties, where the restraining effects peak. In contrast, at higher levels of corrosion, the pits were widespread along the length of the ties; thus, the corroded ties were less effective in confining and inhibiting crack growth through the core. In this study, the model proposed by Razvi and Saatcioglu (1999) is used to estimate the confined strength of the concrete core of the column. This model was chosen because it estimates the non-uniform lateral pressure generated by the restraining effects of the transverse reinforcement, and the lateral pressure is a function of the yield strength and spacing of the ties, which are essential parameters negatively affected by reinforcement corrosion. The model applies to normal and high strength

concrete ranging from 30 to 130 MPa for rectilinear and spiral section configurations. The confined compressive strength f_{core} (MPa) is calculated from:

$$f_{core} = f_c + k_1 f_{le} \quad \textit{Eq. 4.4}$$

where f_c is the unconfined concrete compressive strength (MPa) and k_1 is given by:

$$k_1 = 6.7(f_{le})^{-0.17} \quad \textit{Eq. 4.5}$$

where f_{le} is the equivalent uniform pressure, estimated as follows:

$$f_{le} = k_2 f_l \quad \textit{Eq. 4.6}$$

k_2 is a reduction parameter to account for the non-uniform nature of the average pressure f_l. The average lateral pressure is estimated according to Razvi and Saatcioglu (1999). To account for corrosion effects the cross-sectional area of the tie area (A_{st}) and yield strength (f_y) are reduced depending on the corrosion level. Moreover, tie fracture due to pitting corrosion is accounted for by increasing tie spacing (s).

$$f_l = \frac{\sum_{i=1}^{q} A_{st} f_y sin\theta}{s b_c} \quad \textit{Eq. 4.7}$$

where sb_c is the core surface area, q is the number of tie legs, f_y is the tie yield strength, A_{st} is the tie area, and θ is the angle between the leg of transverse reinforcement and the core side crossed by the same leg.

4.11.1.2 Reduction in Concrete Cover due to Crack Propagation and Widening

Corrosion-induced cracks and spalling reduce the compressive strength of the concrete and its ability to sustain further loads. Vecchio and Collins (Vecchio and Collins 1986) proposed a model later modified model by Cape (Cape 1999) to account for the compressive strength reduction based on crack width. The model is a function of the tensile strain that leads to the development of cracks when the expansive pressure by rust products induces tensile stresses exceeding the tensile strength of the concrete. The compressive strength of the concrete cover $f_{cr-cover}$ is therefore reduced according to:

$$f_{cr-cover} = \frac{f_c}{1+K\,(\frac{\varepsilon_t}{\varepsilon_{co}})} \qquad \textit{Eq. 4.8}$$

where f_c is the normal compressive strength, *K* is a coefficient based on material roughness and diameter (0.1 for ribbed bars (Cape 1999)), ε_t is the average smeared tensile strain in cracked concrete, and ε_{co} is the strain at the maximum compressive stress (0.002 for normal strength and weight concrete). The average tensile strain induced by corrosion products build-up is estimated from according to (Coronelli and Gambarova 2004):

$$\varepsilon_t = \frac{b_f - b}{b} = \frac{n.w_{cr}}{b} \qquad \textit{Eq. 4.9}$$

where b is the original uncracked cross-sectional width, b_f is the cracked cross-sectional width, n is the number of bars, and w_{cr} is the total crack width. The on-site crack width measurements is estimated according to $w_{cr} = \frac{\sum w_{cri} l_i}{L}$, where L is the total length of the affected section, w_{cri} and l_i are respectively the width and length of individual cracks.

4.11.1.3 Reduction in cross-sectional area of the reinforcement

The reduction in the cross-sectional area (A_{sc}) of the rebar is calculated as a function of the penetration attack according to CONTECVET (2001):

$$A_{sc} = \pi(r_0 - P_x)^2 \qquad \textit{Eq. 4.10}$$

where r_0 is the uncorroded radius, and P_x is the attack penetration. The attack penetration (P_x) is a function of corrosion rate and time (CONTECVET 2001):

$$P_x = 0.0116 \cdot i_{corr} \cdot t \qquad \textit{Eq. 4.11}$$

where P_x is the reduction in the bar radius in mm (assuming uniform corrosion), i_{corr} is the current density in μA/cm^2 estimated from periodic measurements of the corrosion rate over a year to account for extreme climatic conditions (dry/wet winter, summer, spring), and *t* is the time in years after corrosion started. Equation (4.11) assumes that the corrosion rate (or current density) has remained constant since the onset of corrosion up to the evaluation time.

The percentage of mass loss (corrosion level) based on the reduction of reinforcement bar radius is expressed as follows:

$$Ms(\%) = \left(1 - \frac{(r_0 - P_x)^2}{r_0^2}\right).100 \qquad \textit{Eq. 4.12}$$

Cairns et al.(Cairns et al. 2005) proposed an empirical equation to estimate the ultimate elongation of corroded bars based on cross-sectional loss.

$$\varepsilon_u = (1 - 0.03(Q_s))\varepsilon_0 \qquad \textit{Eq. 4.13}$$

where Q_s, ε_u are the average cross-sectional loss and strain of the corroded reinforcement, and ε_0 is the ultimate strain of the non-corroded reinforcement.

The potential risk for elastic buckling of the longitudinal reinforcement under compression is estimated according to Euler's load, with the unsupported length taken as the exposed length between adjacent ties. Corrosion decreases the restraining effects provided by the ties due to the reduction of their cross section and stiffness. Thus, the unsupported length of the longitudinal reinforcement increases.

4.11.2 Validation of the Proposed Approach

The reduced strength contributions of the concrete and reinforcement due to reinforcement corrosion are incorporated in the theoretical calculation of the nominal ultimate strength of the column. The results are compared with experimental test results from this study and reported in the literature (Azad and Al-Osta 2014; Tapan et al. 2016). The ratio of the analytical-to-experimental axial capacity of the corroded columns is plotted in Fig. 4.17. The proposed estimation shows very good agreement with the experimental data, with a mean of 1.06 and a standard deviation of 0.11, as illustrated in Fig. 4.17. Values for Azad and Al-Osta (2014) columns, calculated based on this chapter's analytical approach, demonstrate more scatter compared to those reported by Tapan et al. (2016) and those obtained in this experimental study because the condition of the ties and crack widths were not reported by the authors. Hence, the crack widths were estimated according to CONTECVET (2001) based on the reported mass loss.

Fig. 4.18 shows the axial capacity of the corroded columns estimated for different levels of corrosion of either the ties or the entire reinforcement. The figure also shows the experimental results obtained in this study. Results are compared for different scenarios: when the concrete cover is not damaged (full cover); when the compressive strength of the concrete cover is reduced; when the concrete cover is reduced by half; and when the concrete cover is completely removed.

Fig. 4.18 illustrates that the theoretical estimation considering a reduction in both the cracked concrete cover and concrete core strengths best predicts the ultimate capacity of the corroded columns. From Fig. 4.18, it is observed that the ultimate capacity is overestimated when the compressive strength of the entire cover is not reduced due to cracking, while it is underestimated when the entire cover is completely removed. The damaged cover case coincides with half cover at a very high level of corrosion. This agrees with experimental observations where the corners of the cover were spalled off. This indicates that the concrete cover contributes to the ultimate capacity of the column and cannot be neglected. Furthermore, it is estimated that the lateral pressure of the core of the concrete is reduced by 10% as the level of tie corrosion is increased by 5% according to Razvi, S., and Saatcioglu (1999). It was assumed in the calculations that the tie spacing increases due to tie corrosion fracture at 15% mass loss; this assumption is in accordance with the experimental observations. The lateral pressure is estimated for different sizes of tie reinforcement (10M, 15M, 20M). Fracture of the tie due to pitting corrosion was observed for 6M (Rodriguez et al. 1996; Vu et al. 2017) and 10M (this experimental study) at corrosion levels equal to or less than 15%. For tie reinforcement larger (15M, 20M), a fracture may occur at higher corrosion levels >15%.

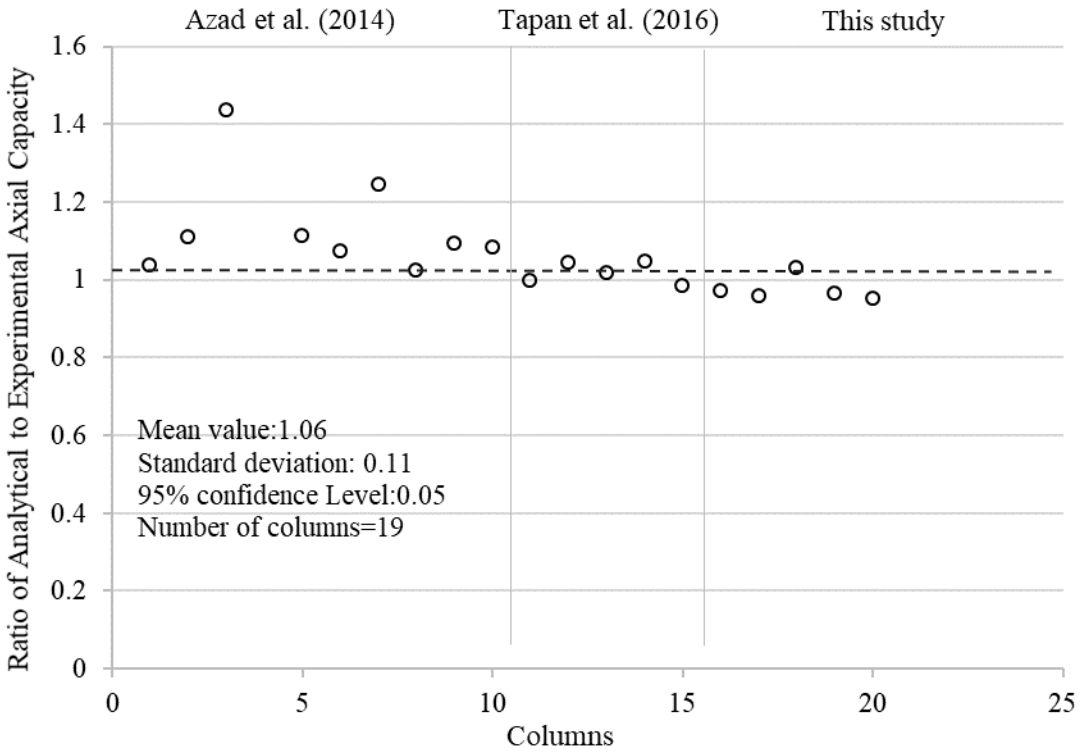

Fig. 4.17: Validation of estimated axial capacity with available experimental work reported in the literature

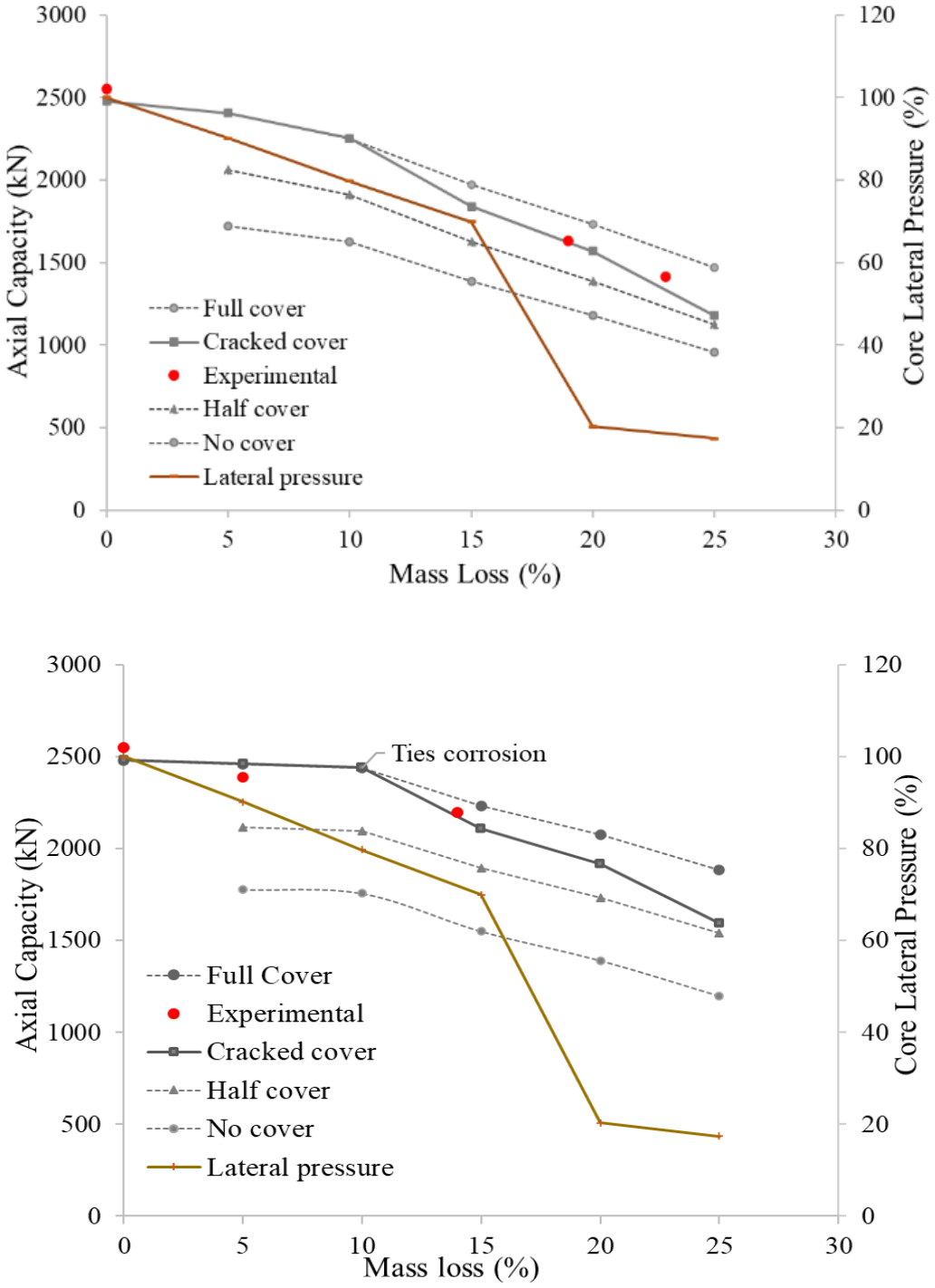

Fig. 4.18. Reduction in axial capacity due to tie corrosion (Top) and corrosion of all reinforcement (bottom)

4.12 Conclusions

This paper presents the results of an experimental investigation of the structural performance of corroded columns subjected to concentric compressive load. It also proposes a practical procedure to estimate the nominal axial capacity of corroded columns considering confinement effects. The following remarks can be concluded from the evaluations:

- Corrosion-induced damage (crack width and staining) increases as the level and widespread of corrosion increases. Tie corrosion is characterized by localized stains on the concrete surface spaced at 150-mm tie spacing. When all the reinforcement is corroded (longitudinal rebars and ties), extensive rust stains cover the entire surface of the column, with wider cracks that spread longitudinally along the rebar length.
- Corroded columns had a faster crack growth rate, which initiated at approximately 70% of the ultimate load and continued until the end of the test compared to the control specimen. This is attributed to degradations of both the concrete cover and reinforcement.
- The failure mechanism was unique for RC columns with different corrosion levels and patterns. Asymmetrical unintended corrosion of the longitudinal bars in specimens whose ties were corroded generated accidental load eccentricities. This led to increased lateral displacement and the development of flexural cracks on the tension side of the column.
- Corrosion of the ties directly affected the post-peak response (ductility) of the column even at low levels of corrosion (m_s<5%) due to degradation in restraining effects. The column post-peak response shifted from ductile to a brittle failure. The estimated residual ductility from the load-deformation responses was 71% of the control specimen, while the residual strength and axial stiffness was not affected.
- The axial stiffness and ultimate capacity gradually decreased to 85% and 86% of the control specimen, respectively, as the corrosion-damage (cracking) level increased for a medium level (m_s<14%) of tie corrosion. The residual ductility was further reduced to a residual value of 50%.
- The residual capacity for column (C-C-All2) was significantly reduced (64%) compared to the control specimen for high levels of corrosion. This is attributed to significant deteriorations of the reinforcement (longitudinal and transverse), concrete cover cracking, and reduction in the ties' restraining effects, leading to lower confinement effects.

- At a higher level of corrosion (m_s>20%) for both transverse and longitudinal bars, there was a significant reduction in the ultimate capacity and ductility of the column. This was attributed to the following: damage of the concrete cover, localized pitting along the bar length and tie corners (junctions), erosion of rebar ribs facing the concrete cover and the reduction in bar diameter along the length, fracture of two of the confining transverse ties in the compression zone, development of concrete cracks along the core concrete with a reduction in confining pressure, and localized buckling occurring between two deep pits along the longitudinal compression bar where the ties were placed.
- A practical theoretical procedure is proposed to estimate the nominal ultimate axial capacity of the corroded columns. This is achieved by combining the reduced strength contributions of the corroded reinforcement and cracked concrete, while considering a reduction in cover and core confined strengths. The proposed analytical approach agrees with experimental work on columns with tie corrosion loaded concentrically. Also, it is concluded that reduction in lateral pressure of the core concrete initiates at a low level of tie corrosion and decreases to 20% for a very high level of corrosion due to the increase in tie spacing. Reduction in ductility for columns with tie corrosion is attributed to a reduction in core confinement strength as the corrosion level increases.

4.13 References

ACI 318-19. (2019). Building Code Requirement for Structural Concrete. American Concrete Institute, American Concrete Institute, Farmington Hills, MI, USA.

ASTM A370. (2020). “Standard Test Methods and Definitions for Mechanical Testing of Steel Products.” ASTM International, West Conshohocken, PA.

ASTM G1-03. (2017). Standard Practice for Preparing, Cleaning, and Evaluating Corrosion Test. West Conshohocken, PA.

Azad, A. K., and Al-Osta, M. A. (2014). “Capacity of corrosion-damaged eccentrically loaded reinforced concrete columns.” ACI Materials Journal, 111(6), 711–722.

Boyle, J., Cunningham, M., and Dekens, J. (2013). Climate change adaptation and water resource management: A review of the literature. Energy Economics, Winnipeg, Manitoba, Canada.

Cairns, J., Plizzari.G.A., Law, D., and Franzoni.C. (2005). “Mechanical properties of corrosion-damaged reinforcement.” ACI Materials Journal, 102(4), 256–264.

Cape, M. (1999). “Residual service-life assessment of existing R/C structure.” Chalmers University of Technology, Goteborg, Sweden and Milan University of Technology Italy, Erasmus Program, 133.

Chauvin, M.., and Elstner, J. (2019). Evaluation of Electrochemical Chloride Extraction, Fiber Reinforced Polymer Wraps, and Concrete Sealers for Corrosion Mitigation in Reinforced Concrete Bridge Structures. Greater Minnesota, USA.

CONTECVET IN30902I. (2001). A validated Users Manual for assessing the residual service life of concrete structures.DG Enterprise, CEC. DG Enterprise, CEC.

CSA-S6.1:19. (2019). Commentary on CSA S6:19, Canadian Highway Bridge Design Code. Canadian Standards Association (CSA Group), Ontario, Canada.

CSA 23.3:19. (2019). Design of concrete structures. Canadian Standards Association, Canadian standards association (CSA Group), Ontario, Canada.

CSA A23.1:19/CSA A23.2:19. (2019). Concrete materials and methods of concrete construction/Test methods and standard practices for concrete. Canadian Standards Association (CSA Group), Ontario, Canada.

Dabas, M., Martin-Perez, B., and Almansour, H. (2021). “Effects of different patterns of reinforcement corrosion on concrete cover and residual strength in aged bridge piers: state-of-the-art-review.” Canadian Society of Civil Engineering (CSCE), Canada, 1–10.

Gode, K., and Paeglitis, A. (2014). “Concrete bridge deterioration caused by de-icing salts in high traffic volume road environment in Latvia.” Baltic Journal of Road and Bridge Engineering, 9(3), 200–207.

Government of Canada. (2019). Canada’s Changing Climate Report. (D. S. Bush, E. and Lemmen, ed.), Environment and Climate Change CANADA, Ottawa.

Lee, H. S., and Cho, Y. S. (2009). “Evaluation of the mechanical properties of steel reinforcement embedded in concrete specimen as a function of the degree of reinforcement corrosion.” International Journal of Fracture, 157(1–2), 81–88.

Li, Q., Niu, D., and Liu, L. (2012). “The experimental study on reinforced concrete short-columns restrained by corroded stirrups.” Advanced Materials Research, 446–449, 1376–1379.

Lounis, Z. (2007). “Aging highway bridges.” Canadian Consulting Engineer, 48(1), 30,34.

Maaddawy, T. A. El, and Soudki, K. A. (2003). “Effectiveness of Impressed Current Technique to Simulate Corrosion of Steel Reinforcement in Concrete.” Journal of Materials in Civil Engineering, 15(February), 41–47.

Ontario Ministry of Transportation. (2008). Ontario Structure Inspection Manual (OSIM). Ministry of Transportation, St. Catharines, Ontario, Canada.

Otieno, M. (2019). “Acceleration of steel corrosion in concrete by cyclic wetting and drying: effect of drying duration and concrete quality.” Materials and Structures, Springer Netherlands, 52(2), 1–14.

Petersen, L., Lohaus, L., and Polak, M. A. (2007). “Influence of freezing-and-thawing damage on behavior of reinforced concrete elements.” ACI Materials Journal, 104(4), 10.

Razvi, S., and Saatcioglu, M. (1999). “Confinement model for high-strength concrete.” Journal of Structural Engineering, 125(3), 281–289.

Rodriguez, J., Ortega, L. M., and Casal, J. (1996). “Load bearing capacity of concrete columns with corroded reinforcement.” Corrosion of reinforcement in concrete construction. proceedings of fourth international symposium, Cambridge, 1-4 July 1996. special publication no 183, 220–230.

Tapan, M., Ozvan, A., and Akkaya, I. (2016). “Effect of stirrup corrosion on Concrete Confinement Strength.” International Journal of Civil and Environmental Engineering, 10(12), 3.

Vecchio, F. J., and Collins, M. P. (1986). “Modified compression-field theory for reinforced concrete elements subjected to shear.” Journal of the American Concrete Institute, 83(2), 219–231.

Vu, N. S., Yu, B., and Li, B. (2017). “Stress-strain model for confined concrete with corroded transverse reinforcement.” Engineering Structures, 151, 472–487.

Wang, X.-H., Liu, X.-L., and Deng, B.-R. (2012). “Effects of length and location of steel corrosion on the behavior and load capacity of reinforced concrete columns.” Journal of Shanghai Jiaotong University (Science), 17(4), 391–400.

Wang, X. H., and Liang, F. Y. (2008). “Performance of RC columns with partial length corrosion.” Nuclear Engineering and Design, 238(12), 3194–3202.

Xia, J., Jin, W., and Li, L. (2016). “Performance of Corroded Reinforced Concrete Columns under the Action of Eccentric Loads.” Journal of Materials in Civil Engineering, 28(2016), 1–16.

Yalciner, H., and Kumbasaroglu, A. (2020). “Experimental evaluation and modeling of corroded reinforced concrete columns.” ACI Structural Journal, 117(4), 61–76.

Zhou, H., Xu, Y., Peng, Y., Liang, X., Li, D., and Xing, F. (2020). “Partially corroded reinforced concrete piers under axial compression and cyclic loading: An experimental study.” Engineering Structures, Elsevier, 203(October 2019), 109880.

Chapter 5 Influence of Reinforcement Corrosion on Ageing Columns: Eccentric Load

5.1 Abstract

This chapter presents the results of an experimental investigation of the effect of different levels and patterns of reinforcement corrosion on the structural performance of reinforced concrete (RC) columns subjected to eccentric axial loads. Experimental testing was conducted on five RC columns, four of which were subjected to an accelerated corrosion regime by corroding either the transverse or longitudinal reinforcement to different levels of steel mass loss. The effect of corrosion of the transverse or longitudinal reinforcement on the column's ultimate capacity, ductility, toughness, and axial stiffness was analyzed. The results indicate a significant reduction in ultimate capacity (28%) and axial stiffness (25%) at high levels of corrosion, while low levels of tie corrosion mostly affected ductility and overall column toughness

Keywords: Reinforcement corrosion, reinforced concrete, bridge columns, concentric load

5.2 Introduction

Reinforcement corrosion remains the lead cause of concrete deterioration in reinforced concrete (RC) infrastructure in Canada due to the heavy use of de-icing salts in the winter. About 40% of Canada's infrastructure is over 40 years old, and the condition of ageing bridges has significantly worsened with the increase in traffic volume and severe environmental conditions (Lounis 2007). In bridges, columns are exposed to combined (axial and flexural) loading action. This, in effect, reduces the ultimate load-carrying capacity of the columns depending on the magnitude of eccentricity. Water mixed with de-icing salt that is cyclically splashed on RC bridge columns by passing traffic is critical in reducing the time to reinforcement corrosion initiation and in inducing higher corrosion rates. Moreover, pits occurring due to chloride-induced corrosion result in material and structural degradation, subsequently reducing the bridge service life and significantly increasing the cost of repairs. Corrosion-induced deterioration in RC bridge columns varies along the surface and elevation of the column due to variations in exposure to de-icing concentrations and moisture levels (Lindvall 2007; Petersen et al. 2007). Surfaces facing heavy traffic are more

exposed to the splashing of saline water due to moving traffic (Gode and Paeglitis 2014). Given the significance of this deterioration mechanism, it is important therefore to understand the influence of variable patterns and levels of corrosion on the structural response of RC bridge columns.

Few studies have investigated the structural performance of corroded RC columns (Dabas et al. 2021). Over the past decade, experimental studies reported in the literature have focused on the lateral response of (less than 1,500 mm long) corroded columns under compression loads (Wang et al. 2008-2012; Azad and Al-Osta 2014; Xia et al. 2016). Wang et al. (2008 - 2012) examined the ultimate capacity and lateral response of corroded columns (1,300-mm long) under loads with eccentricities of 50 and 150 mm. Longitudinal bars were corroded along a partial length of 350 or 700 mm in either the compression, tension, or both compression and tension zones of the middle region of the column. For the larger eccentricity, it was evident that a larger reduction in ultimate capacity had resulted from partial corrosion of the longitudinal bars along the tension zone. Also, it was evident from the load-displacement curves that the flexural stiffness of the columns was not significantly affected as the level of corrosion increased along the compressive reinforcement. Azad and Al-Osta (2014) conducted extensive experimental work on (1,350-mm long) RC columns with different cross-sections and reinforcement sizes. The compressive load was applied at three eccentricity values: 30, 60, and 95 mm for one group and 35, 65, and 115 mm for another one. The authors proposed a reduction factor established from a multi-regression analysis of the test data to account for the effects of corrosion damage. For cases with an eccentricity-to-height ratio of e/h> 0.16, transverse cracks appeared on the tension side of the column. As the level of corrosion increased, the flexural rigidity of the corroded columns was reduced compared to the non-corroded ones. Xia et al. (2016) tested 24 (1,500-mm long) RC columns to determine their structural performance and evaluate the relationship between reinforcement cross-sectional loss and maximum crack width of the concrete cover. Columns were tested at two eccentricity values of 50 and 90 mm for two sets of columns that had different tie spacings (200 and 100 mm). The relationships between cross-sectional area loss of steel, maximum crack width of the concrete cover, and strength loss of the RC column were analyzed. The residual compressive strength of the column was estimated from measured crack widths of the concrete cover. The column stiffness and strength decreased as the loading eccentricity and corrosion level were increased.

More research is needed to establish a good understanding of the structural performance of larger-scale columns (ultimate capacity stiffness and post-peak response) affected by reinforcement corrosion for combined loads (axial and flexural) effects developed due to eccentricities. This paper presents the results of an experimental investigation of the structural behaviour of aged columns under combined bending and axial loads. The effects of variable patterns and levels of reinforcement corrosion on both the material and structural performance of five RC columns were analyzed before and after applying a quasi-static loading applied at a large eccentricity. Accelerated corrosion was applied to the ties in the mid-region for two columns to examine the influence of variable corrosion patterns on structural behaviour. In comparison, another two columns had all longitudinal reinforcing bars in the effective corrosion zone subjected to a constant current for a predetermined time. The mode of failure, ultimate capacity, ductility, resilience, toughness, and stiffness for each column were analyzed.

5.3 Experimental Program

A total of five columns, one control and four subjected to accelerated corrosion, were built as shown in Table 5.1. Following an accelerated corrosion regime, a quasi-static load was applied eccentrically, with an eccentricity of e = 190 mm, using a hydraulic (MTS) machine with an ultimate capacity of 2,500 kN. The columns were designed with transverse reinforcement having a spacing of 150 mm. All columns were tested for quasi-static loading applied eccentrically after exposure to corrosion except for the control specimen (not corroded). Two columns, C-E-T3 and C-E-T4, were exposed to corrosion on two ties in the middle region, while C-E-R1 and C-E-R2 had all four longitudinal rebars corroded in the effective corrosion zone (750 mm in the middle region of the column). This region may be more vulnerable to salted water splashed from moving traffic.

Table 5.1: Test matrix

Label	Acc. Corrosion	Corrosion Connection	Current density (μA/cm²)	No. column	Scenario
C-E C	No	None	0	1	Control
C-E T3/T4	Yes	Series	525	2	Ties
C-E R1/R2	Yes	Parallel	475	2	Rebar

5.4 Specimens Details

The RC columns had a 260-mm solid square cross-section confined using tied reinforcement, as shown in Fig. 5.1. The clear concrete cover of all five columns is 30 mm. The columns were designed using 4-20M longitudinal bars and 10M transverse ties at 150 mm spacing. The columns resistance was determined according to CAN/CSA S6:19 (CSA 2019) and CAN/CSA23.3 (CSA 2019) standard requirements. Corbel sections were designed according to the traditional method specified in the ACI Building Code Section 16.5 (ACI 318 2019). Further details on material properties and specimen construction can be found in Chapter 3.

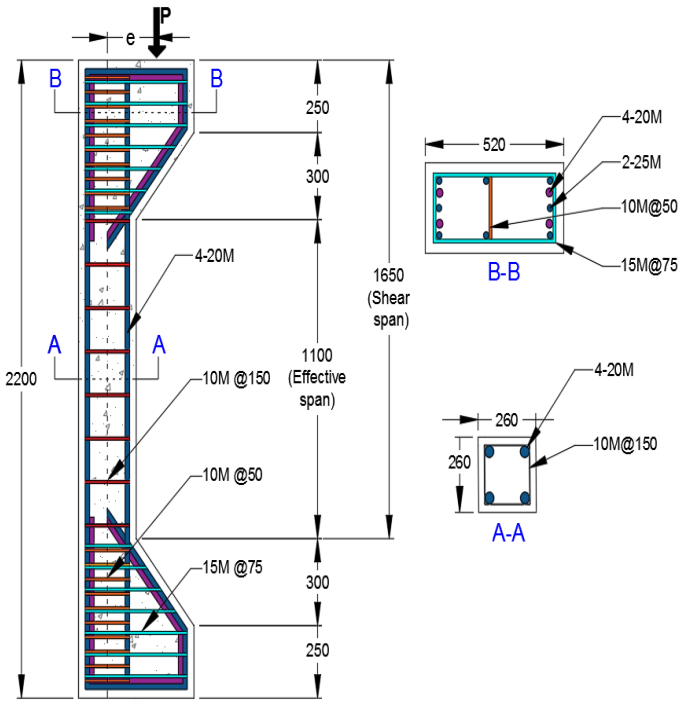

Fig. 5.1: Column details for C-E-C, C-E-T3, C-E-T4, C-E-R1, C-E-R2 (dimensions in mm)

5.5 Accelerated Corrosion Regime

To induce corrosion in the columns, a constant and direct current was impressed against the reinforcement at a specified rate predetermined theoretically according to Faradays' law. The calculated current density was limited to 475 for the C-E-R1 and C-E-R2 and 525 μA/cm² for C-E-T3 and C-E-T4 series (Table 5.1). However, based on the achieved mass loss after 137-days, the actual calculated current densities of C-E-T3/4 and C-E-R1/2 were 62μA/cm^2 for transverse reinforcement corrosion and 398 μA/cm^2 for the longitudinal reinforcement corrosion, as explained in Section 3.5. Group 3 (C-E-T3/4) had a lower current density than initially calculated due to current loss attributed to the set-up of the experiment. The advantage of the DC power supply is that it continuously impresses a constant current (predetermined by the user) throughout the specified time by automatically adjusting the non-constant parameter (voltage). Columns C-E-T3 and C-E-T4 were connected in series to one DC power supply (group 1), while columns C-E-R1 C-E-R2 were connected in parallel to two DC power supplies, one for each column (group 2), as illustrated in Fig. 5.2. Group 3 was assembled to induce corrosion in two contiguous ties in the middle of the effective corrosion zone, whereas group 4 was set up to corrode all four longitudinal bars at the effective zone (see Fig. 5.2). The electrical circuit was assembled such that the reinforcement acted as the anode while stainless steel sheets located outside the specimens functioned as the cathode. The effective corrosion zone was wrapped with a thick sponge to provide a wet medium for the current to flow from the anode (reinforcement being corroded) to the cathode (stainless steel) through the electrolyte (concrete cover). Two and three (250×750 mm) stainless sheets were placed atop the sponges along the effective corrosion zone for groups 3 and 4, respectively.

The specimens were partially immersed in a water pool with 1.5% (by weight of cement) of sodium chloride (NaCl) to prevent potential salt leaching and maintain a high humidity environment (Fig. 5.3). To accelerate and enhance the process of reinforcement corrosion, a cyclic regime of wetting and drying was adopted (Otieno 2019). This experiment found that a three-day wetting, four-day drying regime was the most effective regime in maintaining concrete resistance at a low level. The epoxy coating was applied to the reinforcement of the top and bottom corbel sections and the longitudinal reinforcement in the effective area for specimens C-E-T3 and C-E-T4. The mid-ties

of specimens C-E-R1 and C-E-R2 were also coated with epoxy. The period duration of the accelerated corrosion regime was 137 days.

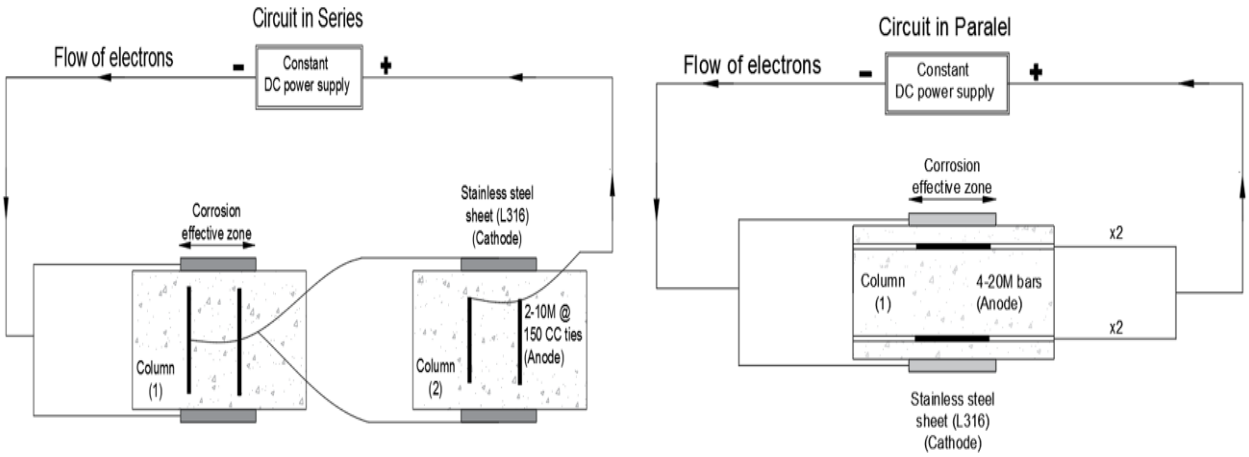

Fig. 5.2: Constant current electric circuits

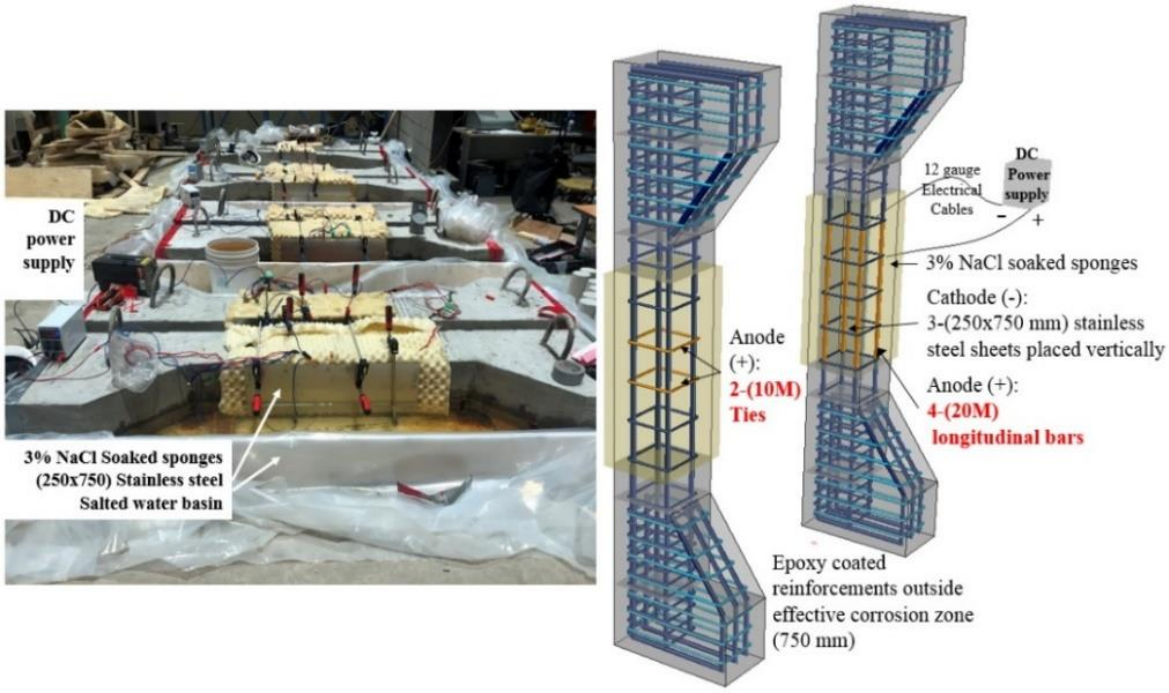

Fig. 5.3: Set-up of the accelerated corrosion test method

5.6 Gravimetric Mass Loss

Once the accelerated corrosion regime was completed, the reinforcement in the effective corrosion zone of the corroded columns was exposed, extracted, and cleaned according to ASTM G1 (ASTM G1-03 2017). Gravimetric mass loss is reported as the ratio of the reduced weight to the original weight of the reinforcements; maximum, minimum, and average mass losses for each column are reported in Fig. 5.4. It was found that only the two mid-section transverse and longitudinal reinforcement in the 750-mm effective zone were corroded, as initially planned. In addition, it was observed that reinforcement corrosion was non-uniform along the rebars. Corrosion was characterized by multiple localized pits on the surface of the rebar facing the concrete cover, whereas the inner face of the rebar facing the core concrete maintained a prominent ribbed surface (Fig. 5.4). This is consistent with findings of natural corrosion in the field inflicted by chloride contamination. According to the results presented in Fig. 5.4, the columns were classified into three different corrosion levels according to the percentage of mass loss m_s in both transverse and longitudinal reinforcement (Ontario Ministry of Transportation 2008):

- Low level for $m_s<5\%$
- High level for $10<m_s\leq20\%$
- Medium level for $5\leq m_s \leq10\%$
- Very High level for $m_s>20\%$

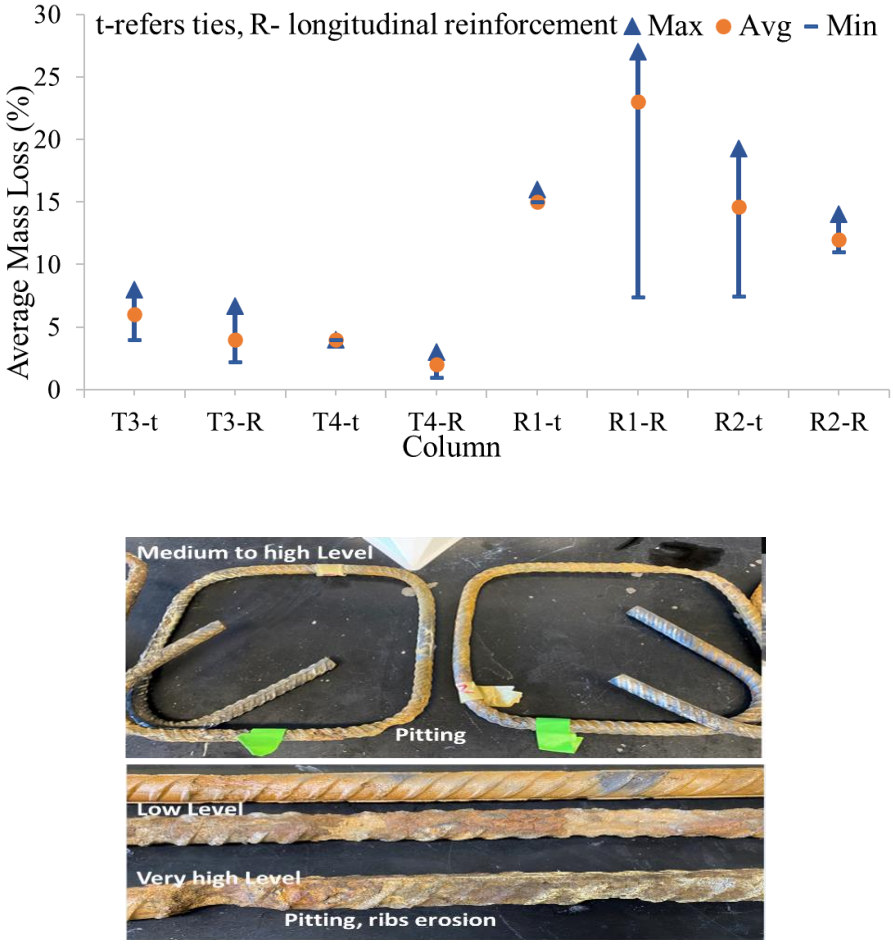

Fig. 5.4: Maximum, minimum, and average gravimetric mass loss in reinforcement (ASTM G1) for C-E-T3 and C-E-T4, C-E-R1, C-E-R2

5.7 Loading Test

A quasi-static load was applied at an eccentricity of 190 mm and a 0.25 mm/min rate using a hydraulic testing machine with a maximum capacity of 2,500 kN. A displacement-controlled method was utilized to capture the post-peak behaviour of the columns. The loading was terminated when the post-peak load reached 25% of the column's capacity. The columns were simply supported at the top and bottoms edges. Seven lateral sensors were attached along the length of the columns to record lateral displacements. All sensors were connected to a data acquisition system to collect and record data.

5.8 Results from the Tested Columns

5.8.1 Effect of Reinforcement Corrosion on Failure Mode

The control specimen (C-E-C) had a typical steel-controlled failure mechanism consistent with a column under combined bending and axial loads due to a large eccentricity. The main signs of load-induced damage were concrete crushing on the compression zone of the column and transverse flexural cracks on the tension zone of the column (Fig. 5.5). Similarly, the remaining corroded columns had the same failure mode as the control specimen, but they exhibited more prominent cover damage due to the widening of pre-existing corrosion-induced cracks, as illustrated in Fig. 5.6 to Fig. 5.8. Experimentally, it was observed that cracks propagated at a faster rate about 70 to 85% of the peak loads. For specimen C-E-T4, the column had a localized stress concentration at the corbel section at the onset of the test, which resulted in initially significant cracking of the section and irregular reduction in column stiffness. Moreover, tie fracture due to pitting corrosion was observed for only one column, C-E-R2, in which the affected tie had a mass loss of 20%. Furthermore, after exposing the reinforcement cage for all the columns, there was no evidence of either cracks propagating through the core or erosion of the reinforcement's ribs on the concrete section's core side

Fig. 5.5: Lateral displacement at the middle section for column (C-E-C)

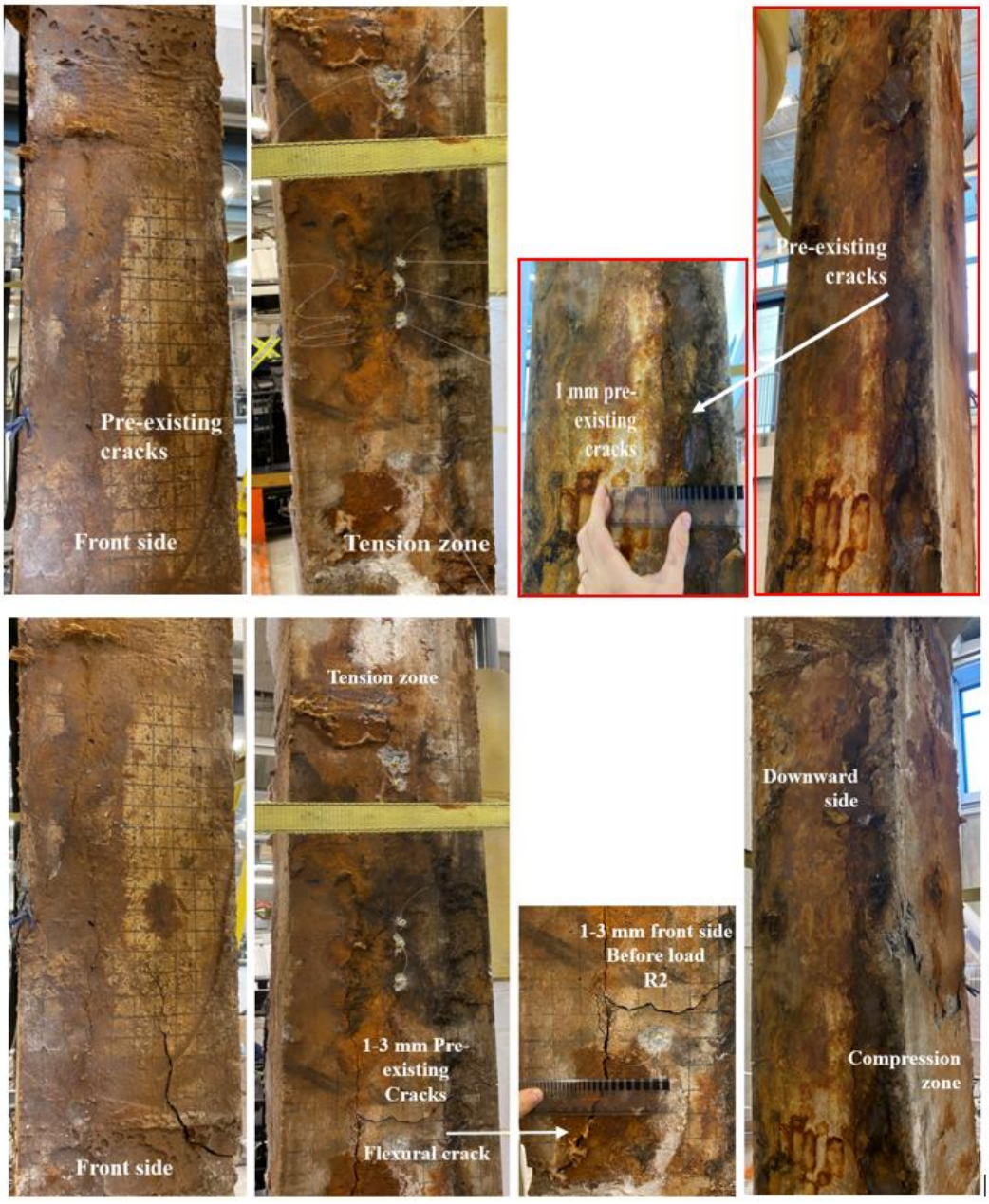

Fig. 5.6: Damage after loading for specimen C-E-R2

Fig. 5.7: Failure mechanism of specimen C-E-R1

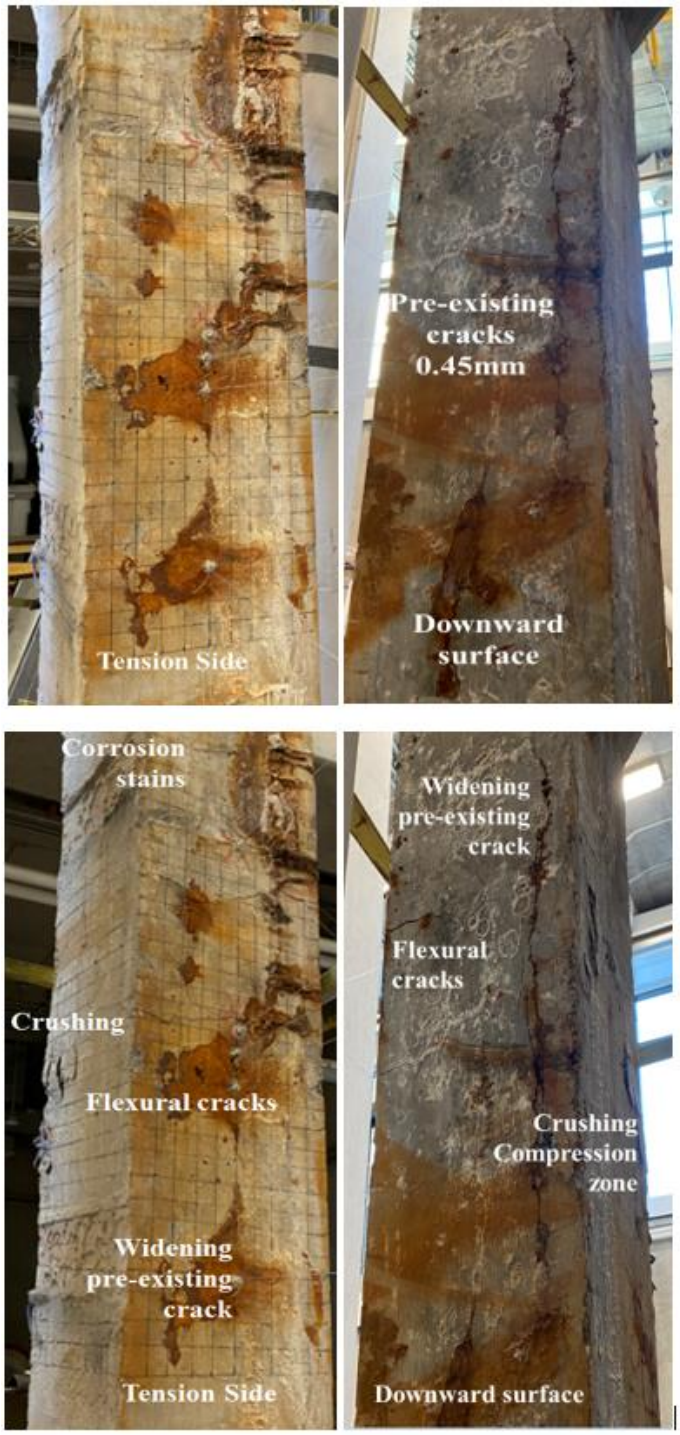

Fig. 5.8: Damage due to reinforcement corrosion before (top) & after load test (bottom) for specimen C-E-T3

5.8.2 Effects of Reinforcement Corrosion on Axial and Flexural Response

Fig. 5.9 illustrates the axial load-deformation response for the overall length of all the columns. As the level and pattern of reinforcement corrosion increase and become more widespread, the response of the columns shifts from a ductile to a brittle response, with a decrease in both strength and ductility. The control column (C-E-C) had a typical ductile response for a non-corroded column, while columns C-E-R1 and C-E-R2 exhibited a brittle response for a medium level of corrosion. Fig. 5.9 shows that as the corrosion level increases, the columns' axial stiffness is reduced. For specimen C-E-R1, which experienced the highest mass loss in both the transverse and longitudinal reinforcement, the reduction in axial stiffness is 25% from the control specimen. Nonetheless, it is observed that the degree of reinforcement corrosion did not affect the flexural stiffness at the mid-section of the columns, as illustrated from the load-lateral deformation curve in Fig. 5.10. The concrete used for column C-E-R2 had a higher compressive strength, which may have contributed to a stiffer response than the remaining columns. Interestingly, both C-E-R1 and C-E-R2 exhibited nonlinear ascending curves (Fig. 5.10), attributed to the brittle nature of the rebars due to a high and medium level of corrosion, respectively.

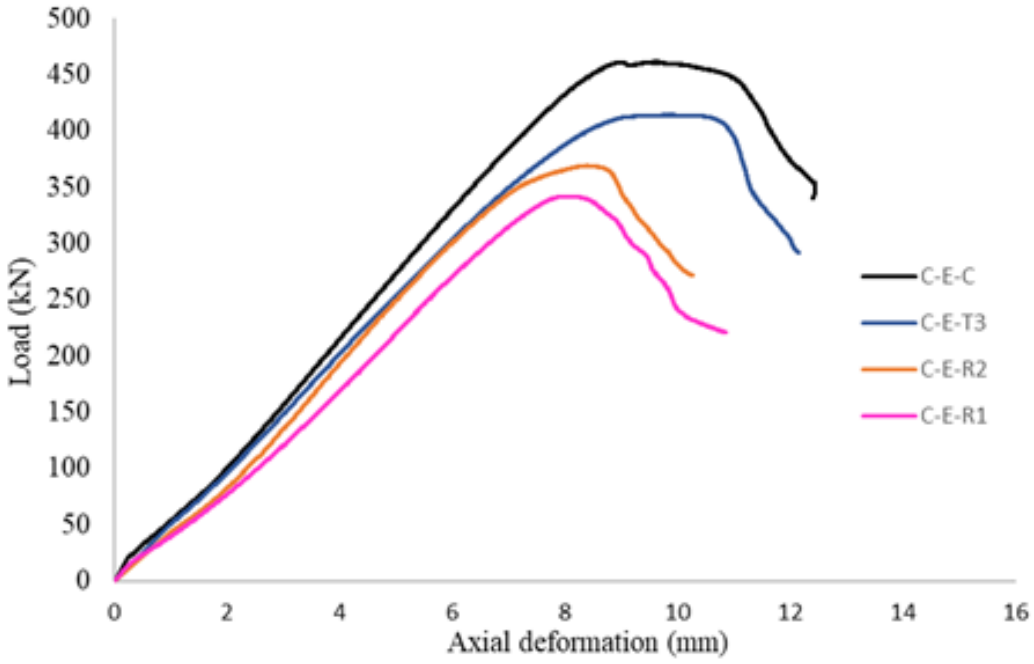

Fig. 5.9: Axial load-deformation curve of the entire length of the column

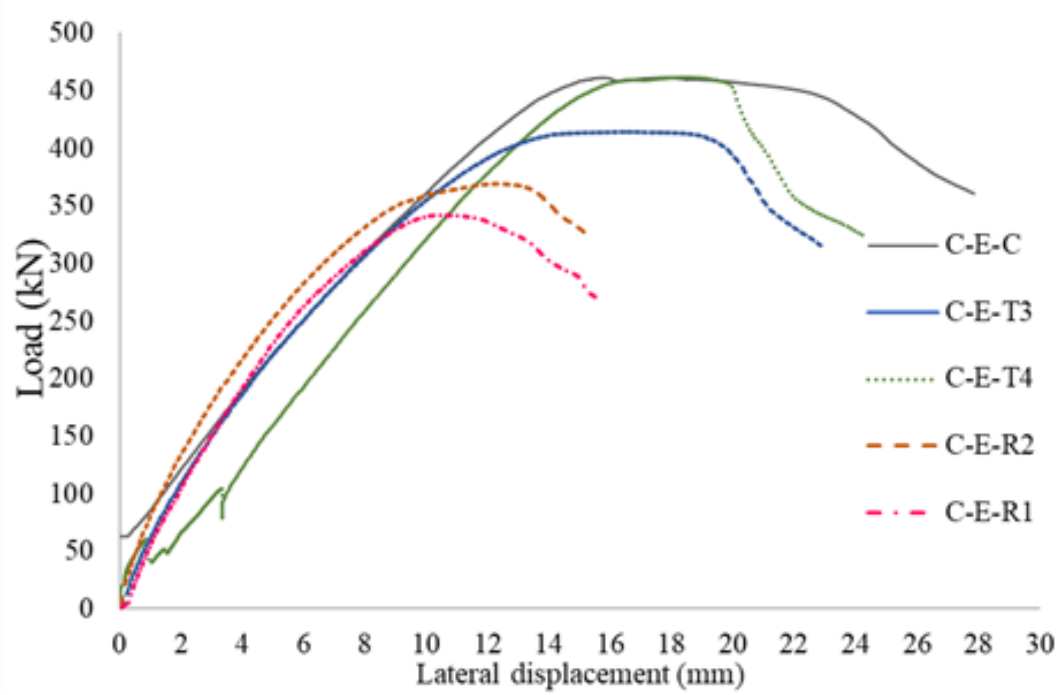

Fig. 5.10: Load-lateral displacement of the mid-section of the columns

5.9 Discussion of Experimental Results

Results of the experimental testing are presented in Table 5.2 for all five columns. The ultimate capacity (P_u) refers to the peak load attained during the test, while the residual strength (P_{ur}) is the ratio of the corroded load to the uncorroded load (P_u), i.e.,

$$P_{ur}(\%) = \frac{P_{u,corroded}}{P_u} \times 100 \qquad \text{Eq. 5.1}$$

where $P_{u,corroded}$ is the ultimate strength of the corroded column, and P_u is the ultimate strength of the control column. The ductility and toughness were determined from the area under the load-deformation curves obtained for the entire length of the column. Ductility (μ) is estimated as the ratio of the deformation measured post peak at 85% of the ultimate load (Δ_{u85}) to the yield deformation (Δ_y), $\mu = \Delta_{u85}/\Delta_y$. The yield load and corresponding deformation are determined according to the energy equivalence method and are equal to the turning point of a bilinear curve idealized from the actual load-deformation curve illustrated in Fig. 5.11 (Zhou et al. 2020). The axial stiffness is determined by estimating the slope in the elastic region of the load-deformation curve using a linear regression equation for both control and corroded columns. Then, the residual

stiffness is obtained by taking the ratio of the axial stiffness of the corroded column to that of the control column. Resilience is the column's ability to absorb energy in the elastic range, and it is calculated as the area under the elastic range in the load-displacement curve. Toughness is the column's ability to absorb energy before failure. It is determined as the area under the entire load-deformation curve. Fig. 5.12 shows the loss of strength, axial stiffness, resilience, and toughness as a function of increasing corrosion-induced steel mass loss in both ties and longitudinal reinforcing bars. From Fig. 5.12, it is observed that column toughness gradually decreases with increasing level of corrosion in the ties. At the same time, it appears to be unaffected by corrosion of the longitudinal rebars. Column resilience, on the other hand, has a sharp decrease when steel mass loss in the ties and longitudinal reinforcement is high (15% and 12%, respectively). As the level of tie corrosion is increased to a medium level, the ultimate capacity is reduced by 10%, the residual ductility is 96%, and the toughness and axial stiffness are 69% and 84% of those of the control specimen, respectively. Reduction in the ultimate capacity, axial stiffness, ductility, and toughness is increased as the level of corrosion increases. At high levels of corrosion (15% mass loss in the ties and 23% mass loss in the longitudinal reinforcement), all the structural attributes of the column are significantly affected, with the residual capacity, residual ductility, residual toughness, and residual axial stiffness being 74%, 89%, 44%, and 75%, respectively. It is interesting to note that as the level of mass loss of the longitudinal reinforcement increased from 12% to 23% for specimens C-E-R1 and C-E-R2, the residual ductility was not affected, whereas the residual strength decreased by 6% (Table 5.2).

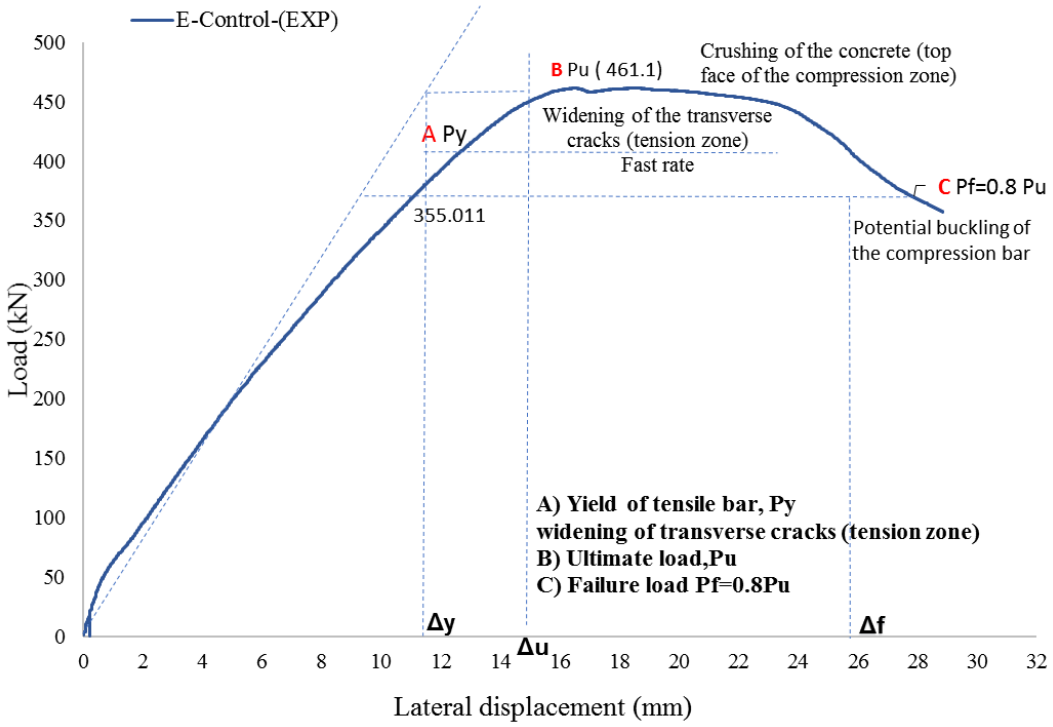

Fig. 5.11: Lateral displacement for all the columns at the middle section of the column

Table 5.2: Results of the effects of corrosion on structural performance

Column Label	Damage level	Mass loss, m_s (%)		Ultimate load, P_u (kN)	Residual strength, P_{ur} (%)	Residual ductility μ_r(%)	Residual Resilience (%)	Residual toughness (%)	Residual Axial. Stiffness, κ_r (%)
		Ties	Rebar						
C-E-C	None	0	0	461	100	100	100	100	100
C-E-T4	Low	4	4	460	100	97	100	83	100
C-E-T3	Medium	7	4	414	90	96	89	69	84
C-E-R2	Medium	15	12	369	80	89	44	45	84
C-E-R1	High	15	23	342	74	89	38	44	75

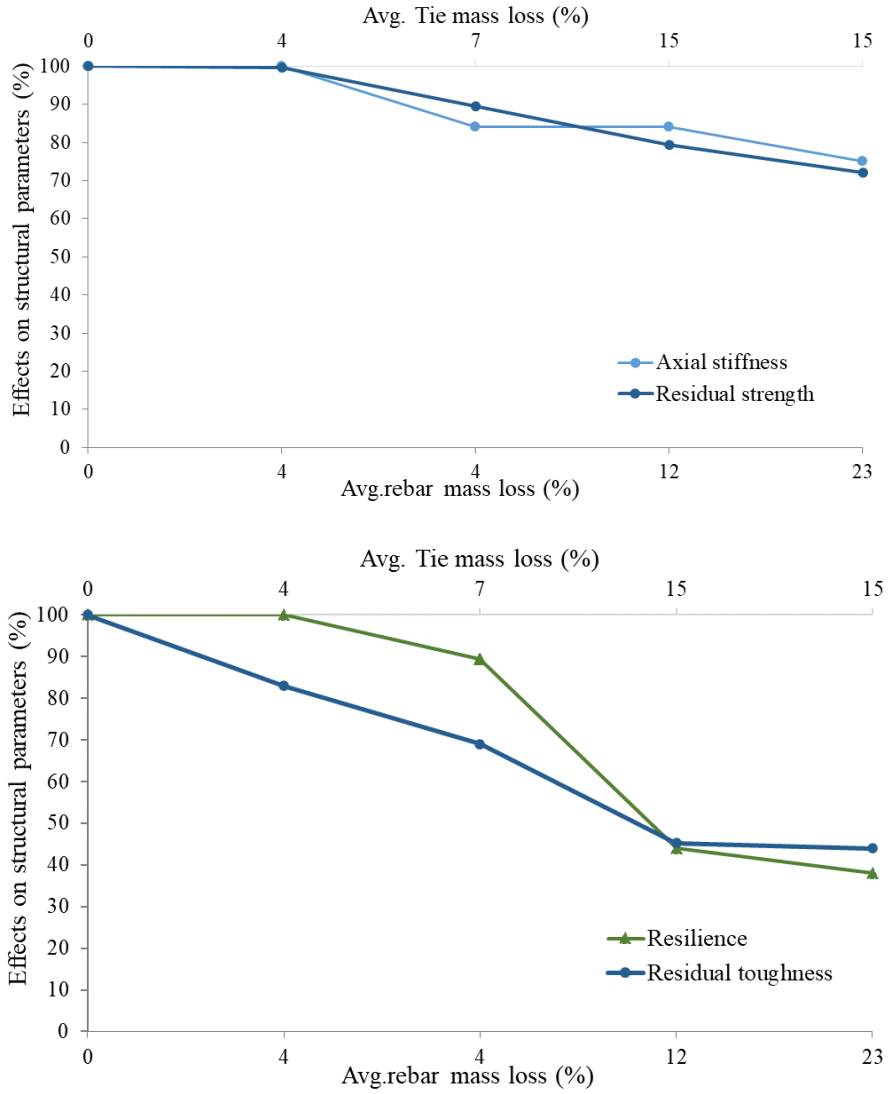

Fig. 5.12: Effects of corrosion on the structural performance of columns

5.10 Failure Mode Comparison

As the level of corrosion is increased the extent of damage (cracking and spalling delamination) under applied load increases. However, columns exhibited different failure responses depending on the level of reinforcement corrosion or type of corrosion (ties, longitudinal or all reinforcement corrosion) and level of eccentricity. A comparison between all concentrically and eccentrically-loaded columns is summarized in Fig. 5.13. Asymmetrical corrosion was observed in specimens (C-C-T2 and C-E-T1) leading to a global failure characterized by excessive mid section lateral displacement compared to the control specimens (C-C-C). Local buckling was observed only when

the ties stiffness is significantly reduced (C-C-T1) or fractured for (C-C-All1). The failure mode of eccentrically-loaded and corroded columns follows a typical a steel-controlled failure characterized by flexural cracks on the tension zone and concrete crushing on the compression zone (C-E-T3 and C-E-T4 and C-E-R1 and C-E-R2).

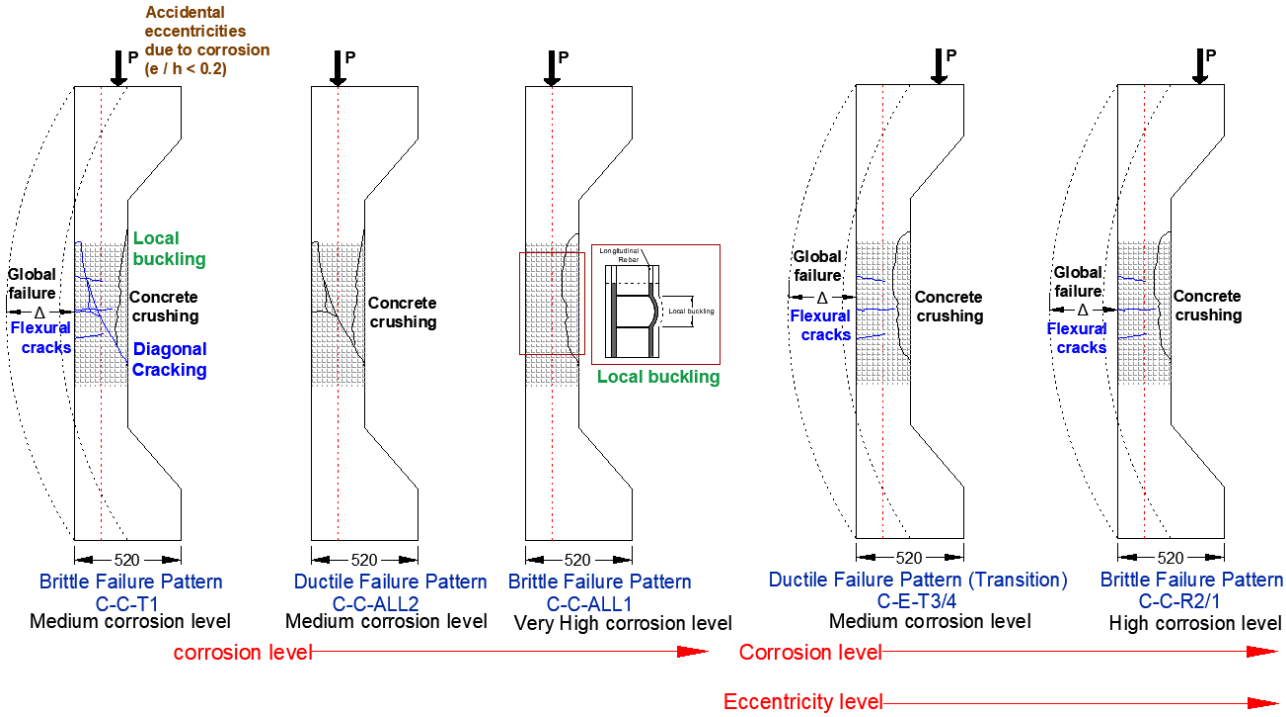

Fig. 5.13: Failure mode comparison for concetrically and eccentrically loaded and corroded columns

5.11 Conclusions

The followings remarks can be concluded from analyzing the results of the experimental investigation on the effects of reinforcement corrosion on RC columns subjected to eccentric loads:

- Columns had a steel-controlled mode of failure (characterized by flexural cracks on the tension side and crushing on the compression side),
- Failure was initiated by yielding the tensile longitudinal reinforcement at 70% of the peak load for corroded specimens. Subsequently, the growth of pre-existing and flexural cracks propagated at a faster rate.
- Reduction in confinement effects (lateral pressure) as a result of a very high level of tie corrosion (>15%) led to buckling of the longitudinal reinforcement.

- Low levels of tie corrosion affected the post-peak response of the column. At this level of damage, the overall toughness and ductility of the column were reduced, while column resiliency and axial stiffness were not affected. As the level of tie corrosion increased to a medium level, the column response shifted to a brittle response, with the axial stiffness and ultimate capacity of the column suddenly decreasing.

At high levels of reinforcement corrosion, reduction on all structural attributes (ultimate capacity, ductility and toughness, resilience, and axial stiffness) of the column was more prominent. However, it was concluded that corrosion of the transverse reinforcement has a predominant effect on the post-peak response of the column and the reduction in column ductility, while corrosion of the longitudinal reinforcement has a predominant effect on the reduction of the ultimate capacity.

5.12 References

ACI 318 committee. (2019). Building Code Requirement for Structural Concrete. ACI standard, Farmington Hills, MI.

Azad, A. K., and Al-Osta, M. A. (2014). "Capacity of corrosion-damaged eccentrically loaded reinforced concrete columns." ACI Materials Journal, 111(6), 711–722.

Dabas, M., Martin-Perez, B., and Almansour, H. (2021). "Effects of different patterns of reinforcement corrosion on concrete cover and residual strength in aged bridge piers: state-of-the-art-review." Canadian Society of Civil Engineering (CSCE), Canada, 1–10.

Gode, K., and Paeglitis, A. (2014). "Concrete bridge deterioration caused by de-icing salts in high traffic volume road environment in Latvia." Baltic Journal of Road and Bridge Engineering, 9(3), 200–207.

Lounis, Z. (2007). "Aging highway bridges." Canadian Consulting Engineer, 48(1), 30,34.

Ontario Ministry of Transportation. (2008). Ontario Structure Inspection Manual (OSIM). Ministry of Transportation, St. Catharines, Ontario, Canada.

Petersen, L., Lohaus, L., and Polak, M. A. (2007). "Influence of freezing-and-thawing damage on behavior of reinforced concrete elements." ACI Materials Journal, 104(4), 10.

Wang, X.-H., Liu, X.-L., and Deng, B.-R. (2012). "Effects of length and location of steel corrosion on the behavior and load capacity of reinforced concrete columns." Journal of Shanghai Jiaotong University (Science), 17(4), 391–400.

Xia, J., Jin, W., and Li, L. (2016). "Performance of corroded reinforced concrete columns under the action of eccentric loads." Journal of Materials in Civil Engineering, ASCE, 28(1), 1–16.

Chapter 6 Finite Element Modelling

6.1 Introduction

The load-carrying capacity of RC columns is strongly affected by patterns of reinforcement corrosion along the column height. The degree of corrosion and region of reinforcement corrosion in the column is of great interest to investigate. This research has studied from an experimental point of view three scenarios of reinforcement exposure to corrosion that may potentially affect ageing bridge piers:

- Corrosion of the transverse reinforcement
- Corrosion of longitudinal reinforcement
- Corrosion of both transverse and longitudinal reinforcement

A 3D non-linear finite element analysis (NLFEA) is presented in this chapter to further analyze the structural performance of RC columns under concentric and eccentric loading combined with environmental effects. The structure performance is assessed by analyzing the ascending portion of the load-displacement curve, ultimate capacity, post-peak response and failure mode.
The 3D NLFEA was developed using Diana software (v.10.4) to further analyze the influence of very high corrosion levels (beyond those obtained in the experimental study) on the structural response of the columns. It was also used to supplement and explain experimental data where no measurements were available, such as the yielding load and bond-slip response. To achieve this, the calibrated model was validated with the aforementioned corrosion scenarios established from experimental tests. Then, additional corrosion scenarios were examined, such as the effect of a very high level of corrosion on the transverse reinforcement.

6.2 Development of the Finite Element Model

The column cross-section was purposefully divided into different regions with distinct constitutive behaviour, as shown in Fig. 6.1. The concrete in the column was divided into four zones: unconfined concrete corbel, unconfined concrete cover, fully-confined concrete core and partially-confined concrete core. Concrete was modelled using 3D solid brick isoparametric elements (designated as CHX60 in Diana 10.4), while reinforcement was modelled using discrete 3D truss

elements (L6TRU) in the effective corrosion zone and embedded elements in the rest of the column. The interaction between the concrete and the longitudinal reinforcement was accounted for using embedded constitutive models for bond-slip behaviour. A quadratic mesh with a scale of one was selected for all.

The top and bottom plates were restrained against translation but no rotation, rendering the beam-column supports as a simply-supported beam. The load was uniformly distributed along the top plate of the loading set-up to mimic experimental load conditions. Geometrical nonlinearity due to potentially large displacements and rotations was accounted for in Diana software using the Total Lagrange formulation. Moreover, a total strain-based crack model was utilized to model crack propagation due to the increasing loads.

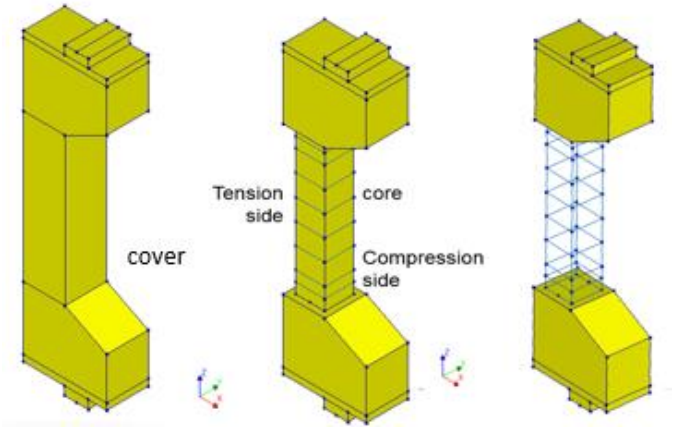

Fig. 6.1: The column cross-section was divided into different regions (cover, core and reinforcement)

6.2.1 Element Mesh Size

Mesh sensitivity analysis was conducted to determine an accurate prediction of the column response and to verify that the predicted results were mesh size independent. The column was discretized with different elements' sizes ranging from 13 to 26 mm and with a height-to-width-to-depth ratio of 1. This corresponded to 20 to 10 elements per cross-sectional area. The optimal mesh size was determined by assessing the largest element size that does not influence the FEA results and by comparing the numerical results with the experimental results from this study. An initial analysis with a mesh size of 10 elements/width was conducted, and then the mesh was further refined to 15 and 20 elements/width until convergence of results. The results of the mesh sensitivity analysis are presented in Table 6.1 and illustrated in Fig. 6.2 for the control specimen

under eccentric load. From observing Fig. 6.2, it was concluded that an element size of 26 mm is the most suitable mesh for conducting analysis for both concentrically and eccentrically-loaded columns in a reasonable amount of time.

Table 6.1: Comparison between processing time for each mesh size

Element size (mm)	26	17.3	13
No. of elements/width	10	15	20
Processing time (hours)	8	24	40

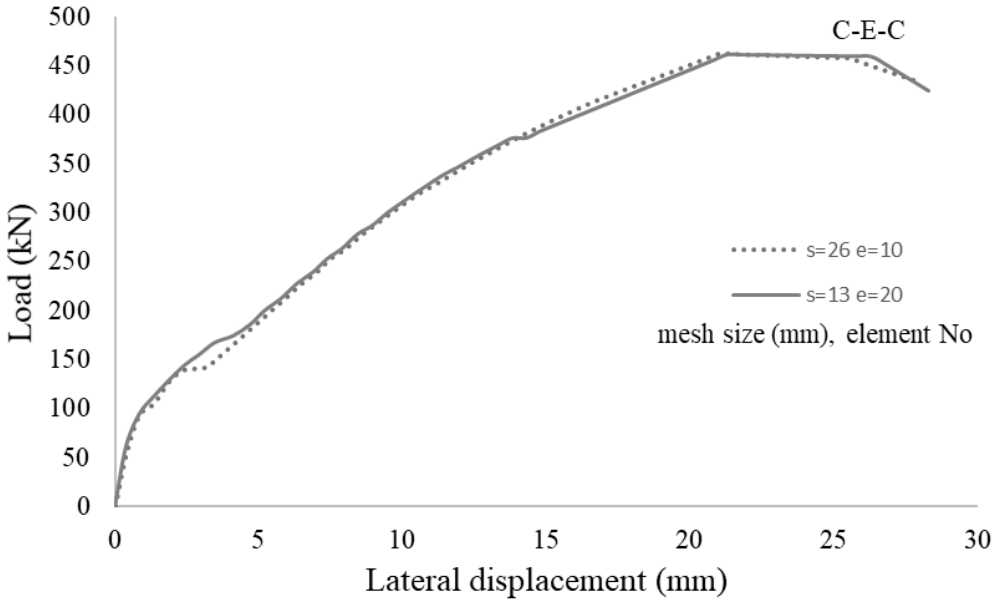

Fig. 6.2: Numerical axial-load vs lateral displacement of specimen C-E-C with two different mesh sizes

6.2.2 Load Analysis Approach

The modelling analysis adopted here involved two procedures: incremental and iterative parts. In the incremental procedure, the external load or prescribed deformation is increased. Numerical analyses of previous experimental work, as presented later in Section 6.3, compared simulation results using the load-controlled and displacement-controlled approaches. It was found that once peak load is attained, the solution of the model does not converge for either approach. Instability occurs after peak load is reached, and the system fails as it cannot sustain a further increase in load

increment Δλ, as shown in Fig. 6.3. This is common for buckling analysis and materials that have a nonlinear response and a region of softening. Therefore, the indirect displacement analysis method was adopted in the FEA of specimens reported in the literature and of concentrically-tested columns in the experimental program of this research. This is because indirect displacement utilizes the modified Riks method (or arc length control) to solve nonlinear systems beyond peak load. As illustrated in Fig. 6.3, the arc length method updates both load (Δλ) and displacement (Δu) increments to reach equilibrium (DIANA FEA BV 2021). To obtain accurate results within reasonable computation time, both the displacement and force norms were selected to attain convergence.

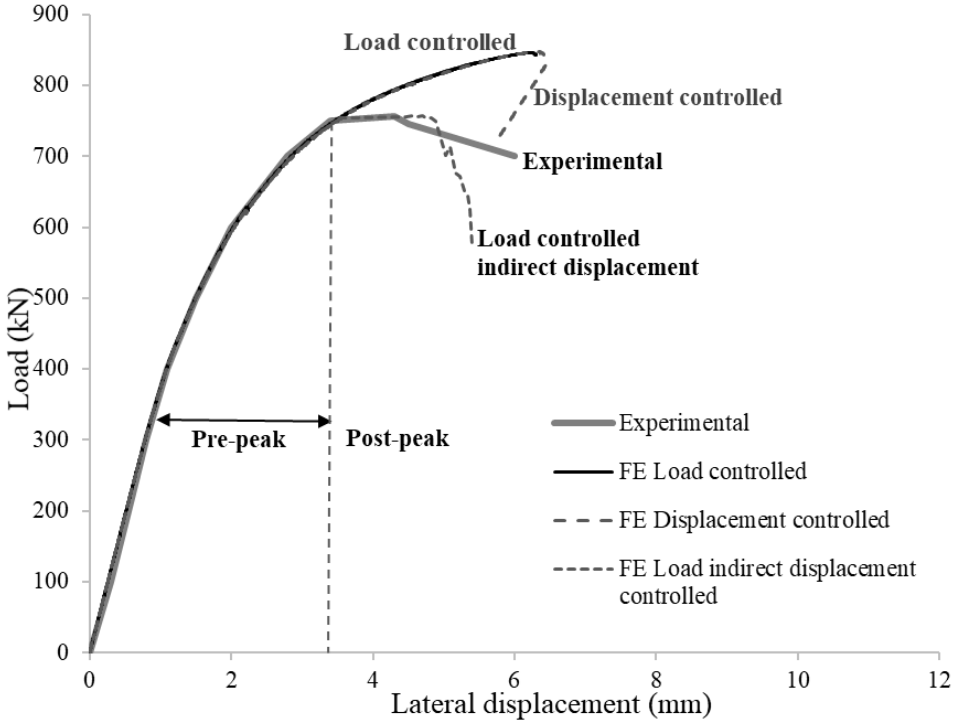

Fig. 6.3: Comparison between different analysis approaches

On the other hand, for eccentrically-tested columns where the columns undergo excessive displacements under applied loads, a displacement (DC) controlled method was adopted. Fig. 6.4 compares numerical results between indirect displacement (LDC) controlled and displacement controlled (DC) analyses for eccentrically-loaded columns. Both the load controlled analysis and indirect displacement analysis predicts a stiffer response compared to the displacement controlled

analysis. Moreover, the indirect displacement analysis under predicts the peak strength when the Hognestand concrete model was used.

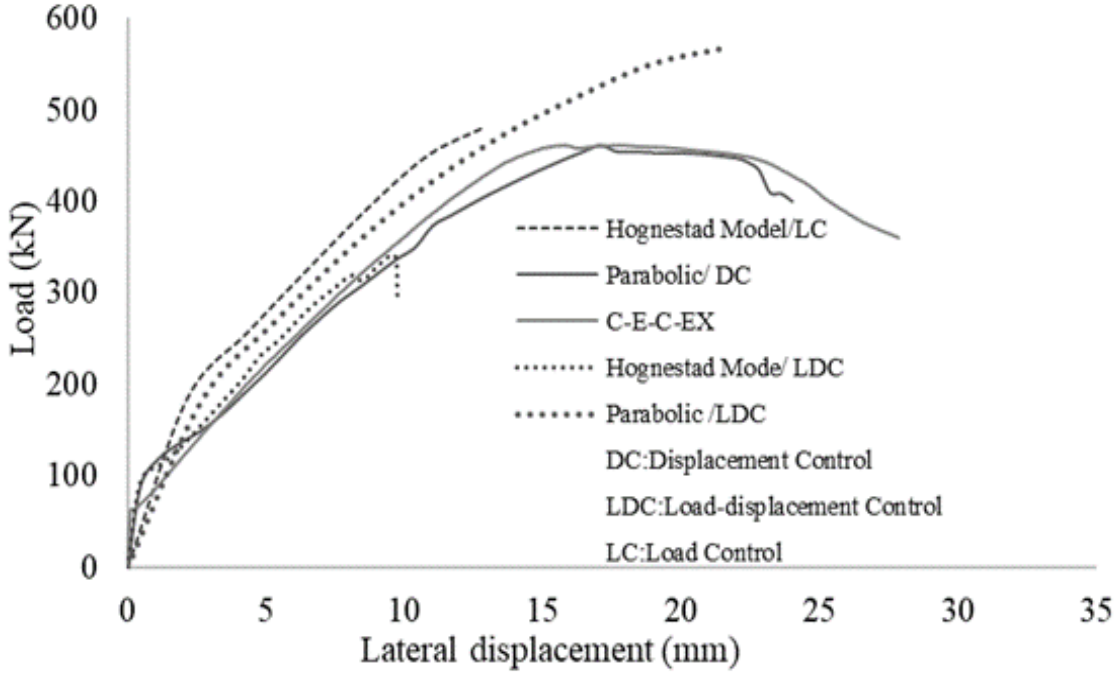

Fig. 6.4: Sensitivity analysis of the load analysis approaches and concrete models for eccentrically-loaded control column (C-E-C)

6.2.3 Modelling Corrosion Effects

The effects of reinforcement corrosion on cracking of the concrete cover, reduction of the cross-sectional area of the reinforcement, and bond loss were accounted for by integrating deterioration models into the different regions of the finite element model (FEM). These deterioration models were complemented with actual measurements obtained from the experimental program described in Chapter 3, such as material properties and observed corrosion-induced damage. An overview of corrosion-induced effects accounted for in the NLFEA is presented in Fig. 6.5.

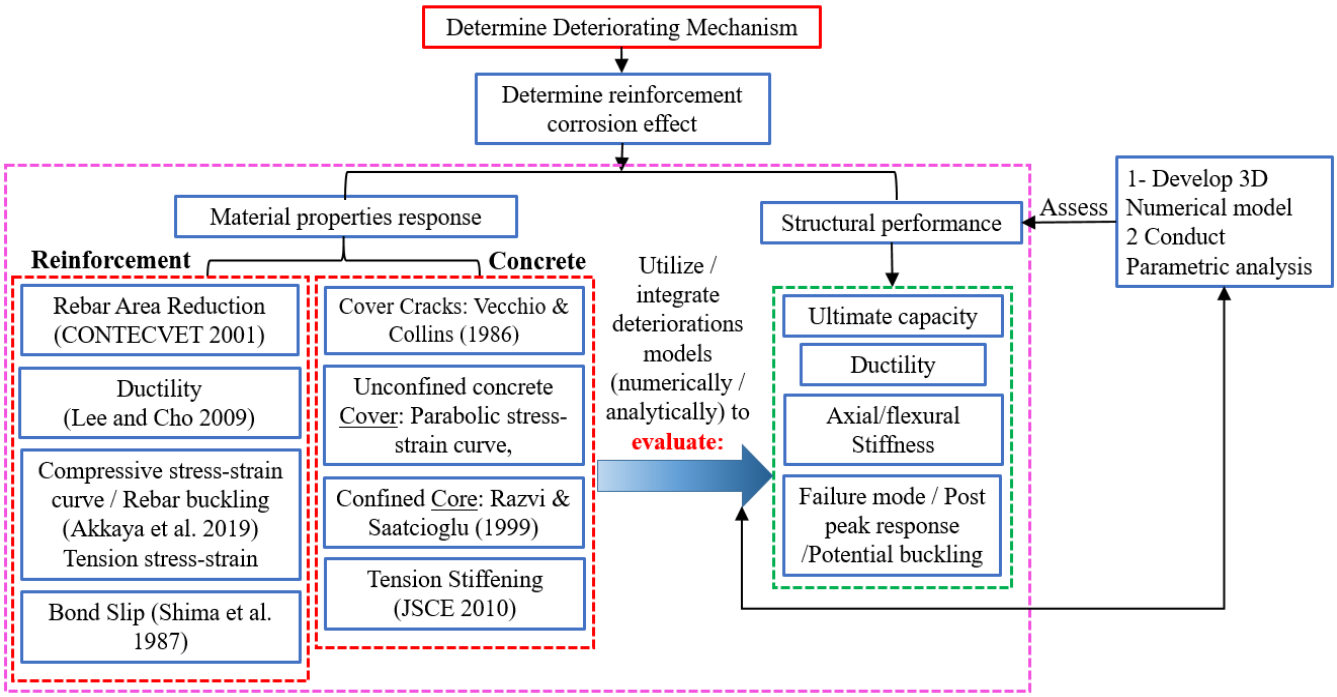

Fig. 6.5: Flow chart of the effects of steel corrosion on both concrete and steel materials

6.2.4 Concrete Material

6.2.4.1 Concrete cover

Cracking of the concrete cover, induced by the expansion of rust products, deteriorates the compressive strength of the concrete. This reduction was expressed by a model proposed by Cape (1999) as given by Eq. 2.18, which is a modification of Vecchio and Collins (1986) model to account for the effect of transverse tensile strains in decreasing the compressive strength. The model by Cape (1999) was used to indirectly account for corrosion-induced cracking, in addition to utilizing test measurements of the average crack width along the column surfaces obtained from the experimental results.

6.2.4.2 Concrete in Compression

Diana software offers several constitutive models to simulate concrete in compression. A sensitivity analysis was conducted to determine the model that would best simulate the response of the columns. The models that were considered were Hognestad's model (Hognestad 1951),

Thorenfeldt et al. (1987) and the parabolic model (Feenstra 1993). A brief description of each model is presented here.

The parabolic curve is based on the model proposed by Feenstra (1993) given as follows (Diana FEA 2020):

$$f = \begin{cases} -f_c \frac{\alpha_j}{3\alpha_{c/3}}, & if \ \alpha_{c/3} \leq \alpha_j < 0 \\ -f_c \left(1 + 4\left(\frac{\alpha_j - \alpha_{c/3}}{\alpha_c - \alpha_{c/3}}\right) - 2\left(\frac{\alpha_j - \alpha_{c/3}}{\alpha_c - \alpha_{c/3}}\right)^2\right), & if \ \alpha_c \leq \alpha_j \leq \alpha_{c/3} \\ -f_c \left(1 - \left(\frac{\alpha_j - \alpha_c}{\alpha_u - \alpha_c}\right)^2\right), & if \ \alpha_c \leq \alpha_j \leq \alpha_{c/3} \\ 0, & if \ \alpha_j \leq \alpha_u \end{cases}$$

Eq. 6.1

where f and α_j represent the concrete compressive principal stress and strain, respectively, and f_c is the concrete compressive strength. The parabolic stress-equivalent strain model given by Eqs. 6.1-6.4 is formulated based on concrete's fracture energy (Feenstra 1993). The parabolic curve is determined using three parameters (Fig. 6.6) the strain at one-third of the peak compressive strength $\alpha_{c/3}$, the strain at peak compressive strength α_c and the ultimate strain α_u. These parameters are defined as follows (Diana FEA 2020):

$$\alpha_{c/3} = -\frac{1}{3}\frac{f_c}{E} \qquad \textit{Eq. 6.2}$$

$$\alpha_c = \frac{5}{3}\frac{G_c}{h f_c} = 5\alpha_{c/3} \qquad \textit{Eq. 6.3}$$

$$\alpha_u = \alpha_c \frac{3}{2}\frac{G_c}{h f_c} \qquad \textit{Eq. 6.4}$$

where E is concrete's elastic modulus, G_c is the compressive fracture energy, and h is the characteristic length.

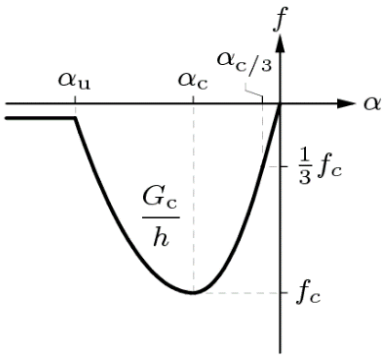

Fig. 6.6: Parabolic curve describing concrete uniaxial compressive response (reproduced from Diana FEA 2020)

According to Hognestad's model (Hognestad 1951), the concrete compressive principal stress *f* is determined as:

$$f = f_c \left(2\frac{\varepsilon_c}{\varepsilon_0} - \left(\frac{\varepsilon_c}{\varepsilon_0}\right)^2\right), \qquad \textit{Eq. 6.5}$$

where ε_0 is the strain at peak concrete stress and is equal to 0.002, f_c is peak compressive stress (MPa), and ε_c is the concrete compressive principal strain. The initial tangent modulus of elasticity is determined as:

$$E_i = \frac{2f_c}{\varepsilon_0} \qquad \textit{Eq. 6.6}$$

Hognestad's model is typically suited for concretes with a compressive strength lower than 40 MPa.

Thorenfeldt et al. (1987) proposed a stress-strain model for unconfined concrete that can be adjusted to account for high-strength concrete, and it is given by:

$$\frac{f}{f_c} = \frac{n_0\left(\frac{\varepsilon}{\varepsilon_0}\right)}{(n_0-1)+\left(\frac{\varepsilon}{\varepsilon_0}\right)^{nk_c}} \qquad \textit{Eq. 6.7}$$

where k_c=1 for $\varepsilon_0 < \varepsilon < 1$, k_c=0.67+$\frac{f_{core}}{62}$ for $\varepsilon \leq \varepsilon_0$, $n_0 = 0.8 + \frac{f_{core}}{17}$, and $f_{core}$is the confined concrete core strength calculated according to Razvi and Saatcioglu (1999)

The above three models were investigated in the calibration analyses for concrete response in compression by simulating experimental results from the literature reported by Wang et al. (2012)

(see Section 6.3). FEA results using the three constitutive models for eccentrically-loaded column ZDT 700 are presented in Fig. 6.16. The shortcoming of using the Hognestad and Thorenfeldt et al. models, in this case, is underestimating the column's ultimate load-carry capacity. The results highlight that the parabolic model (based on fracture energy) is the best suited for modelling concrete in compression for the specimens tested in this study.

6.2.4.3 Compressive Fracture Energy

Since the parabolic model used to model concrete in compression is based on concrete's fracture energy (Feenstra 1993), the value used in the FEA was calibrated against the experimental test results of this study. An increase in concrete deterioration (cracking damage) significantly increases the fracture energy (Hanjari et al. 2013). The compressive fracture energy (G_c) for normal weight concrete was determined according to the CIB-Fib Model (fib 2013) and depends on the tensile fracture energy (G_{ft}), which is calculated from:

$$G_{ft} = 73 f_c^{0.18} \times 0.001 \text{ (N/mm)} \qquad \textit{Eq. 6.8}$$

where f_c is the mean compressive strength obtained from experimental tests in MPa. The compressive fracture energy (fib 2013) is then calculated as:

$$G_c = 250 G_{ft} \left(\frac{N}{mm}\right) \qquad \textit{Eq. 6.9}$$

Several values of the fracture energy were used in modelling the response of the control RC column subjected to eccentric load, as illustrated in Fig. 6.7. Based on the results, the best comparison was obtained for a fracture energy of 28 N/mm (Fig. 6.7).

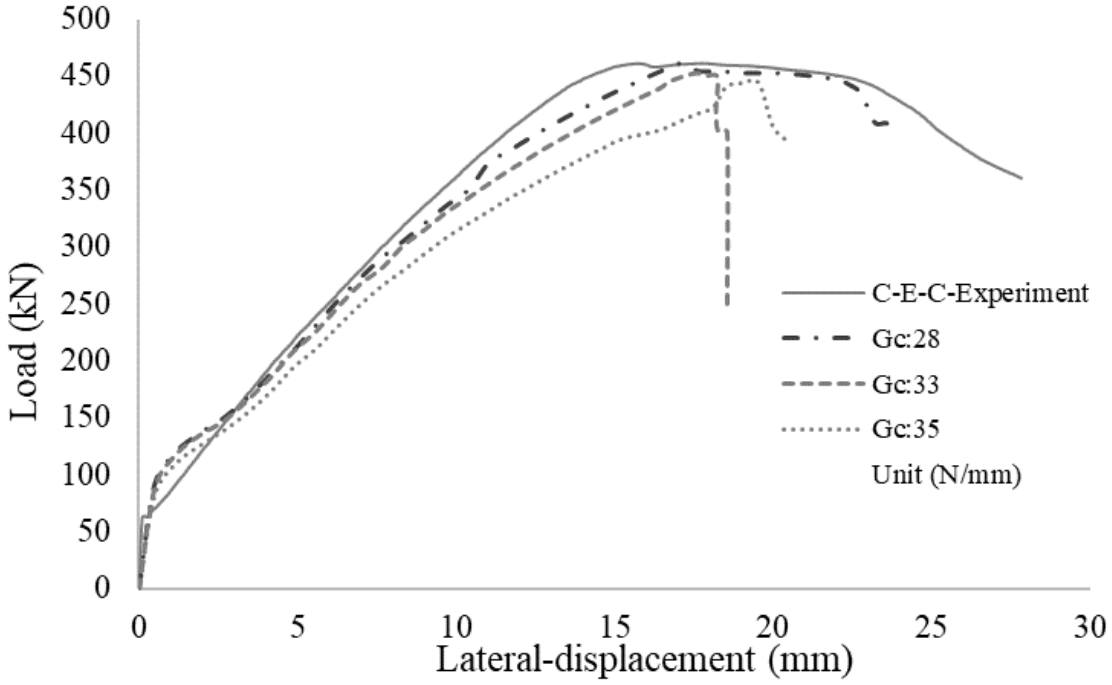

Fig. 6.7: Sensitivity analysis of the compressive fracture energy for eccentrically-loaded columns

6.2.4.4 Confinement Effects

To model confinement in the concrete core of the column, the model proposed by Razvi and Saatcioglu (1999) was used, as given by Eqs. 6.10-6.15. Core confinement increases the concrete compressive strength compared with unconfined core defined according to Hognestad's model as illustrated in Fig. 6.8. Transverse reinforcement provides both lateral support and confinement to the concrete core, which increases with smaller tie spacing. Moreover, lateral support provided by the transverse reinforcement allows longitudinal reinforcement in compression to reach yielding before buckling, which leads to a safer failure mode. The model by Razvi and Saatcioglu (1999) reflects a reduction in confinement pressure of the concrete core due to a reduction in the tie cross-sectional area; it also accounts for the increase in ties' spacing along the column length due to tie fracture and reduction in yield capacity of the ties due to corrosion. Several factors improve the core strength of concrete:

- The volumetric ratio of the transverse reinforcement

  Increasing the volumetric ratio of the transverse reinforcement will increase core confinement pressure.

- Yield strength of the transverse reinforcement

  The developed lateral pressure depends on the transverse reinforcement's stiffness at the corners. The lateral pressure and subsequent core strength is reduced when the ties yield under high loads.
- Configuration of the transverse reinforcement

  The lateral pressure due to expanding concrete is nonuniformly distributed along the transverse restraining reinforcement for different cross-section configurations. For example, the lateral pressure peaks at the corners of rectilinear cross sections
- Spacing of the transverse reinforcement

  Closely spaced ties reduce the longitudinal bars' unsupported length, preventing potential local buckling.
- Volumetric ratio of the longitudinal bars

  A higher volume ratio of the longitudinal bars improves the ultimate capacity and reduces the potential risk of local buckling.

In this study, the confined concrete core f_{core}(MPa) was defined according to Razvi and Saatcioglu (1999).

$$f_{core} = f_c + k_1 f_{le} \qquad \textit{Eq. 6.10}$$

where f_c is the unconfined compressive stress (MPa). Parameter k_1 is defined as:

$$k_1 = 6.7(f_{le})^{-0.17} \qquad \textit{Eq. 6.11}$$

The equivalent uniform pressure f_{le} is determined from:

$$f_{le} = k_2 f_l \qquad \textit{Eq. 6.12}$$

where $k_2$is introduced to reduce the average pressure and is estimated according to Razvi and Saatcioglu (1999). The average lateral pressure (f_l) is estimated as follows:

$$f_l = \frac{\sum_{i=1}^{q} A_s f_{st} sine\alpha}{sb_c} \qquad \textit{Eq. 6.13}$$

where q is the number of tie legs, sb_c is the core surface area, α is the angle between the leg of transverse reinforcement and the core side crossed by the same leg, and f_{st} is the yield strength of

the transverse reinforcement. The strain corresponding to peak stress of confined concrete is given by:

$$\varepsilon_{01} = \varepsilon_0(1 + 5k_2) \qquad \textit{Eq. 6.14}$$

$$k_2 = \frac{k_1 f_{le}}{f_c} \qquad \textit{Eq. 6.15}$$

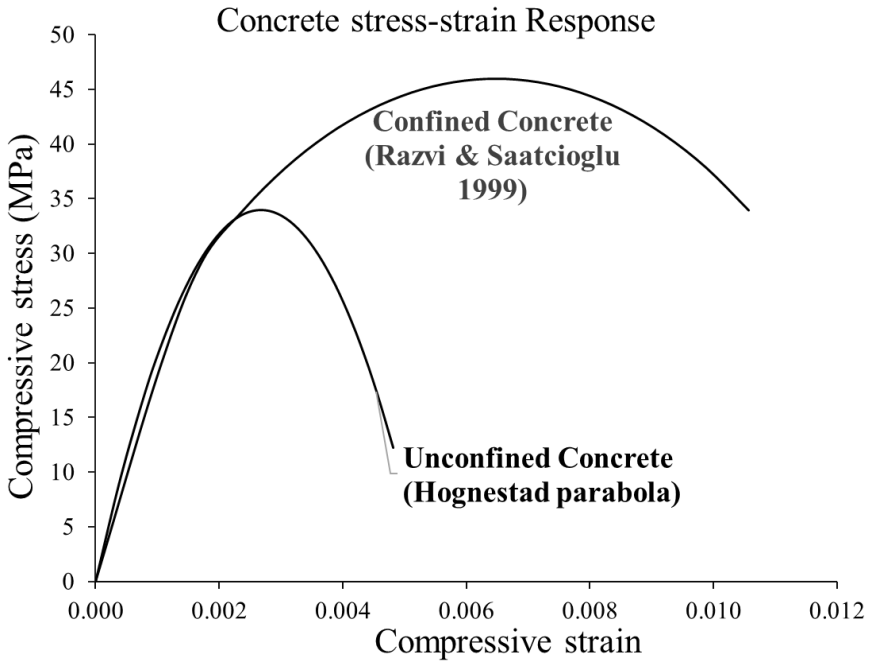

Fig. 6.8:Compression stress-strain model for confined and unconfined concrete

6.2.4.5 Concrete in Tension

In reinforced concrete, tensile stresses at crack locations are carried by the reinforcement and transferred to the concrete in-between cracks through the bond between the steel and concrete. This mechanism is known as tension stiffening mechanism (Allam et al. 2013). In this study, the concrete response in tension was defined using the tension stiffening model in JSCE (2010), in which average principal tensile stresses σ_t in the concrete are determined from:

$$\begin{matrix} \sigma_t = E\varepsilon & \varepsilon < \varepsilon_{cr} \\ \sigma_t = f_t & \varepsilon_{cr} \le \varepsilon \le \varepsilon_{tu} \\ \sigma_t = f_t(\varepsilon_{tu}/\varepsilon)^{0.4} & \varepsilon > \varepsilon_{tu} \end{matrix} \qquad \textit{Eq. 6.16}$$

where E is the elastic modulus of concrete, ε is the average principal tensile strain in the concrete, ε_{cr} is the strain at which cracking initiates ($\varepsilon_{cr} = f_t/E$), f_t is the concrete's tensile strength, and ε_{tu} is the end of the plateau strain.

The tensile strength (f_t) and fracture energy G_{ft} of the concrete were estimated according to:

$$f_t = 0.33\sqrt{f_c}\ (MPa) \qquad Eq.\ 6.17$$

$$G_{ft} = 73 f_c^{0.18}.0.001\ (N/mm) \qquad Eq.\ 6.18$$

6.2.5 Crack Models

This analysis involves the significant development of cracks due to both incremental loading and corrosion conditions. While the latter is pre-accounted for in modelling the corrosion effects, crack propagation due to applied load is addressed using a crack model embedded in Diana, such as the total strain-based crack model. The orthogonal rotating orientation-based crack model was selected because the principal stress directions and the cracks directions constantly vary as the applied load increases. The energy dissipated due to material fracture is affected by element size or volume. In Diana, this is accounted for using a crack width parameter which is related to the area or volume of the element.

6.2.6 Steel Reinforcement

Corrosion of the reinforcement was accounted for by reducing the cross-sectional area according to Eq. 2.8. In addition, the steel mechanical properties of the corroded bars were reduced by applying the empirical equations proposed by Lee and Cho (2009), as given by Eqs. 2.40-2.46, to the results of tensile tests according to ASTM A370 (ASTM 2020) of uncorroded rebars, as shown in Fig. 4.2.

At a very high levels of tie corrosion (≥20%) , corroded ties were completely removed in the model due to their severe deterioration condition (pitting fracture and very brittle).

To account for potential buckling of the longitudinal reinforcement, the response of reinforcing steel in compression was defined according to the Redefined Dhakal Maekawa (RDM) model proposed by Akkaya et al. (2019), explained in Appendix B.2. The model parameters (tie spacing, steel ultimate strain and bar area) were reduced depending on the level of steel corrosion attained.

Moreover, the unsupported length L was taken as the spacing between adjacent ties. The longitudinal reinforcement response in tension was accounted for using a multilinear model, as shown in Fig. 6.9.

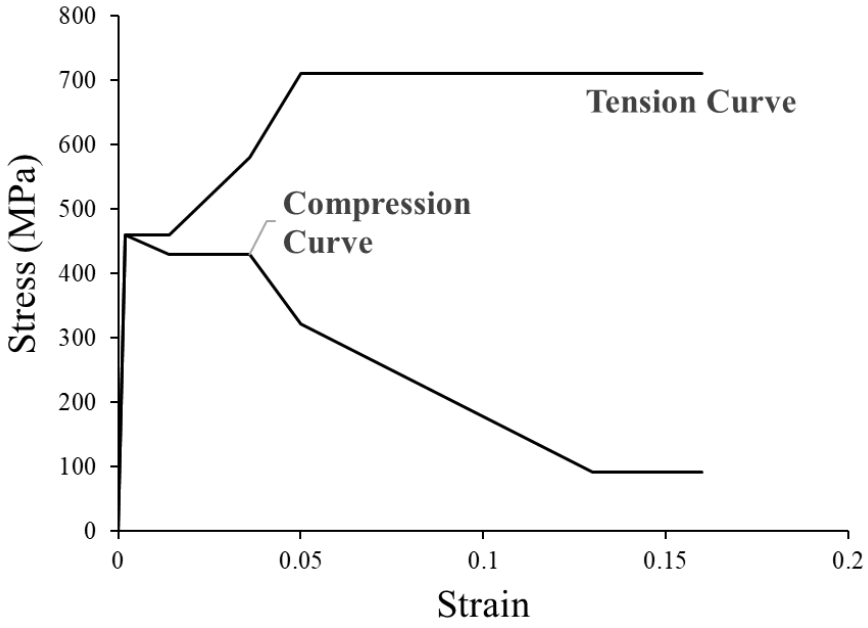

Fig. 6.9: Reinforcement model in tension and RDM in compression

6.2.7 Bond Loss

Reinforcement corrosion leads to significant concrete deterioration (cracking and spalling), degradation of the mechanical properties of the reinforcements (area and ductility) and bond loss. Subsequently, the ultimate capacity of the column is reduced, and the failure mode is altered to a brittle mode. The bond capacity between concrete and steel is a result of chemical adhesion, friction, and mechanical interlock due to the ribs of deformed reinforcing bars. Therefore, the bond strength is affected by mechanical interlock of the ribs, steel to concrete adhesion, steel diameter, shape, spacing, strength and ductility, and concrete compressive and tensile strength. When a slip or relative interface displacement occurs between the concrete and reinforcement, bond stresses develop between the concrete and steel and increase as the slip increases.

At the corbel uncorroded sections of the column, the reinforcement was defined as embedded elements, which the software Diana assumes to be in perfect bond with the concrete. At the corroded zone in the middle section of the column, a bond-slip failure model was adopted to account for potential slippage due to bond loss. Corrosion effects were considered by reducing the concrete compressive strength due to tensile cracking and reducing the cross-sectional area and ductility of the corroded reinforcement. Several bond-slip models are pre-defined in Diana software, such as CEB- fib Model Code (2010) and Shima et al. (1987) models. The bond-slip model by Shima et al. (1987) was selected to define the interaction between the concrete and the steel, and it is defined as follows:

$$g(\varepsilon) = \frac{1}{1+\varepsilon\times 10^5} \qquad \textit{Eq. 6.19}$$

$$\frac{\tau}{f_c} = \frac{0.73\left(ln\left(1+5s_{slip}\right)\right)^3}{1+\varepsilon\times 10^5} \qquad \textit{Eq. 6.20}$$

where τ is the bond stress (MPa), f_c is the concrete compressive strength (MPa), ε is the strain of the steel bar, and s_{slip} is the slip between steel and concrete. The non-dimensional slip s_{slip} is expressed a function of the total relative displacement $\Delta u_t(slip)$ and the diameter of the steel bar as follows:

$$s_{slip} = 1000\frac{\Delta u_t(slip)}{d} \qquad \textit{Eq. 6.21}$$

6.3 Model Validation with Literature Work

The modelling scheme implemented in Diana (v.10.4) was validated by comparing the numerical results with published experimental data by Rodriguez et al. (1996) and Wang et al. (2012). In the validation, both the ultimate strength and load-displacement curves were compared. The variations between the experimental and FEM load-displacement curves were calculated using root mean square deviation (RSMD). It was concluded that the methodology adopted captures well both the corroded column's ultimate capacity, deformation, and axial stiffness.

6.3.1 Rodriguez et al. (1996)

Rodriguez et al. (1996) tested corroded RC columns 2,000-mm long with three different reinforcing details. An axial load was applied concentrically atop the column (Fig. 6.10). The experimental results highlighted a reduction in the overall load capacity, mean strain, and the RC columns' compressive stiffness. The column's overall capacity was affected by several parameters, mainly an increase in the load eccentricity due to asymmetrical deterioration associated with reinforcement corrosion. This led to premature buckling of the reinforcement and craking/spalling of the concrete cover. Premature buckling of the rebar, observed after column failure, was attributed to a reduction in stiffness of the concrete cover and failure of a corroded tie. Comparison between the average strain at the mid-column section of the experimental (EX) and FEA model results for the control column results in a good agreement for the load-average strain curve, as illustrated in Fig. 6.11. However, the FEM underestimates the overall capacity for the control specimen. For corroded columns, the FEM is excellent in predicting the overall response and ultimate capacity (Fig. 6.12). The ascending line for the load-strain curve for the corroded specimen has a lower stiffness value (more flexible) due to stiffness, strength, and ductility reduction of the longitudinal and transverse reinforcement (Fig. 6.13). Fig. 6.14 illustrates reinforcement stress distribution (right) and crack damage due to small eccentricities resulting from asymmetrical reinforcement corrosion. The FEM results illustrate a concentration of cracks on the tension side of the column while buckling of the rebar at the compression zone (Fig. 6.14). These zones were generated due to biaxial eccentricities detected during experimental set-up and measurements. The total Cauchy stresses of the concrete exceeded the concrete compressive strength of 35 MPa, denoting concrete crushing on the compression zone.

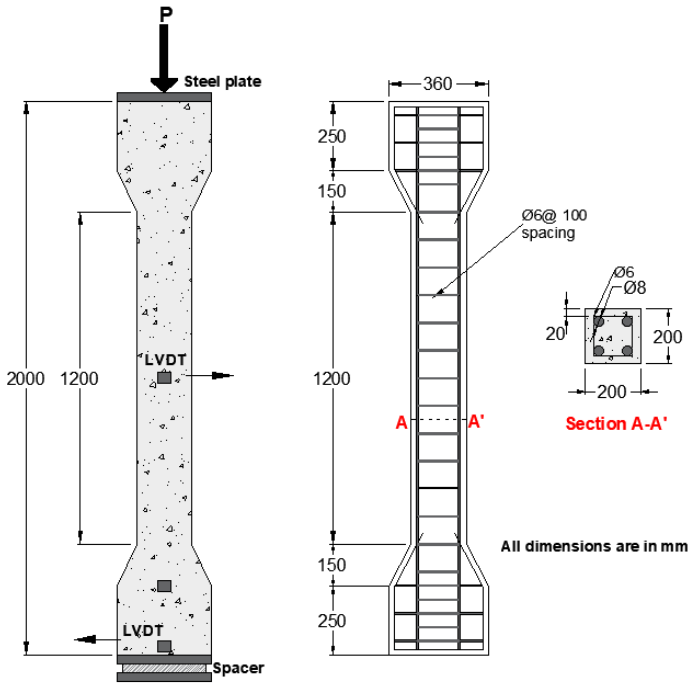

Fig. 6.10: Details of the tested reinforced concrete column adopted from (Adapted from Rodriguez et al. 1996)

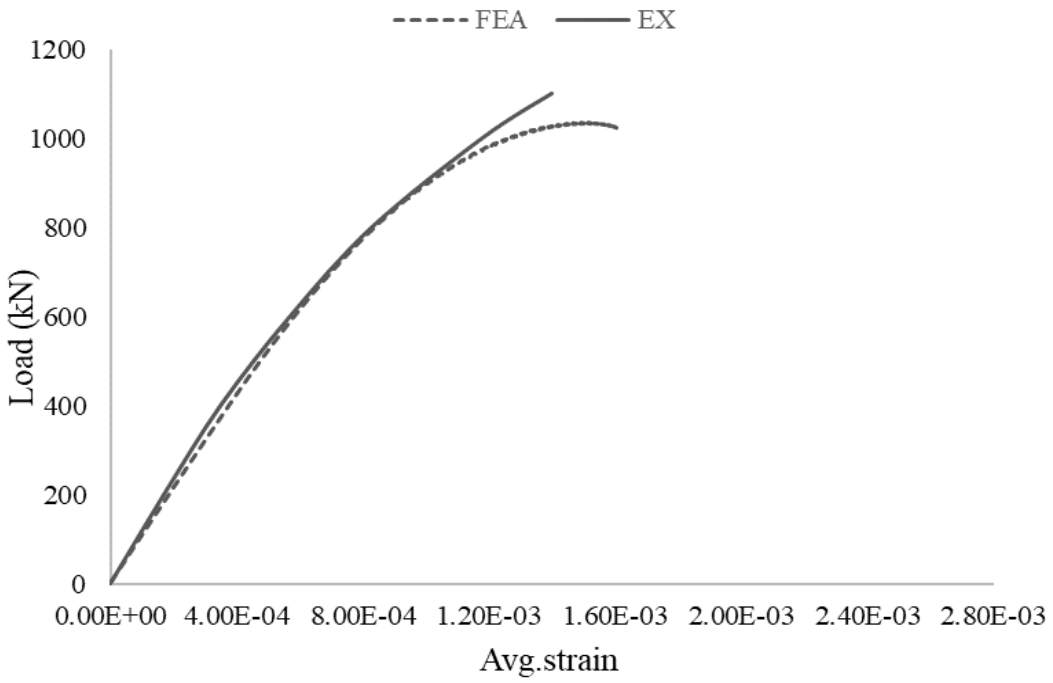

Fig. 6.11: Comparison between the average strain at mid column section of the experimental (EX) and FEA model for control column

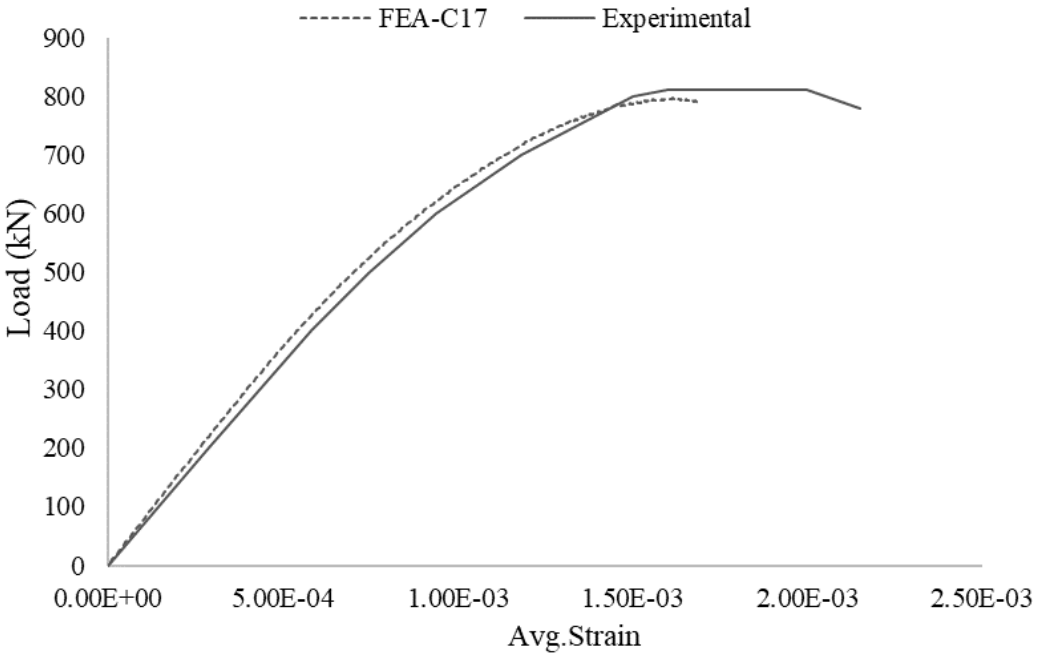

Fig. 6.12: Comparison between the average strain at mid column section of the experimental (EX) and FEA model for corroded column referred to as No.17 (C17)

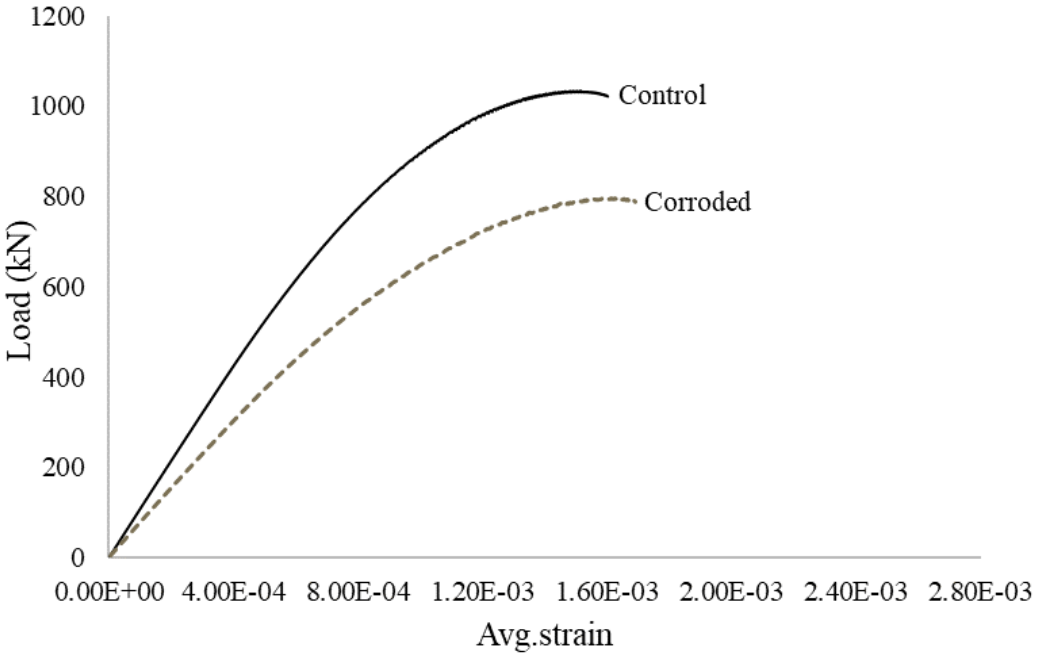

Fig. 6.13: FE results of load vs. average strain measured on four sides of the mid-section of the column,

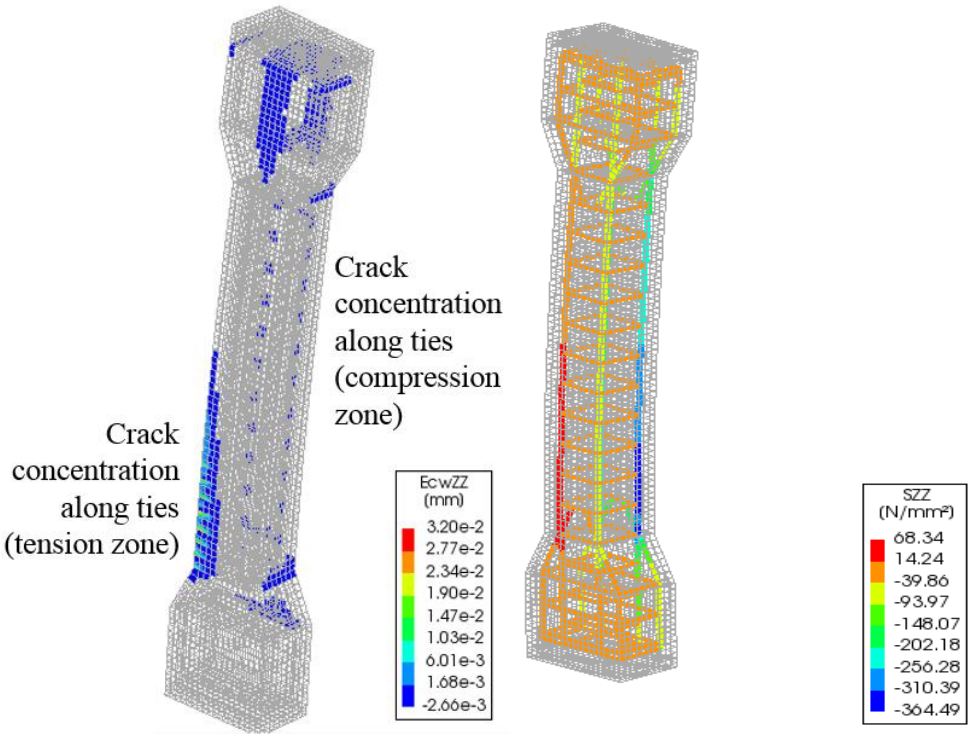

Fig. 6.14: Left) crack widths, Right) reinforcement stress

6.3.2 Wang and Liang (2008) and Wang et al. (2012)

Wang et al. (2012) extended previous work by Wang and Liang (2008) to include all tested specimens in their study. The authors investigated the effect of the extent and location of corrosion on the structural performance of 20 (1,300-mm long) RC columns subjected to loading at small (50 mm) and large (150 mm) eccentricities (Fig. 6.15). For both eccentricity values, eighteen (18) columns were either corroded along the tensile, compressive, or tensile and compressive zones for a partial length of 700 mm.

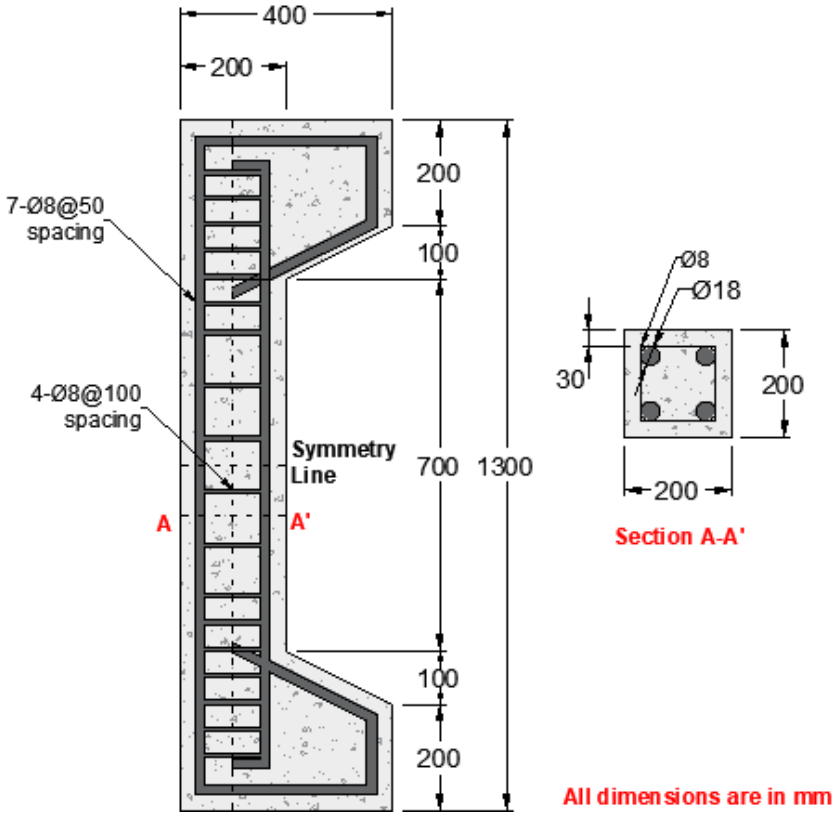

Fig. 6.15: Detail of the modelled RC column (adapted from Wang et al. 2012)

6.3.2.1 Model Calibration

Several FE models were developed and calibrated with the experimental data to determine the best concrete material model that captures the column response. Among these material models were Thorenfeldt et al. (1987), parabolic curve (Feenstra 1993) and Hognestad (1951) models for concrete in compression. It was found that both Thorenfeldt et al. and Hognestad models

underestimated the bearing capacity of the column. Moreover, the parabolic model (Feenstra 1993), which is based on the compression fracture energy, was also considered. However, considering the uncertainties associated with the fracture energy parameter, selecting the best model and fracture energy value was validated through parametric analyses as shown in Fig. 6.16: and Fig. 6.17. Based on the results and comparison with experimental data reported by Wang et al. (2012), the selected model was a parabolic model with G_{fc}=35 N/mm^2, as shown in Fig. 6.16: and Fig. 6.17.

Numerical simulation of the experimental work reported by Wang et al. (2012) was also conducted and compared using two analysis approaches: load-controlled approach and displacement-controlled approach. It was determined that the load indirect displacement-controlled method is better suited for this analysis as this method captures well the significant deformation the columns undergo at a large load eccentricity (Fig. 6.18).

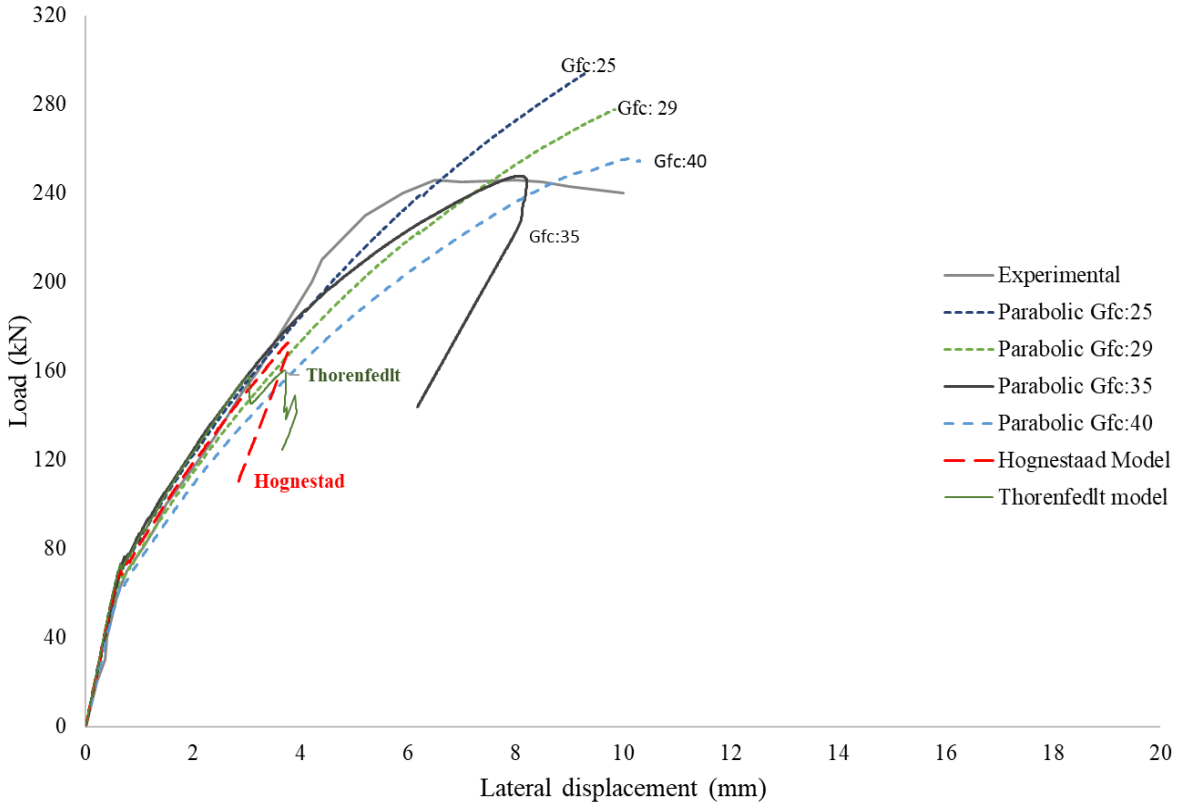

Fig. 6.16: Calibration of the compression model for concrete of an eccentrically loaded column (designated as ZDT700)

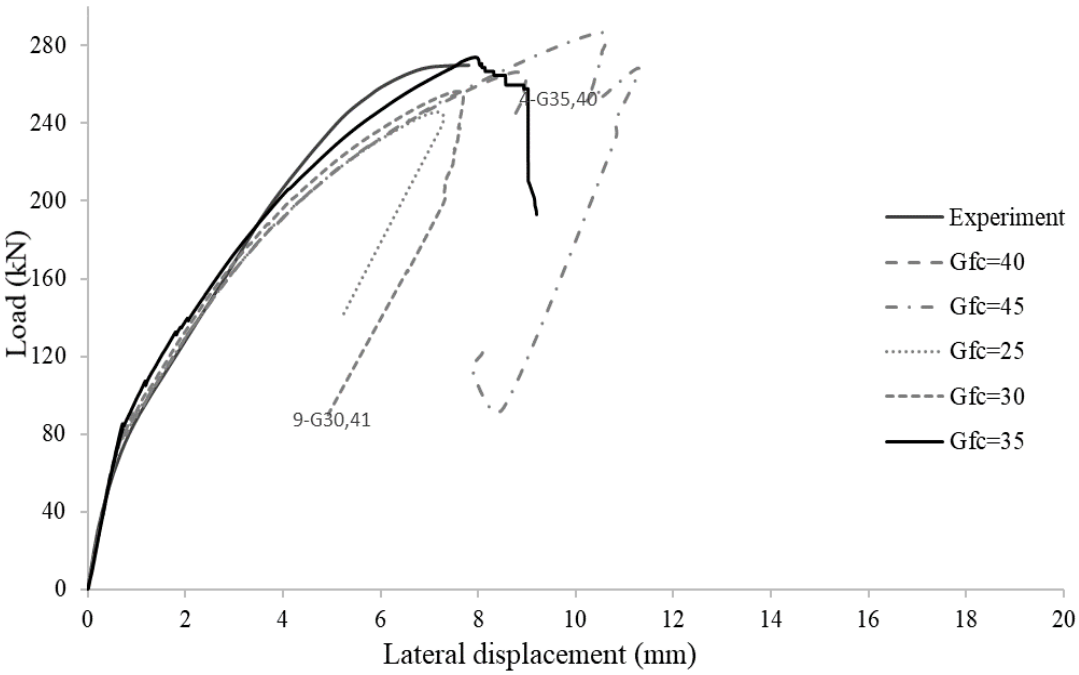

Fig. 6.17: Calibration of the compressive fracture energy (Gfc)

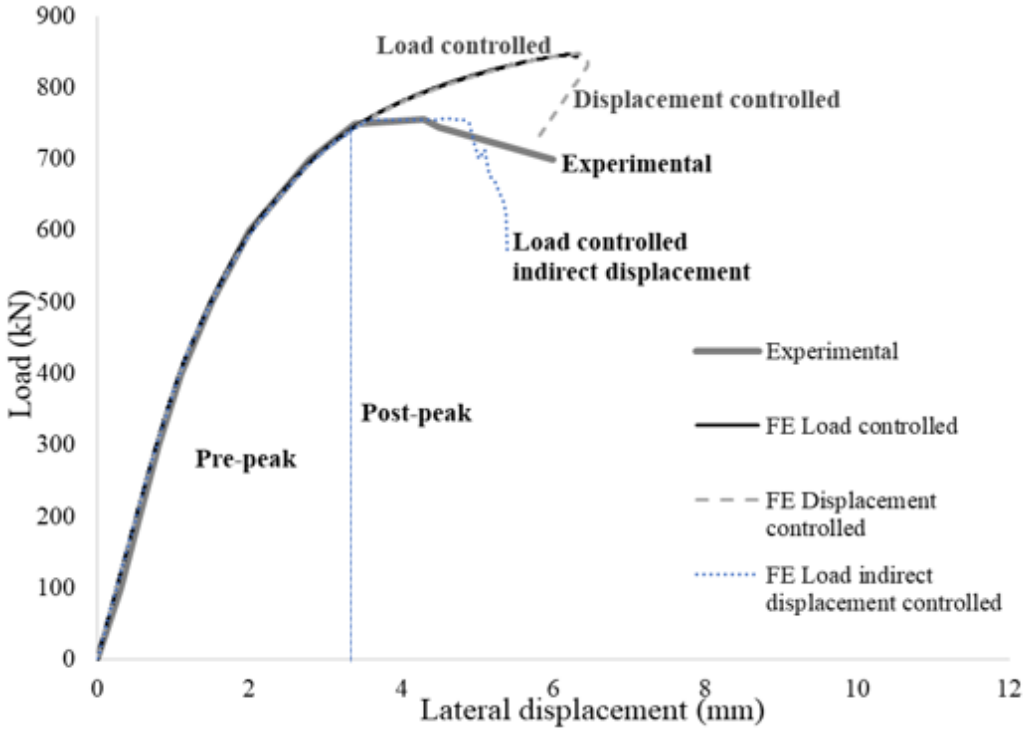

Fig. 6.18: Sensitivity analysis of the load analysis approaches adopted in the FEM

6.3.2.2 Model Validation

The FEM was validated with six columns tested by Wang et al. (2012) under concentric and eccentric loads. A set of three columns were tested under small eccentricity (50 mm): one column was corroded on the tension side (ZXT), one on the compression zone (ZXC), and one on both the tensile and compressive faces (ZXTC). Another set of three columns were tested under large eccentricity (150 mm): one was corroded on the tension side (ZDT), one on the compression zone (ZDC) and one on both tensile and compressive faces (ZDTC). Numerical results were compared to experimental ones in terms of ultimate capacity, overall column response and column stiffness (see Fig. 6.19 to Fig. 6.21 for group ZX and Fig. 6.23 to Fig. 6.25 for group ZD). Comparison of results show that the FEM predicts well the ultimate capacity (0-4% variations) and captures the overall column response. The difference between FEM results and the experimental results reported by Wang et al. (2012) was estimated to be between 8-18%, as shown in Table 6.1.

For the group tested under small eccentricity, a more significant reduction in the mass loss in the compression zone resulted in a reduction in the ultimate capacity and stiffness, in addition to a higher mid-span deflection (Fig. 6.22). For equally corroded reinforcements on both compression and tension zones, it was observed that there is a higher decrease in the column stiffness and ultimate capacity compared to columns that were partially corroded along either the tension or compression zones (Fig. 6.22). Also, the reduction in ultimate capacity was more significant when the corrosion level was increased and spread along the compression and tension zones of the column. As the corrosion level was increased on both tension and compression reinforcement and ties, the ultimate capacity and stiffness of the column were reduced, and the response was less ductile (Fig. 6.22).

Table 6.1: Comparison between FEM results and experimental ones

Column	$P_{u\text{-}EXP}$	$P_{u\text{-}FEM}$	$P_{FEM/EXP}$	RSMD
ZXT	756	756	1.00	0
ZXC	741	766	1.03	14
ZXTC	671	723	1.08	18
ZDT	255	246	0.96	8
ZDC	269	266	0.99	8
ZDTC	246	247	1.00	10
		Avg.	1.01	

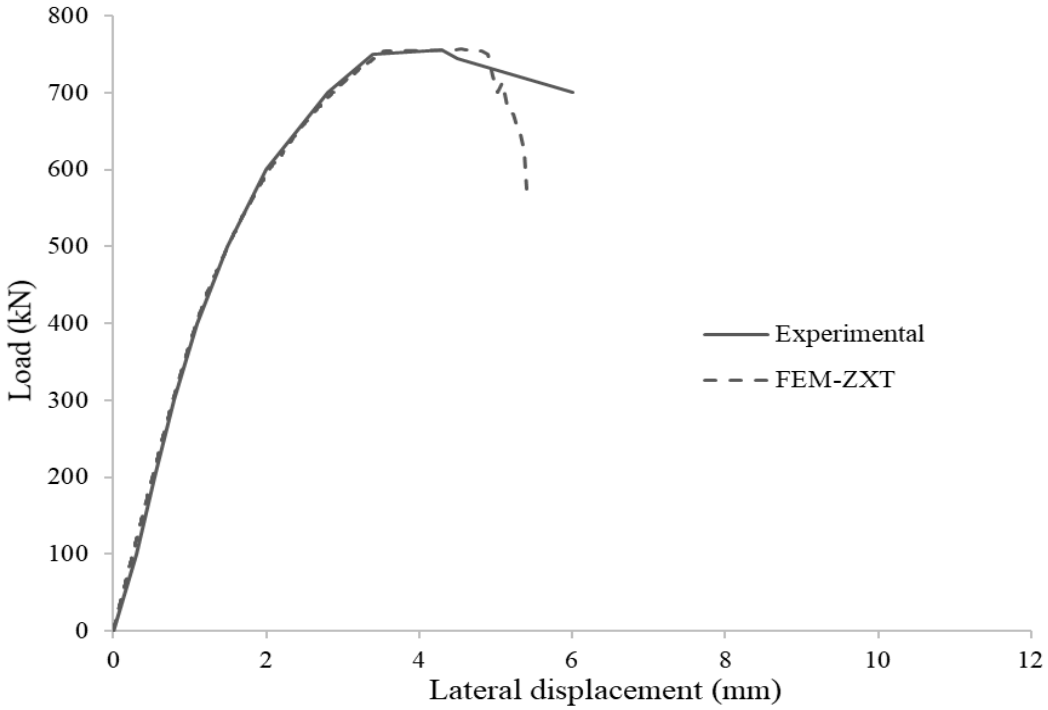

Fig. 6.19: Comparison between FEM and experimental results for ZXT700

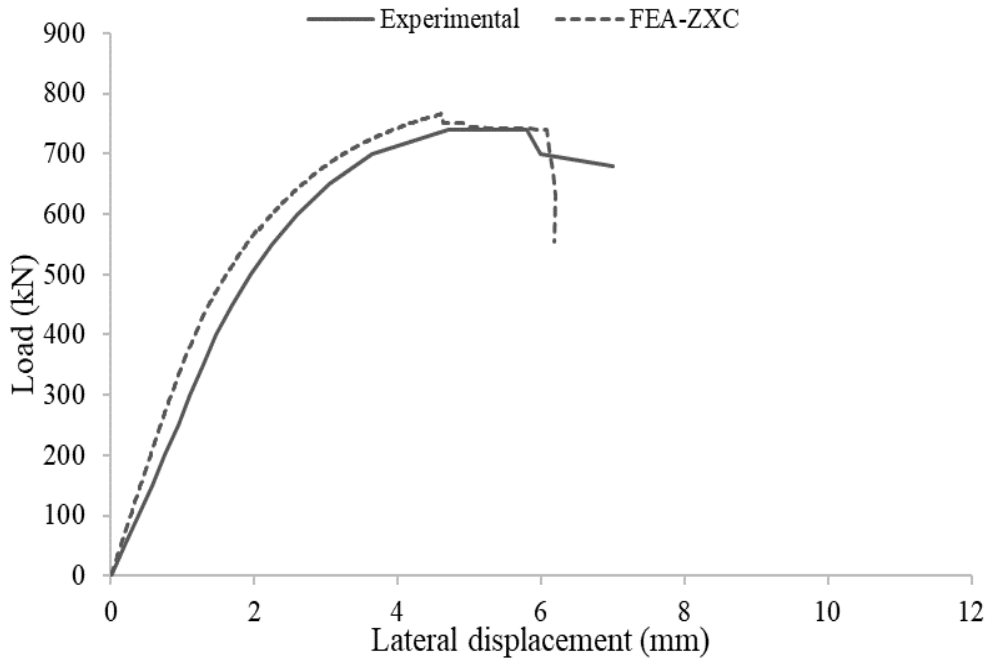

Fig. 6.20: Comparison between FEM and experimental results for ZXC700

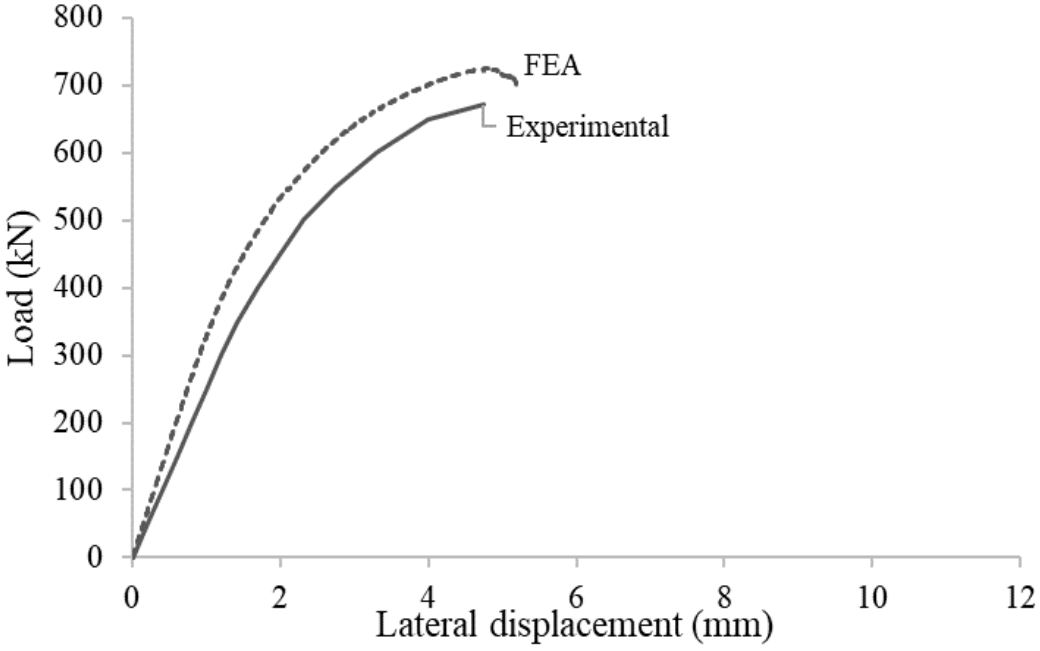

Fig. 6.21: Comparison between FEM and experimental results for specimen ZXTC700-1

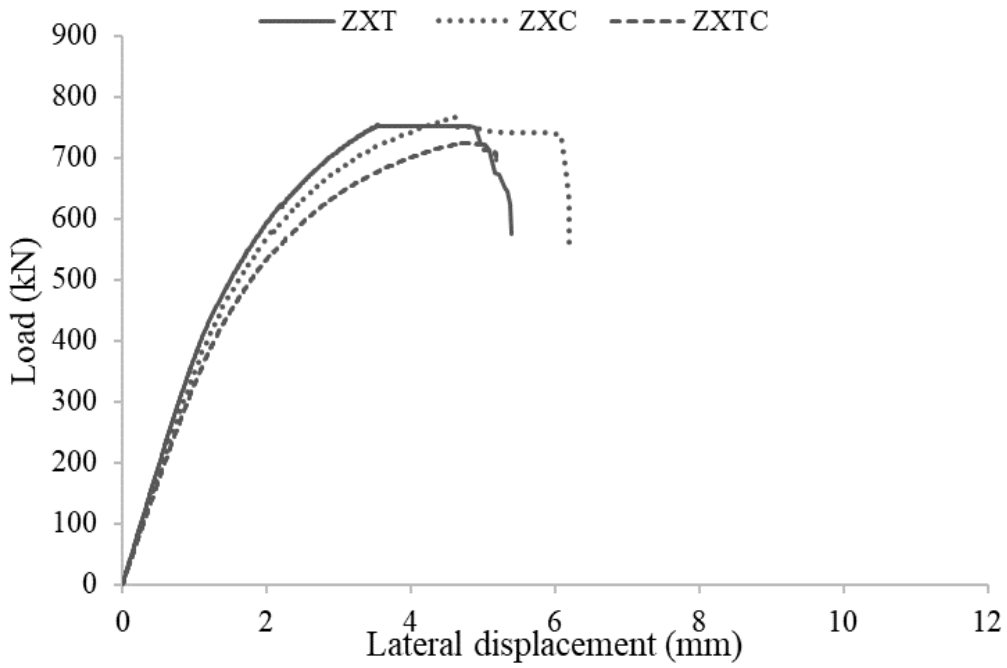

Fig. 6.22: FEM comparison between reinforcement corrosion on tension (ZXT), compression (ZXC) and tension and compression reinforcement (ZXTC)

For columns loaded at large eccentricities (group ZD), a high corrosion level in both compression and tension zones resulted in a reduction in the ultimate capacity of the columns. A more significant reduction in the ultimate capacity and ductility response was attributed to corrosion on the compression and tension reinforcements and ties (Fig. 6.23 to Fig. 6.26). Fig. 6.26 illustrates a reduction in flexural stiffness (more mid-span deflection) for column ZDTC because the level of corrosion was slightly higher than that of ZDT, which was also corroded on both the compressive and tensile longitudinal bars. In contrast, ZDC had a higher corrosion level along the compressive longitudinal reinforcement. Thus, the authors concluded that corrosion on the tensile reinforcement results in a higher reduction in load capacity for columns loaded at large eccentricities. Furthermore, for columns loaded at large eccentricity, the failure mode is comprised primarily of the development of flexural cracks along the tension side of the column (Fig. 6.27) and yielding of the reinforcement before attainment of peak load (Fig. 6.28).

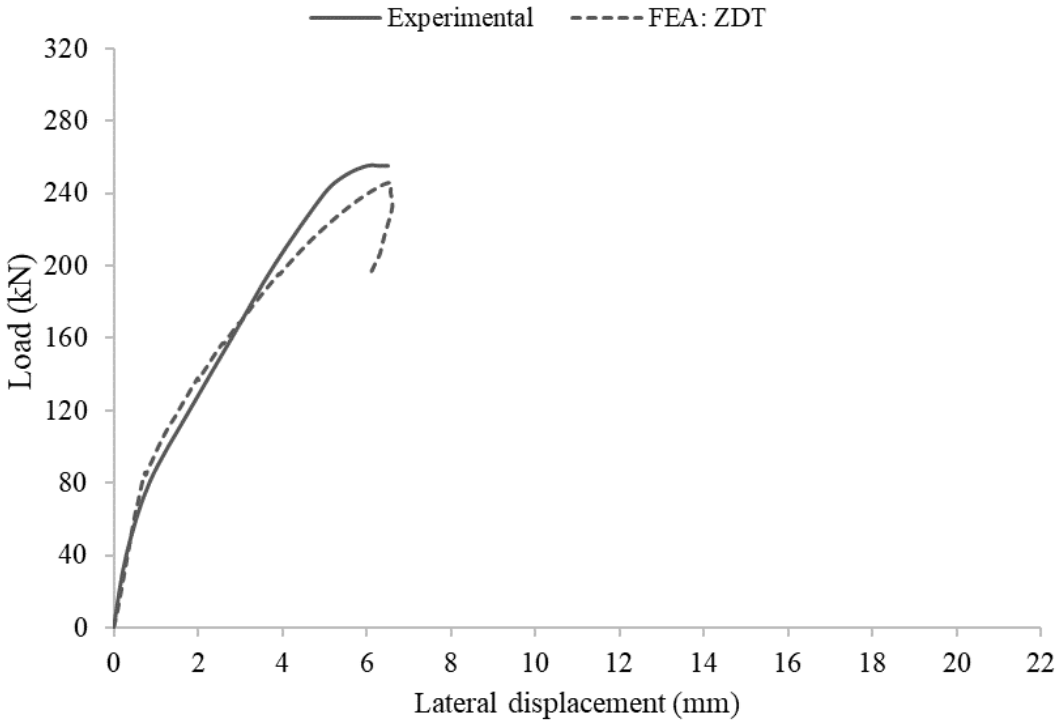

Fig. 6.23: Comparison between experimental/numerical for ZDT

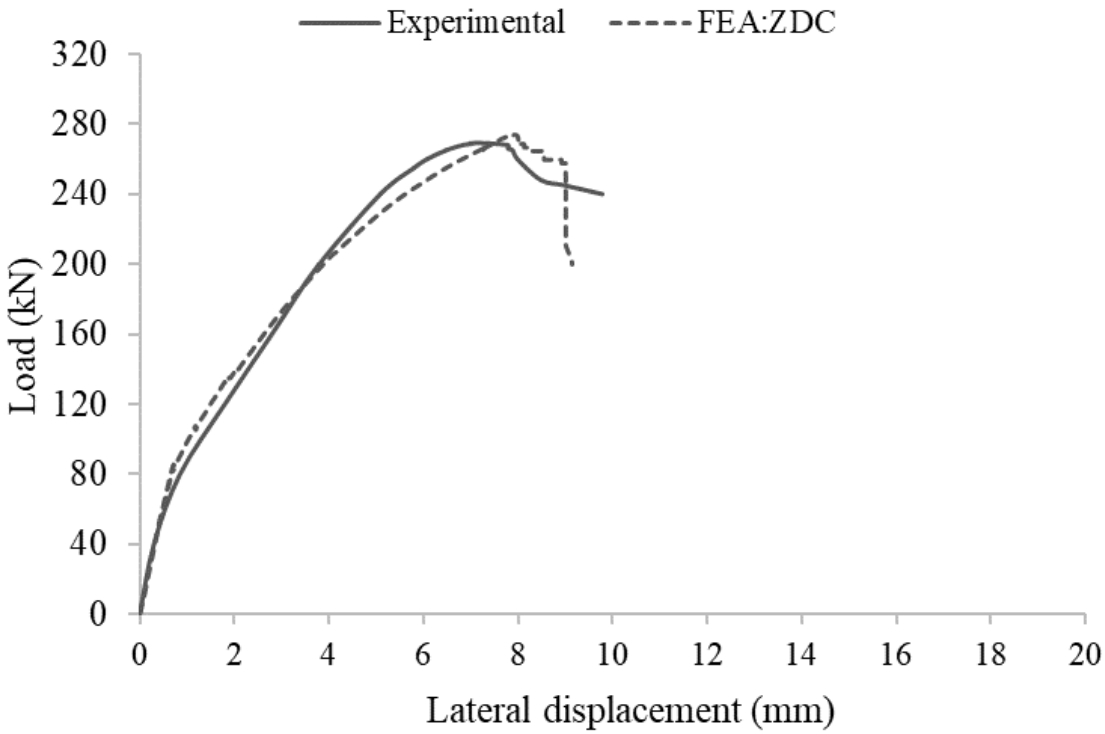

Fig. 6.24: Comparison between experimental and FEM results for ZDC

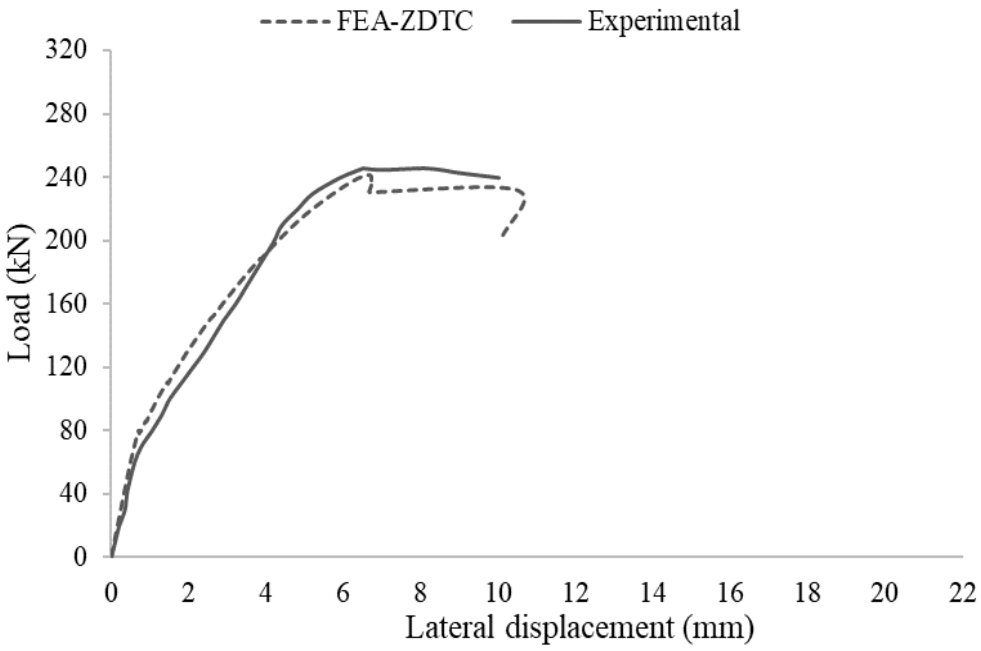

Fig. 6.25: Comparison between experimental and FEM results for ZDTC

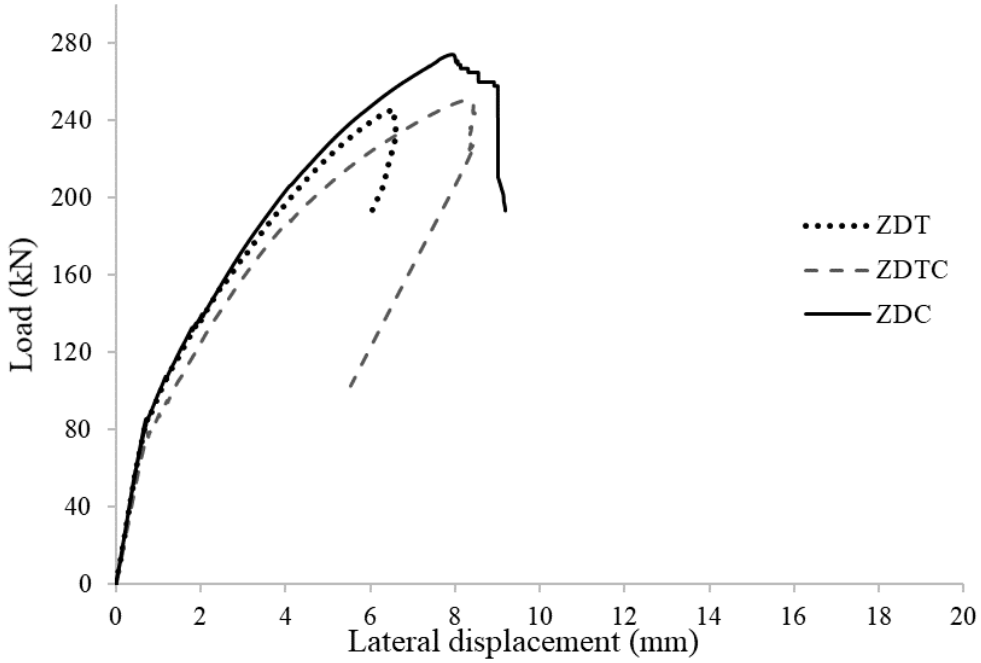

Fig. 6.26: FEM comparison between reinforcement corrosion on tension (ZDT), compression (ZDC) and tension and compression reinforcement (ZDTC)

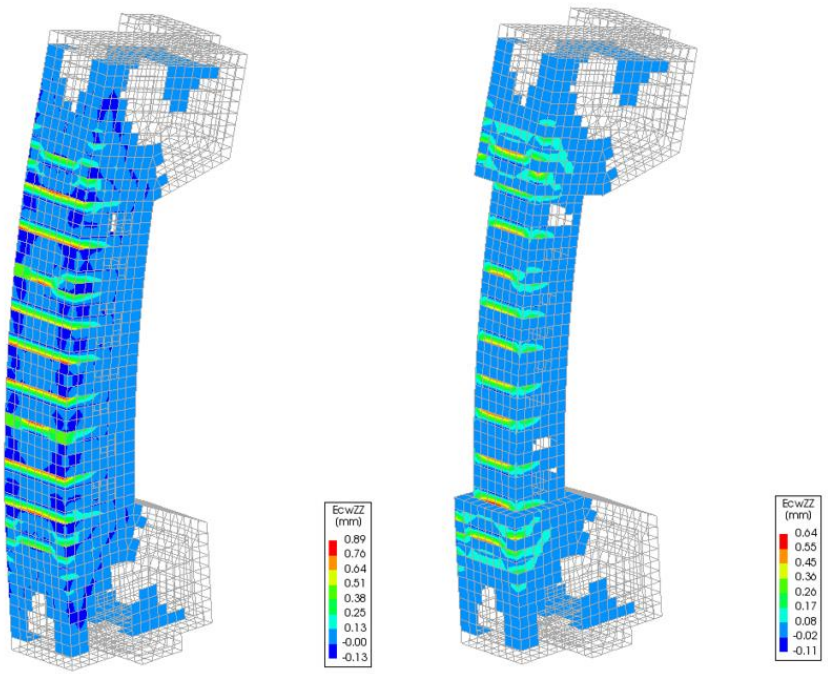

Fig. 6.27: Development of flexural cracks along the tension zone of the concrete cover (left) and core (right) for column ZDC

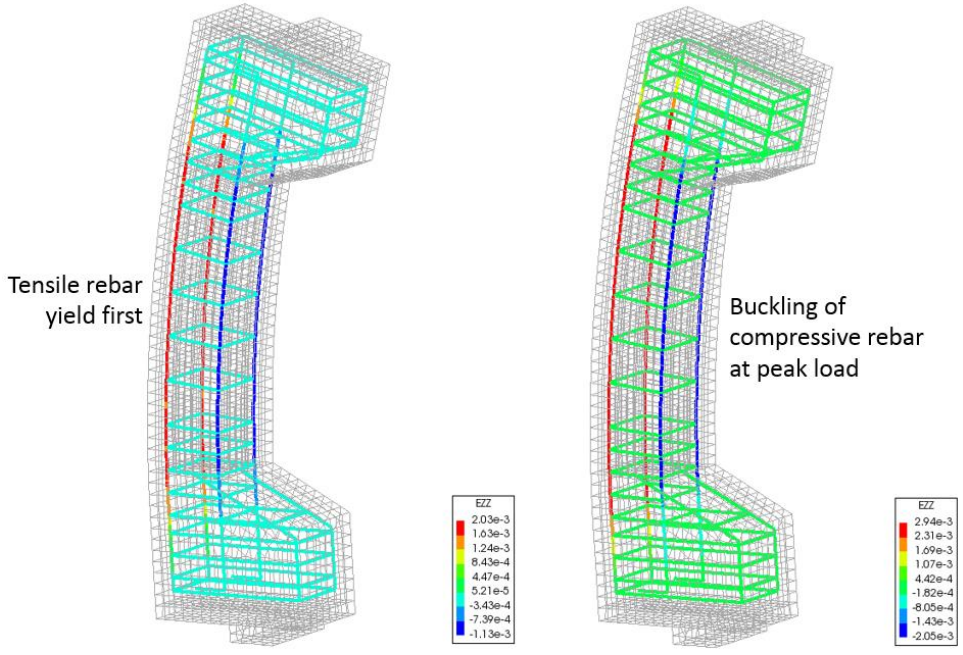

Fig. 6.28: Yielding of the tensile bars and buckling of the compressive bars for column ZDC

6.4 Model Validation with Experimental Tests

The FEM presented in this chapter was validated with the results of the experimentally tested columns presented in Chapters 4 and 5. The model was verified by comparing the axial and flexural performance of the RC columns tested under concentric or eccentric load under different scenarios of exposure (patterns and levels) of reinforcement corrosion, as follows:

- Scenario 1: corrosion on mid-section transverse reinforcement under concentric load, referred to as C-C-T1 and C-C-T2
- Scenario 2: corrosion on mid-section transverse reinforcement and longitudinal rebars, referred to C-C-ALL1 and C-C-ALL2
- Scenario 3: corrosion on mid-section transverse reinforcement under eccentric load, referred to as C-E-T3 and C-E-T4
- Scenario 4: corrosion on longitudinal reinforcement under eccentric load, referred to as C-E-R1 and C-E-R2

Numerical analysis of the experimental tests of columns loaded at zero to low eccentricity values reported in Section 6.3 illustrated that the degradation of the ultimate capacity of the columns due to reinforcement corrosion is primarily influenced by concrete cover cracking and reduction in core concrete confinement effects. Thus, the methodology adopted here in modelling columns in scenarios 1 and 2 was to reduce the compressive strength of the concrete cover due to concrete cover cracking. At the same time, spalled sections of the concrete cover of the tested columns that were observed in the experimental testing were removed in the numerical model. This required an iterative process to precisely capture the crack density (number of cracks within the surface area of the column) observed experimentally. Moreover, reduction in core confinement effects for different corrosion levels was incorporated into the model analysis of scenarios 1 and 2.

On the other hand, for scenarios 3 and 4, the column response under eccentric load is dependent on the sectional loss and ductility degradation of the reinforcement due to corrosion.

The axial and flexural response of the columns due to reinforcement corrosion in the column's middle region was examined. Overall, a good correlation was found between the FEM and the overall response of the tested RC columns.

6.4.1 Concentrically-Loaded Columns

6.4.1.1 Axial Response

This section presents the axial response of the columns expressed as axial load-axial strain under a concentric load. The maximum load, peak strain, post peak response and column stiffness were observed as the level of corrosion was increased for each corrosion scenario, and the results are presented in the following sections.

6.4.1.1.1 Control Specimen (C-C-C)

The FEM shows an excellent prediction of the maximum load (9% difference), post peak response and column stiffness (ascending branch of the slope) for the uncorroded specimen (C-C-C), as shown in Fig. 6.29. Both the FEM and experimental results exhibit a typical ductile response.

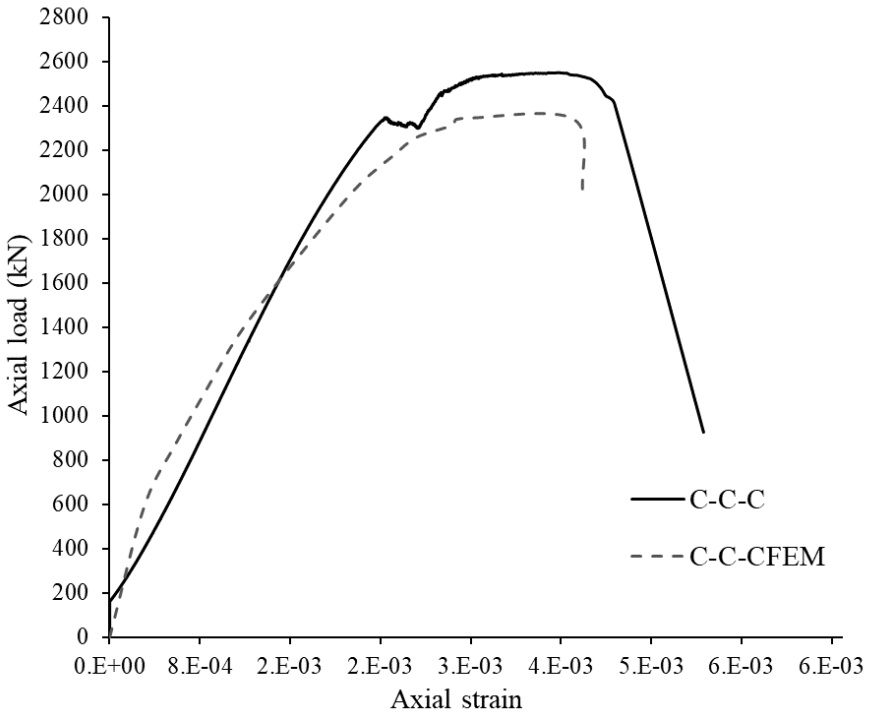

Fig. 6.29: Validation of the FEM with the experimental results for specimen C-C-C, C-C-CFEM

6.4.1.1.2 Scenario 1: C-C-T2 and C-C-T1

Validation of the FEM with the experimental tests results for specimens C-C-T1 and C-C-T2 demonstrate an agreement in the maximum strength, stiffness, and post-peak response, as shown in Fig. 6.30 and Fig. 6.31. The columns demonstrate reduced elongation post-peak (brittle response) compared to the control specimen due to tie corrosion. Furthermore, the compressive stiffness of the column, ascending branch of the load-axial strain curve, is reduced for both C-C-T1 and C-C-T2 compared to the control specimen.

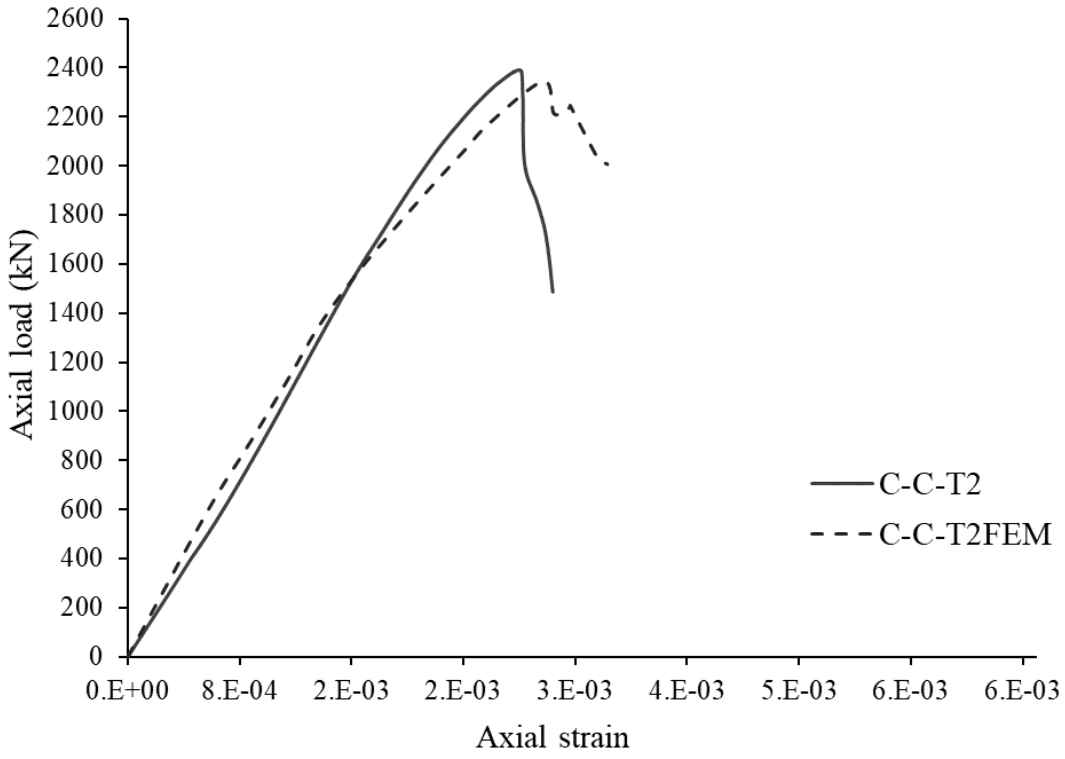

Fig. 6.30: Validation of the FEM with the experimental results for specimen C-C-T2, C-C-T2FEM

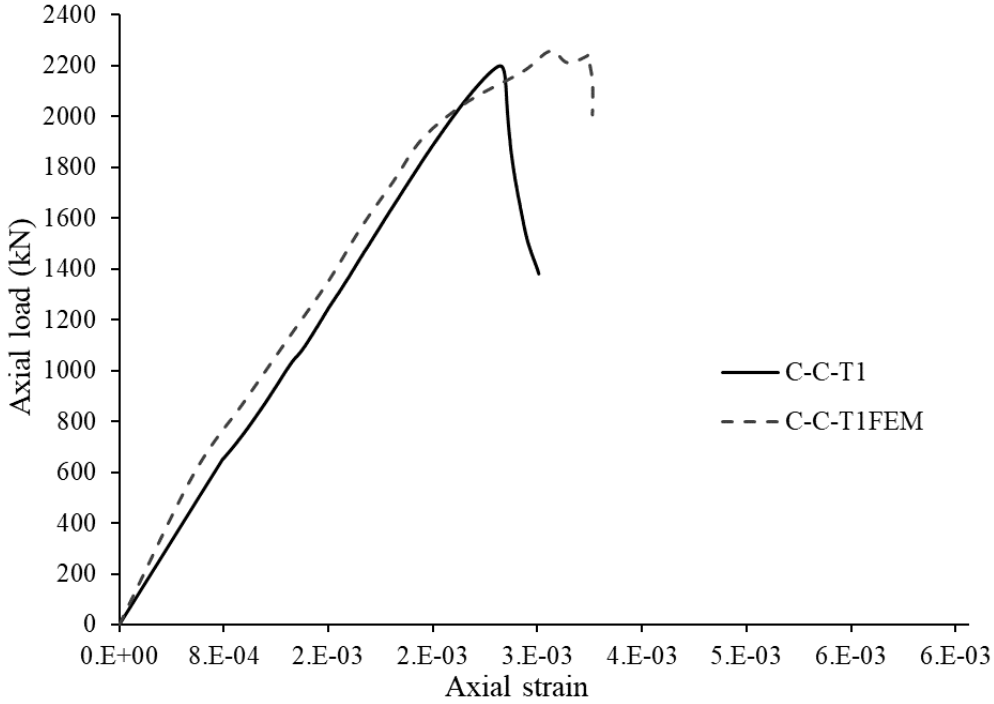

Fig. 6.31: Validation of the FEM with the experimental results for specimen C-C-T1, C-C-T1FEM

6.4.1.1.3 Scenario 2: C-C-All2 and C-C-All1

Fig. 6.32 and Fig. 6.33: show the axial load-axial strain curves for specimens C-C-ALL2 and C-C-ALL1, respectively. Validation results of the FEM with experimental ones illustrates good prediction of the maximum strength, stiffness and post-peak response. The maximum strength is reduced by over 45% from the control specimen due to medium and high level of corrosion of all the reinforcement. Furthermore, the compressive stiffness of the load-axial strain is reduced as the corrosion level increased from scenario 1 to scenario 2. Additionally, the columns exhibit a brittle response.

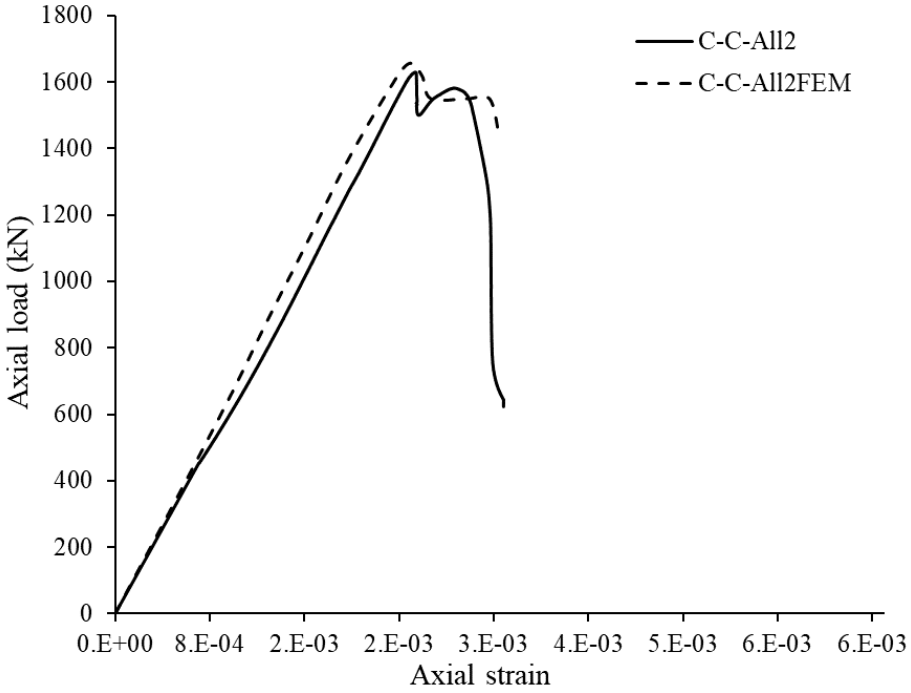

Fig. 6.32: Validation of the FEM with the experimental results for specimen C-C-ALL2, C-C-ALL2FEM

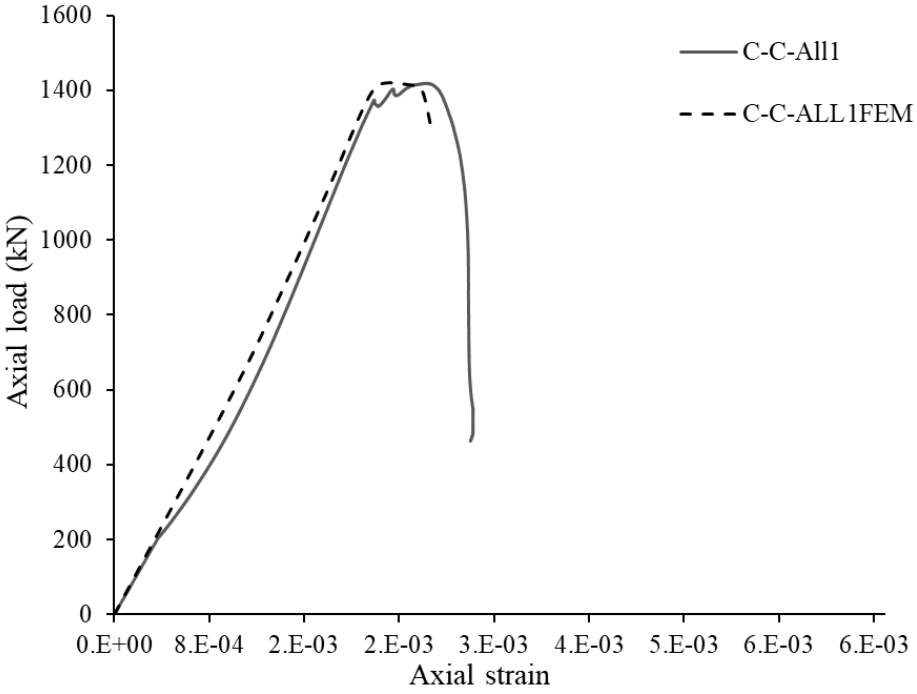

Fig. 6.33:Validation of the FEM with the experimental results for specimen C-C-ALL1, C-C-ALL1FEM

6.4.1.2 Flexural Response

6.4.1.2.1 Control Specimen: C-C-C

The FEM shows a good prediction of the maximum strength (9% difference) for all the columns, although the FEM slightly overestimates the flexural stiffness of the tested columns (Fig. 6.34). The control column exhibits a typical ductile response.

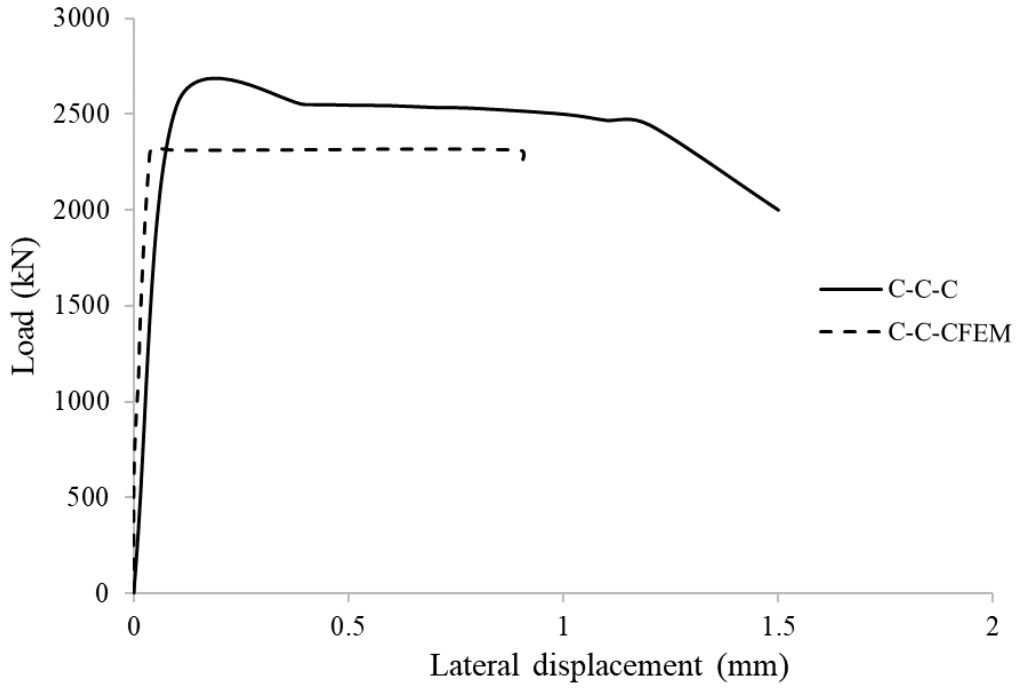

Fig. 6.34: Validation of the FEM with the experimental results for specimen C-C-C, C-C-CFEM

6.4.1.2.2 Scenario 1: C-C-T1 and C-C-T2

The FEM shows a good prediction of the ultimate capacity (0-2% difference) for all the columns, although the FEM significantly overestimates the flexural stiffness of the tested columns (Fig. 6.35). The experimental results display a significant lateral deformation for specimens C-C-T1 and C-C-T2 compared to the FEM.

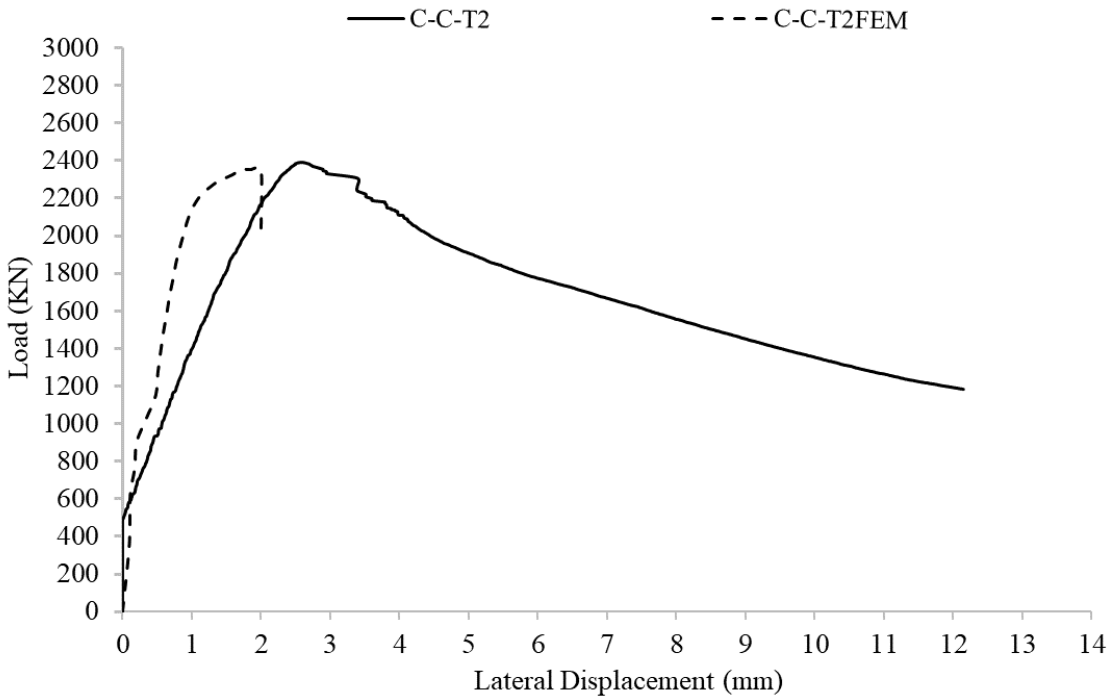

Fig. 6.35: Validation of the FEM with the experimental results for specimen C-C-T2 at zero eccentricity

6.4.1.2.3 Scenario 2: C-C-All1/2

In modelling columns under scenario 2, the compressive strength of the concrete cover of the middle section of the column was reduced between the longitudinal reinforcing bars. At the same time, the corners of the concrete cover were removed entirely along the 700-mm of the mid-region to simulate spalling. The FEM predicts very well the ultimate capacity of the tested columns, as shown in Table 6.2.

The FEM predicts very well the load-bearing capacity of specimen C-C-All2, as illustrated in Fig. 6.36. The column, however, depicts a brittle failure response because the ties were highly corroded in the FEM compared to a medium level of corrosion for the tested column. Similarly, The FEM results capture well the behaviour of column C-C-All1, as shown in Fig. 6.37. The load-displacement curve initiates with microcrack localization in a narrow band and the development of primary macrocracks. The model exhibits a brittle response marked by a sharp drop in load-carrying capacity due to reinforcement buckling on the compression zone. As the reinforcement corrosion level increases from a medium to a high level from specimen C-C-All2 to specimen C-C-All1, respectively, the ultimate capacity is reduced (Fig. 6.36 and Fig. 6.37).

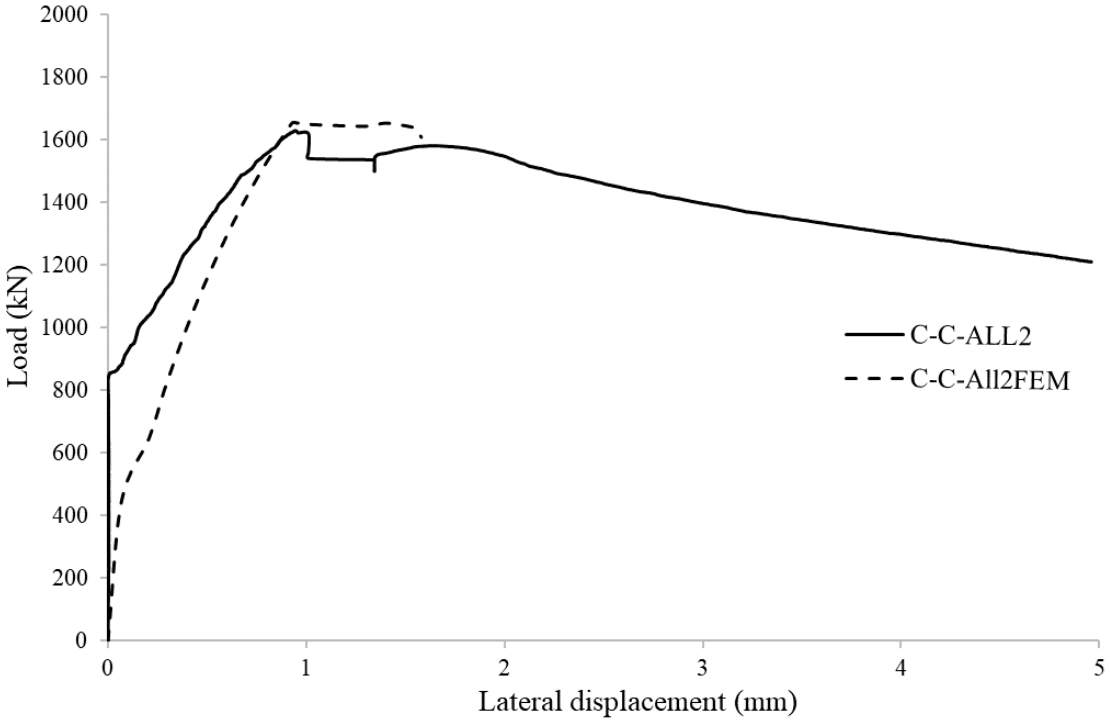

Fig. 6.36: Comparison between the FEM and experimental results for specimen C-C-All2

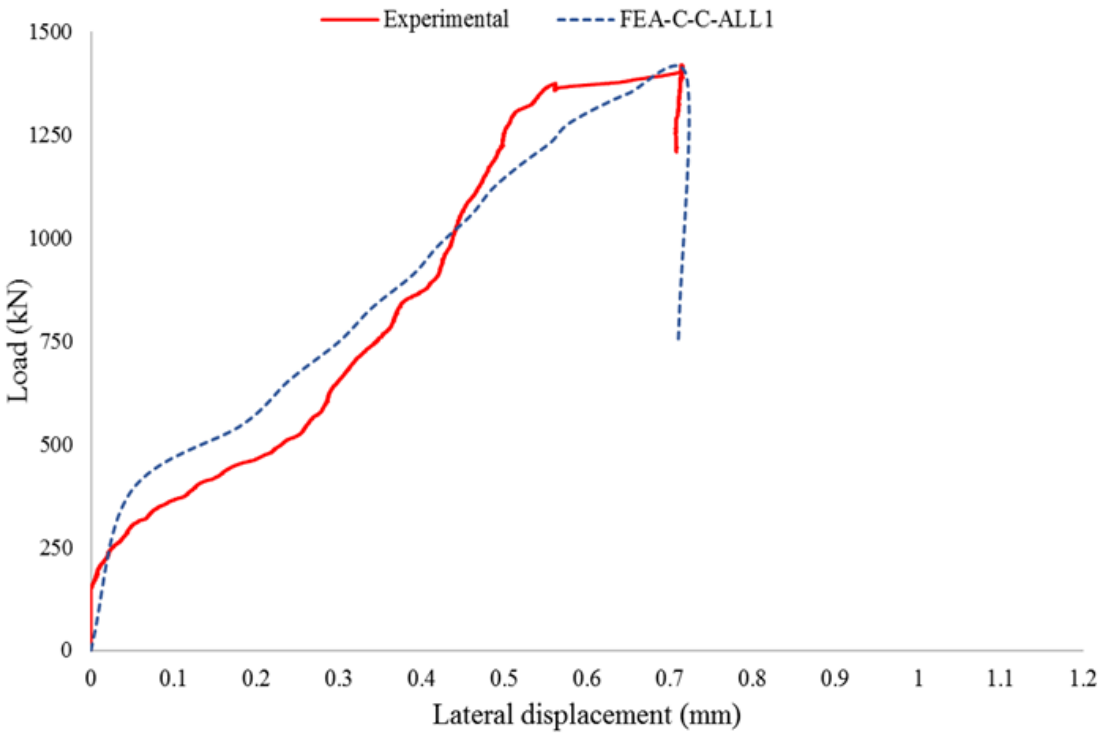

Fig. 6.37:Validation of the FEM with the experimental results for specimen C-C-All1

Table 6.2: Flexural response results of FEM validation with tested columns

Column label	Corrosion level	m_s (%)		$P_{u,exp}$ (kN)	$P_{u(FEM)}$ (kN)	$P_{u(FEM)}/P_{u,exp}$	Potential buckling
		Tie	Rebar				
C-C-C	None	0	0	2,550	2,350	0.92	No
C-C-T2	Low	5	1	2,389	2,350	0.98	No
C-C-T1	Medium	14	5	2,199	2,198	1	Yes
C-C-All2	High	17	20	1,622	1.622	1	No
C-C-All1	Very high	20	26	1,418	1,418	1	Yes
					Avg.	1.01	

6.4.2 Eccentrically-Loaded Columns

Comparison between FEM results with the experimental ones shows that the FEM predicts very well (with a maximum variation of 5%) the ultimate capacity and residual strength degradation due to reinforcement corrosion for each column tested under eccentric load, as illustrated in Fig.

6.39 to Fig. 6.43. Moreover, the model captures well the overall response and failure mechanism of the tested columns. The columns had a steel-controlled failure mechanism characterized by yielding of the reinforcement and development of flexural cracks on the tension zone and crushing the concrete on the compression zone, as shown in Fig. 6.38. Depending on the corrosion level and pattern severity, the longitudinal reinforcement on the compression zone either buckled abruptly or yielded after attaining the ultimate capacity. Moreover, the size (2-3 mm) and spread of flexural cracks along the column span grew wider as the level of corrosion increased compared to the control specimen (Fig. 6.38 and Fig. 6.44). On the other hand, lateral displacement at the mid-section of the column reduced from 25 mm for column C-E-C to 15 mm for column C-E-R2. This is attributed to loss of ductility and bar area of the longitudinal reinforcement, subsequently reducing the load carrying capacity and lateral displacement. Table 6.3 shows the results of the finite element analysis compared with experimental results for the control column and columns exposed to different levels of reinforcement corrosion.

Table 6.3: Results of FEM validation with columns tested under eccentric loads

Column	level	m_s (%)		$P_{U,exp}$ kN	$P_{Y(FEM)}$ (kN)	$P_{U(FEM)}$ (kN)	FEM (%)	$P_{U(FEM)}/P_{U,exp}$	Rebar Buckling	Δ_{m-Exp} (mm)	Δ_{m-FEM} (mm)	$\Delta_{mFEM/Exp}$
		Tie	Rebar									
C-E-C	None	0	0	461	443	461	100	1.00	No	25.0	24.0	0.96
C-E-T4	Low	4	4	461	440	461	100	1.00	No	21.0	20.4	0.97
C-E-T3	Medium	7	4	414	350	435	94	1.11	No	21.0	20.5	0.98
C-E-R2	Medium	15	12	369	272	356	77	0.96	No	15.1	15.6	1.03
C-E-R1	High	15	23	342	221	330	72	0.96	No	14.8	15.8	1.07
FEM %: ratio of corroded to uncorroded value, Δ_{m} Lateral displacement at middle span							Avg.	1.01			Avg.	1.00

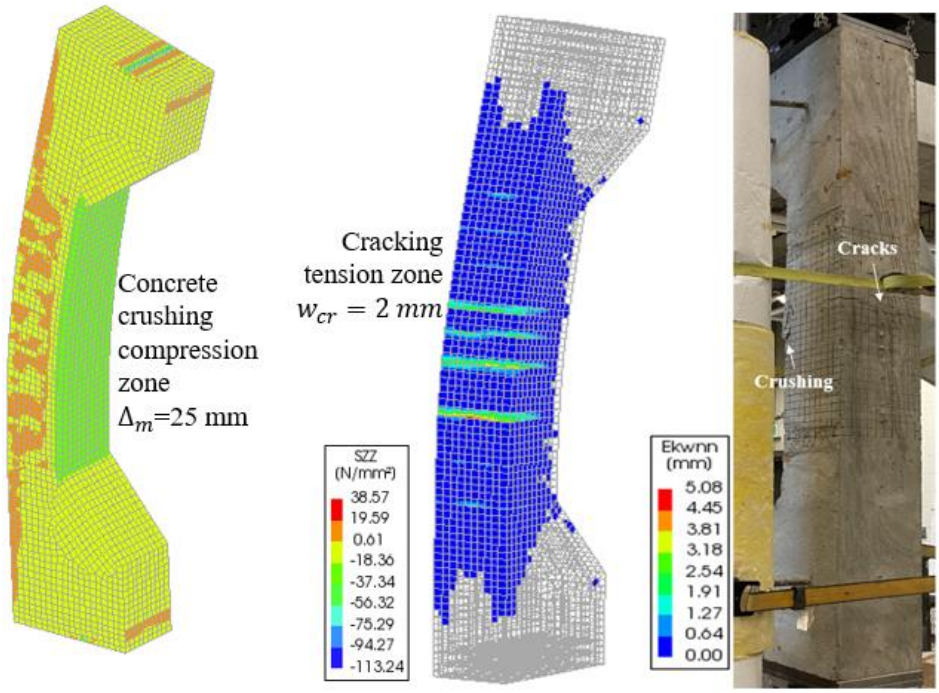

Fig. 6.38:Steel controlled failure for eccentrically-loaded control column C-E-C

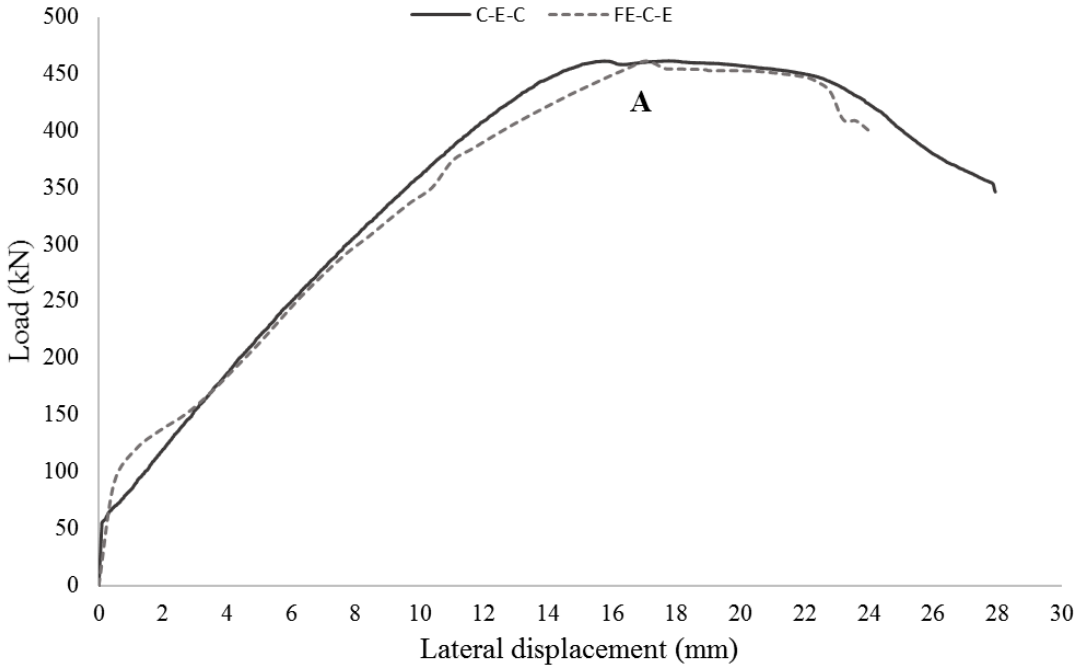

Fig. 6.39: Validation of the FEM with the experimental results of the control specimen C-E-C

6.4.2.1 Scenario 3: C-E-T3 and C-E-T4

The load-displacement curves for columns C-E-T3 and C-E-T4 were initiated by the development of microcracks followed by a linear elastic response along the ascending branch until the ultimate load was reached (Fig. 6.40 and Fig. 6.41: In the experimental testing of column C-E-T4, the top corbel of the column had a localized stress concentration underneath the loading plate before the load was redistributed along the entire column, which led to concrete cover cracking. Subsequently, a reduction in the flexural stiffness of the column is illustrated in Fig. 6.41: For both columns C-E-T3 and C-E-T4, results of the FEM analysis demonstrate yielding of the tensile reinforcement at 80-90% of peak load; then, the compressive reinforcement yielded after ultimate capacity was attained. Furthermore, a reduction in ductility is observed at a low level of corrosion in specimen C-E-T4 compared to the control specimen C-E-C, as shown in Fig. 6.41: As the level of corrosion is increased to a medium level, both the ultimate capacity and ductility are further reduced as depicted in column specimen C-E-T3 (Fig. 6.40 and Table 6.4).

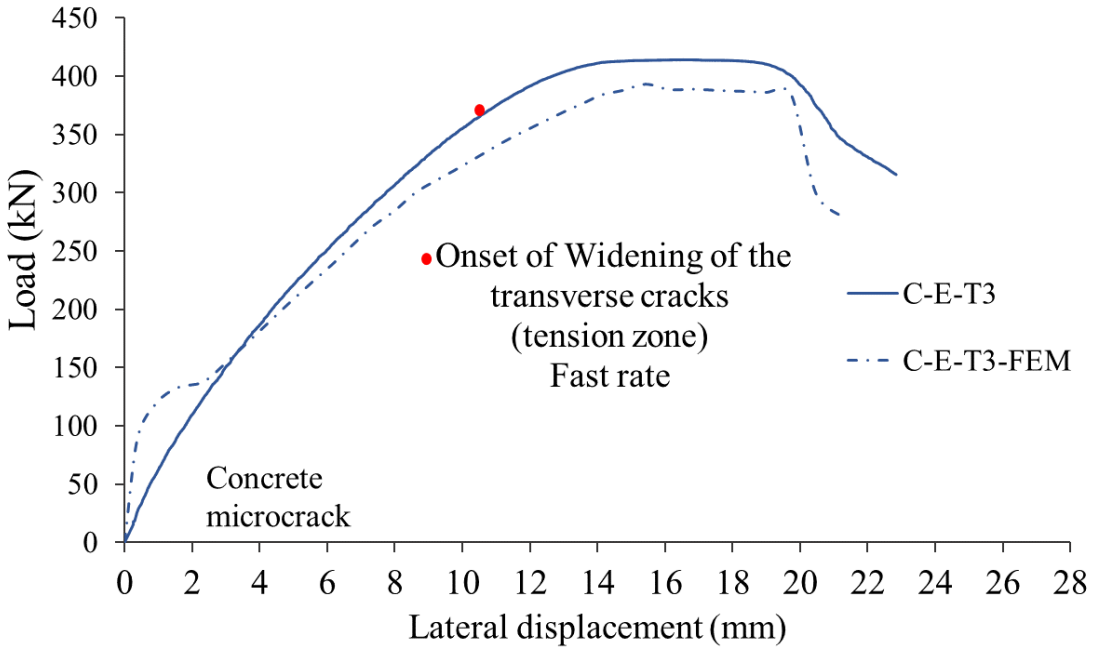

Fig. 6.40: Validation of the FEM with the experimental results for specimens C-E-T3

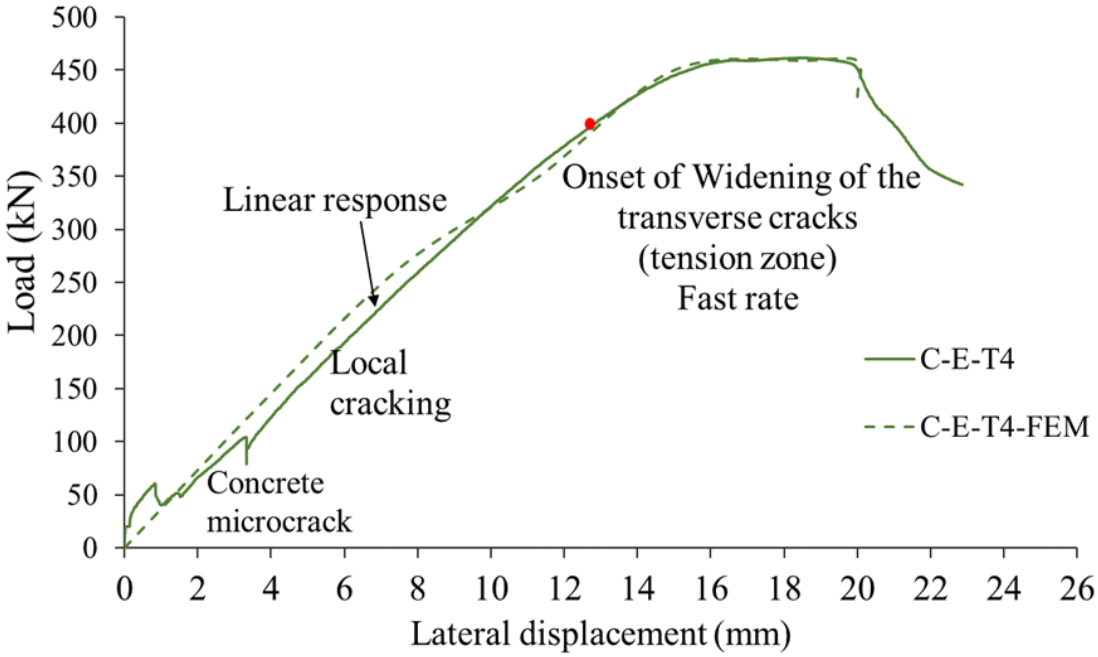

Fig. 6.41: Validation of the FEM with the experimental results for specimens C-E-T4

6.4.2.2 Scenario 4: C-E-R1 and C-E-R2

The FE results predict very well the ultimate capacity and post-peak response of columns whose longitudinal reinforcement was corroded, as illustrated in Fig. 6.42 and Fig. 6.43. However, the model does not capture the columns' nonlinear response observed prior to peak load attainment. This response is attributed to the brittle nature of the medium-to-highly corroded longitudinal bars. In both experimental and numerical results, the compressive bars did not buckle. This is because the ties effectively provided sufficient restraining to support the longitudinal bars. From observing the results of the FE analysis for columns C-E-R1 and C-E-R2, it is noted that the tensile reinforcement yielded at 65-70% respectively of peak load, followed by the compressive reinforcement's yield after ultimate capacity is reached (Fig. 6.42 and Fig. 6.43). Columns C-E-R2 and C-E-R1 had a medium and high level of longitudinal reinforcement corrosion, respectively, showed no sign of tie fracture, and the longitudinal reinforcement did not buckle. After C-E-R2 failure, the maximum crack width reported numerically is 1.5 -3.3 mm at the tension zone of the column mid-span (Fig. 6.44).

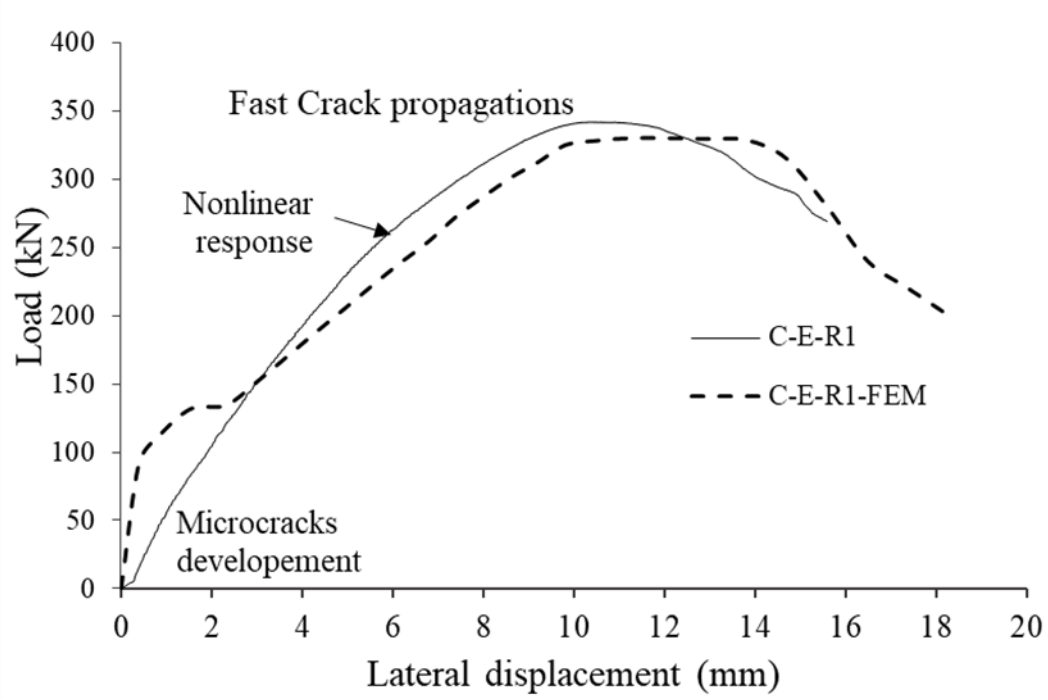

Fig. 6.42: Validation of the FEM with the experimental results for specimen C-E-R1

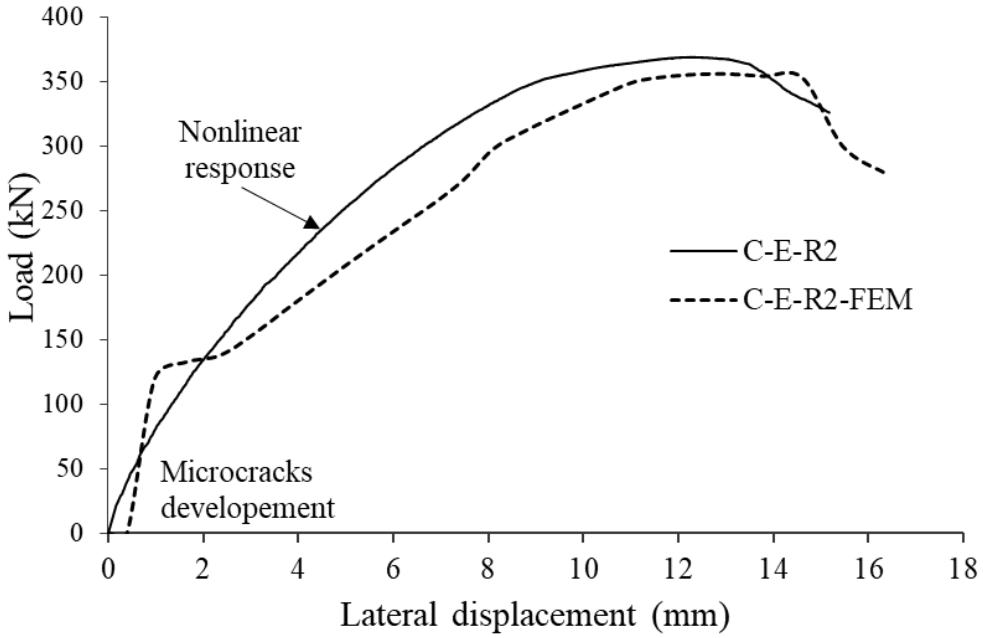

Fig. 6.43: Validation of the FEM with the experimental results for specimen C-E-R2

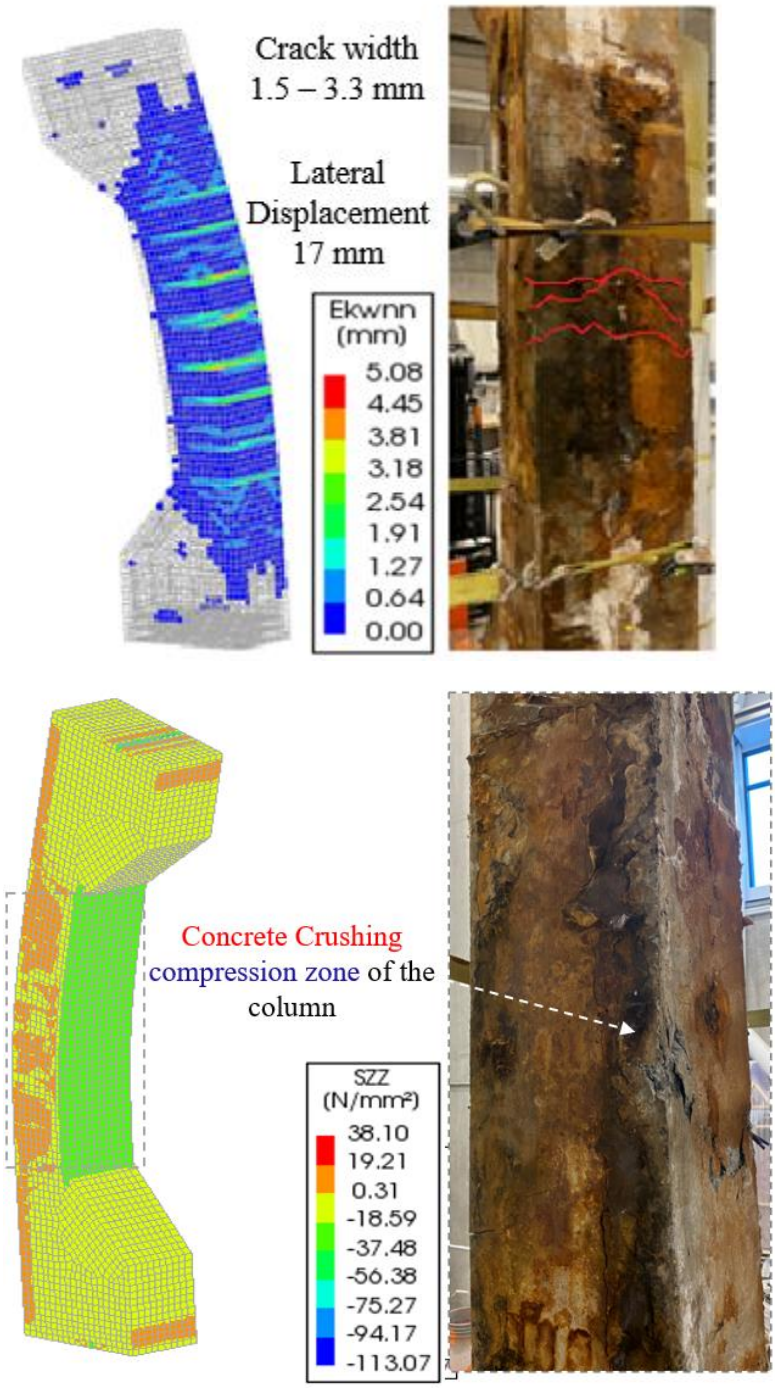

Fig. 6.44: FEM steel-controlled response for column C-E-R2 marked by crack growth along the tension zone

Experimental test results showed that the rebar ribs at the cover interface were eroded, and the area's circumference was reduced for high levels of corrosion. As a result, the contact area between concrete and steel was reduced, which increased the potential risk of slippage due to bond loss. This can be illustrated from the FEM results in Fig. 6.45; for example, for C-E-R1, the longitudinal reinforcement on the tension side underwent a large relative displacement (slip) through the surrounding concrete. As a result, the corresponding bond stresses increased with the increase of the applied loads. Then, a sharp decrease in the local bond stress occurred as the deformed tensile rebar yielded.

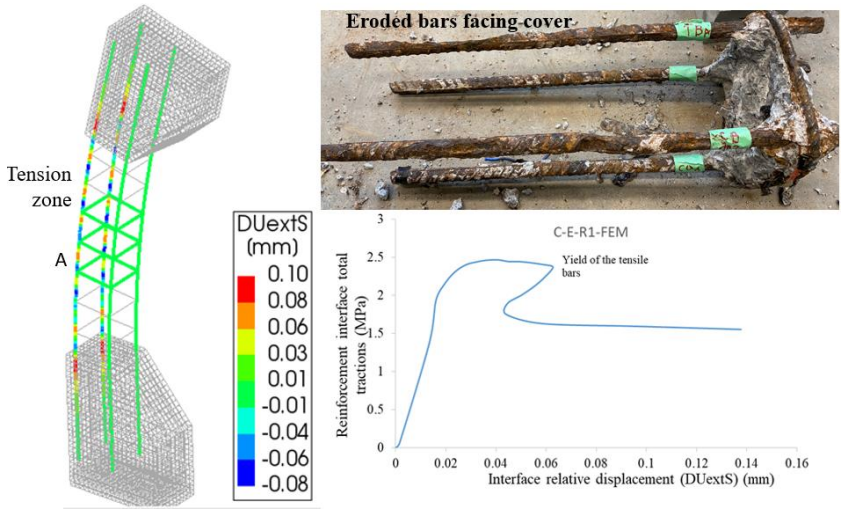

Fig. 6.45: Local (point A) bond-slip of tensile reinforcement

6.5 Parametric Investigation

A parametric investigation using the FEM was conducted to examine the effect of different levels and patterns of reinforcement corrosion beyond those tested in the present experimental program on the ultimate capacity of columns subjected to eccentric axial loading. In addition to the analyses conducted on specimens experimentally tested in this study, the FEA was extended to specimens with a high level of corrosion on the ties (cases C-C-T3 and C-E-T5) and a medium to very high level of corrosion on the longitudinal reinforcement (cases C-E-R3, C-E-R4 and C-E-R5), as tabulated in Table 6.4.

Fig. 6.46 displays the numerical results of the applied load-lateral displacement response of all analyzed columns under eccentric axial loads and subjected to different corrosion patterns and

levels. The FEM results for the case with a very high level of tie corrosion under concentric loading (column C-C-T3) displayed a residual strength of 89%, and failure was abrupt due to longitudinal reinforcing bar buckling. The FEM results illustrate that for the noncorroded column (C-E-C) and low tie corrosion levels columns (C-E-T3 and C-E-T4) under eccentric axial loading the failure was steel-controlled characterized by yielding of the reinforcement on the tension zone and crushing of the concrete on the compression zone. Depending on the severity of corrosion level and pattern, the longitudinal reinforcement on the compression zone either buckled abruptly or yielded after attaining the ultimate load capacity.

Results of the FE models for low to medium levels of corrosion for specimens C-E-T3 and C-E-T4 under eccentric load show that the tensile reinforcement yielded at 80-90% of peak load, and the compressive reinforcement yielded after the ultimate column capacity was reached. On the other hand, for a very high level of tie corrosion (C-E-T5), the compressive longitudinal reinforcement buckled abruptly after the peak load was reached due to a significant reduction in confinement effects. Furthermore, a reduction in ductility is observed at a low level of corrosion in specimen C-E-T4 (Fig. 6.46). As the level of corrosion is increased for column C-E-T3, both the ultimate load capacity and ductility are further reduced.

For specimens C-E-R1 and C-E-R2, the tensile reinforcement yielded at 70% of peak load, followed by yielding of the compressive reinforcement after ultimate capacity was reached. With low to medium corrosion levels, these columns showed no sign of tie fracture, and the longitudinal compressive reinforcement did not undergo buckling. The FEM results for a very high level of corrosion of the longitudinal reinforcement in specimen C-E-R5 show that the column maintained a ductile response as depicted in Fig. 6.47, with the residual strength reduced to 55% from that of the control specimen. The FEM results for a very high corrosion level of transverse and longitudinal reinforcement in specimen C-E-R4 illustrate that the residual column strength was further reduced to 48%, and the longitudinal compressive reinforcing bars buckled (Table 6.4). In this case, there is a significant reduction in strength associated with a reduction in core pressure due to pitting fracture of the ties leading to longitudinal compressive bar buckling. For all corrosion scenarios, it was evident that as the level and widespread of reinforcement corrosion increases, the reduction in the load-carrying capacity increases, as illustrated in Fig. 6.47.

Table 6.4: Results for all FEA for columns under concentric and eccentric loadings

Column	Level of corrosion	m_s (%)		$P_{u,exp}$ (kN)	Case	P_u (FEM) (kN)	$P_{u(FEM)}/P_{u,exp}$	Rebar Buckling
		Tie	Rebar					
C-C-C	None	0	0	2,550	Tested	2,350	0.92	No
C-C-T5	Very high	30	0	--	FEM	2,102	--	Yes
C-E-C	None	0	0	461	Tested	461	1.00	No
C-E-T4	Low	4	4	461	Tested	461	1.00	No
C-E-T3	Medium	7	4	414	Tested	435	1.10	No
C-E-T5	Very high	30	0	--	FEM	313	--	Yes
C-E-R3	Medium	0	10	--	FEM	432	--	No
C-E-R2	Medium	15	12	369	Tested	356	0.96	No
C-E-R1	High	15	23	342	Tested	330	0.96	No
C-E-R4	Very high	30	23	--	FEM	222	--	Yes
C-E-R5	Very high	0	30	--	FEM	252	--	No

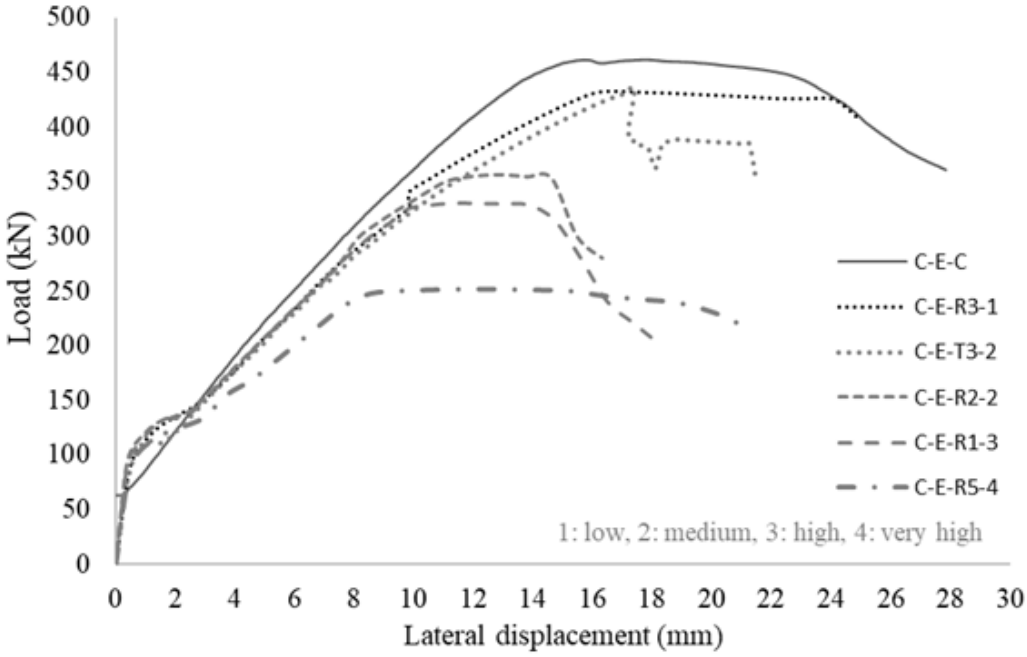

Fig. 6.46: Load-lateral displacement curves of columns under eccentric loads at different corrosion levels

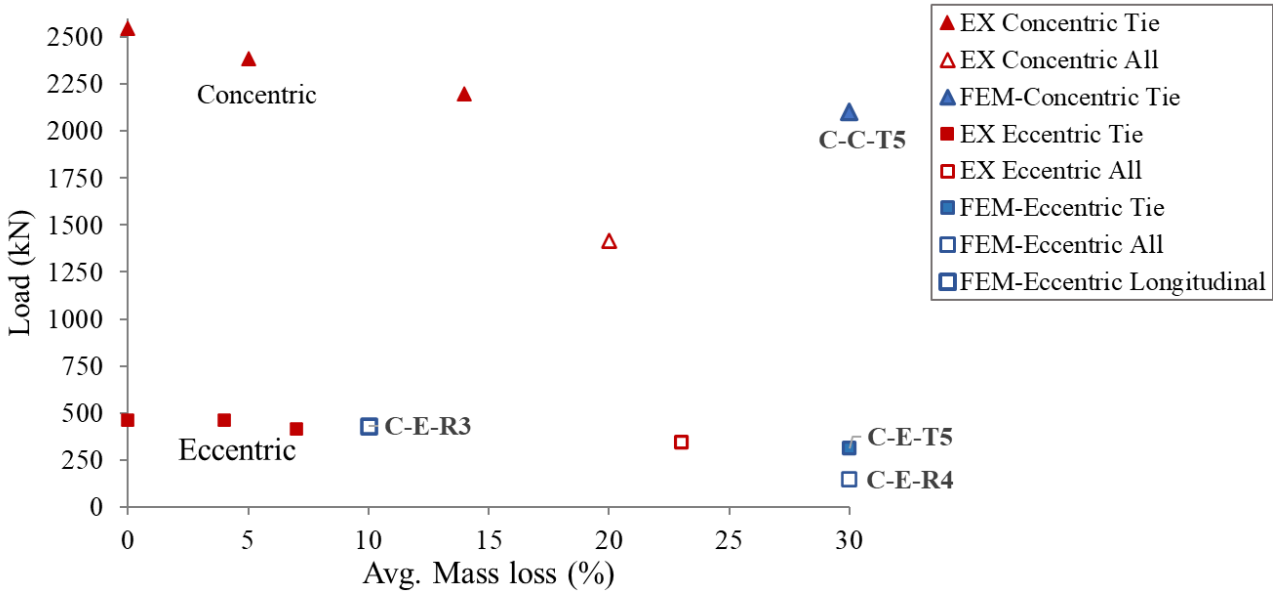

Fig. 6.47: Effect of reinforcement corrosion on the load-carrying capacity of columns under concentric and eccentric loads

6.6 Conclusions

The followings remarks can be concluded from analysing the results of the numerical investigations on the effects of reinforcement corrosion on columns subjected to concentric and eccentric loads:

- The effect of reinforcement corrosion on the structural response of columns was modelled as a change in the mechanical and geometrical properties of concrete and steel materials. This was achieved by integrating constitutive and deteriorating models into the 3D-NLFEM. The model accounts for the bond-slip behaviour between longitudinal bars and concrete (for eccentrically-loaded columns), the confinement of the concrete core and strength reduction of the concrete cover, and the buckling potential of longitudinal reinforcement.
- The validated model was used to conduct a parametric analysis to investigate the effect of several influencing variables such as damage level and patterns and to explore scenarios beyond those tested in a laboratory setting. The FEM provides good correlations with the experimental results. It predicts the peak capacity of all the columns with high accuracy

(with a maximum of 2-11% difference for concentrically-loaded columns and 5% for eccentrically-loaded columns).

- The FEM predicts very well the post-peak response and mode of failure for corroded columns.
- Failure was initiated by yielding of the tensile longitudinal reinforcement at 70% of the peak load for corroded specimens along with a sharp reduction in bond stress. Subsequently, the growth of pre-existing and flexural cracks propagated at a faster rate,
- Reduction in confinement effects (lateral pressure) because of a very high level of tie corrosion (>15%) led to buckling of the longitudinal reinforcement.
- Low levels of tie corrosion affected the post-peak response of the column. At this level of damage, the overall toughness and ductility of the column were reduced.
- As the level of tie corrosion increased to a medium level, the column response shifted to a brittle response, with the axial stiffness and ultimate capacity of the column suddenly decreasing.
- At high levels of reinforcement corrosion, there is a significant reduction in the bearing of the corroded columns. However, it was concluded that corrosion of the transverse reinforcement has a predominant effect on the post-peak response of the column and the reduction in column ductility. In contrast, corrosion of the longitudinal reinforcement has a predominant effect on the reduction of the ultimate capacity.
- In developing the FEM, a high level of tie corrosion was modelled by the complete removal of the affected tie. Experimental findings supported this decision because the ties were very brittle and fractured at a high level of corrosion.
- There is a general trend for both concentrically and eccentrically loaded columns in which the ultimate bearing capacity is reduced as the corrosion level increases from noncorroded to very high corrosion level. Moreover, the corroded columns shift to a brittle response at a low level of tie corrosion for specimens C-C-T1, C-C-T5 and C-E-T3, C-E-T4. Buckling of the longitudinal reinforcement was evident for very high levels of tie corrosion due to loss of confinement effects for specimens C-C-T5 and C-C-All2.

- The size and spread of flexural cracks along the tension zone for eccentrically loaded columns increased from 2 to 3mm for a medium level of corrosion (C-E-R2) compared to a control specimen (C-E-C).
- The analyses provide good insight into the structural performance of corroded columns with different corrosion patterns and levels. Thus, FEM analyses extended to model more corrosion scenarios beyond those experimentally tested.

6.7 References

Akkaya, Y., Guner, S., and Vecchio, F. J. (2019). "Constitutive model for inelastic buckling behaviour of reinforcing bars." ACI Structural Journal, 116(2), 195–204.

Allam, S. M., Shoukry, M. S., Rashad, G. E., and Hassan, A. S. (2013). "Evaluation of tension stiffening effect on the crack width calculation of flexural RC members." Alexandria Engineering Journal, Faculty of Engineering, Alexandria University, 52(2), 163–173.

Alonso, C., Andrade, C., Castellote, M., and Castro, P. (2000). "Chloride threshold values to depassivate reinforcing bars embedded in a standardized OPC mortar." Cement and Concrete Research, 30(7), 1047–1055.

ASTM A370. Standard Test Methods and Definitions for Mechanical Testing of Steel Products. ASTM Int 2020. https://doi.org/10.1136/vr.155.23.739.

Behfarnia, K. (2010). "Studying the effect of freeze and thaw cycles on bond strength of concrete repair materials." Asian Journal of Civil Engineering, 11(2), 165–172.

Blomfors, M., Zandi, K., Lundgren, K., and Coronelli, D. (2018). “Engineering bond model for corroded reinforcement.” Engineering Structures, Elsevier, 156(November 2017), 394–410.

Cairns, J., Plizzari.G.A., Law, D., and Franzoni.C. (2005). "Mechanical properties of corrosion-damaged reinforcement." ACI Materials Journal, 102(4), 256–264.

Cape, M. (1999). "Residual service-life assessment of existing R/C structure." Chalmers University of Technology, Goteborg, Sweden and Milan University of Technology Italy, Erasmus Program, 133.

Coronelli, D., and Gambarova, P. (2004). "Structural Assessment of Corroded Reinforced Concrete Beams: Modelling Guidelines." Journal of Structural Engineering, 130(8), 1214–1224.

Diana FEA. (2020). "Finite element analysis documentation." Diana FEA Bv, Netherlands.

Du, Y. G., Clarkt, L. A., and Chan, A. H. C. (2005). "Effect of corrosion on ductility of reinforcing bars." Magazine of Concrete Research, 57(7), 407–419.

Feenstra, P. H. (1993). "Computational aspects of biaxial stress in plain and reinforced concrete." Delft University Press, The Netherlands.

fib. (2013). fib model code of structures 2010. Lausanne, Switzerland.

Hognestad, E. (1951). "A Study of Combined Bending and Axial Load in Reinforced Concrete Members." Bulletin Series No. 399, 128.

Hordjik, D. (1991). "Local Approach to Fatigue of Concrete." Ph.D. Thesis, Delft University of Technology, Delft, The Netherlands.

JSCE. (2010). "JSCE Guidelines for Concrete No. 15: Standard Specifications for Concrete Structures - 2007 Design." Japan Society of Civil Engineers, Japan.

Lee, H. S., and Cho, Y. S. (2009). "Evaluation of the mechanical properties of steel reinforcement embedded in concrete specimen as a function of the degree of reinforcement corrosion." International Journal of Fracture, 157(1–2), 81–88.

Li, K., and Li, L. (2019). "Crack-altered durability properties and performance of structural concretes." Cement and Concrete Research, 124(January), 1–11.

Lim, J. C., and Ozbakkaloglu, T. (2014). "Confinement Model for FRP-Confined High-Strength Concrete." Journal of Composites for Construction, 18(4), 04013058.

Mathisen, K. M. (2012). "(PPT) Solution Methods for Nonlinear Finite Element Analysis (NFEA)." Lecture, 11, 39.

Razvi, S., and Saatcioglu, M. (1999). "Confinement model for high-strength concrete." Journal of Structural Engineering, 125(3), 281–289.

Rodriguez, J., Ortega, L. M., and Casal, J. (1996). "Load-bearing capacity of concrete columns with corroded reinforcement." Corrosion of reinforcement in concrete construction. proceedings of fourth international symposium, Cambridge, 1-4 July 1996. special publication no 183, 220–230.

Shima, H., Chou, L. L., and Okamura, H. (1987). "Micro and macro models for bond in reinforced concrete." Journal of the Faculty of Engineering, University of Tokyo, Series B.

Thorenfeldt, E., Tomaszewicz, A., and Jensen, J. (1987). "Mechanical properties of HSC and application in design." Symposium on Utilization of High-Strength Concrete, Stavanger, Norway, 149–159.

Vecchio, F. J., and Collins, M. P. (1986). "Modified compression-field theory for reinforced concrete elements subjected to shear." Journal of the American Concrete Institute, 83(2), 219–231.

Wang, X.-H., Liu, X.-L., and Deng, B.-R. (2012). "Effects of length and location of steel corrosion on the behaviour and load capacity of reinforced concrete columns." Journal of Shanghai Jiaotong University (Science), 17(4), 391–400.

Wang, X. H., and Liang, F. Y. (2008). "Performance of RC columns with partial length corrosion." Nuclear Engineering and Design, 238(12), 3194–3202.

Chapter 7 Analytical Assessment Procedures of Corroded RC Columns

7.1 Abstract

A practical approach is proposed to the engineering community to evaluate the residual load-bearing capacity of reinforced concrete columns subjected to reinforcement corrosion. The analytical approach is established from sectional analysis and the experimental testing and numerical analyses of ten reinforced concrete columns subjected to quasi-static concentric and eccentric loads. Eight of the columns were subjected to different patterns of accelerated reinforcement corrosion for 137-days. Three-dimensional finite element analyses were conducted to investigate more corrosion scenarios beyond those experimentally tested. The presented approach accounts for material deteriorations (strength, cross-sectional area, bond, and confinement effects) using constitutive models and incorporates data from experimental testing (damage level from crack development). The analytical estimation compares well with experimental and numerical results and may provide a practical tool of assessment for practicing engineers.

Keywords: Structural assessment, experimental investigation, numerical modelling, RC corroded columns

7.2 Introduction

Reinforcement corrosion coupled with growth in traffic volume, higher loads, potential inadequate design or improper installation during construction decrease the service life of ageing bridges. Statistics Canada (Statistics Canada 2018) and the Canada Infrastructure Report Card (Canada Infrastructure Report Card 2019) have estimated that 40% of Canadian highway bridges are 80 years old. Moreover, 40% of these bridges have deteriorated and are currently in very/poor to fair condition (Canada Infrastructure Report Card 2019). Over time, the premature deterioration of reinforced concrete (RC) bridges due to reinforcement corrosion leads to concrete cover cracking and spalling/delamination, loss of bond between reinforcement and concrete, and reduction in the structural capacity and ductility of the structure. The Champlain Bridge in Montreal city in QC,

built in 1962, was recently decommissioned in 2019 due to extensive deterioration of its elements; chloride-induced reinforcement corrosion due to de-icing exposure was one of the main deterioration mechanisms observed (The Jacques Cartier and Champlain Bridges Incorporated (JCCBI). 2018).

The commentary on the Canadian Highway Bridge Design Code (CSA 2019; CSA 2019) addressed the need to develop a detailed quantitative evaluation approach for practicing engineers to assess the condition of deteriorated bridges vulnerable to environmental elements. Evaluation procedures should be conducted according to ULS and SLS where applicable to determine a suitable safety level for the bridge (CSA 2019). Moreover, it is essential to regularly inspect signs of deterioration visually and to use NDT procedures when necessary (CSA 2019).

Several authors have proposed analytical models to estimate the axial load capacity of columns (Rodriguez et al. 1996; Tapan and Aboutaha 2008, 2011; Campione et al. 2017). Rodriguez et al. (1996) calculated the axial force of RC columns tested using conventional sectional models. The cross-sectional area of the steel was reduced, while the concrete cover was removed on one side or all sides to account for corrosion-induced delamination. The authors developed four axial load-moment curves that consider: non-deteriorated case, removal of two or three ties, and complete removal of concrete on all sides. It was found that the structural behaviour of the analysed columns (eccentricity values of 0 and 20 mm) is mainly controlled by: concrete cover degradation, increased load eccentricities due to irregular damage associated with reinforcement corrosion, and premature buckling of longitudinal reinforcing steel.

Tapan and Aboutaha (2008, 2011) investigated the effect of reinforcement corrosion and loss of concrete cover on the structural response of RC columns using interaction diagrams. Six different cases of reinforcement corrosion patterns with different corrosion levels were investigated for a concrete cover-to-rebar diameter ratio of 1. This was established using a modified analytical approach. The authors proposed a modified procedure to calculate interaction diagrams by considering material degradation in concrete and steel due to section and bond loss and damage asymmetry. A bilinear stress-strain curve for corroded reinforcement was used, taking into account the strength reduction of the reinforcement. Tapan and Aboutaha (2008) did not consider the softening effect of the core of the concrete.

Campione et al. (2017) proposed a simple analytical model to estimate the moment-axial force interaction diagrams for corroded columns. The model considers material deterioration, concrete cover spalling, loss of bond, rebar buckling, and reduction in confinement effects due to tie corrosion. The model accounts for the reduction in confinement effects, bond loss and potential buckling of the reinforcement.

Currently, there is no standard methodology for the engineering community to evaluate the residual capacity of corroded RC columns. Design procedures used for the evaluation of RC columns overestimate the actual load-bearing capacity of deteriorated columns because they do not consider corrosion effects on the material, geometrical and ductility degradations. Hence, there is a need to establish a practical assessment approach that incorporates field observations and inspections with analytical assessment procedures to determine the residual capacity of corroded columns. Moreover, it is essential to account for material degradation and reduction in the structural performance of columns due to reinforcement corrosion.

This paper proposes a simplified approach to determine the residual load-bearing capacity of corroded columns, considering cover cracking, reduction in confinement effects of the core concrete, potential buckling of the longitudinal bars and bond loss for both concentrically and eccentrically loaded columns. This approach is established based on sectional analysis and the results of experimental testing and numerical analyses of ten columns subjected to concentric and eccentric loadings. Eight of the columns were exposed to different patterns of reinforcement corrosion (ties only, longitudinal bars only, and all the reinforcement cage) after 137-days of accelerated corrosion. The experimental program was extended by conducting three-dimensional nonlinear finite element analyses of corrosion scenarios beyond those tested experimentally. The analytical procedure can predict the residual capacity of corroded columns well when validated with both experimental and numerical analyses.

7.3 Evaluation of the Residual Capacity of Corroded RC Columns

In practical engineering design applications, the nominal axial load-carrying capacity of non-corroded RC columns is evaluated according to procedures similar to those outlined in CAN/ CSA A23.3 (CSA 2019). The axial capacity (P_c) of an undamaged RC column is estimated by summing the strength contributions of both concrete and steel reinforcement.

$$P_c = \alpha \cdot f_c A_g + f_y A_s \quad \text{Eq. 7.1}$$

where α is assumed 0.8 (equivalent stress block), f_c is the concrete compressive strength, A_g is the gross concrete area, f_y is the yield strength of the longitudinal bars, and A_s is the area of the longitudinal bars

Conventional sectional analysis is established based on stress-strain relationships, strain compatibility and equilibrium equations to estimate the axial and flexural capacity of the column. The primary assumption of this analysis is that there is a perfect bond response between concrete and steel implying strain compatibility (CSA 2019). However, for corroded columns, the bond between the concrete and steel significantly deteriorates as the level of corrosion increases along the reinforcement. Moreover, the accumulation of rust products around the reinforcing steel creates expansive forces against the concrete that lead to radial splitting cracks through the concrete cover. As corrosion-induced cracks increase, the bond strength significantly decreases (Almusallam et al. 1996; Apostolopoulos and Koulouris 2020).

Experimental results carried out by the authors (Dabas 2022) indicate that corroded columns fail prematurely before attaining the ultimate load-bearing capacity estimated through conventional methods. This indicates that conventional equation used for non-corroded columns cannot safely predict (as it overestimates) the actual axial capacity of corroded columns. Moreover, experimental results on the structural performance of corroded columns demonstrate that the columns' residual capacity is primarily affected by a reduction in concrete cover due to spalling and cracking, reduction in core strength due to cracking and loss of restraining effects provided by the ties, reduction in cross-sectional area and ductility of reinforcing steel, and bond loss between the steel and concrete (Dabas 2022). Therefore, to estimate the residual load capacity for statically loaded columns subjected to reinforcement corrosion, Eq. 7.1 is modified by incorporating available deteriorating models pertaining to reinforcement corrosion and collected data obtained from field investigations.

The modified ultimate capacity (P_c^{corr}) of the corroded column subjected to concentric loads is modified to reflect the corrosion effects as follows:

$$P_c^{corr} = \alpha \cdot \left(f_{cr-cover}(A_{cover}) + f_{core}(A_{core})\right) + f_y A_{sc} \quad \text{Eq. 7.2}$$

where A_{cover} the cross-sectional area of the concrete cover, A_{core} the cross-sectional area of the concrete core, $f_{cr-cover}$is the reduced compressive strength of the concrete cover, f_{core} is the compressive strength of the concrete core, and f_y and A_{sc} are respectively the yield strength and the cross-sectional area of the corroded reinforcement.

For eccentrically loaded columns, the reduction in bond strength of the tensile longitudinal reinforcement due to reinforcement corrosion is accounted for by using a reduction factor γ, which represents the ratio of the corroded bond strength to the non-corroded bond strength for different levels of corrosion. Thus, the nominal axial capacity of a corroded column subjected to reinforcement corrosion becomes:

$$P_c^{corr} = \alpha(f_{cr-cover}(A_{cover}) + f_{core}(A_{core})) + \gamma f_y A_{sc} \quad \text{Eq. 7.3}$$

Basic assumptions are made in this estimation:

- Strain distribution varies linearly over the depth of the cross section satisfying plane section assumption where the maximum concrete strain is 0.0035.
- An equivalent concrete stress block is assumed from the parabolic compressive stress-strain curve,
- The stress-strain response of the reinforcement is simplified into a bilinear elastic-plastic relationship, as follows.

$$f_s = \begin{cases} \varepsilon_s E_s, & \varepsilon_s \le \varepsilon_{sy} \\ f_y, & \varepsilon_s > \varepsilon_{sy} \end{cases} \quad \textit{Eq. 7.4}$$

where $\varepsilon_s, f_s, \varepsilon_{sy}, f_y$ are the steel strain, the steel stress, the strain at yield, and the yielding stress, respectively,

- Axial and flexural capacities are estimated according to conventional mechanics and equilibrium equations,

The models used to account for corrosion-induced damage in Eq. (7.3) are detailed in the following subsections.

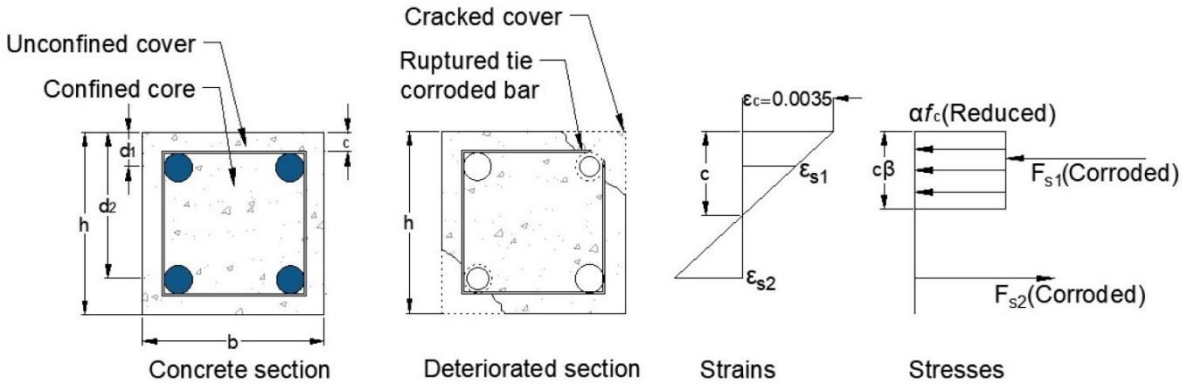

Fig. 7.1: Stress and strains distributions for corroded sections

7.3.1 Reduction in the Compressive Strength of Concrete Cover

Rust that results from corrosion of the reinforcing steel accumulates around the reinforcement and expands as a result of its lower density (Cairns et al. 2005). The pressure build-up from rust expansion causes concrete cracking. Reduction in compressive strength of the concrete cover due to corrosion-induced cracking $f_{cr\text{-}cover}$ is estimated according to Vecchio and Collins model (Vecchio and Collins 1986), later modified by Cape (1999), i.e.,

$$f_{cr-cover} = \frac{f_c}{1+K\left(\frac{\varepsilon_t}{\varepsilon_{co}}\right)} \qquad \textit{Eq. 7.5}$$

where f_c is the compressive strength of the concrete, K is a coefficient based on material roughness and diameter (0.1 for ribbed bars (Cape 1999)), ε_t is the average smeared tensile strain in cracked concrete, and ε_{co} is the strain at the maximum compressive stress (0.002 for normal strength and weight concrete). The concrete average tensile strain (ε_t) resulting from the accumulation of corrosion products is estimated from experimentally-measured crack widths of affected members according to (Coronelli and Gambarova 2004):

$$\varepsilon_t = \frac{b_f - b}{b} = \frac{n_{bars}.w_{cr}}{b} \qquad \textit{Eq. 7.6}$$

where b is the original uncracked cross-sectional width, b_f is the cracked cross-sectional width, n is the number of bars for one side, and w_{cr} is the total crack width. The total width of cracks can be estimated from on-site crack width measurements according to $w_{cr} = \sum w_{cr} l_i / L$,where L is the total length of the affected section, and l_i is the length of each crack.

7.3.2 Reduction in Core Confinement Strength

Corroded ties are less effective in confining and inhibiting crack growth through the core as corrosion level increases. At high corrosion levels, pitting corrosion leads to tie fracture; subsequently, the spacing between adjacent ties changes. The effects of corrosion on the restraining capabilities of the transverse reinforcement are incorporated using a model proposed by Razvi and Saatcioglu (Razvi, S., and Saatcioglu 1999). This model is applicable to normal and high strength concretes (30 to 130 MPa) and different section layouts (rectilinear and spiral). The confined compressive strength f_{cc} (MPa) is defined as:

$$f_{cc} = f_c + k_1 f_{le} \qquad \textit{Eq. 7.7}$$

where f_c is the unconfined compressive strength (MPa), and k_1 is given by:

$$k_1 = 6.7(f_{le})^{-0.17} \qquad \textit{Eq. 7.8}$$

where f_{le} is the equivalent uniform pressure resulting from confinement, and it is estimated as follows:

$$f_{le} = 0.15\sqrt{\left(\frac{b_c}{s}\right)\left(\frac{b_c}{s_1}\right)}\left(\frac{\sum_{i=1}^{q} A_{stcorr} f_y sin\theta}{sb_c}\right) \qquad \textit{Eq. 7.9}$$

where s_1 is the spacing of the longitudinal reinforcement, sb_c is the core surface area, q is the number of tie legs, f_y is the tie yield strength, A_{stcorr} is the reduced tie area, and θ is the angle between the leg of transverse reinforcement and core side crossed by the same leg.

7.3.3 Reduction in Reinforcement Area and Mechanical Properties

Pitting corrosion, a severe form of localized corrosion leads to irregular area loss and a significant reduction in bar ductility (Cairns et al. 2005). This adversely affects the structural behaviour of RC columns. In this evaluation, the reduction in the cross-sectional area (A_{sc}) of the rebar is calculated as a function of the penetration attack according to CONTECVET (2001):

$$A_{sc} = \pi(r_0 - P_x)^2 \qquad \textit{Eq. 7.10}$$

where r_0 is the uncorroded radius, and P_x is the attack penetration. The attack penetration (P_x) is a function of corrosion rate and time (CONTECVET 2001):

$$P_x = 0.0116 \cdot i_{corr} \cdot t \qquad \textit{Eq. 7.11}$$

where P_x is the reduction in the bar radius in mm (assuming uniform corrosion), i_{corr} is the current density in μA/cm^2 estimated from periodic measurements of the corrosion rate over a year to account for extreme climatic conditions (dry/wet winter, summer, spring), and *t* is the time in years after corrosion started. Equation (7.11) assumes that the corrosion rate (or current density) has remained constant since the onset of corrosion up to the evaluation time.

The percentage of mass loss (corrosion level) based on the reduction of reinforcement bar radius is expressed as follows:

$$Ms(\%) = \left(1 - \frac{(r_0 - P_x)^2}{r_0^2}\right).100 \qquad \textit{Eq. 7.12}$$

Cairns et al. (2005) proposed an empirical equation to estimate the ultimate elongation of corroded bars based on cross-sectional loss.

$$\varepsilon_u = (1 - 0.03(Q_s))\varepsilon_0 \qquad \textit{Eq. 7.13}$$

where Q_s, ε_u are the average cross-sectional loss and strain of the corroded reinforcement, and ε_0 is the ultimate strain of the non-corroded reinforcement

For reinforcement under compression, the potential risk of elastic buckling is estimated according to Euler's load. From experimental work (Dabas 2022), it has been observed that rebar buckling occurs locally between two consecutive ties affected by corrosion. Hence, in determining the critical buckling load of the corroded compressive longitudinal bars the unsupported length is based on the spacing of the ties. The spacing between ties increases when the ties are fractured or their stiffness is reduced due to corrosion. Thus, the potential risk of buckling for reinforcement under compression increases before the bars reach their yield strength.

7.3.4 Bond Loss

The volumetric expansion of the rust products induces cracks in the concrete cover and weakens the bond between the reinforcement and concrete. Further increase in corrosion levels erodes the ribs of the deformed bars reducing both frictional and bearing forces. This increases the risk of longitudinal bar slippage leading to an overall reduction in column ductility and ultimate capacity at high levels of corrosion.

In the non-corroded region, a sufficient force transfer (bond) exists between the concrete and steel materials. The amount of bar slippage is assumed small compared to the corroded region; thus, the effective bond force on the bar is in equilibrium with the tensile force of the bar ($F_{eb} = F_{s,max} = f_y A_s$). The "effective" bond force of the reinforcing bar F_{eb} is estimated assuming a uniformly distributed bond stress along the bar length, as illustrated in Fig. 7.2.

$$F_{eb} = F_{s,max} = \tau_{max} l_s (\pi d) = f_y A_s \qquad \textit{Eq. 7.14}$$

where l_s is the slip length (equal to the tie spacing, as shown in Fig. 7.2, *d* is the rebar diameter, and τ_{max} is the maximum bond strength attained in the non-corroded region, which is calculated according to the CEB-FIB Model Code (fib 2013).

In a corroded region (flexural cracks zone), the effective bond strength decreases as the corrosion level increases, leading to significant bar slippage due to inadequate force transfer between concrete and steel. Therefore, the effective bond stress of the corroded bar is estimated based on section properties and corrosion level according to an expression proposed by Rodriguez et al. (Rodriguez et al. 1996).

This expression defines bond strength decay due to corrosion considering the contribution of the transverse reinforcement, i.e.,

$$\tau_{res} = \tau_{concrete} + \tau_{ties} = 0.6\,(0.5 + c/d) f_t \left(1 - \beta P_x^{\mu}\right) + k A_t f_{yt}/sd \qquad \textit{Eq. 7.15}$$

where β, μ, k are empirical constants (0.16, 0.1 and 0.26-0.4, respectively), f_t is the concrete tensile strength, A_{st} is the tie cross-sectional area, f_{yt} is the yield strength of the ties, *d* is the original rebar diameter, *s* is the tie spacing, c is the thickness of the concrete cover, P_x is the attack penetration

For eccentrically loaded columns, the tensile force (Eq. 7.14) of the corroded reinforcement is reduced by a reduction factor (γ) to account for bar slippage. The reduction factor (γ) is estimated as the ratio of the corroded bond strength to the noncorroded one (Campione et al. 2017), as follows:

$$\gamma = \frac{\tau_{res}}{\tau_0} \qquad \textit{Eq. 7.16}$$

where the noncorroded bond strength (τ_0) is calculated according to Eq. 7.15, considering no reduction in the bar radius (P_x = 0).

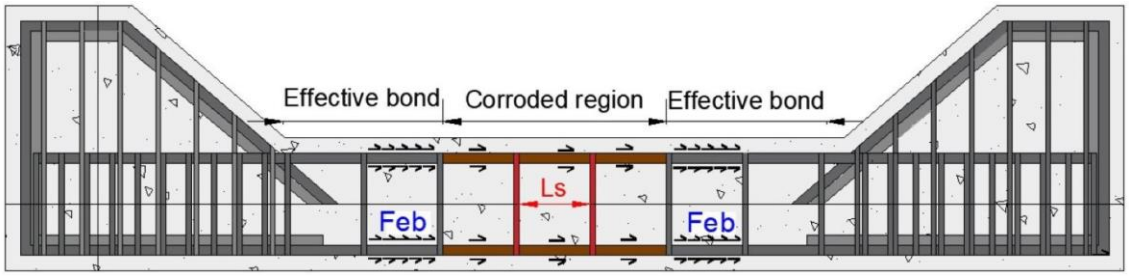

Fig. 7.2: Effective bond and corroded region along reinforcement length

7.3.5 Summary of the Evaluation Procedure

The evaluation procedure adopted herein to estimate the residual capacity of corroded columns is illustrated in Fig. 7.3 and summarized as follows:

- Input column geometry and materials' properties,
- Determine crack widths and patterns (widespread and location) from field investigations,
- Determine current intensity using non-destructive methods and estimate the reduced area of the reinforcement and corrosion level, Eqs (7.10-7.13),
- Calculate the reduced area of the concrete cover and core,

$$A_{cover} = 2bc + 2hc - 4c^2 \qquad \textit{Eq. 7.17}$$

$$A_{core} = hb - 2bc - 2hc + 4c^2$$

$$A_{cover-reduced} = bc + hc - 2c^2 \qquad \text{for a high level of corrosion}$$

Based on experimental observations reported in Chapters 4 and 5, 10% of the cover thickness was reduced from the original thickness for low levels of corrosion (C-C-T1/2 and C-E-T3/4), while 50% of the cover was removed for medium and high levels of corrosion (C-C-All1/2 and C-E-R1/2).

- Calculate the position of the neutral axis C_b at the balanced point using strain compatibility. This point is taken as the threshold point between small and large eccentrically loads. Accordingly, the neutral axis position for small and large eccentricity loading conditions can be assumed C_c, C_e, respectively.

$$C_e < C_b = \frac{d_2}{1+\frac{f_s}{(\varepsilon_c E_s)}} < C_c \qquad \textit{Eq. 7.18}$$

where d_2 is the distance to the second layer of reinforcement, E_s is the steel modulus of elasticity, and ε_c is the ultimate concrete strain at the top section, taken as 0.00035.

- Determine strain values at the compressive and tensile layers of reinforcements from the strain distribution for large and small load eccentricities, respectively. At small loading eccentricities, the compressive bars are assumed to yield, and potential buckling is calculated according to the Euler's formulation. The compressive steel stress is, then, taken as the minimum of the two values. At large eccentricities, the tensile bars are assumed to yield,
- Calculate the compressive F_{s1} and tensile F_{s2} forces for large and small eccentricities, respectively,
- Calculate the maximum bond strength for non-corroded regions τ_{max} and τ_0 (Eqs. 14-15),
- Estimate the residual bond strength τ_{res} (Eq.7.15)
- Multiply the strain of the tensile bars (eccentric conditions) by a bond reduction factor to account for excessive bar slippage due to corrosion (Eq. 7.16),
- Calculate the tensile force considering steel cross-sectional area reduction and bond loss (Eqs 7.10-7.11 and 7.16),
- Calculate the concrete strength C_r incorporating material degradations and geometrical changes (Eqs.7.5-7.9 and 7.17),
- Calculate the residual load capacity (Eqs. 7.2-7.3)
- Calculate moment capacity from conventional mechanics,
- Estimate eccentricity (e).

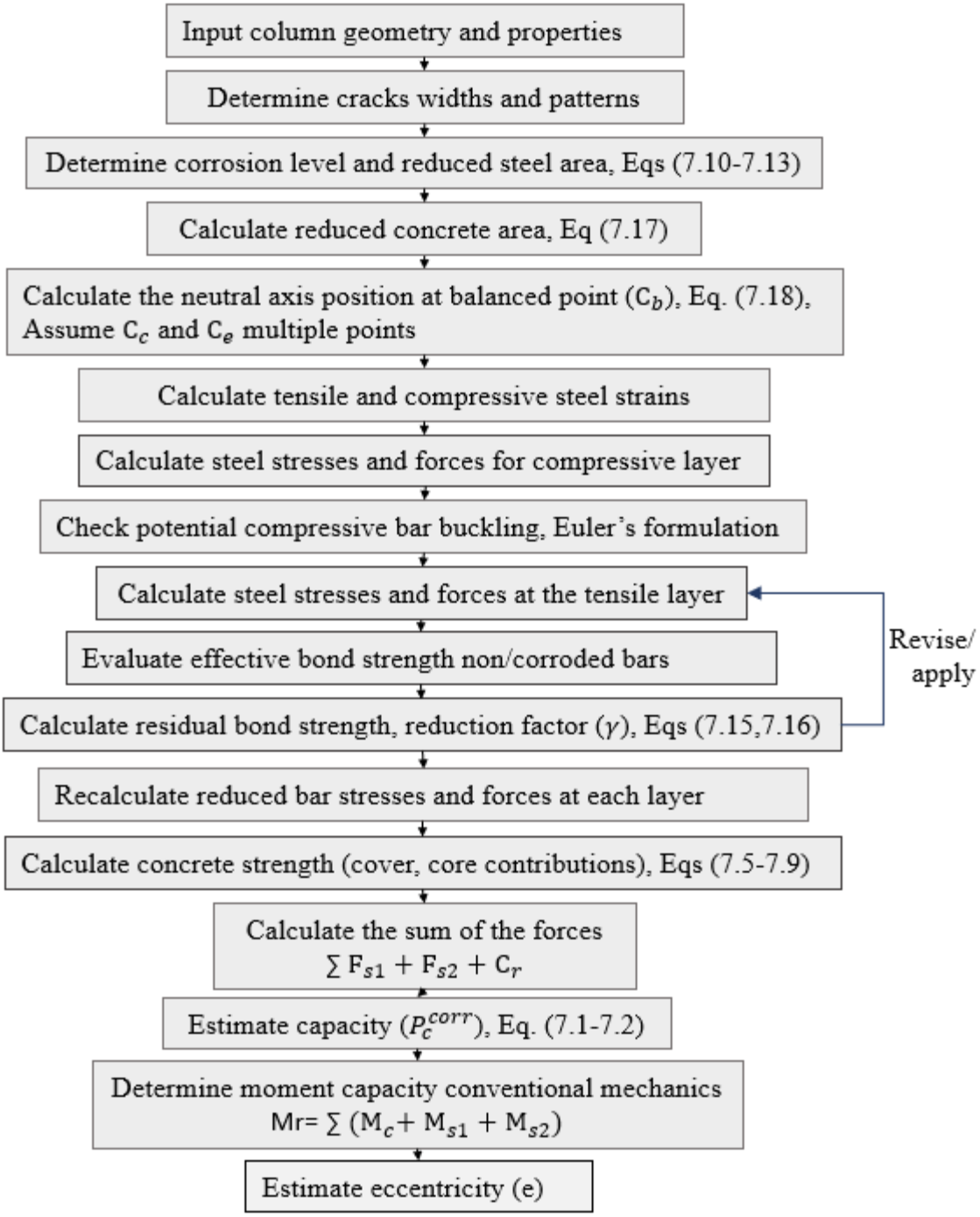

Fig. 7.3: Flow chart of the procedure adopted to account for corrosion effects

7.4 Finite element model

The evaluation approach proposed in Section 7.3 was validated with both numerical results from finite element analysis (FEA) and experimental results of ten RC columns tested by the authors (Dabas 2022). FEA was also used to supplement the experimental data by including more corrosion scenarios than those experimentally tested, thus increasing the database against which the approach is validated. This section presents the FEM and its validation.

7.4.1 Development of the Finite Element Model

A 3D nonlinear finite element analysis was developed using Diana software (v.10.5) (DIANA FEA BV 2021) to analyze further the influence of different corrosion levels on the structural response of columns. In the development of the FEM, the cross-section of the reinforced column was divided into three zones: unconfined concrete cover, confined concrete core, and reinforcement (Fig. 7.4). The division is necessary to properly account for the variations in the inherent materials characteristics by defining different stress-strain relationships on each region. These relations were selected from the calibration of the model with the tested control column (no corrosion).

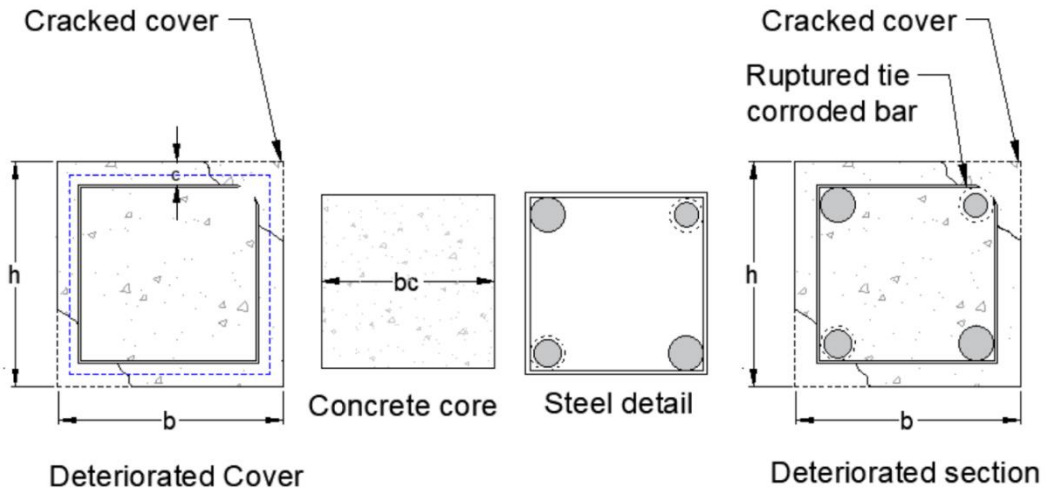

Fig. 7.4: The column cross-section was divided into different materials (cover, core and reinforcement)

The effects of reinforcement corrosion on cracking of the concrete cover, reduction of the cross-sectional area of the reinforcement, and bond loss are accounted for by integrating deteriorations models into different sections of the simulated model. Cracking of concrete cover, induced by expansion of the rust products, deteriorates the compressive strength of the concrete. This

reduction is expressed by a model proposed by Vecchio and Collins (1986), utilizing test measurements of the average crack width along the column surfaces. The uncorroded compressive strength of the concrete was obtained from cylinder tests on the day of column testing and is incorporated into the developed FEM. Concrete response in compression was modelled using the parabolic model, which considers fracture energy. For the concrete core, the model proposed by Razvi and Saatcioglu (1999) was used (Fig. 7.5). This model accounts for changes in concrete strength and deformation capacity of the structure due to changes in lateral reinforcements details. This model is most suitable as it captures a reduction in core confinement pressure and overall column capacity due to a reduction in tie stiffness and its restraining capabilities. For low levels of tie corrosion, reduction in mechanical properties due to corrosion was accounted for according to the empirical equations of Lee and Cho (2009). For a very high level of tie corrosion, ties were removed entirely in the model due to their severe deteriorating condition (pitting fracture and very brittle). Concrete response in tension is defined using the stiffening model in JSCE (2010). Potential premature buckling of longitudinal bars is accounted for using the Redefined Dhakal Maekawa (RDM) model proposed by Akkaya et al. (Akkaya et al. 2019) (Fig. 7.5). Bond-slip failure due to bar slippage is defined using Shima et al. (Shima et al. 1987) model. This model was based on the effect of bar diameter and concrete strength on the bond and slip behaviour of the steel/concrete interface. This model accounts for the steel yielding and expresses bond degradation post-yield of the steel. As for the analysis method, a load-displacement analysis for concentrically loaded columns, while an indirect displacement analysis was the most suitable method to capture the behaviour of eccentrically loaded columns.

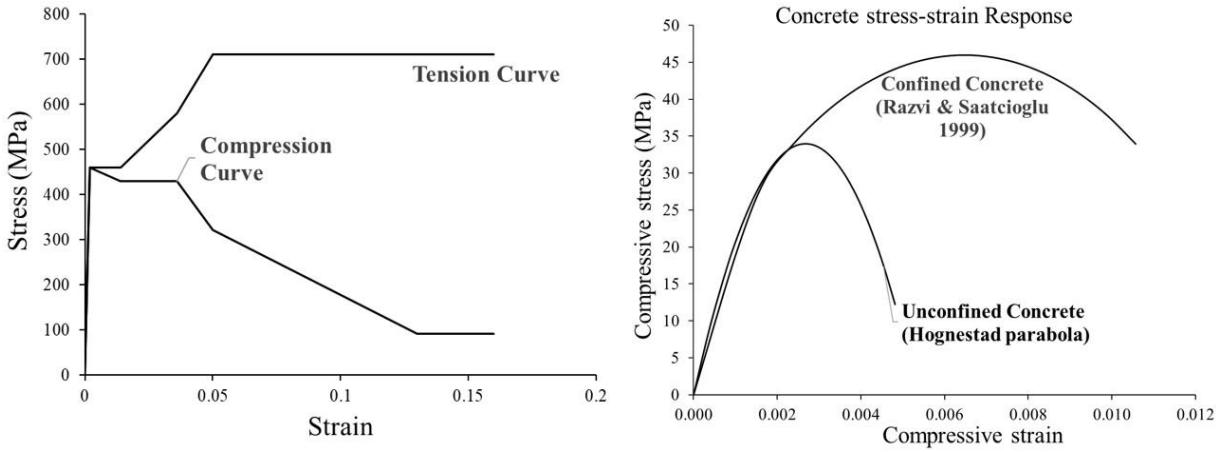

Fig. 7.5: Stress-strain curves of the steel (Left) and concrete (Right)

7.4.2 Summary of Experimental Program

Ten RC columns were built and tested by the authors (Dabas 2022) five columns were subjected to concentric loads, while the other five were subjected to an eccentric load with an eccentricity value of 190 mm. Geometry and cross-sectional details are illustrated in Fig. 7.6. Two columns were control specimens, and eight were subjected to an accelerated corrosion regime, as shown in Fig. 7.7. Four cases were tested as follows:

- Case 1: Non-corroded, control specimens (C-C-E, C-C-C)
- Case 2: Corrosion of the middle two transverse reinforcement (C-C-T1, C-C-T2, C-E-T3, C-E-T4)
- Case 3: Corrosion of the longitudinal reinforcement (C-E-R1, C-E-R2)
- Case 4: Corrosion of both middle two transverse and longitudinal reinforcement (C-C-All1, C-C-All2)

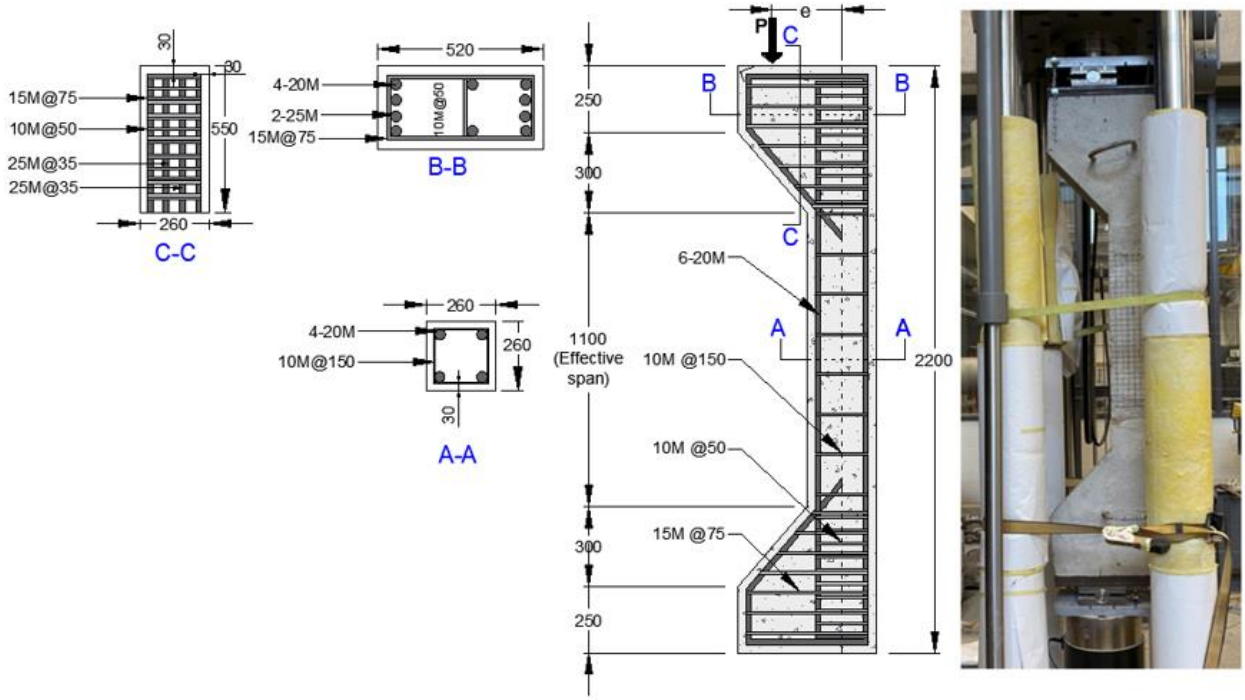

Fig. 7.6:Set-up of loading test

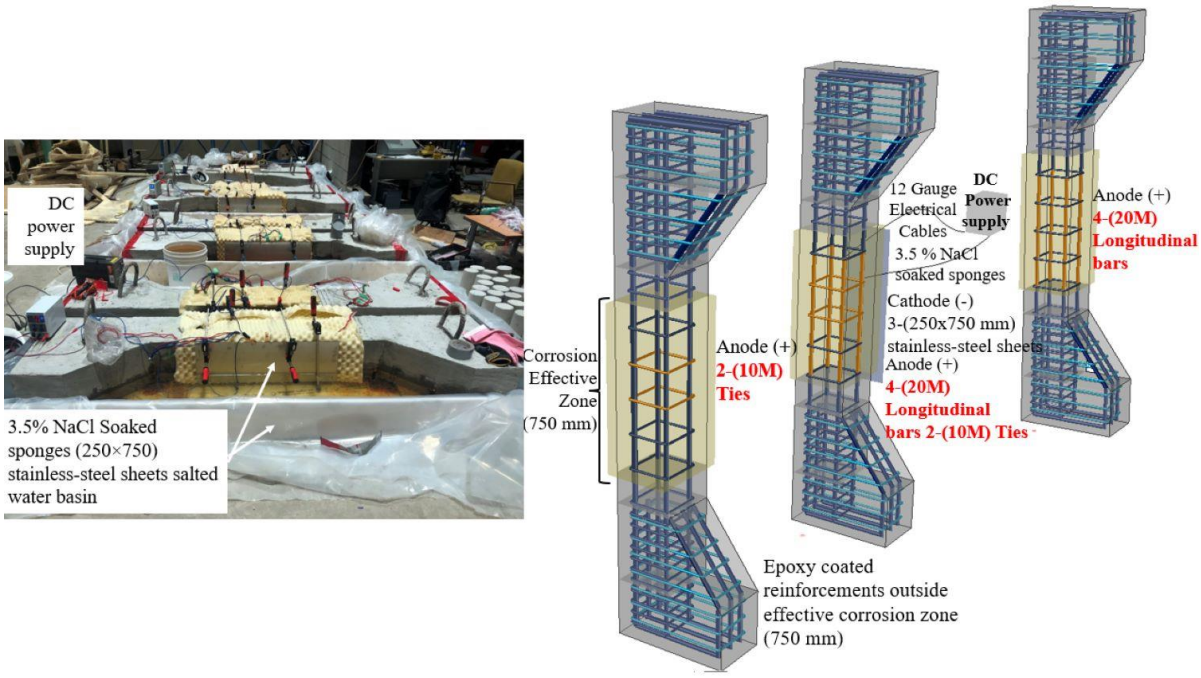

Fig. 7.7: Set-up of the accelerated corrosion test

Following the accelerated corrosion process, all columns were subjected to a static axial load applied either concentrically or eccentrically up to failure at a rate of 0.25 mm/min under

displacement-controlled conditions. Ordinary Portland cement concrete ready mix was specified for normal exposure conditions and non-air entrainment. The concrete had a maximum coarse aggregate of 14 mm and a water-to-cement ratio (w/c) of 0.55. The intended compressive strength at 28 days was 30 MPa. For those columns that were subjected to an accelerated corrosion regime, 3.5% of sodium chloride (NaCl) by weight of cement was added to the mixing water to depassivate the protective film on the reinforcement. For the 20M rebars the estimated yield strength was 446 MPa and the ultimate strain was 0.18. The average values of concrete compressive strength of the columns on the day of the loading test and the average mass loss are reported in Table 7.1. In Table 7.1, the ultimate load of corroded columns is 55% and 75% of noncorroded columns for concentric and eccentric conditions, respectively. The failure mode of column C-C-All1 was characterized by the widening of pre-existing cracks and spalling, whereas for column C-E-T3 it had a steel-controlled failure (Fig. 7.8). The ultimate lateral displacement of corroded columns eccentrically loaded is 60-84% of noncorroded columns, as shown in (Fig. 7.9).

Table 7.1: Experimental and model validation results

Column label	f_c, (MPa) (Test day)	m_s Tie	m_s Rebar	$P_{u,\ Exp}$ (kN)	$P_{u,FEM}$ (kN)	$P_{u,\ FEM}/P_{u,\ Exp}$	$\Delta_{m,\ Exp}$ (mm)	$\Delta_{m,\ FEM}$ (mm)	$\Delta_{m,\ FEM/Exp}$	Failure mode
C-C-C	31.9	0	0	2,550	2,350	0.92	1	2	1.50	Concrete controlled
C-C-T2	32.9	5	1	2,389	2,350	0.98	5	4	0.70	Widening of pre-existing cracks (0.3 to 1mm), local stains, spalling corners, asymmetrical corrosion,
C-C-T1	33.7	14	5	2,199	2,198	1.00	4	3	0.75	
C-C-All2	32.1	17	20	1,622	1.622	1.00	2	2	0.75	Widening of pre-existing cracks (0.9 to 3mm), widespread uniform stains, local buckling C-C-All2, ties pitting fracture
C-C-All1	34.0	20	26	1,418	1,418	1.00	1	1	0.71	
					Avg.	1.01		Avg	0.88	
C-E-C	31.8	0	0	461	461	1.00	25	24	0.96	Steel controlled failure, No bar buckling, Nonlinear response due to bar brittleness at a high corrosion level
C-E-T4	33.3	4	4	461	461	1.00	21	21	0.98	
C-E-T3	31.8	7	4	414	435	1.11	21	20	0.97	
C-E-R2	31.8	15	12	369	356	0.96	15	16	1.03	
C-E-R1	33.6	15	23	342	330	0.96	15	16	1.05	
					Avg.	1.01		Avg	1.00	

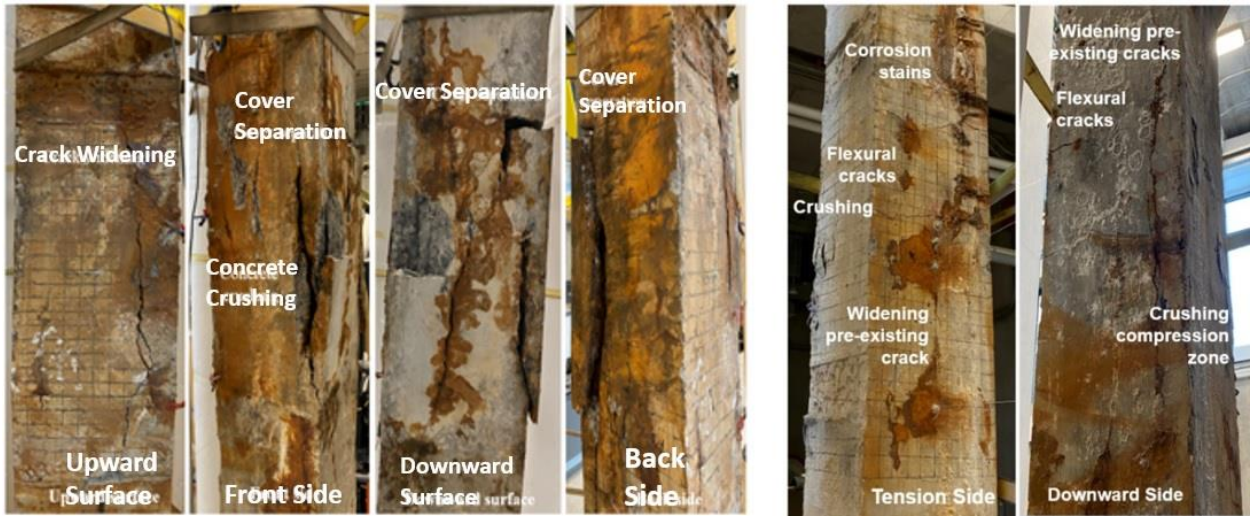

Fig. 7.8: Damage due to reinforcement corrosion after load test for Left: concentrically loaded specimen C-C-All2, Right: Eccentrically loaded specimen C-E-T3

7.4.3 Validation of the Numerical Model

The ultimate capacity and displacement from the numerical results were validated with those determined from experimental testing, demonstrating a good agreement (Fig. 7.9). Moreover, the numerical models' load-displacement curves capture failure mode and ultimate displacement as corrosion levels increase (see Fig. 7.9).

The FEA captures the widespread distribution of flexural cracks and size growth (from 2 to 3 mm), as it can be seen by comparing the corroded column C-E-R1 to the noncorroded column C-E-C (see Fig. 7.10). Refer to Section 6.4 for all columns validations.

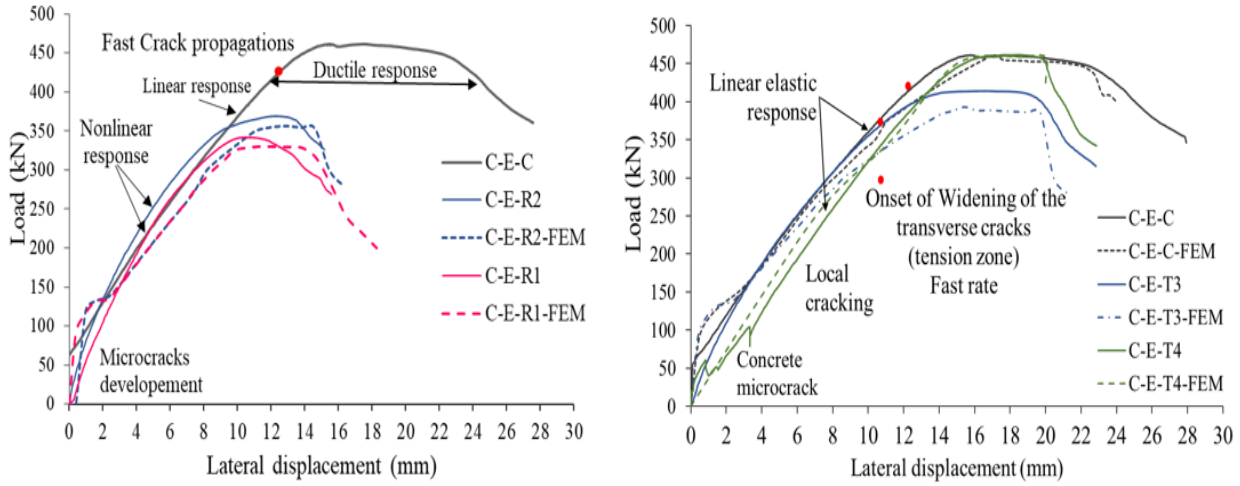

Fig. 7.9: Validation of the experimental results with FEM for eccentrically loaded columns

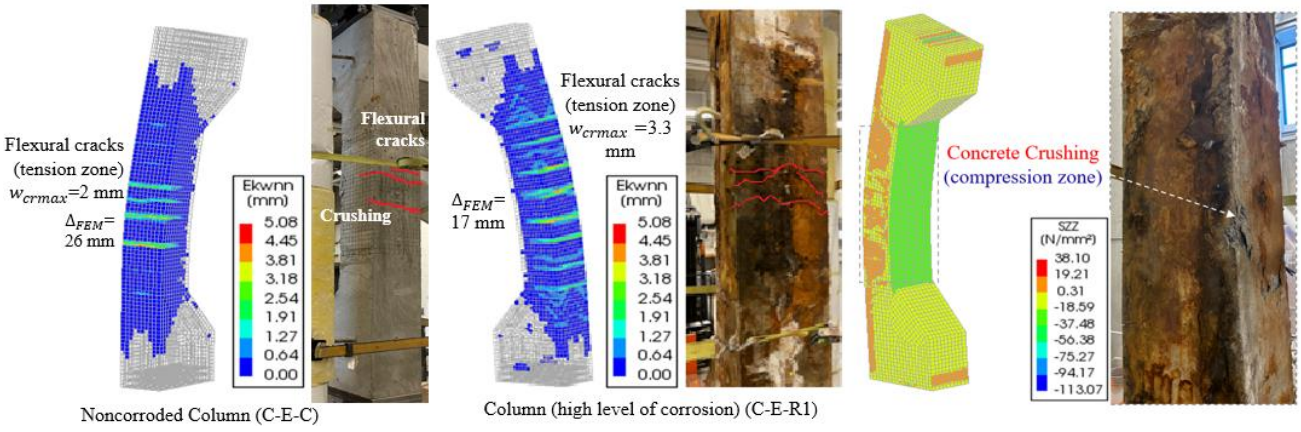

Fig. 7.10: Crack development: (a) tension zone of C-E-C, (b) tension zone of C-E-R1, (c) compression zone of C-E-R1

7.5 Analysis of the Effect of Reinforcement Corrosion on the Residual Capacity of Columns

Based on the simplified sectional analysis presented in Section 2, the residual axial and flexural capacities of the corroded columns tested experimentally were established at different eccentricities levels and different corrosion scenarios. Numerical analyses extended experimental results to include nine different eccentricities from e = 0 to e = 190 mm, covering both concrete-controlled and steel-controlled regions of the column interaction diagram. The columns are grouped into four cases as presented in Section 7.4.2. Different levels of corrosion were classified according to the guidelines for reinforcing steel mass loss m_s provided by OSIM (Ontario Ministry of Transportation 2008):

- Intact level (I) for $m_s \leq 1\%$,
- Low level (II) for $m_s < 5\%$,
- Medium level (III) for $5 \leq m_s \leq 10\%$,
- High (severe) level (IV) for $10 < m_s \leq 20\%$
- Very high (very severe) $m_s > 20\%$.

Table 7.2 summarizes the results of the ultimate capacity obtained from the analytical estimation, numerical analysis, and experimental testing of the RC columns. Table 7.2 illustrates that both the numerical and analytical estimations predict well the load capacity for the different cases of reinforcement corrosion. The mean and coefficient of variations (CV.%) values for the ratio of the FEM to experimental, analytical to experimental and analytical to FEM are presented in Table 7.2.

Table 7.2: Summary table of ultimate capacity for all tested columns

Column	Corrosion level	$P_{u,\ Exp}$ (kN)	$P_{u,\ FEM}$ (kN)	$P_{u,\ Analytical}$ (kN)	$P_{u,FEM}/P_{u,Exp}$	$P_{u,\ Analytical}/P_{u,Exp}$	$P_{u,\ Analytical}/P_{u,FEM}$	Rebar-buckle	Tie fracture
C-C-C	None	2,550	2,350	2,552	0.92	1.00	1.09	No	No
C-C-T2	Low	2,389	2,350	2,352	0.98	0.98	1.00	No	No
C-C-T1	Medium	2,199	2,198	2,206	1.00	1.00	1.00	Yes	No
C-C-All2	High	1,622	1,622	1,645	1.00	1.01	1.01	No	Yes
C-C-All1	Very high	1,418	1,418	1,420	1.00	1.00	1.00	Yes	Yes
C-E-C	None	461	461	461	1.00	1.00	1.00	No	No
C-E-T4	Low	461	461	461	1.00	1.00	1.00	No	No
C-E-T3	Medium	414	435	437	1.05	1.06	1.00	No	No
C-E-R2	Medium	369	356	361	0.96	0.98	1.01	No	No
C-E-R1	High	342	330	328	0.96	0.96	0.99	No	No
				Mean	0.99	1.00	1.01		
				CV.%	3.40	2.51	2.65		

7.5.1 Control Columns

Fig. 7.11 illustrates the resulting interaction diagram as well as the experimental results of specimens C-C-C and C-E-C. Also shown in Fig. 7.11 are the FEA results corresponding to eccentricities of 0, 40, 100, 130, and 190 mm. The interaction diagram predicts well the capacity of the experimentally-tested and numerically-analyzed columns C-C-C and C-E-C. However, the FEA underestimates the axial capacity at zero eccentricity by 8% (Fig. 7.11). The experimental results for the corroded columns (C-C-T1, C-C-T2, C-C-All1, C-C-All2, C- E-T3, C-E-T4, C-E-R1 and C-E-R2) are also plotted in Fig. 7.11. It is evident that the tested corroded columns failed prematurely before reaching the capacity of the control specimen. This indicates that the interaction diagram for non-corroded columns cannot safely predict RC columns' axial and flexural capacities affected by reinforcement corrosion. Thus, the analytical approach is established to assess the ultimate capacities of columns subjected to different corrosion levels.

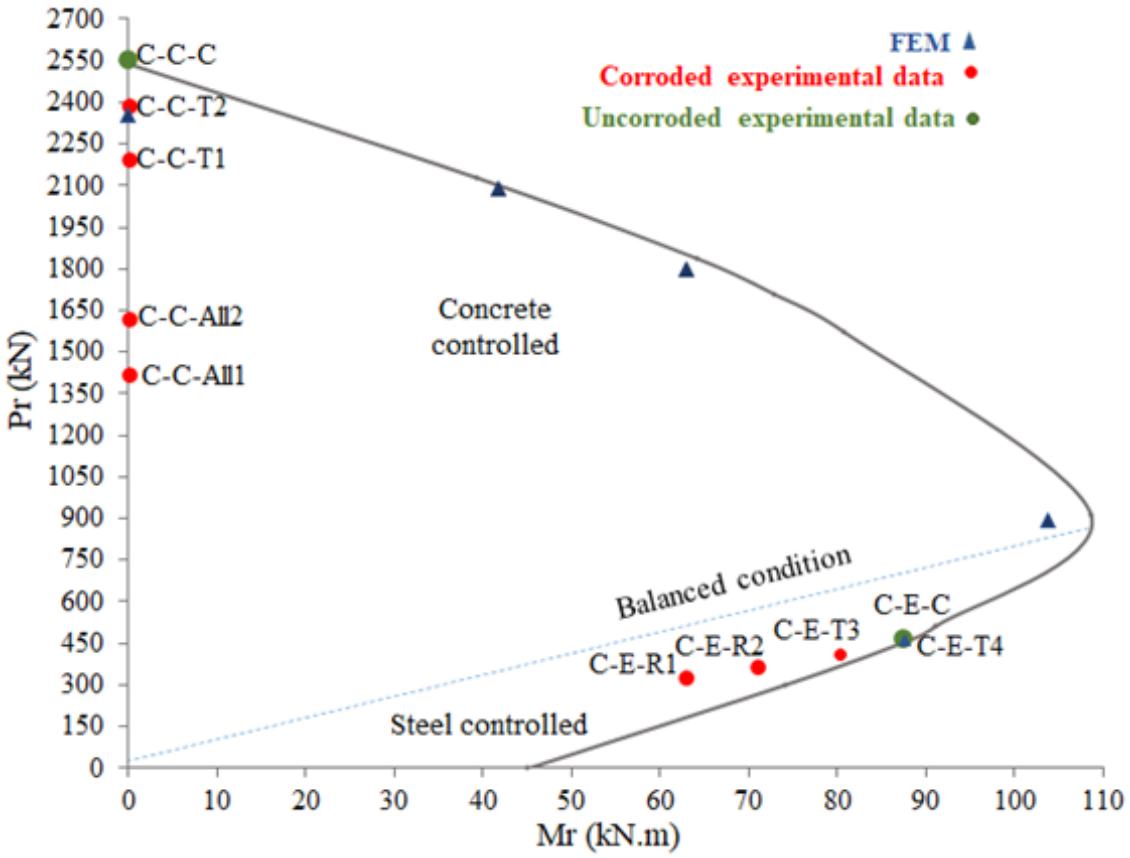

Fig. 7.11: Interaction diagram for control column

7.5.2 Effect of Corrosion of Transverse Reinforcement (Case 2)

The axial and flexural capacities of columns damaged by transverse reinforcement corrosion with an average mass loss ranging from 5% (low) to 20% (very high) are plotted in Fig. 7.12. Numerical results compared well with the interaction diagrams developed from the sectional analysis. Results indicate that the bearing capacity of the corroded columns is primarily governed by cracking of the concrete cover, reduction in the compressive strength of the concrete core and reduction in confinement effects. Such reduction in confinement was due to a decrease in the lateral pressure on the core concrete, which was reduced by 10% as the tie corrosion level increased by 5% according to Razvi and Saatcioglu (1999). For high corrosion levels, the spacing between adjacent ties increased due to tie pitting fracture. This assumption is supported by experimental observations from specimens C-C-All1 and C-C-All2. Subsequently, local buckling of the longitudinal bars is observed. Moreover, it is evident that as the level of tie corrosion increases,

the reduction in the bearing capacity increases. This reduction is more significant in concrete-controlled columns than steel-controlled columns due to the decrease in confinement provided by the corroded ties.

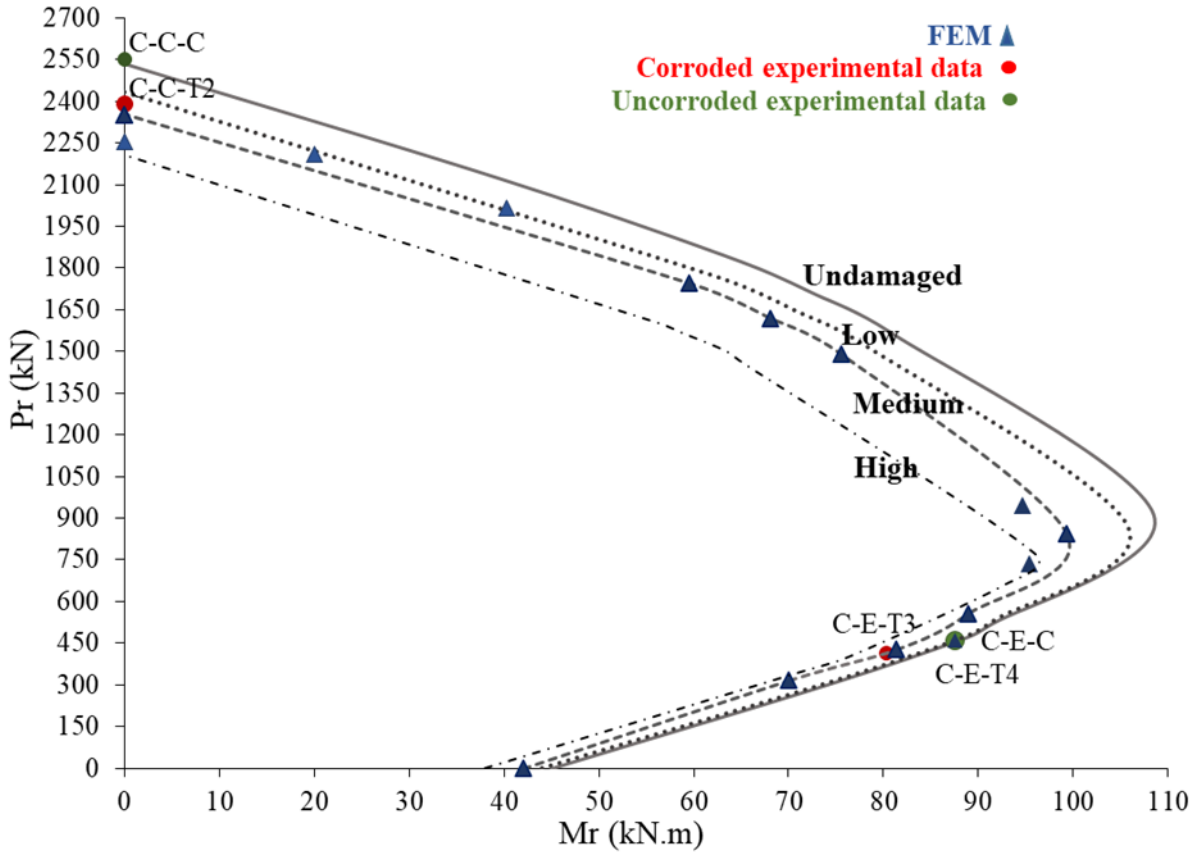

Fig. 7.12: Interaction diagram for transverse reinforcement (C-C/E-T2) corrosion

7.5.3 Effect of Reinforcement Corrosion of Longitudinal Reinforcement (C-C/E-R1) (Case 3)

Fig. 7.13 illustrates more than a 20% decrement in the axial capacity of RC columns whose longitudinal reinforcement is corroded to a medium level when loaded concentrically. For this case, the transverse reinforcement had an average mass loss of 12%. For this case, it is found that the ties provided adequate restraining effects to prevent local buckling.

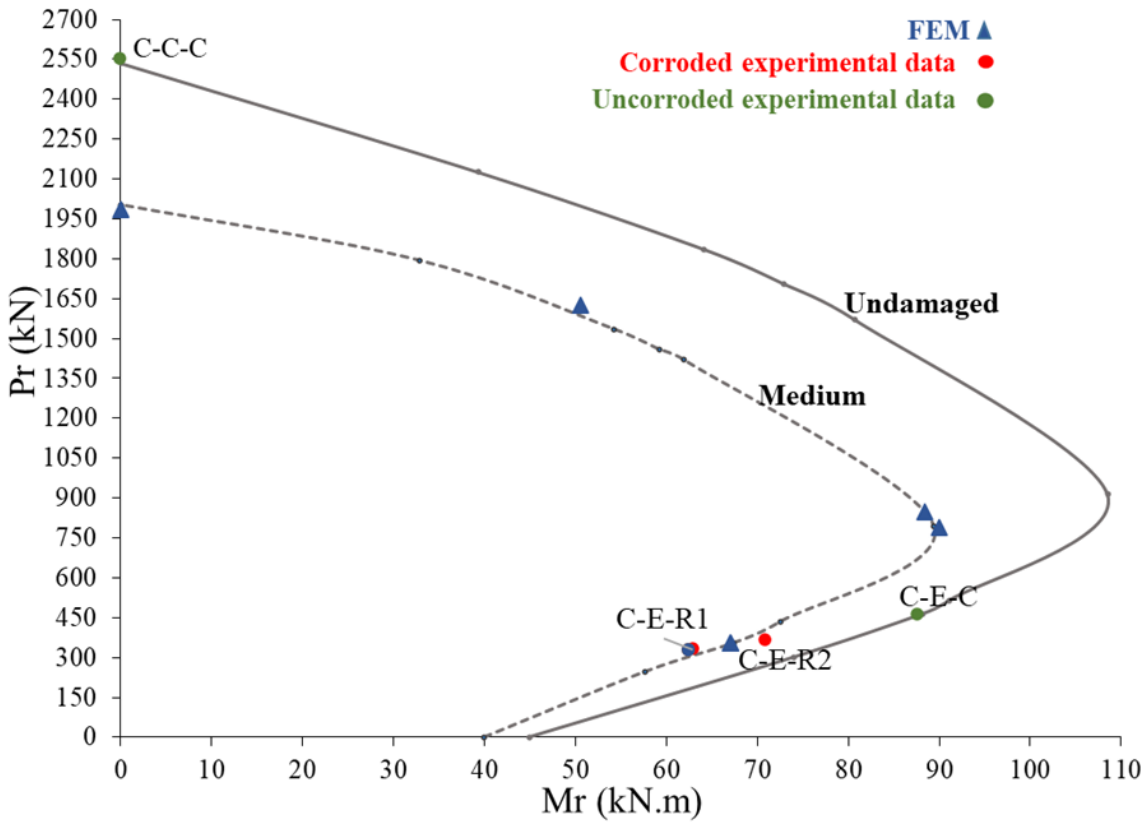

Fig. 7.13: Interaction diagrams for columns with longitudinal reinforcement corrosion (C-C/E-R)

7.5.4 Effect of Reinforcement Corrosion of All Reinforcement (C-C/E-ALL1) (Case 4)

Fig. 7.14 and Fig. 7.15 illustrate a 30-45% reduction in the bearing capacity for eccentric and concentric loadings, respectively, as the corrosion level is increased for case 4 compared to case 2. This is attributed to significant material deteriorations of the reinforcement and concrete (core and cover) and bond loss. For medium to high levels of corrosion, the concrete cover was reduced based on experimental observations of tested columns (C-C-All1, C-C-All2). It was determined that 50% of the concrete cover was still effective in withstanding the applied load. Moreover, local buckling of the longitudinal bars was reported for high levels of corrosion where the corroded ties fractured with a subsequent reduction of the core strength.

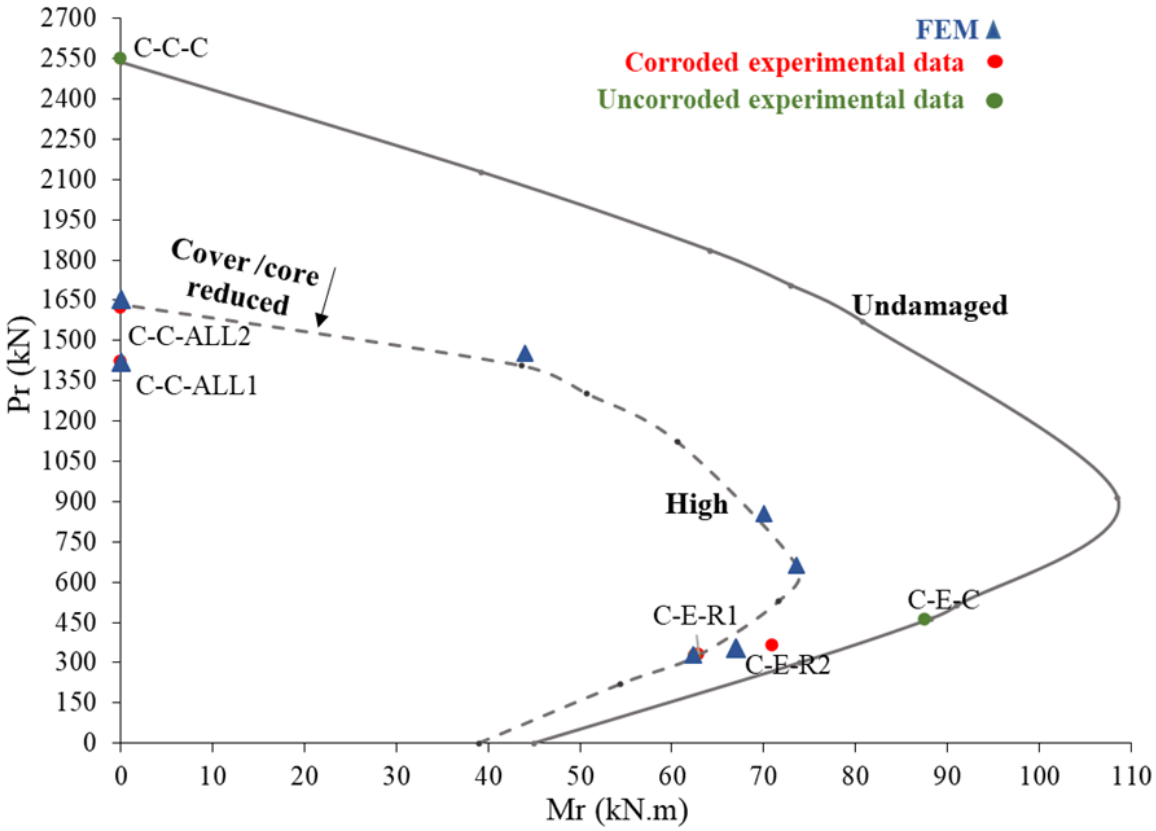

Fig. 7.14: Interaction Diagrams for specimens C-C-ALL and C-E-R

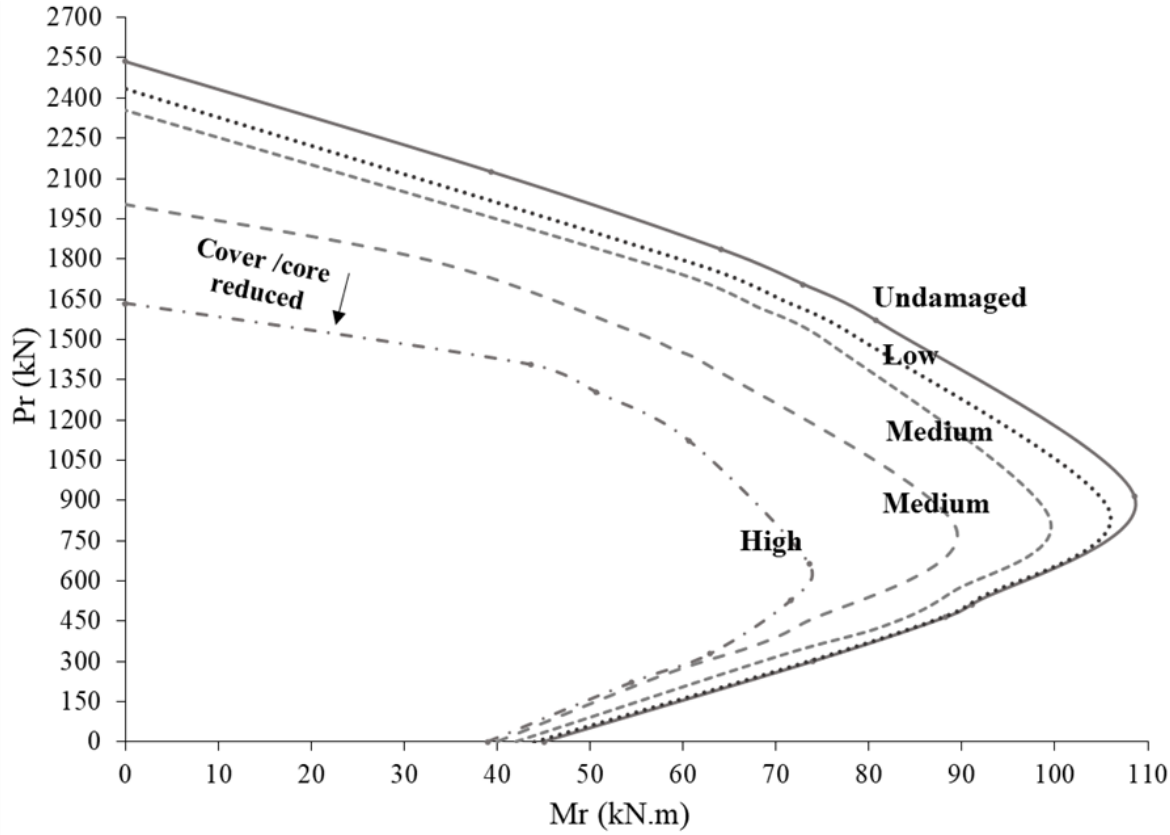

Fig. 7.15: Interaction Diagrams for specimens C-C-C, C-C-ALL, C-E-T, C-E-R

7.6 Conclusions

Reinforcement corrosion leads to premature material and structural deteriorations of RC columns, ultimately reducing the overall column's capacity and ductility. Experimental results show that conventional methods cannot safely predict the ultimate capacity of corroded columns without considering corrosion effects.

In this study, an analytical approach is proposed to estimate the residual capacity of the corroded columns by considering cover cracking, reduction in confinement effects of the core concrete, potential buckling of the longitudinal bars and bond loss at different loading eccentricities. The analytical approach compares very well with experimental and numerical results. This shows that the analytical approach can reproduce results and predict the residual capacity of columns for different levels and patterns of reinforcement corrosion.

The feasibility of this approach requires incorporating data collected from the field or experimental investigations (e.g., corrosion rate, crack widths and distributions) along with a good engineering

judgement. Further improvements to the analytical approach should be considered to account for variable bond deterioration along the column span.

The analytical assessment provides a simplified approach to estimating the corroded columns' residual strength, while the FEA successfully captures crack distribution, failure mode, and ultimate displacement to better understand the corroded column's performance.

7.7 References

Akkaya, Y., Guner, S., and Vecchio, F. J. (2019). "Constitutive model for inelastic buckling behavior of reinforcing bars." ACI Structural Journal, 116(2), 195–204.

Almusallam, A. A., Al-Gahtani, A. S., Aziz, A. R., and Rasheeduzzafar. (1996). "Effect of reinforcement corrosion on bond strength." Construction and Building Materials, 10(2), 123–129.

Apostolopoulos, C., and Koulouris, K. (2020). Corrosion Effect on Bond Loss between Steel and Concrete. Structural Integrity and Failure, IntechOpen.

Cairns, J., Plizzari.G.A., Law, D., and Franzoni.C. (2005). "Mechanical properties of corrosion-damaged reinforcement." ACI Materials Journal, 102(4), 256–264.

Campione, G., Cannella, F., Cavaleri, L., and Ferrotto, M. F. (2017). "Moment-axial force domain of corroded R.C. columns." Materials and Structures/Materiaux et Constructions, Springer Netherlands, 50(1), 1–14.

Canada Infrastructure Report Card. (2019). Canada Infrastructure Report Card 2019-Monitoring the State of Canada's Core Public Infrastructure. Canadian Infrustructure.

Cape, M. (1999). "Residual service-life assessment of existing R/C structure." Chalmers University of Technology, Goteborg, Sweden and Milan University of Technology Italy, Erasmus Program, 133.

CONTECVET. (2001). A validated User's manual for assessing the residual service life of concrete structures. EC Innovation Programme IN30902I, GEOCISA, Madrid, Spain.

Coronelli, D., and Gambarova, P. (2004). “Structural Assessment of Corroded Reinforced Concrete Beams: Modeling Guidelines.” Journal of Structural Engineering, 130(8), 1214–1224.

CSA-S6.1:19. (2019). Commentary on CSA S6:19, Canadian Highway Bridge Design Code. Canadian Standards Association (CSA Group), Ontario, Canada.

CSA 23.3:19. (2019). Design of concrete structures. Canadian Standards Association, Canadian standards association (CSA Group), Ontario, Canada.

CSA Group. (2019). CSA S6:19 Canadian highway bridge design code. CSA Group, Toronto, Ontario.

Dabas, M. (2022). “Evaluation of the effect of reinforcement corrosion on the structural performance of RC columns.” thesis presented to the University of Ottawa in partial fulfilment of the requirements for the degree of Doctor in Philosophy in Civil Engineering (Ph.D.), Ottawa, Canada.

DIANA FEA BV. (2021). “User’s Manual -Release 10.5.” Diana FEA Bv, Netherlands, <https://dianafea.com/manuals/d105/Diana.html> (Mar. 22, 2022).

fib model code for concrete structures. (2013). CEB. CEB-FIP Model Code 2010. Lausanne, Switzerland.

JSCE. (2010). “JSCE Guidelines for Concrete No. 15: Standard Specifications for Concrete Structures - 2007 Design.” Japan Society of Civil Engineers, Japan.

Lee, H. S., and Cho, Y. S. (2009). “Evaluation of the mechanical properties of steel reinforcement embedded in concrete specimen as a function of the degree of reinforcement corrosion.” International Journal of Fracture, 157(1–2), 81–88.

Ontario Ministry of Transportation. (2008). Ontario Structure Inspection Manual (OSIM). Ministry of Transportation, St. Catharine’s, Ontario, Canada.

Razvi, S., and Saatcioglu, M. (1999). “Confinement model for high-strength concrete.” Journal of Structural Engineering, 125(3), 281–289.

Rodriguez, J., Ortega, L. M., and Casal, J. (1996). “Load bearing capacity of concrete columns with corroded reinforcement.” Corrosion of reinforcement in concrete construction. proceedings of fourth international symposium, Cambridge, 1-4 July 1996. special publication no 183, 220–230.

Shima, H., Chou, L. L., and Okamura, H. (1987). “Micro and macro models for bond in reinforced concrete.” Journal of the Faculty of Engineering, University of Tokyo, Series B.

Statistics Canada. (2018). Canada’s Core Public Infrastructure Survey: Roads, bridges, and tunnels, 2016. The Daily Statistics Canada’s official release bulletin, Canada.

Tapan, M., and Aboutaha, R. S. (2008). “Strength Evaluation of Deteriorated RC Bridge Columns.” Journal of Bridge Engineering, 13(3), 226–236.

Tapan, M., and Aboutaha, R. S. (2011). “Effect of steel corrosion and loss of concrete cover on strength of deteriorated RC columns.” Construction and Building Materials, 25(5), 2596–2603.

The Jacques Cartier and Champlain Bridges Incorporated (JCCBI). (2018). “Pont Champlain, Services de consultant, Inspections annuelles des sections 5, 6 et 7 et services d ’ assistance pour inspections sur demande (2015-2018) – Contrat 62450 Rapport d ’ inspection 2018 – Volume 1 : Inspection annuelle des sections 5 et 7.” N/Réf : P-159000038 | M04024D | MTR-00229620, Quebec, Canada, <https://jacquescartierchamplain.ca/en/the-corporation/reports-and-publications/reports-and-studies/#deconstruction> (Mar. 27, 2022).

Vecchio, F. J., and Collins, M. P. (1986). “The modified compression-field theory for reinforced concrete elements subjected to shear.” ACI Journal Proceedings, 83(2), 219–231.

Chapter 8 Concluding Remarks

8.1 Conclusions

This chapter aims to integrate all the findings and conclusions drawn from each chapter. Moreover, the focus of this chapter is to restate the findings and interpretations made. A brief recommendation of future work follows the conclusion.

8.1.1 Accelerated Corrosion Test

The experimental work conducted on ten RC columns successfully provided a good understanding of the structural performance of corroded columns under eccentric and concentric quasi-static loadings. The following findings were concluded from this work's accelerated corrosion test:

- The corrosion process had an initiation period (time to depassivate reinforcement and the onset of corrosion) and retained a propagation period (crack growth over time) while connected to a DC system, following Tuutti's model.
- The resulting corrosion products were reddish-brown. Since their kinetics were not tested, it is presumed that they are FeOOH (lepidocrocite and akageneite) based on their colour. This is similar to the corrosion products observed in in-service RC structures.
- These corrosion products expanded, causing concrete internal cracks that propagated outwards. The measured mass loss according to ASTM G1 follows the predetermined mass loss according to Faraday's law.
- After removing the DC power supply for all columns, the corrosion rate slowed down and crack widths did not increase further. Thus, there is a tendency for reinforcement corrosion to decay after removing the power supply.
- The effective region of the column was crushed open to expose the corrosion-contaminated reinforcement; it was found that the corrosion damage was exclusive to the middle region.
- Reinforcement corrosion leads to significant concrete and steel deterioration depending on the corrosion level and pattern. The shape of the stress-strain curve of corroded reinforcement differs significantly from its counterpart (low or intact reinforcement).

The yield plateau after attainment of the yield point completely disappeared as the level of corrosion increased from low to high. Moreover, the corroded reinforcement had a significant loss in ductility (60% reduction). The residual yield strengths for high and very high levels of corrosion are estimated to be 55% and 60% of the non-corroded reinforcement.

- The above findings show that the adopted method of accelerated corrosion was a practical and effective method to analyze the effects of corrosion on RC columns.

Based on the findings mentioned in the experimental work, the following recommendations are suggested:

- It is recommended that accelerated corrosion be carried out after 20 to 28-days of casting. This is because RC columns will have lower resistivity,
- It is necessary to provide a fresh supply of chloride ions (chloride solution) to the concrete to maintain the growth of active anodic zones (local pits),
- The addition of strain gauges along the longitudinal length at the effective zone at the inner surface facing the core and strain gauges along the concrete surface was considered. However, they were not added because they are likely to disengage and yield inaccurate or no reading as the reinforcements corrode.
- It would have been insightful to take core samples of the concrete core and test the residual compressive strength.

8.1.2 Loading Test: Concentrically-Loaded Columns

Five RC columns were concentrically loaded after four of them were exposed to accelerated reinforcement corrosion. The followings findings can be concluded from the test:

- Tie corrosion is characterized by localized stains spaced at the 150-mm tie spacing. When all the reinforcement is corroded (longitudinal rebars and ties), extensive rust stains cover the entire surface of the column, with wider cracks (0.95 mm) spreading longitudinally along the rebar length.
- For all columns, a faster rate of crack growth initiated at approximately 70% of the ultimate load and continued until the end of the test.

- The failure mechanism is unique for RC columns with different corrosion levels and patterns. Corrosion of the ties directly affects the column's post-peak response even at low corrosion levels (m_s<5%). The estimated residual ductility and residual toughness were 71% and 38%, respectively, from those of the control specimen, while the axial stiffness was not affected. As the corrosion of the ties increased to m_s<14%), only ductility is affected with a residual value of 50%. A moderate level of tie corrosion reduces the axial stiffness and ultimate capacity to a lesser extent to 85% and 86%, respectively. High levels of corrosion for both transverse and longitudinal reinforcement have more pronounced effects on both ultimate capacity and axial stiffness.
- Low levels of tie corrosion (m_s<5%) affected the column post-peak response by shifting the column response from ductile to brittle. The overall column toughness and ductility were reduced while the axial stiffness and ultimate capacity were maintained. However, an increase in tie corrosion to a moderate level resulted in pronounced damage (cracks and localized staining) to the concrete cover, subsequently reducing the column's ultimate capacity, stiffness, and ductility.
- Unpredicted asymmetrical corrosion of the longitudinal bars and ties for groups 1 and 2 (tie corrosion) led to accidental eccentricities. This led to increased lateral displacement and the development of flexural cracks on the tension side of the column.
- At a higher level of corrosion (m_s>20%) for both transverse and longitudinal bars, there was a significant reduction in the ultimate capacity and ductility of the column.
- Damage of the concrete cover, localized pitting along the bar length and tie corners (junctions), erosion of rebar ribs facing the concrete cover and the reduction in the circumference along the length, corrosion fracture of two of the confining transverse ties in the compression zone, development of concrete cracks along the core concrete, reduction in confining pressure, and localized buckling occurring between two deep pits along the longitudinal bar where the ties were placed.
- A practical, analytical estimation is proposed to estimate the nominal ultimate capacity of corroded columns. This is achieved by combining the reduced strength contributions of the corroded reinforcements and cracked concrete, while considering a reduction in cover and core confinement strengths. The proposed analytical approach agrees with experimental

work on columns with tie corrosion loaded concentrically. Also, it was concluded that the residual lateral pressure of the core concrete initiates at a low level of tie corrosion and decreases to 20% for a very high level of corrosion due to the increase in tie spacing. The reduction in ductility for columns with tie corrosion is attributed to a reduction in core confinement strength as the corrosion level increases.

- Corrosion of the longitudinal reinforcement directly affects the corroded columns' axial capacity, whereas tie corrosion affects the post-peak response of the corroded column.
- Corrosion of the tie and longitudinal reinforcement increases the potential risk of longitudinal reinforcement buckling due to tie corrosion fracture leading to a brittle failure.
- At a high level of corrosion, the core concrete compressive strength is reduced due to cracking and loss of confinement caused by tie corrosion fracture.

8.1.3 Loading Test: Eccentrically-Loaded Columns

The followings remarks can be concluded from analyzing the results of the experimental investigation on the effects of reinforcement corrosion of columns subjected to eccentric loads:

- Columns had a steel-controlled mode of failure (characterized by flexural cracks on the tension side and crushing on the compression side),
- Failure was initiated by yielding of the tensile longitudinal reinforcement at 70% of the peak load for corroded specimens along with a sharp reduction in bond stress. Subsequently, the growth of pre-existing and flexural cracks propagated at a faster rate.
- Reduction in confinement effects (lateral pressure) because of a very high level of tie corrosion (>15%) led to buckling of the longitudinal reinforcement.
- Columns with corroded longitudinal reinforcement may have a gradual failure response as long as the transverse reinforcement is intact or lightly corroded.
- Low levels of tie corrosion affected the post-peak response of the column. At this level of damage, the overall toughness and ductility of the column were reduced, while column resiliency and axial stiffness were not affected.

- As the level of tie corrosion increased to a medium level, the column response shifted to a brittle response, with the axial stiffness and ultimate capacity of the column suddenly decreasing.
- At high levels of reinforcement corrosion, reduction on all structural attributes (ultimate capacity, ductility and toughness, resilience, and axial stiffness) was more prominent. However, it was concluded that corrosion of the transverse reinforcement has a predominant effect on the post-peak response of the column and the reduction in column ductility. In contrast, corrosion of the longitudinal reinforcement has a predominant effect on the reduction of the ultimate capacity.

Comparison between eccentric and concentric loads:

- Cracking development was predominant by flexural cracks and crushing of the concrete, with no significant cracks growth or spalling of the pre-existing corrosion-induced cracks.
- Flexural rigidity did not change as the level of corrosion increased,
- The same trend of increased degradations of the bearing capacity as the level of corrosion increased.

8.1.4 Finite Element Analyses

The developed finite element model was based on modelling the effect of reinforcement corrosion on the structural performance of RC columns. This was achieved by integrating constitutive models while incorporating experimental data and observations into the numerical analyses. The FEM was validated with experimental work from both the literature and this experimental study. The following findings and remarks were concluded:

- The FEM successfully captured column post-peak response (ductile or brittle response) and mode of failure (potential buckling).
- The model predicts very well the maximum bearing capacity of concentrically and eccentrically loaded columns with variations of a maximum of 11%.
- The FEM analyses were extended to model more corrosion scenarios beyond those experimentally tested. The parametric analyses provide a good insight into the structural performance of corroded columns with different corrosion patterns and levels.

- The bearing capacity of concrete-controlled columns decreased significantly as the corrosion level increased from an intact to a high level.
- The bearing capacity of concrete-controlled columns is significantly affected by the degradations of the concrete cover and loss of confinement, and an increase in the eccentricity values.
- The bearing capacity of steel-controlled columns is significantly affected by the degradations of the mechanical properties of the reinforcement (yield strength and ductility) and loss of confinement due to tie fracture.
- In developing the FEM, a high level of tie corrosion was modelled by completely removing the affected tie. Experimental findings supported this decision because the ties were very brittle and fractured at a high level of corrosion.
- Columns had a steel-controlled mode of failure (characterized by flexural cracks on the tension side and crushing on the compression side) for specimens C-E-T3/4 and C-E-R1/2.
- The longitudinal reinforcement on the tension side underwent a large relative displacement (slip) through the surrounding concrete. As a result, the corresponding tractions increased with the increase of the applied loads. Then, a sharp decrease in the local traction stress occurred as the deformed tensile rebar yielded.
- There is a general trend for both concentrically and eccentrically loaded columns where the peak bearing capacity is reduced as the corrosion level increases from intact to very high. Moreover, the corroded columns shift from ductile to brittle response at a low level of tie corrosion for specimens C-C/E-T1, C-C/E-T2, C-C/E-T3 and C-C/E-T4. Buckling of the longitudinal reinforcements was evident for very high levels of tie corrosion due to loss of confinement effects for specimens C-C/E-T5.
- At high levels of reinforcement corrosion, there is a significant reduction in the bearing of the corroded columns. However, it was concluded that corrosion of the transverse reinforcement has a predominant effect on the post-peak response of the column and the reduction in column ductility for specimens (C-C/E-T1, C-C/E-T2, C-C/E-T3, C-C/E-T4). In contrast, corrosion of the longitudinal reinforcements for specimens (C-C/E-ALL1 and C-C/E-R1 and C-C/E-R2) has a predominant effect on reducing the ultimate capacity. The

corroded column can maintain its ductile response (continue to deform) as long as the ties are intact or lightly corroded, as observed in specimen C-E-R5.

- The residual strength of eccentrically loaded columns is 18-24% of the concentrically loaded columns.
- Corrosion of the ties at a low level (ms ≤5%) primarily affects the column's post-peak response for both concentrically- and eccentrically-loaded columns. In contrast, the ultimate strength was slightly reduced by less than 5%.
- When the corrosion level of the ties increased to a medium level, the residual strength decreased to 86% and 89% for concentrically- and eccentrically-loaded columns, respectively. There was no evidence of tie fracture.
- For a high level of tie corrosion (m_s >15%), ties fractured at the corners. This is similar to the findings reported by Vu et al. (2017). In comparison with Tapan et al. (2016), the author found that at a medium level of tie corrosion, the residual strength was 89%.

For a high level of corrosion of both transverse and longitudinal reinforcement, there is a significant reduction in strength associated with a reduction in core pressure due to pitting fracture of the ties and subsequent bar buckling. It was estimated that the residual lateral pressure reduction increases by 10% as the level of mass loss of the ties increases by 5%.

8.1.5 Estimation of the Bearing Capacity of the Corroded Columns

The following findings were concluded from the estimation of the bearing capacity of corroded columns:

- The conventional approach of estimating the axial and flexural capacities of the columns cannot be used safely to determine the capacity of corroded columns. The effect of reinforcement corrosion on the mechanical and geometrical properties of concrete and steel should be considered.
- There is a general trend where all concrete-controlled columns had a significant decrement in the bearing capacity as the corrosion level increased from an intact to a high level.
- The bearing capacity of concrete-controlled columns is significantly affected by the degradations of the concrete cover and loss of confinement, and an increase in the eccentricity values.

- There is a significant drop in the bearing capacity as corrosion and eccentricity are increased for concrete-controlled columns compared to steel-controlled columns.
- Reduction in the load-bearing capacity for steel-controlled columns is governed by degradations of the mechanical properties of the transverse and longitudinal reinforcement and bond loss.
- There is a higher reduction in the bearing capacity for concrete-controlled columns with corrosion along the transverse and longitudinal reinforcement. Moreover, there is a greater risk of buckling when the ties suffer from more than 15% mass loss (medium level). When the extent of tie corrosion is medium or higher, the restraining and confinement effects are significantly reduced (80% reduction in lateral pressure).
- The axial and flexural capacities of column with corroded transverse reinforcement are analytically estimated by reducing the compressive strength of the concrete core and cover for low and medium levels and by decreasing the mechanical properties of the transverse reinforcement.
- For high levels of corrosion, the bearing capacity is reduced by removing all four corner sections of the concrete cover (about 65 mm from the edge). This was supported by experimental observations where all four corners were stripped off the column.
- For corroded columns, 10% of the cover thickness is reduced from the original thickness for low levels of corrosion, while 50% of the cover was removed for medium and high levels of corrosion.
- As the level of corrosion increases, the contribution of the concrete cover to the bearing capacity reduces due to deterioration (cracking and spalling). At 26% mass loss of reinforcement corrosion, 50% of the concrete cover was ineffective.
- The behaviour of the column subject to axial compressive loads strongly relies on the level of confinement provided by the transverse reinforcement
- The risk of potential buckling of the longitudinal reinforcement is checked for corroded reinforcement acting in compression. At the same time, bond degradation is accounted for the reinforcement acting in tension by applying a reducing factor.
- The proposed model accounts for bond degradation at different levels and patterns of reinforcement corrosion. Corrosion damage is considered by reducing concrete cover and

core strength, concrete cover area, mechanical properties of steel while accounting for potential buckling of the longitudinal reinforcements.

The proposed analytical estimation provides a simplified tool for practicing engineers to predict corroded RC columns' axial and flexural bearing capacity. This is done by integrating theoretical models and incorporating field observations. The estimation can also be verified with FEM utilizing the adopted methodology.

8.1.6 Limitations

- Experimental testing of large-scale corroded columns is challenging to execute and extend for a long period of time. As a result, some of the applied current densities are higher than those observed in the field. Furthermore, the results presented in this thesis are limited to the corrosion levels and patterns attained in the experimental testing.
- Corroded columns are comparable only with those corroded at roughly the same corrosion rate, otherwise, results may potentially be misleading. For example, group 1 compares with group 2, while group 3 compares with group 4.
- The analytical approach requires a good understanding of the overall axial and flexural performance of the RC columns and a comprehensive collection of field data by a practicing engineer to accurately predict the ultimate capacity of corroded columns.
- The analytical approach predicts only the ultimate capacity of corroded columns. To evaluate the post-peak response (displacement) of columns, FEA is required.

8.2 Future Research

The primary and most recognizable theories inducing frost damage (hydraulic and osmotic pressure) provide a good understanding of the mechanism of frost damage in concrete. Most of the studies investigating the effect of freeze/thaw cycles on concrete have focused on the impact of frost damage on concrete mechanical properties (compressive and tensile strength, elastic modulus) or its interaction with reinforcing steel (bond). A review of the literature has shown that there is a significant reduction in the mechanical properties of concrete with an increase in the number of FTC.

This is essential to explore as the effect of frost damage on material deterioration and structural performance of RC columns is not fully understood. A minimal number of experimental tests on RC columns under the effect of FTC with/without reinforcement corrosion and subjected to either sustained or seismic loading has revealed that cumulative exposure to FTC resulted in a decrease in the bearing capacity due to strength reduction and overall stiffness degradation, in addition, to change to a brittle failure mode. With the increase in extreme weather conditions due to climate change, it is necessary to thoroughly investigate the effect of multiple deteriorating environmental mechanisms such as FTC and exposure to salt-laden wetting and drying that lead to structural deterioration of RC bridge columns at an accelerated rate. The review of the literature has therefore identified several research gaps, as outlined below, that could dictate potential future research:

- Currently, there is limited research available investigating RC columns' structural performance (in terms of ultimate capacity, ductility, stiffness and failure mode) under the effect of FTC. More experimental testing should be carried out to investigate the effect of frost damage on the structural performance of columns of various sizes, cross-sectional shapes, material compositions, reinforcement layouts and loading conditions.
- These limited number of experimental tests on columns have relied on existing standard methods and procedures to evaluate the effects of FTC, mainly based on the two equivalent standards ASTM C666 and GB/T50082 to test concrete resistance to rapid FTC (ASTM 2015 and Chinese standard 2009). The shortcoming of these standards' tests is that they are specified for small unreinforced concrete specimens. In structural RC members, the temperature in concrete is not uniform across the section, and thus the subsequent frost damage along the depth of the concrete section due to FTC is not uniform. Testing protocols for large structural members subjected to FTC should be developed. At the very least, there is a need for more research to adapt existing testing standards to larger scale of RC specimens.
- The impact of frost damage on RC columns should be studied along with the damage induced by reinforcement corrosion. While there are several studies on the effect of reinforcement corrosion on the structural response of RC members, there is a lack of understanding of its synergistic effect with other concrete deterioration mechanisms such as frost damage. Limited experimental work investigating the combined effect of seawater immersion and FTC on columns under either sustained or cyclic load has revealed a reduction in both ultimate capacity

and ductility. There is, therefore, a need to extend experimental efforts to study the combined impact of FTC and reinforcement corrosion on RC columns' performance.

- The aforementioned research gaps can be further addressed and complemented by integrating deteriorating models into 3D nonlinear finite element modelling to explore scenarios beyond those tested in a laboratory setting. The effect of frost damage and reinforcement corrosion on the structural response of columns can be modelled as a change in the mechanical properties of both concrete and steel materials. In addition, these modelling efforts should account for the bond-slip behaviour between longitudinal bars and concrete (for eccentrically-loaded columns), the confinement effects of the concrete core and strength reduction of the concrete cover, and the buckling potential of longitudinal reinforcement. Such a modelling approach would enable evaluating the structural performance (ultimate strength, ductility, stiffness and failure mode) of RC columns under the effects of frost damage, reinforcement corrosion, and their combined effect. Once validated with test data, numerical modelling complements experimental testing by allowing for parametric studies that highlight the role of essential variables and from which simplified expressions can be proposed to be used by the engineering community to assess affected RC columns.

Appendix A. Combined Effects of Multiple Deteriorations Mechanisms on the Performance of RC Columns

A.1. Frost Damage Mechanism

The primary mechanism of frost damage in concrete in the presence of de-icing salts is described by both the hydraulic pressure theory developed by Powers (1949) and the osmotic pressure theory by Power and Helmuth (Powers and Helmuth 1953, Hudec 1991; Pigeon 1996; Valenza and Scherer 2007). Although one mechanism might dominate the other during FTC, depending on pore size (osmotic pressure dominates in concrete with relatively small pore size), both mechanisms are attributed to concrete deterioration (Powers 1975; Hudec 1991). Internal frost damage is caused by the thermal expansion of freezing water and ice in the concrete pores. Ice or freezing water occupies a larger volume than water by 9% (Fagerlund 1993). As a result, freezing water escapes or redistributes to the surrounding empty and larger pores during a freezing cycle (Valenza and Scherer 2007). When water molecules held in the pores displace quickly, pressure is relieved by Darcy's flow mechanism; otherwise, hydraulic pressure develops (Valenza and Scherer 2007). Incorporating salt into the concrete's pore solution exposed to FTC significantly aggravates concrete deterioration (Hudec 1991). Hudec (1991) found that low concentrations of NaCl (3%) accelerate the scaling of the concrete surface due to the higher osmotic potential generated between the pores (see Fig. A.1). It is found that the osmotic potential decreases above a NaCl concentration of 5% until the potential ultimately diminishes at 20% concentration when the concrete pores are fully saturated. At this point of 20% concentration, the pores can no longer adsorb more ions but rather repel them (Hudec 1991).

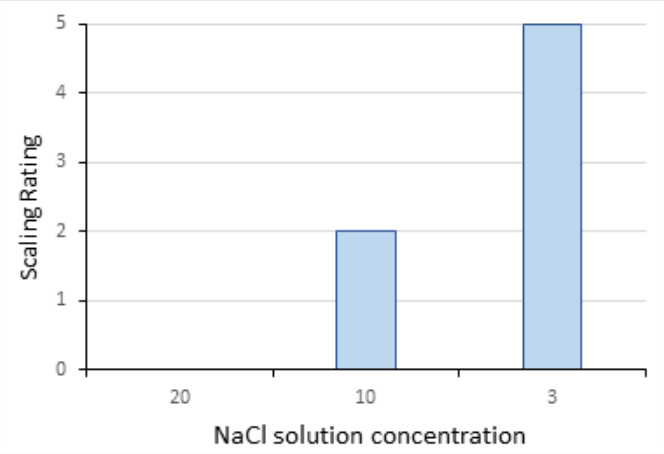

Fig. A.1: Scaling of the concrete at NaCl concentrations of 3%, 10% and 20% (reproduced from Hudec 1991)

It is essential to understand that although salt reduces the overall freezing point of the water and subsequently the hydraulic pressure caused by freeze-thaw action, salt addition to the concrete accelerates concrete deterioration. This is because salt ions accelerate the degree of saturation of the pores (Hudec 1991). In a concrete network comprised of a large ratio of small-to-large pores, small pores hold adsorbed water (a thin layer of water adhering to the surface of the concrete pores), whereas large pores are filled with water (Hudec 1991). Only the solution in large pores freezes during the freezing stage (Sun et al. 2020). Furthermore, since vapour pressure is proportional to the pore radius, small pores will have a low vapour pressure compared to normal pressure in large pores, which creates a pressure differential (Hudec 1991). As a result, water molecules with high vapour pressure and low concentrations of salt diffuse from large pores to smaller ones by osmosis until the pores are fully saturated (Hudec 1991). The osmotic flow creates expansive forces against the walls of the pore that eventually exceed the tensile strength of the concrete leading to cracks (Hudec 1991; Sun et al. 2020). The osmotic flow creates expansive forces against the walls of the pores that eventually exceed the concrete's tensile strength leading to cracking (Pigeon et al. 1996). As a result, the chloride ions concentration in small pores is increased (Sun et al. 2020). During the thawing stage, chloride ions migrate to small pores (Sun et al. 2020). According to Sun et al. (2020), the cyclic phase changes of the pore solution during the freeze/thaw process promote the migration of salt ions within the pores into the deeper layers of concrete, accelerating concrete deterioration. The freezing of water in large pores diffuses salts to

small pores, as shown in Fig. A.2. As a result, the concentration of the solution in small pores is increased, and the number of small pores along with the capillaries active in the process of osmosis is increased. On the other hand, thawing of ice increases the vapour pressure at the large pores (Hudec 1991). Thus, salt addition accelerates concrete deterioration due to an increase in pores and capillaries occupied by adsorbed water and affected by the osmosis mechanism (Hudec 1991).

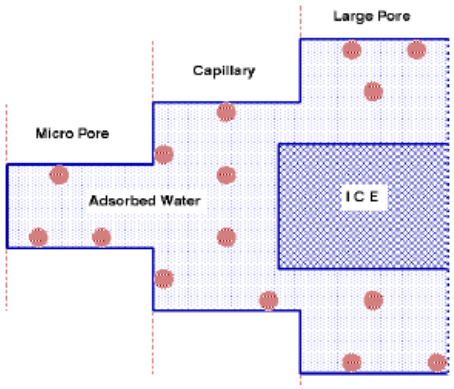

Fig. A.2: Freezing of water in large pores expels salt into smaller pores (reproduced from Hudec 1991)

In reality, the action of freezing/thawing can occur at different states of concrete saturation. In general, throughout these states, the strength and resilience of concrete are reduced (Powers 1945). However, at the critical saturation point (>91% pore saturation), the concrete paste is no longer capable of withstanding the hydraulic pressure imposed by the development of ice (Valenza and Scherer 2007). Subsequently, concrete disintegrates and is neutralized by the development of micro-cracks propagating outward-inward (Powers 1945; Petersen et al. 2007). This is because when ice is restrained, internal tensile stresses develop as ice pushes against the cement paste. This, in effect, leads to cracks, scaling and concrete spalling. The cause of damage in concrete is attributed to thermal expansion of ice in concrete and volume expansion of freezing water in concrete. Cracks development is aggravated by the presence of de-icing agents (Pigeon 1995).
In general, FTC causes both external and internal damage. The two events are independent of each other and should be considered separately according to Pigeon et al. (1996):

1. External damage: scaling and spalling, which does not affect the mechanical properties of the concrete,
2. Internal damage: cracks and bond-slip, which affect the mechanical properties of the concrete.

A.2. Modelling Frost Damage

The internal damage due to freeze/thaw action alone is modelled by applying thermodynamics concepts using a poor mechanical approach at a mesoscale level (the level at which unfrozen water redistributes and frozen ice produces internal cracks) as proposed by Gong and Maekawa (2018). As mentioned before, the internal stress-inducing cracks are developed due to a combination of hydraulic, crystallization (pressure induced due to formation of ice crystals) and cryo-suction pressure (pressure induced as a result of the thermodynamic equilibrium between ice and liquid water, water migrating to the freezing region through capillary action), as expressed by and illustrated in Fig. A.3 (Gong and Maekawa 2018):

$$P = P_{Hydraulics} + P_{Crystalization} + P_{Cryo} \qquad \textit{Eq. A.1}$$

Where $P_{Hydraulics}$ is the hydraulic pressure, $P_{Crystalization}$ is the crystallization pressure, and P_{Cryo} is the cryo-suction pressure.

The damage due to volume increase as a result of ice formation is roughly calculated using the following equation:

$$\Delta V_{ice}^{'} = \Delta V_{ice} - Q = 0.09 S_{ice} \phi \varphi_{cp} - 0.1 \phi_{air} \qquad \textit{Eq. A.2}$$

Where ΔV_{ice} is the total volume increment, Q is the volume consumed by effective air bubbles (amount of water into entrained air), S_{ice} is the ice saturation, ϕ_{air} is the total air content, φ_{cp} is the volume ratio of the paste in the concrete, and f is the total void ratio of the cement paste excluding air bubbles.

The total stress is defined as the stress due to solid ice plus the effective stress on the concrete skeleton and liquid pore pressure (Gong and Maekawa 2018). Permeability of the concrete is enlarged significantly along two directions, k_1 and k_3, following a crack opening as shown in Fig. A.4.

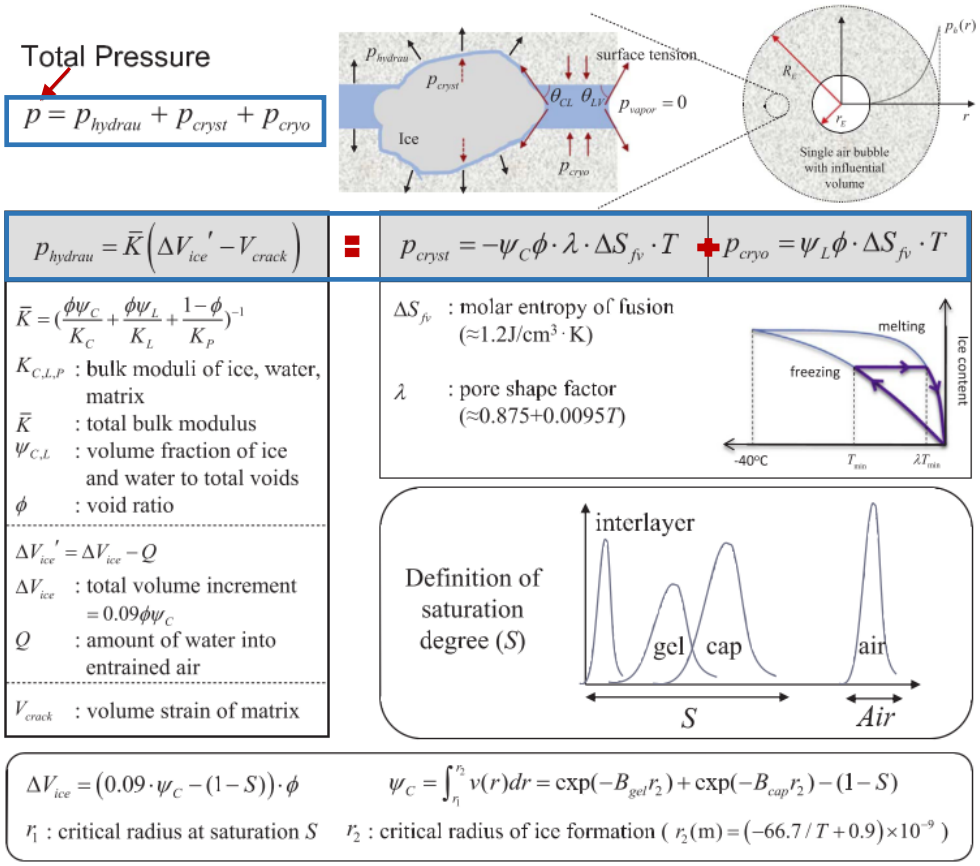

Fig. A.3: Estimation of total pressure developed due to FT action (reproduced from Gong and Maekawa 2018)

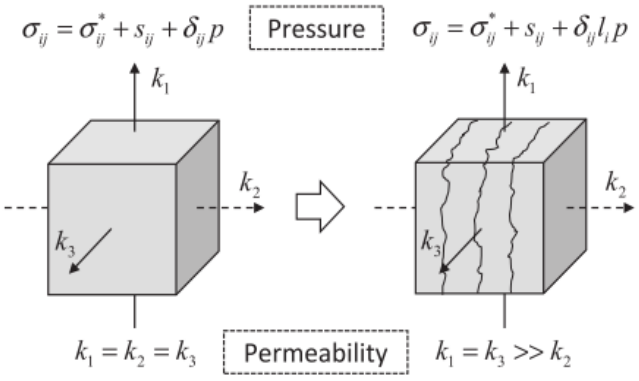

Fig. A.4: Total stress due to FT action (reproduced from Gong and Maekawa 2018)

Montejo et al. (2008), Xu et al. (2016), Qin et al. (2017) and Gong and Maekawa (2018) found that as the number of FTC increases, the bearing capacity and ductility of concrete decreases significantly. This effect is more significant as the specimen size is increased due to heat transfer effects, which are variable along the concrete depth and conductivity of the material incorporated in (Gong and Maekawa 2018). Temperature change along the depth of the RC specimen is estimated using a 3D thermal conduction equation (Gong and Maekawa 2018).

A.3. FTC Effects on Concrete Mechanical Properties

Several researchers have studied the effects of frost damage on the physical and mechanical properties of concrete (Hasan et al. 2004; Shang and Song 2006; Petersen et al. 2007; Hassanzadeh & Fagerlund 2007; Hanjari et al. 2011; Duan et al. 2011). They relied on damage indicators: i) compressive strength, ii) tension strength, iii) modulus of elasticity, and iv) bond-slip response, to give a detailed description of the changes that occur to the specimens upon cyclic exposure to FT. Hasan et al. (2004) conducted experimental tests on cylinders and prisms according to ASTM C666 to determine the stress-strain relationship in compression and tension of concrete. The authors also proposed a numerical simulation with meso-scale models for stress-strain relationships. Shang and Song (2006) conducted an experimental study on the strength and deformation of plain concrete by applying a biaxial compression load, instead of the standard uniaxial compression, against concrete cubes and prisms after exposure to FTC, which were conducted according to the GB/T 50082-2009 standard test method. Petersen et al. (2007) examined the internal damage and distribution of FT action along the concrete depth using ultrasound measurements. The FTC experiments were performed according to RILEM tc176. Hanjari et al. (2011) studies were aimed towards not only understanding the effects of FTC on concrete but also quantifying a test methodology to assess deteriorated structures when subjected to mechanical loading and FTC conditions. Contrary to previous analytical models, which were mainly focused on mechanical behaviour of concrete after FTC, Hanjari et al. (2011) also proposed an analytical analysis framework to quantify damage of concrete structures due to mechanical loading and FTC. Both experimental and numerical testing were conducted according to RILEM TC 176-IDC and finite element analysis using Diana software, respectively. In the analytical analysis, Hanjari et al. (2011) analyzed the structural performance of RC beams following FT

damage. The authors validated the numerical results with experimental results reported by Hassanzadeh and Fagerlund (2007). On the other hand, Duan et al. (2011) conducted experiments to determine the stress-strain relationship along with the compressive strength of unconfined and confined columns and prisms using different concrete strengths after exposure to FTC according to the GBJ85-82 standard.

A.3.1 Compressive Strength

Shang and Song (2006) and Hasan et al. (2004; 2008) found that the static strength of concrete is reduced as the number of FTC is increased. Shang and Song (2006) applied a biaxial compressing loading on plain concrete cubes and prisms after FTC exposure. The authors found that the biaxial compression strength is greater than that of uniaxial compression after FTC exposure. They attributed this added effect on strength and deformation to the confinement effect produced by the stress-induced in the other direction. However, the ultimate biaxial strength in compression is reduced after FTC compared to non-exposed specimens, just at a lower stress rate than the case of uniaxial load application. Hasan et al. (2008) found that specimens exposed to FTC have considerable strain following the peak stress and exhibit a ductile behaviour compared to non-damaged ones (Hanjari et al. 2011). From the uniaxial compression tests they conducted, the authors found that there is a reduction in the compressive strength and initial static elastic modulus in compression. Hasan et al. (2004) developed a stress-strain model based on the reduction in the initial value of stiffness under the application of static and fatigue loading exposed to cyclic FT exposure. They attributed the linear reduction in the compressive strength and stiffness to the significant increase in the tensile plastic strain (also referred to as FTC equivalent plastic strain) as the number of FTC is increased (Fig. A.5).

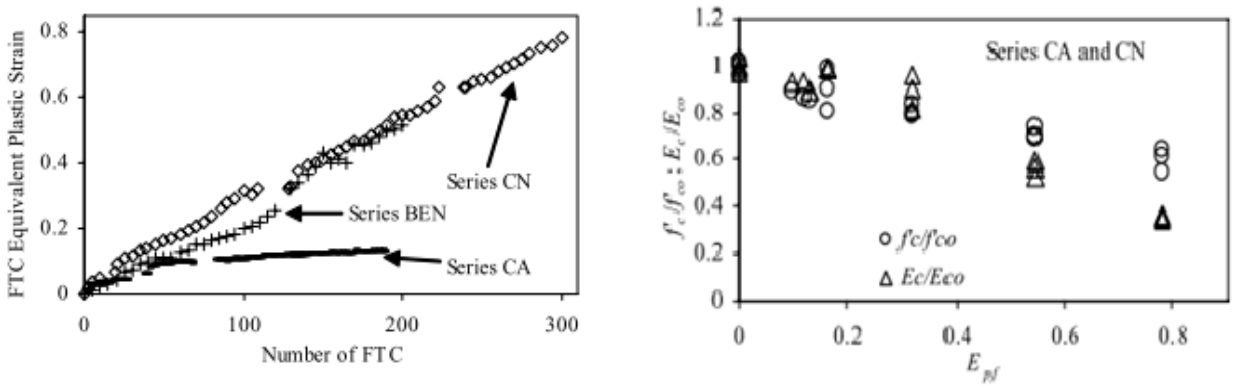

Fig. A.5: Left: Increase in the plastic tensile strain as FTC is increased, Right: Compressive strength and stiffness reduction with the increase of FTC equivalent plastic strain (Reproduced from Hasan et al. 2004)

Hanjari et al. (2011) applied a uniaxial compression test to analyze the mechanical response of concrete cylinders after FTC exposure. Tests results concluded that there is a 25-50% reduction in compression for damaged concrete cylinders, in addition to stiffness loss, as shown in Fig. A.6. Duan et al. (2011) compared the compressive strength of unconfined columns and found that as the number of FTC increased, there was a linear decrease in the value of the compressive strength for unconfined (plain concrete) columns. Meanwhile, the peak strain is increased due to the concrete's softening effect (increase in concrete strain). After FTC exposure, the columns were subjected to a uniaxial compressive load. For unconfined columns, it was observed that the 28-day compressive strength decreases, and strain increases as the number of FTC increases. Subsequently, the modulus of elasticity continuously decreases as illustrated in the stress-strain curve developed in Fig. A.7.

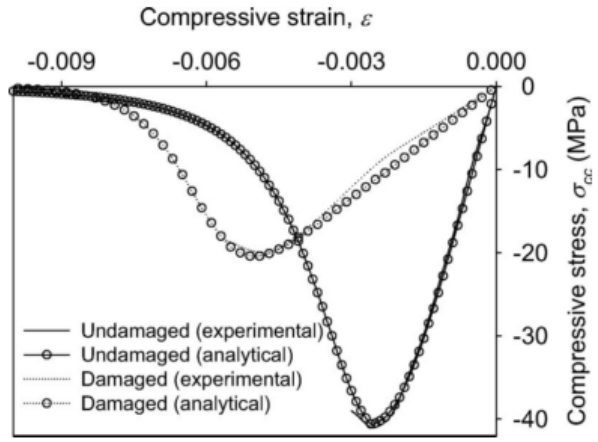

Fig. A.6: 50% reduction in the compressive strength of FTC damaged specimens (Reproduced from Hanjari et al. 2011)

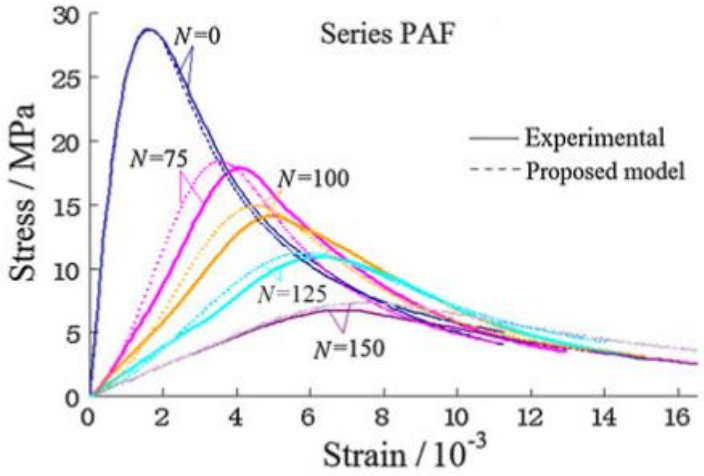

Fig. A.7: Stress-strain curve for unconfined concrete after FTC exposure (Reproduced from Duan et al. 2011)

Duan et al. (2011) found that a lower value of $f_c^{'}$ (the 28-day compressive strength of the concrete) leads to lower value of the ratio $\frac{f'_{CD}}{f'_{CO}}$ (expression of the ratio of the compressive strength of the concrete after FTC ($f^{'}_{CD}$) to the compressive strength before FTC ($f^{'}_{CO}$)) (Fig. A.8). Using a regression method, the following equation was developed:

$$\frac{f_{CD}^{'}}{f_{co}^{'}} = 1 - 200N \times f_c^{-3.0355} \qquad \textit{Eq.A.1}$$

where f'_{CD} is the compressive strength after FTC exposure, f'_{c0} is the compressive strength before FTC exposure, and *N* is the number of FT cycles.

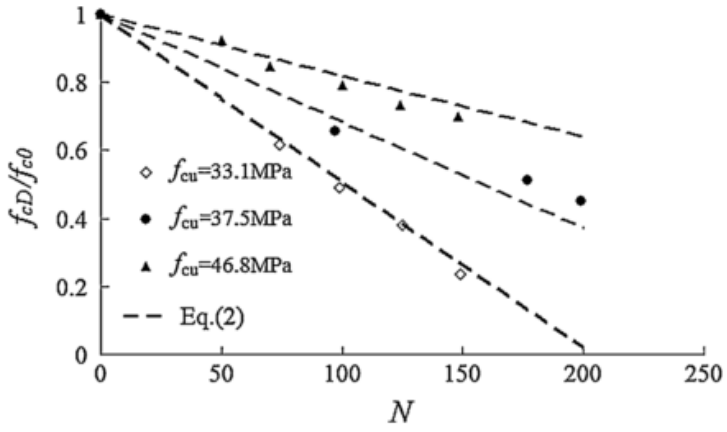

Fig. A.8: Normalized compressive strength of the concrete after N (number of FTC) for different concrete strengths (Duan et al. 2011)

A.3.2 Tensile Behaviour

Hasan et al. (2004) also found a linear relationship between the reduction in the tensile strength and the reduction of both the RDME and stiffness as the number of FTC, expressed in equivalent plastic strain, is increased after a strain value of 0.24 (Fig. A.5). Comparison with FTC damaged specimens response in compression, illustrated in Fig. A.9, shows a reduction in RDME, compression strength, and stiffness values occur almost immediately. This indicates that the behaviour of FTC damaged specimens is different in compression and tension. The authors attributed this to the fact that reduction in compression strength is associated with the increase in plastic strain, whereas reduction in tensile strength is associated with the development of cracks. The concrete behaviour in tension has been analyzed using splitting tensile and wedge tests (Fagerlund 1994; Shang and Song 2006; Hanjari et al. 2011). More damage has been observed for concrete in tension compared to compression (Hanjari et al. 2011). However, there is not enough information on the tensile softening behaviour of concrete, which is essential for modelling (Hanjari et al. 2011). Therefore, Hanjari et al. (2011) proposed a bi-linear relation between tensile stress and crack opening (σ–w) using inverse analysis with results from splitting wedge tests, and

then the relation was inputted into finite element analysis for frost damaged specimens. In this analysis, it was observed that at zero tensile stress, the fracture energy and critical crack opening notably increased for damaged specimens (Hanjari et al. 2011) (Fig. A.10). Hanjari et al. (2011) results showed a 29% decrease in the tensile strength along with crack opening and an increased in the fracture energy as the number of FTC is increased.

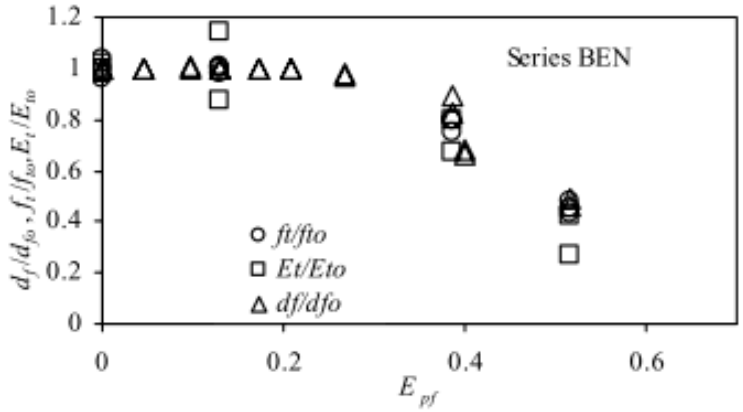

Fig. A.9: RDME, tensile strength and stiffness reduction with the increase of FTC equivalent plastic strain (Reproduced from Hasan et al. 2004)

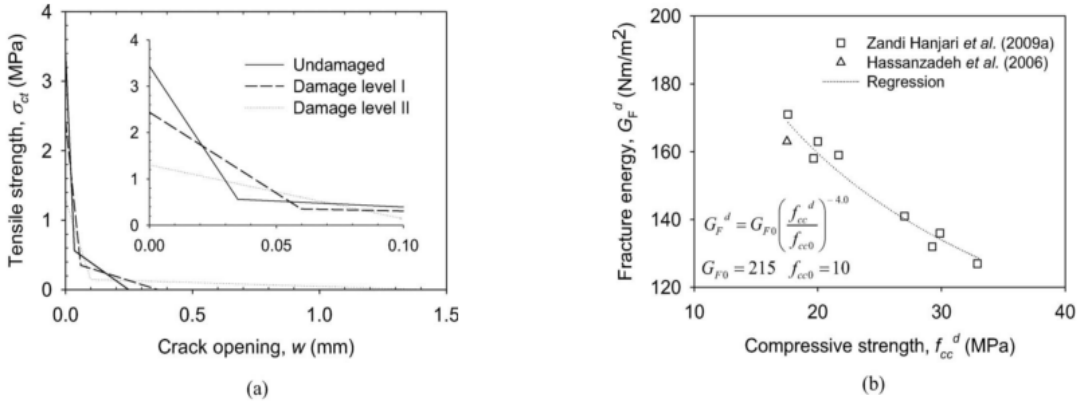

Fig. A.10: a) Reduction in tensile strength along with crack opening (Level I & II corresponds to 25 and 50% reduction in compressive strength), b) fracture energy after applied tests (Hanjari et al. 2011)

A.3.3 Modulus of Elasticity

Shang and Song (2006) defined the Relative Dynamic Modulus of Elasticity (RDME) as the ratio of the dynamic modulus of elasticity measured after FTC to the initial modulus of elasticity prior

to FTC. The authors measured the RDME from 25 up to 75 FTC. The authors defined a 60% reduction in the value of RDME as a failure criterion and an indication of FTC-induced damage. Shang and Song (2006) found that increasing the FTC results in a reduction in the elastic modulus of elasticity for both uniaxial and biaxial compression loading. It was estimated that there is a 62% and 59%, respectively, reduction in the elastic modulus of elasticity after 50 FTC, as shown in Fig. A.11, illustrates the influence of increasing the number of FTC, conducted at various stress ratios α, on the reduction of the elastic modulus. In addition, it illustrates that increasing the stress ratios α under biaxial compression increases the value of the elastic modulus for the same number of FTC.

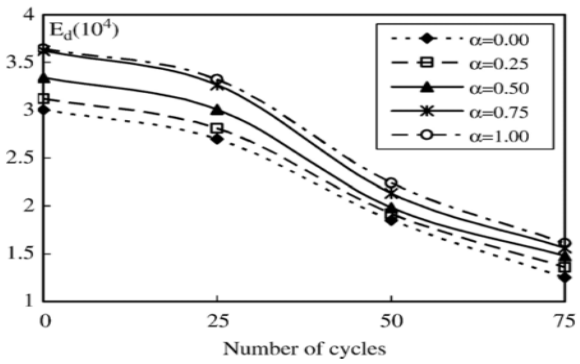

Fig. A.11: Reduction in the elastic modulus of elasticity as a function of FTC (Reproduced from Shang & Song 2006)

Hasan et al. (2004) also observed a reduction in the initial modulus of elasticity as a function of the equivalent plastic strain under the application of compressive loads and FTC, as shown in Fig. A.12. The authors observed that the reduction in compressive strength due to FTC is accompanied by an increase in the equivalent plastic strain Fig. A.5. However, the authors did not establish a relationship between the compressive strength and the dynamic modulus of elasticity (Fig. A.13). On the other hand, tensile strength and stiffness reduction due to FTC is attributed to crack development, which is determined by the reduction of the RDME (Fig. A.14).

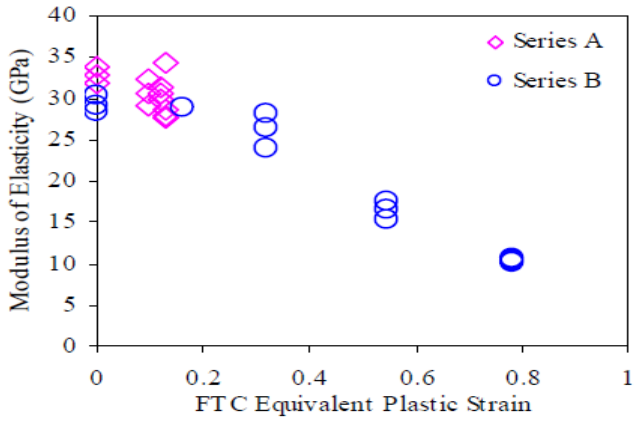

Fig. A.12: Reduction in the initial modulus of elasticity as a function of the equivalent plastic strain (Hasan et al. 2004)

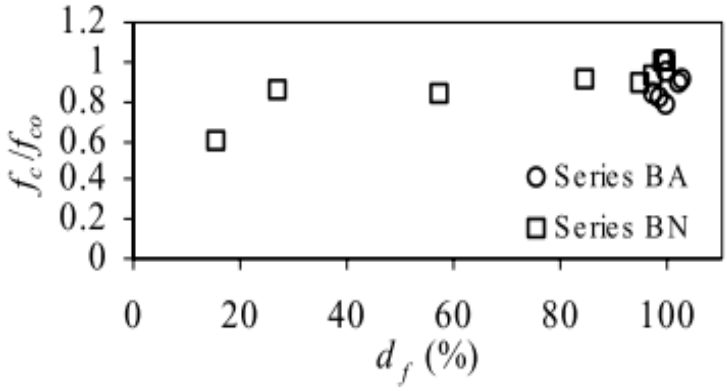

Fig. A.13: Compressive strength as a function of the RDME (Reproduced from Hasan et al. 2004)

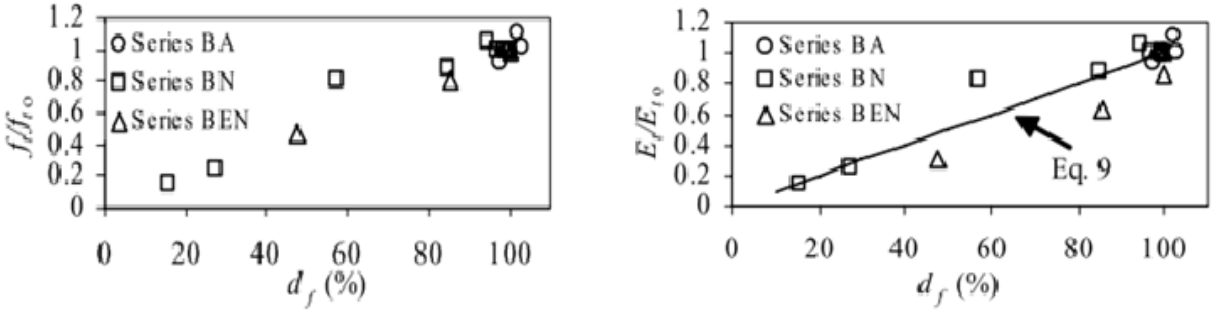

Fig. A.14: Left: Tensile strength as a function of the RDME, Right: Tensile stiffness as a function of the RDME (Reproduced from Hasan et al. 2004)

Petersen et al. (2007) and Hanjari et al. (2011) believe that the dynamic modulus of elasticity is a substantial damage indicator for frost damage in concrete. Such that the growth in the internal damage due to the rise in the number of FTC is described by the RDME (Petersen et al. 2007; Qin et al. 2017). Hanjari et al. (2011) found that the RDME decreased to 80% after 20 FTC (according to RILEM TC176-IDC test method). The authors used this value as a failure criterion for the specimens to be considered damaged. Petersen et al. (2007) used ultrasound technology to measure the value of the dynamic modulus of elasticity and compared its value to the static value. The author found that internal damage within the concrete microstructure lengthens the travel time of the wave emitted through the concrete depth and reduces the value of the dynamic modulus of elasticity. Hence, the difference between the dynamic modulus of elasticity and the static one becomes large. The static modulus of elasticity is determined according to German standard DIN 1048-5:1991-06.9. Furthermore, Petersen et al. (2007) found that the degree of deterioration in concrete due to FT action varies from the outer surface through the depth of the concrete cross section. The internal damage, described by the RDME and obtained from ultrasonic measurements, is more evident at the surface and spread along the depth of the concrete, as shown in (Fig. A.15).

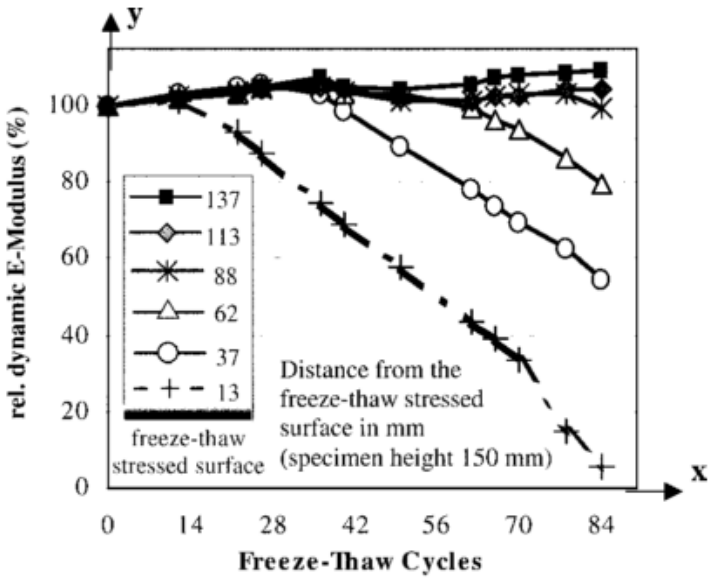

Fig. A.15: RDME as a function of the number of FTC (Petersen et al. 2007)

By applying regression analysis to their experimental results, Petersen et al. (2007) proposed an equation for the static modulus of elasticity at different depths for specimens exposed to FTC (E_{ci}^{d}), and it is given in Eq. 9.4:

$$E_{ci}^{d} = \left(0.9RDME - 0.06\right) \times E_c \qquad \textit{Eq.A.2}$$

where $E_c = 5000\sqrt{f_c}$ is the static modulus of elasticity for undamaged specimens (MPa), and f_c is the compressive strength of concrete in MPa.

Duan et al. (2011) measured the elastic modulus as the secant modulus at 40% of the peak stress. The author found that with the reduction in the compressive strength after exposure to FTC, there is a reduction in the value of the modulus of elasticity of the concrete due to concrete softening (Fig. A.16). Furthermore, the decrease in the value of the normalized modulus of elasticity is more significant for concrete with lower 28-day compressive strengths (f'_c), as shown in (Fig. A.16). From the regression analysis, Duan et al. (2011) expressed the normalized modulus of elasticity as follows:

$$\frac{E_{CD}}{E_{c0}} = \exp\left(-1.1345\times10^{7}\, f_c^{-5.7089}\right) \times N \qquad \textit{Eq. A.3}$$

Where E_{CD} is the modulus of elasticity after FTC exposure, while E_{C0} is the modulus of elasticity before FTC exposure, N is the number of FTC, and f'_c is the 28-day compressive strength (MPa).

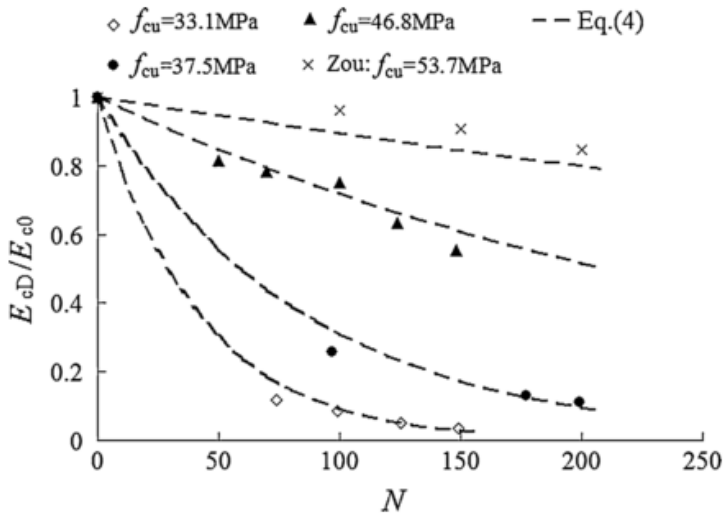

Fig. A.16: Normalized modulus of elasticity vs. N (number of FTC) for different concrete strengths (Reproduced from Duan et al. 2011)

A.3.4 Bond-Slip Behaviour

Shih et al. (1988) found that frost damage on the concrete cover significantly decreased the bond strength between concrete and the reinforcement as the number of FTC increased. There is an observed 15% to 50% reduction in bond strength between concrete and reinforcement (Hanjari et al. 2011b). Fagerlund (1994) suggested a 30% to 70% reduction. Hassanzadeh and Fagerlund (2006) conducted experimental work on beams with different cross-sections and reinforcement ratios. Results showed that frost effects reduced the bond strength, stiffness and strength capacity of the beams. Beams had a reduced compressive strength and, as a result, had a brittle type of failure, such that the beams failed due to compression fracture instead of reinforcement yield-typical failure. Also, it was observed that there is an overall reduction in the load-carrying capacity due to FT damage. The beams tested by Hassanzadeh and Fagerlund (2006) were analyzed using a 2D finite element model. The beams were modelled using plane-stress elements. The interaction between the longitudinal reinforcement and the concrete was modelled with a bond-slip mechanism. Moreover, the transverse reinforcement was embedded in the plane-stress concrete elements by assuming the entire interaction. Hanjari et al. (2011) completely immersed their specimens in the water while Petersen et al. (2007) immersed their specimens in water from one side only, which required more cycles to achieve the same FT damage (Qin et al. 2017). Petersen et al. (2007) conducted pull-out tests to determine the relationship between bond stress and slip

response between the concrete and steel. Results in Fig. A.17 illustrate a linear decrease in the bond stress and a linear increase in the slip along the concrete cover following pull-out tests. However, the degree of slip values and bond stress varies with the degree of deterioration in the concrete along the depth. Specimens were exposed to high-to-low degrees of damage from cyclic exposure to freeze/thaw (specimens A to C). Thus, specimens A to C response shows a trend associated with the degree of damage, a linear increment in the bond stress until it reaches a peak value along the concrete cover followed by an accelerated decrement in the bond tension and an increase in the slip value when the damage reaches the reinforcing bars, as illustrated in (Fig. A.17) (Shih et al. 1988; Petersen et al. 2007; Hanjari et al. 2011). However, since specimens A to C were exposed to a higher degree of damage, higher values in the maximum bond stress and a faster rate in the drop of the slip value were observed. At 0.5 slip value, specimen A had a bond tension of 0.4, while specimen C had a 0.5 tension value (Fig. A.17). Fig. A.17 also illustrates that frost damage need not reach the reinforcement layer to initiate loss in bond strength; frost damage can initiate at the concrete cover even at a low number of FTC.

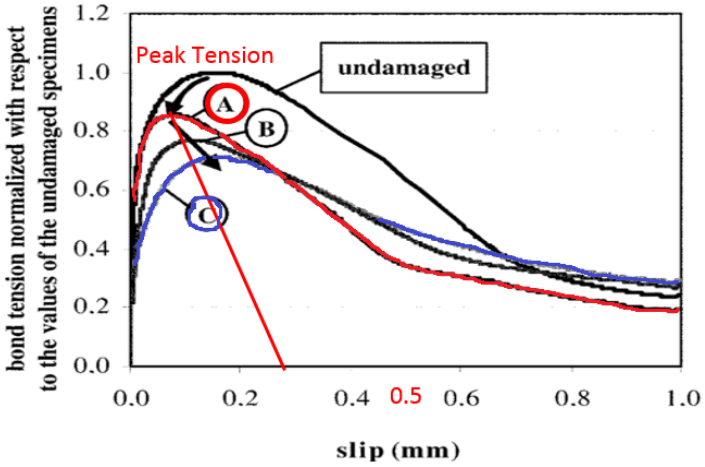

Fig. A.17: Relationship between the bond stress and slip following cyclic exposure to freeze/thaw (adapted from Petersen et al., 2007)

Petersen et al. (2007) proposed an empirical relation to estimate the reduction in bond strength due to frost damage given by:

$$\left(\tau_{max}\right)^{d} = \left(0.17 + 0.007E_{rdy}^{d}\right)\tau_{max} \qquad \textit{Eq. A.4}$$

Where $(\tau_{max})^d$ is the bond strength of damaged concrete (MPa), τ_{max} is the bond strength for non-damaged concrete (MPa), and $(E_{rdy})^d$ is the RDME for damaged concrete.

A.3.5 Summary

In summary, there is a significant reduction in the mechanical properties of concrete with the increase in the number of FTC. Damage indicators, such as compressive and tensile strength, modulus of elasticity and bond-slip relations, are essential parameters to provide a good understanding of concrete response and degree of damage following FTC exposure. In addition, the modified stress-strain relation of concrete provides a good understanding of the concrete behaviour in tension and compression. Those relations can be used to develop a numerical model of the specimens. The effect of frost damage can also be quantified using ultrasonic measurements of RDME along variable depths of the concrete cross section.

A.4. FTC Effects on Structural Performance

Few researchers have investigated the effects of FTC on the structural performance of RC columns (Montejo et al. 2009; Xu et al. 2016; Qin et al. 2017). Qin et al. (2017) conducted both experimental testing and numerical analysis to predict the seismic behaviour of RC columns. The effects of cyclic FT on the structural behaviour of the reinforced columns were assessed in terms of column ductility, stiffness, strength, displacement, and bearing capacity. For the experimental study, both Qin et al. (2017) and Xu et al. (2016) tested square cross-section half-scale columns; one was a control specimen, while the others were subjected to both FTC and seismic loads. The exposure to FTC conditions was conducted according to the current Chinese code (GB/T 50082-2009). Qin et al. (2017) provide a detailed scheme for the experimental program used to run the tests. After a curing period of 24 days (Xu et al. 2016)and 28 days (Qin et al. 2017), the columns were placed in plain water at 20°C for 4 days (Xu et al. 2016) and 7 days (Qin et al. 2017). Then, the specimens were moved to the environmental chamber, where they were exposed to FTC. The specimens were exposed to 0, 100, 200 and 300 FTC, each FTC lasting for 260 min, about 4.3 hrs (Xu et al. 2016) and 5.5 hrs (Qin et al. 2017). Before the start of each cycle, specimens were sprayed for 5 min (Xu et al. 2016) and five times for 15 min (Qin et al. 2017) to accelerate the effects of FT on the specimens. It is estimated that 300 FTC would last for about three months (Qin et al. 2017). To predict the seismic performance of the columns, pseudo-static experiments

were conducted for different exposure of FTC. The columns were assembled to foundation blocks that were not exposed to FTC conditions. Results of the experimental tests showed that cyclic conditions definitely have a significant impact on the structural performance of RC columns. Cumulative exposure of FTC exposure resulted in a decrease in bearing capacity due to strength reduction and an increase in the structure displacement. Ductility increased initially (up to 100 cycles) due to the increase in yield and ultimate displacement but gradually declined after 100 cycles due to the gradual reduction in ultimate displacement. In addition, after the peak load was reached, the stiffness degradation became more significant. More damaging effects (loss of strength characteristics and aesthetic appearance) were observed at 300 FTC compared to 100 FTC (Qin et al. 2017). The yield load of the specimens decreased by 19% for 300 FTC compared to 10% for 100 FTC (Qin et al. 2017). Specimens exposed to FTC had a premature and brittle failure. Montejo et al. (2009) analyzed the seismic performance of flexural-dominated reinforced columns at low temperatures. For the experimental work, circular cross-section and half-scale columns were designed and detailed as flexural-dominant columns, four (4) of the columns were reinforced concrete-filled steel tube RCFST columns, and the other two (2) were Ordinary Reinforced Concrete (ORC) columns. The latter is the focus of this review. Contrary to previous researchers, Montejo et al. (2009)'s footing and columns were positioned horizontally to accommodate for the environmental chamber size. In addition, the loading test was carried out while the specimens were inside the chamber. The work of this study was conducted in two stages; in stage II, which is relevant to this review, the columns were designed to represent the structural behaviour of a real bridge column. Hence, the reinforcement ratio was increased from ρ=1% to ρ=2-3%, and the columns were subjected to a constant axial load. For the ORC columns, two columns were tested: one at 22℃ and another at -36℃. Structural performance was investigated using a pseudo-static method. In stage I, it was observed that for ORC, there is a reduction in the spread of plastic deformation for columns tested at low temperatures (Montejo et al. 2008).

Results of the experimental work showed that there is an increase in the strength and stiffness of the column when exposed to FTC. For both shear and flexural dominated columns, there is an increase in the flexural and shear strength under cyclic loadings and FTC exposure. However, there is a significant reduction in the displacement and ductility capacity. The reduction in the ductility capacity results from the decrease in the spread of plasticity of the columns. As a result, it was

suggested to decrease the adopted plastic hinge length. This effect was analyzed using two methods, the pushover method and inelastic time history analysis. The first was used to determine strain and hinge formations. The increase in flexural strength was determined using the equivalent hinge method, while the decrease in ductility was calculated using the force-displacement response of the member obtained from moment-curvature analysis (Montejo et al. 2014). Xu et al. (2016) calculated the ductility factor (m) for all specimens, which is the ratio of the ultimate displacement to the yield displacement. It was found that there is a continuous reduction in the value of the ductility factor as the load ratios and FTC are increased. In addition, Xu et al. (2016) results indicate that the displacement capacity of the columns was reduced following FTC due to a decrease in the bond strength and an increase in the slip between the concrete and the reinforcement. Contrary to Montejo et al. (2014)'s results, Xu et al. (2016) found that the higher the applied compression ratio along with FTC exposure, the higher the reduction in the stiffness of the columns.

The discussed studies provide a good overview of the experimental program procedures and set-ups to test the structural performance of RC members exposed to FTC, especially since there are no current standards in North America for FTC testing tailored for large-scale RC members. Most researchers provide a good insight into the seismic behaviour of square-section columns exposed to FTC but not multi-deteriorating environmental mechanisms such as FTC and corrosion. Also, none have examined the potential for longitudinal reinforcement buckling in circular RC columns under the combined effect of FTC and corrosion environment. Montejo et al. (2008; 2014) assessed the seismic performance of circular-section columns subjected to Freezing non-cyclic conditions, whereas both Qin et al. (2017) and Xu et al. (2016) tests were focused on square-section RC columns under FTC conditions. Generally, most researchers agree that exposure to FTC under applied loads leads to significant degradation in the cumulative energy dissipation, ductility and load-carrying capacity. Therefore, one can safely predict aggravated results for an existing structure weakened by multi-environmental exposure of FTC and corrosion under applied loads, a case that few of the mentioned researchers have yet to explore. Thus, it is the focus of the research study presented herein.

A.5. Effect of the Combined Action of FTC and Corrosion on RC

Diao et al. (2012) studied the synergistic effects of environmental conditions of corrosion and FTC and sustained loads on both mechanical properties and structural behaviour of RC columns. The authors found that the compressive strength is reduced by 33% after 300 FTC. Furthermore, the ultimate capacity is reduced by 11.5% when the RC columns are subjected to the combined action of corrosion and FTC. This decrease in ultimate capacity is aggravated to a 15% to 26.9% drop when the environmental conditions are coupled with a sustained load applied eccentrically. The test program was carried on RC columns with a cross-section of 100×200 mm attached to a hunched beam at the top and base, with a total span of the RC column of 700-mm, as shown in (Fig. A.18).

The FTC test was conducted in an environmental chamber according to the GB/T 50082 standard. After 3 FTC, the specimens were immersed in a mixed solution of 3% NaCl and $MgSO_4$ for 12.5 hours until the number of 300 FTC was achieved while a sustained eccentric load was applied simultaneously. The sustained load was applied by tightening bolts attached to spiral rebars from the two sides. Finally, a static eccentric load was applied until failure. After the coupling effect of corrosion and FTC at zero sustained load, all the stirrups were corroded and 70% of the rebar surface area was covered with rust layer, as shown in (Fig. A.19). The rust layer covering the surface area of the rebar was further increased to 90% as the sustained load was increased to 52 kN. (Fig. A.20) illustrates ultimate strength degradation as the sustained load is increased. For COL-2, the ultimate strength was reduced by 15% with a sustained load of 52 kN in comparison to COL-4, which had a 26.9% reduction in ultimate load capacity as the sustained load was increased to 130 kN.

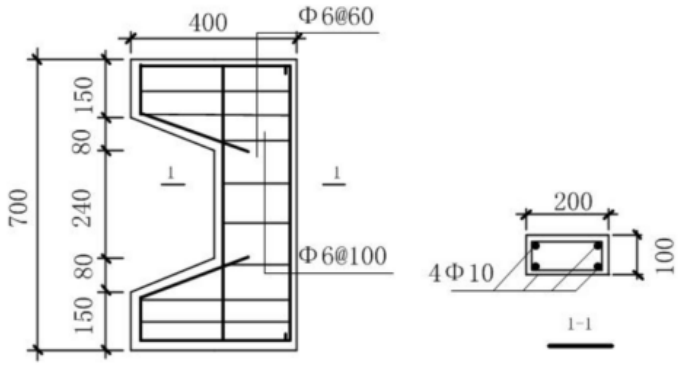

Fig. A.18: Details of the RC column (Diao et al. 2012)

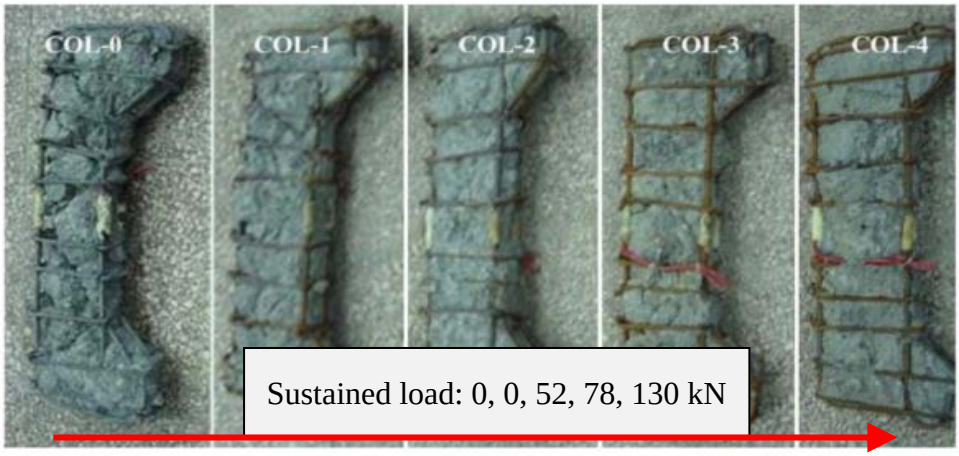

Fig. A.19: Corrosion of the RC columns (adapted from Diao et al. 2012)

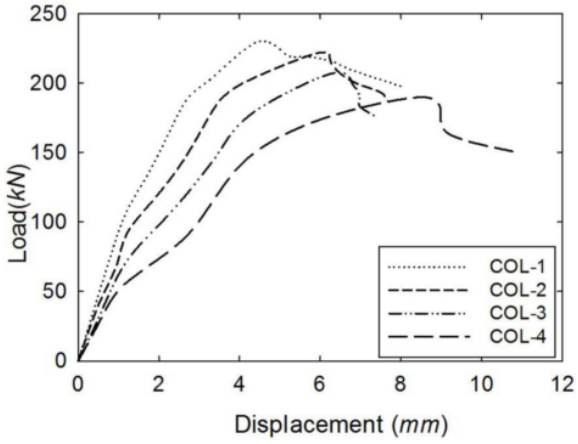

Fig. A.20: Load-displacement relation after a static eccentric load is applied (Reproduced from Diao et al. 2012)

On the other hand, Kosior-Kazberuk and Berkowski (2017) focused their research on the synergistic effects of steel corrosion, FTC and flexural loads on the scaling resistance of RC beams. The FTC test was conducted according to the CEN TC 12390 standard on 80 × 120 ×1,100-mm specimens. From this research, it was concluded that the exposure and load conditions accelerated the external damage (scaling) of the concrete, as illustrated in (Fig. A.21). The authors explain that the damage associated with the conditions presented is due to the development of microcracks along the Interfacial Transition Zone (ITZ) due to a loss of bond between the aggregates and the cement.

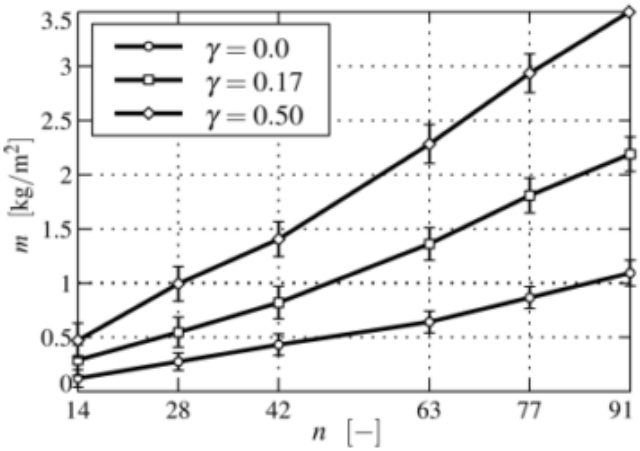

Fig. A.21: Increase in mass loss as the stress ratio, and the number of FTC n is increased (Reproduced from Kosior-Kazberuk and Berkowski 2017)

The previous studies provide a good overview of concrete's structural and mechanical performance and behaviour under the synergistic effect of combined environmental action of corrosion and FTC and external loads. Diao et al. (2012) was the only author who examined the synergistic effects between environmental conditions and sustained load on RC columns.

Finally, Kosior-Kazberuk and Berkowski (2017) mainly focused on the scaling effects of RC beams immersed in chloride salts after FTC exposure.

A.6. Current Standards Test Methods for the Evaluation of FTC Damage

Currently, in Canada, there is no available standard for evaluating FTC damage on RC structural members. As discussed previously, several researchers have relied on different international standards to assess the FTC damage on the concrete. These standards differ in the testing method used and in the methodology carried out for evaluating the damage in concrete specimens. RILEM TC 117-CDF and CEN/TS 12390:9, 2006 evaluate the external damage, while ASTM C666, CEN/TS 15177, GB/T 50082-2009, RILEM TC 176-IDC assess the internal damage. Both ASTM C666 and GB/T 50082-2009 have a 5 hr cycle period, while others have a 24 hrs/ cycle. RILEM TC 117-CDF and CEN/TS 12390:9, 2006 and CEN/TS 15177 specify a testing procedure for de-icing agent exposure in addition to FTC. Both ASTM C666 and GB/T 50082-2009 require water immersion during thawing and dry freezing, while CEN/TS 12390:9, 2006 and CEN/TS 15177 specify no water immersion. It is worth noting that these standards propose testing procedures for small-scale unreinforced concrete specimens and not for large-scale RC structures. Hence, none of the researchers mentioned followed exactly the conditions of standards procedures due to physical restrictions or non-applicability constraints. Therefore, the number of cycles (N) according to one standard must be converted to an equivalent number N_{eq} to provide the same FTC effects. Berto et al. (2015) proposed an equation to transform the number of FTC N conducted according to a different test to an equivalent number of cycles according to ASTM C666 N_{eq} as follows:

$$N_{eq} = \chi N^{\Upsilon} \qquad Eq.A.5$$

γ and χ are parameters dependent on the condition of the test, such as size. Parameter γ takes into account the non-linear reduction in strength due to concrete grade. Since the size of the specimens in this research is different than what is specified in ASTM C666, N_{eq} needs to be estimated. Therefore, using Berto's method, the $N_{eq} = N_{exp}$ is determined as illustrated in Table A.1.

Table A.1: The equivalent number of FTC according to different standards (Qin et al. 2017)

N_{exp} (GB/T 50082)	N_{eq} (ASTM C666)	N_{eq} (RILLEM TC176-IDC)
100	50	13
200	130	40
300	229	76

Berto et al. (2015) estimated the parameters (γ andχ) from samples of RC specimens exposed to FTC and flexural loading. For example, when specimens are tested according to ASTM C666 both γ and χ are equal to 1.

Petersen et al. (2007), who conducted their experiments according to RILEM tc176, similar to conditions used in Hanjari's research, used the ordinary least-square approach to estimate parameters γ and χ based on (Berto et al. 2015):

$$N_{eq} = 11.71 N_{Hanjari}^{0.87} \qquad Eq.A.6$$

A comparison of all current standards used to evaluate the damage induced in concrete by FTC is provided in Table A.2.

Table A.2: A comparison summary of available standards regarding freeze/thaw cyclic testing

Standard	ASTM C666 (ASTM 2015)	GB/T 50082-2009 (Chinese standard 2009)	RILEM TC 117-DFC (Setzer 1997)	RILEM TC 176-IDC (Setzer 2004)	CEN/TS 12390:9 (2016)	CEN/TS 15177 (2006)
Objectives	Resistance of concrete to rapid FT	Longterm performance & durability of ordinary concrete	Concrete resistance exposed to FT & deicing	Internal damage of concrete due to frost action	Scaling resistance of concrete exposed to FT & salt solution	FT resistance of concrete with both water & salt solution
Method	A: FT in water. B: freezing in air & thawing in water	--	Capillary suction Deicing (CDF) & Freeze test	A: Ultrasonic transmission time, B: Fundemental frequency time	Slab test (reference) CDF test, German cube test	Slab test or (UPTT & FF**), CIF test, beam test
Specimen Age	Young concrete, or hardened one	28 days	28 days for high water saturation		Curing and conditioning	Curing & conditioning
Conditions	Saturated in lime water. Covered to maintain moisture	Fully immersed in water to reach a fully saturated state	--	--	65% RH for 7 days	65% RH for 7 days
Temperature	(-18 to 4°C)	(-17 to 15°C)	Rates of 10/hr	(-20 to +20°C)	(-20 to +20°C)	(-18 to +5°C)
Cycles	5 hrs	5 hrs	24 hr/cycle	24 hr/cycle	Freezing: 16-18 hrs. Thawing: 6-8 hrs.	Freezing: 16-18 hrs. Thawing: 6-8 hrs.
Total Cycles	0 to 300	0 to 300		56 to 112	25	25
Environment	Environmental chamber	Environmental chamber	Suitable chamber		3% NaCl solution	3% NaCl solution
Water Immersion	Yes, during thawing	Yes, during freezing	Yes, thawing		No	No
Dry Freezing	Yes, during freezing	Yes, during freezing	No		Yes	Yes
Surface Exposure	Complete exposure air and water	Complete exposure air and water	One surface in 3% NaCl solution	One surface to Salt water	One surface	One surface
Record	*Durability Factor	*Durability Factor	Scale mass	A: Length dilation & ultrasonic velocity. B: DME	Scaled mass, max. depth of damage.	Scaled mass, max. depth of damage.
Damage	60% reduction in DM. Spalling, cracking, exposed rebar	Internal damage	Scaling	Internal Damage	Scaling	Internal damage

*Durability Factor (DF) the ratio between the elastic modulus and length change after 300 cycles & the initial one.
**UPTT: Ultrasonic Puse Transit Time, FF: Fundemental transverse Frequency

A.7. Conclusion

Corroded RC structures are more vulnerable to environmental elements; hence, the damage is aggravated and more serious compared to new structures that are corrosion-free. Therefore, damage may potentially be more significant when specimens are exposed to reinforcement corrosion conditions followed by cycles of FTC. This is partially supported by the fact that FTC conditions before corrosion exposure slows down the degradation of RDME. Furthermore, there is a significant mass loss, and a reduction in the value of the DME as the number of FTC is increased. However, it is essential to distinguish between the effects of FTC and corrosion compared to corrosion in a freezing temperature environment, as the latter leads to slower degradation in the RDME value as the rate of corrosion becomes null at freezing temperature. On the other hand, the cycles of freezing and thawing and exposure to wetting and drying play a crucial role in producing severe damaging effects and faster degradation in the mechanical properties of concrete. This effect is aggravated in a vulnerable corroded RC structure, where FT action build-up along the cracks increases their openings and propagation. Both RDME and bond-slip relations decrease with the increase of FTC. The coupling of a sustained load with FTC and corrosion would considerably accelerate the deterioration process of reinforcement, as the cracks induced by the loading allow the corrosive solution to easily penetrate the concrete and reach the reinforcing bar inside faster.

A.8. References

ASTM. (2015). “Standard Test Method for Resistance of Concrete to Rapid Freezing and Thawing.” ASTM C666, West Conshohocken, PA.

Berto, L., Saetta, A., and Talledo, D. (2015). “Constitutive model of concrete damaged by freeze-thaw action for evaluation of the structural performance of RC elements.” Construction and Building Materials, Elsevier Ltd, 98, 559–569.

CEN/TR. (2006). “Testing the freeze-thaw resistance of concrete. Internal structural damage.” BSI Group.

CEN/TS. (2016). “Testing hardened concrete. Freeze-thaw resistance with de-icing salts. Scaling.” BSI Group.

Chinese. (2009). “Standard for test methods of long-term performance and durability of ordinary concrete.” China Architecture and Building Press.

Diao, B., Sun, Y., Cheng, S., Eng, P., and Ye, Y. (2011). “Effects of Mixed Corrosion, Freeze-Thaw Cycles, and Persistent Loads on Behavior of Reinforced Concrete Beams.” Journal of Cold Regions Engineering, 25(1), 887–381.

Diao, B., Sun, Y., Ye, Y., and Cheng, S. (2012). “Impact of seawater corrosion and freeze-thaw cycles on the behaviour of eccentrically loaded reinforced concrete columns.” Ocean Systems Engineering, 2(2), 159–171.

Duan, A., Jin, W., and Qian, J. (2011). “Effect of freeze-thaw cycles on the stress-strain curves of unconfined and confined concrete.” Materials and Structures/Materiaux et Constructions, 44(7), 1309–1324.

Fagerlund. (1993). “Contribution to the International Workshop on Freeze-Thaw and Deicing Salt Scaling Resistance of Concrete.”

Hanjari, K. Z., Utgenannt, P., and Lundgren, K. (2011). “Experimental study of the material and bond properties of frost-damaged concrete.” Cement and Concrete Research, Elsevier Ltd, 41(3), 244–254.

Hasan, M., Okuyama, H., Sato, Y., and Ueda, T. (2004). “Stress-Strain Model of Concrete Damaged by Freezing and Thawing Cycles.” Journal of Advanced Concrete Technology, 2(1), 89–99.

Hasan, M., Ueda, T., and Sato, Y. (2008). “Stress-Strain Relationship of Frost-Damaged Concrete.” 20(January), 37–45.

International Institute for Sustainable Development (IISD). (2013). “Climate change adaptation and water resource management: a review of the literature.” climate Change Adaptation and Canadian Infrastructure, (November), 40.

Kanazawa, T. (2015). “Bond Deterioration Mechanism and Its Modeling for Reinforced Concrete Subjected to Freezing-Thawing Action.” ASCE, 1245–1250.

Li, A. (2017). “Effects of Frost-damage on Mechanical Performance of Concrete.” Journal of Wuhan University of Technology-Mater. Sci. Ed. www.jwutms.net, 129–135.

Ma, Z., Zhao, T., and Yang, J. (2017). “Fracture Behavior of Concrete Exposed to the Freeze-Thaw Environment.” 29(8).

Mitchell, P. A. (2010). “Freeze-Thaw and Sustained Load Durability of Near-Surface Mounted FRP Strengthened Concrete.” Master Thesis.

Montejo, L. A., Kowalsky, M. J., and Hassan, T. (2009). “Seismic Behavior of Flexural Dominated Reinforced Concrete Bridge Columns at Low Temperatures.” Journal of Cold Regions Engineering, 23(1), 18–42.

Oldershaw. (2008). “Combined effects of freeze-thaw and sustained loads on reinforced concrete beams strengthened with frps.” A thesis submitted to the Department of Civil Engineering in conformity with the requirements for the degree of Master of Science (Engineering).Queen’s University Kingston, Ontario, Canada, (February), 134.

Pan, D. F., Qiao, Y. F., Sun, C. S., and Liu, X. B. (2011). “The frost model of concrete in the view of damage mechanics.” Advanced Materials Research, 194–196, 919–923.

Petersen, L., Lohaus, L., and Polak, M. A. (2007). “Influence of freezing-and-thawing damage on the behavior of reinforced concrete elements.” ACI Materials Journal, 104(4).

Pigeon, M., Marchand, J., and Pleau, R. (1996). “Frost resistant concrete.” Construction and Building Materials, 10(5 SPEC. ISS.), 339–348.

Powers, T. C. (1945). “Working Hypothesis for Further Studies of Frost Resistance of Concrete.” ACI JOURNAL, Proceedings, 41(4), 245–272.

Qin, Q., Zheng, S., Li, L., Dong, L., Zhang, Y., and Ding, S. (2017). “Experimental Study and Numerical Simulation of Seismic Behavior for RC Columns Subjected to Freeze-Thaw Cycles.” Advances in Materials Science and Engineering, 2017(2011).

RILEM TC 117-FDC. (1995). “Draft recommendation for test method for the freeze-thaw resistance of concrete. Tests with water (CF) or with sodium chloride solution (CDF).” Material and Structures.

Setzer, P. M. J., Heine, P., Kasparek, S., Palecki, S., Auberg, R., Feldrappe, V., and Siebel, E. (2004). “Test methods of frost resistance of concrete : CIF-Test : Capillary suction , internal damage and freeze thaw test – Reference method and alternative methods A and B.” 37(December), 743–753.

Shang, H. S., Cao, W. Q., and Wang, B. (2014). “Effect of fast freeze-thaw cycles on mechanical properties of ordinary-air-entrained concrete.” Scientific World Journal, Hindawi Publishing Corporation, 2014.

Shang, H. S., and Song, Y. P. (2006). “Experimental study of strength and deformation of plain concrete under biaxial compression after freezing and thawing cycles.” Cement and Concrete Research, 36(10), 1857–1864.

Shih, T. S., Lee, G. C., and Chang, K. C. (1988). “Effect of Freezing Cycles on Bond Strength of Concrete.” Journal of Structural Engineering, 114(3), 717–726.

Sun, L., Jiang, K., Zhu, X., and Xu, L. (2020). “An alternating experimental study on the combined effect of freeze-thaw and chloride penetration in concrete.” Construction and Building Materials, Elsevier Ltd, 252, 119025.

Valenza, J. J., and Scherer, G. W. (2007). “A review of salt scaling: II. Mechanisms.” Cement and Concrete Research, 37(7), 1022–1034.

Xu, S., Li, A., Ji, Z., and Wang, Y. (2016). “Seismic performance of reinforced concrete columns after freeze-thaw cycles.” Construction and Building Materials, Elsevier Ltd, 102(November 2015), 861–871.

Appendix B. Calculations

This appendix provides information about design considerations, stress-strain relationship adopted for the compressive longitudinal bars in the FEAs and calculations for the column base plate used in the load set-up, for the RC column, and for the top and bottom corbels.

B.1. Design Consideration

Several considerations were accounted for in the design of the RC columns: load application, slenderness, structural response (mode of failure), and design requirements pertaining to highway and bridge design in North America for existing and pre-1971 structures. The RC member was comprised of a 260×260-mm square column attached at the top and base to a 260×520-mm corbel; dimensions and cross-sections. After the RC specimens had been conditioned for corrosion-induced damage, they were subjected to an increasing axial load until failure. An axial compressive load was applied concentrically and eccentrically at the top of the columns at zero rotation using a hydraulic load actuator. The response of the RC column depends on column slenderness and load eccentricity (Brzev and Pao 2013) While columns in this study are short, concentric columns were subjected to axial load, and eccentric columns were subjected to both axial load and bending moment. Failure of a concentric column (e=0) with moderate reinforcement often occurs after yielding of the steel (ε_y=0.002) followed by crushing of the concrete at a maximum strain of ε_{cmax} =0.0035. Subsequently, longitudinal rebar buckling occurs between the ties (Wight and Macgregor 2012; Brzev and Pao 2013; Moehle 2015). However, for closely spaced ties, yielding of the rebar is accompanied by spalling and cracking of the concrete, with the ties being fully engaged in preventing rebar buckling. Increasing the applied load imposes considerable lateral pressure in the concrete core against the ties. Eventually, columns fail when ties yield. Therefore, the amount of longitudinal steel and spacing of transverse reinforcements are significant contributors to column capacity. At larger eccentricities, the effect of the bending moment M=Pe is very significant when the concrete strain reaches a maximum $\varepsilon_c = \varepsilon_{cmax}$ and steel strain exceeds the yield value, $\varepsilon_s > \varepsilon_y$. While concentric columns fail in concrete-controlled mode (brittle failure), eccentric columns fail in steel-controlled mode (ductile failure) (Wight and Macgregor 2012; Brzev and Pao 2013; Moehle 2015).

Confinement reinforcement improves flexural ductility by resisting the transverse expansion of the concrete core and preventing buckling of the longitudinal reinforcement (MacGregor 2009; Brzev and Pao 2013). In addition, several considerations were taken to promote a flexure (ductile) behaviour and prevent brittle response by providing adequate reinforcement detailing: top and bottom reinforcement along the member length and confinement of the critical regions of the columns.

Column resistance was determined according to current standards for new structures AASHTO LRFD and CAN/CSA S6:19 (Canadian Highway and Bridge Design-CHBD) (CSA 2019), CAN/CSA A23.3 Clause 7.6.4.3 (CSA 2019). It is important to note that only nominal values were considered in the experimental work. Column resistance was then compared with pre-1971 design standards, which were designed according to the AASHTO ASD (1969) handbook as shown in Table 3.2. The concentric column capacity at the onset of spalling was estimated to be 1,492 kN according to CAN/CSA A23.3 CL10.10.4 (CSA 2019) and CAN/CSA-S6:19 Clause 8.8.5.3 (CSA 2019):

$$P_0 = \left(\alpha \phi_c f_c A_g + \phi_s f_y A_s\right) \qquad \textit{Eq. B.1}$$

where α is 0.8 (CSA S6-Cl: 8.8.3) (CSA 2019), ϕ_c is the resistance factor (0.75, CAN/CSA S6:19 Table 3.2), f_c is the concrete compressive strength, A_g is the gross concrete area, ϕ_s is the steel resistance factor (0.9), f_y is the steel yield strength (400 MPa), and A_s is the steel area.

For eccentric loading, the axial capacity and moment resistances were respectively estimated according to CAN/ CSA A23.3:

$$P_r = C_r + F_{rs1} + F_{rs2} \qquad \textit{Eq. B.2}$$

$$P_r e = C_r \left(\frac{h}{2} - \frac{\beta c}{2}\right) + F_{rs1}\left(\frac{h}{2} - d_1\right) + F_{rs2}\left(\frac{h}{2} - d_2\right) \qquad \textit{Eq. B.3}$$

where C_r is the concrete resistance, β is 0.9, c is the neutral axis distance, F_{rsi} is the reinforcement resistance of layer *i*, *h* is the concrete depth, and d_1 is the depth to the first layer of the reinforcement and d_2 to the second layer of the reinforcement.

According to AASHTO ASD (1969) code adopted pre-1971, the column capacity was estimated to be 941 kN according to Eq. B.4:

$$P_0 = \left(0.225 f_c A_g + f_y A_s\right) \qquad \textit{Eq. B.4}$$

The axial and bending stresses were calculated based on the uncracked section, where e/t <0.5, t being the depth of the concrete cross-section in the direction of eccentricity (Eq. 3.5 and Eq. 3.6):

$$f_c = \frac{P_0}{A_g} \frac{1 \pm k\left(\frac{e}{t}\right)}{1+(n-1)\rho} \qquad \textit{Eq. B.5}$$

where f_c is the combined fiber stress in compression, n is the ratio of modulus of elasticity of steel to that of concrete, $k = t^2/2r^2$ (with r being the radius of gyration) or 5 for a tied column, a factor used for members subjected to combined axial and bending.

$$f_a = \frac{0.225 f_c + f_s \rho}{1+(n-1)\rho} \qquad \textit{Eq. B.6}$$

where f_a is the allowable stress, and ρ is the longitudinal steel ratio.

According to the AASHTO LRFD current code used for highway and bridge design in the US, the column capacity is estimated to be 1,748 kN from:

$$P_0 = \left(0.85 f_c A_g + f_y A_s\right) \qquad \textit{Eq. B.7}$$

B.2. Rebar Buckling

The stress strain relationship of the compressive longitudinal bars is defined according to Akkaya et al. (2019).

Dhakal and Maekawa (2002) proposed a simple method to predict the buckling length of the longitudinal reinforcement. In the formulation of this methodology the authors modelled the longitudinal bars as flexural members fixed at each end by transverse reinforcement (ties). Thus, the effective length of the reinforcement refers to the length between boundary points (tie spacing). The resistance provided by the ties against longitudinal bars buckling is governed by the stiffness of the ties. Deteriorations of the concrete cover due to compressive strain and splitting cracks were also considered.

Dhakal and Maekawa (2002) proposed a stress-strain model (DM) to estimate the buckling stress of compressive longitudinal bars. The difference between the tensile and compressive curves in

the proposed model represents the loss in compressive stress due to buckling. The average behaviour of rebar is governed by slenderness, bar diameter, yield strength related to the expression $\frac{L}{d}\sqrt{\frac{f_y}{100}}$ essential for high strength bars (Dhakal 2005).

Bar experiences significant stress degradation post-buckling due to compressive load (Dhakal and Maekawa 2002; Dhakal 2005), and the average compressive stress becomes constant after 20% of yield stress. The maximum compressive strain at the main bar will be equal to the ultimate core strain since there will be no contribution from the cover due to spalling. The maximum core concrete strain is a function of the tie stiffness.

Redefined Dhakal Maekawa (RDM) model proposed by Akkaya et al. (2019) (Fig. B.1) was to eliminate some of the criticized points in the DM model (Wong. P.S, Vecchio. F.J 2008). Both models define an intermediate point (ε_i, f_i). However, with RDM the location of the f_i is defined easily in accordance with ε_i which is obtained from the tension curve. $\varepsilon_y, \varepsilon_i, \varepsilon_{sh}, \varepsilon_i, \varepsilon_{ii}, \varepsilon_{sc}, \varepsilon_u$ strain values are required to build the compressive stress-strain model. A constant negative stiffness of $0.02f_s$ is used until the average compressive stress is equal to $0.2f_y$. The slenderness ratio r_b is determined as follows:

$$r_b = \frac{L}{d}\sqrt{\frac{f_y}{100}} < 8 \text{ (premature buckling could be avoided)} \qquad \textit{Eq. B.8}$$

r_b Indicates the reduction in the normalized stress f_i/f_y

$$\varepsilon_{imax} = \varepsilon_y\left[55 - 2.3\sqrt{\frac{f_y}{100}} \times 5\right] \qquad \textit{Eq. B.9}$$

For $\varepsilon_i \geq 7\varepsilon_y$

$$\varepsilon_i = \beta\varepsilon_y[5.5 - 2.3r_b] \qquad \textit{Eq. B.10}$$

Otherwise, $\varepsilon_i = 7\varepsilon_y$

For $\varepsilon_{imax} > \varepsilon_u$,

$$\beta = \varepsilon_u/\varepsilon_{imax}, \qquad \textit{Eq. B.11}$$

Otherwise, $\beta = 1$

For $\varepsilon_{imax} \geq \varepsilon_u$ and $\varepsilon_i > 7\varepsilon_y$, P=1, Otherwise; P=4

For $\varepsilon_i \leq \varepsilon_{sh}$

$$f_{it} = f_y \qquad \textit{Eq. B.12}$$

For $\varepsilon_i \geq \varepsilon_{sh}$

$$f_{it} = f_u + (f_y - f_u)\left(\frac{\varepsilon_u - \varepsilon_i}{\varepsilon_u - \varepsilon_{sh}}\right)^p \qquad \textit{Eq. B.13}$$

For $\varepsilon_{sc} \leq \varepsilon_{sh}$

$f_{st} = f_y$ Eq. 8.1

For $\varepsilon_{sc} \leq \varepsilon_{sh} \leq \varepsilon_{sc}$

$$f_{st} = f_u + (f_y - f_u)\left(\frac{\varepsilon_u - \varepsilon_{sc}}{\varepsilon_u - \varepsilon_{sh}}\right)^p \qquad \textit{Eq. B.14}$$

These values correspond to the stress on the tension curve relating to the intermediate strain value. To obtain the strain at the compression curve, the stresses must be multiplied by a parameter (α) as follows.

$$\alpha f_i = f_y \alpha; \;\; f_i \leq f_{it}$$

For $\varepsilon_i \geq \varepsilon_{sh}$

$$\alpha = [1.1 - 0.016 r_b]\left[0.8 + 1.8\frac{f_u}{f_y}\frac{D}{L}\right] \qquad \textit{Eq. B.15}$$

For $\varepsilon_i \leq \varepsilon_{sh}$

$$\alpha = 0.75[1.1 - 0.016 r_b]\left[0.8 + 1.8\frac{f_u}{f_y}\frac{D}{L}\right] \qquad \textit{Eq. B.16}$$

For $\varepsilon_{imax} \geq \varepsilon_u$

$$\alpha = 0.75\frac{f_u}{f_y}[1.1 - 0.016 r_b]$$

For $\varepsilon_{SC} \leq \varepsilon_Y$

$$f_{st} = E_s \varepsilon_{sC} \qquad \textit{Eq. B.17}$$

$$f_{sc} = f_{st}\left[1 - \left(1 - \frac{f_i}{f_{it}}\right)\left(\frac{\varepsilon_u - \varepsilon_{sc}}{u - \varepsilon_{sh}}\right)^p\right] \quad \textit{Eq. B.18}$$

$$\varepsilon_i \leq \varepsilon_{sc} \leq \varepsilon_{ii}$$

$$f_{sc} = max[f_i - 0.02E_s(\varepsilon_{sc} - \varepsilon_i); 0.2f_i] \quad \textit{Eq. B.19}$$

$$\varepsilon_{ii} \leq \varepsilon_{sc} \leq \varepsilon_u$$

$$f_{sc} = max[0.75f_i - 0.02E_s(\varepsilon_{sc} - \varepsilon_i); 0.2f_i] \quad \textit{Eq. B.20}$$

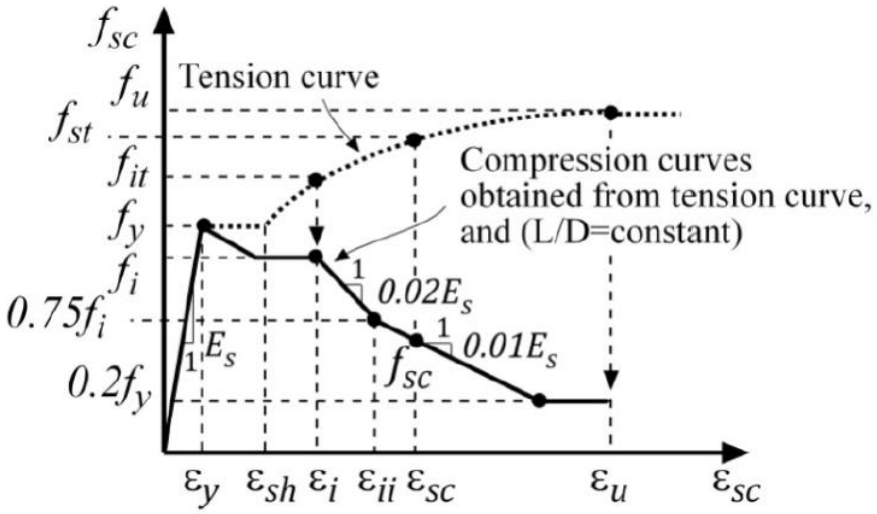

Fig. B.1: Redefined Dhakal Maekawa (RDM) model proposed by Akkaya et al. (2019) (adapted from Akkaya et al. (2019))

The axial stiffness of the tie influences the restraining effects provided by the transverse reinforcement. The axial tie stiffness is estimated as follows:

$$k = \frac{\pi^4 EI}{s^3} \quad \textit{Eq. B.21}$$

$$k_t = \frac{E_t A_t}{L} \quad \textit{Eq. B.22}$$

$$k_{eq} = \frac{k_t}{k} \quad \textit{Eq. B.23}$$

B.3. Column Base Plate Design

The design of the column base plate was carried out according to CSA S16:19 (2019) and ANSI/ AISC 360-16 (2017). To determine the required area of the column base plate, the larger value of the three formulations is taken (Fig. B.2 and Fig. B.3):

$$A_{req} = \frac{P_u}{0.6 \times 1.7 f_c}$$

$$= \frac{2500 \times 10^3 (N)}{0.6 \times 1.7 (28MPa)} = 87.5 \times 10^3 mm^2$$

$$A_{req} = \frac{P_u}{f_c} = \frac{2500 \times 10^3 (N)}{28\ MPa} = 89.2 \times 10^3 mm^2$$

$$A_{req} = \frac{1}{A_2}\left[\frac{P_u}{0.6 \times 0.85 f_c}\right]^2 = \frac{1}{520 \times 520}\left[\frac{2500 \times 10^3 (N)}{0.6 \times 0.85 (28MPa)}\right]^2 = 113.7 * 10^3 mm^2$$

Try a plate with a size
$520 \times 520 = 270.4 \times 10^3 mm^2 > 113 \times 10^3 mm^2$

The actual bearing stress from the concrete footing:

$$f_p = \frac{2500}{270.4 \times 10^2} = 9.24MPa$$

LOAD CASE 1: base plate for an axially loaded column without a moment (e=0):

$$M_{max} = 8\left(\frac{130 \times 130}{2}\right) = 67.6KN.mm$$

The resistance of the plate:

$$M_r = \frac{\phi f_y t^2}{4}$$

Equating the two eq's, Fy=400MPa

The minimum required thickness of the plate:

$$t = \sqrt{\frac{4 \times M_r}{\emptyset \times F_y}} = 32\ mm$$

$$t = \sqrt{\frac{4 \times 67.6 \times 10^3}{0.9 \times 400}} = 27.4mm$$

Hence, use a plate 520 x 520 x 32 mm for Fy= 400 MPa

LOAD CASE 2: BASE PLATE FOR AN AXIALLY LOADED COLUMN WITH A MOMENT (E<ECRIT)

Case I: $A_1=A_2$

Area of the bearing support= area of the structure

M=Pe

=400×190mm

=76000 kN.mm

F_c=28MPa, F_p=0.85(28) =23.8MPa

Resultant bearing force: q_{max}=23.8 MPa(260mm) =6,188N/mm

$e_{critical} = \frac{N}{2} - \frac{P}{2q_{max}} = \frac{520}{2} - \frac{400}{2(6{,}188)}$=260mm e<$e_{critical}$

Bearing length: y=N-2P=520-2(190) =140 mm

$$q = \frac{P}{y} = \frac{400}{140} = 2.86\frac{KN}{m} < qmax\ Ok$$

$$\therefore \quad f_p = \frac{P}{BY} = \frac{400}{260(140)} = 10.99\ MPa$$

According to AISC design Guide eq 3.3.14a-1 for Y>= m (130)

$$t_{min} = 1.49(m)\sqrt{\frac{f_p}{f_y}}$$

$$= 1.49(130)\sqrt{\frac{11}{400}} = 32.1\ mm \qquad t_{min} = 32\ mm$$

Use 520 x 260 x 32 for Fy=400 Mpa

PIN-SUPPORT DESIGN

Outer cylinder diameter

$$P_{ult} = \sigma A_{req}$$

$$A_{req} = \frac{1}{4}\pi(D_1^2 - D_2^2)$$

Bearing stress (σ_{BS})

Ultimate load subjected to the column 2000KN or 8000 N/mm (line load, L=260mm)

$$\sigma_{BS} = \frac{8000\ N/mm}{520mm \times 1mm} = 15.4\ N/mm^2$$

$$8000\frac{N}{mm} = \frac{15.4}{4}\pi(D_1^2)$$

D_1=26 mm

Bearing capacity of the steel plate:

$\sigma_{BS} = 300\ MPa$

$$A_{req} = \frac{2000 \times 10^3 N}{350\ N/mm^2} = 6666.7\ mm^2$$

Outer diameter required: 260 D_1=6666.7

D_1=26 mm

ALLOWABLE ROTATION OF MINIMUM 10 DEG

The angle of rotation is a function of the torque, polar moment of inertia and modulus of rigidity

$$\theta = \frac{T\ N.mm \times L\ mm}{Jmm^4\ (G)N/mm^2}$$

For the minimum required angle of rotation of 10degrees, the minimum required outer diameter is:

e=190mm, capacity load: 400KN

$$(10 \times 2 \times \pi)/360 = \frac{(190mm \times 400000\ N.mm)260\ mm}{J\ (95 \times 10^3)N/mm^2}$$

$$\therefore \quad J = \frac{360(2 \times 10^{10} N.mm^3)}{(20\pi)(95 \times 10^3)N/mm^2}$$

θ: Angle of rotation (2 π/360) in radians

Since $J = \frac{1}{32}(D_1^4)$ mm^4

$J = \frac{1}{32}\pi(D_1^4) = 1.2 \times 10^6 mm^4$ D_1=59.1 mm, use 60mm

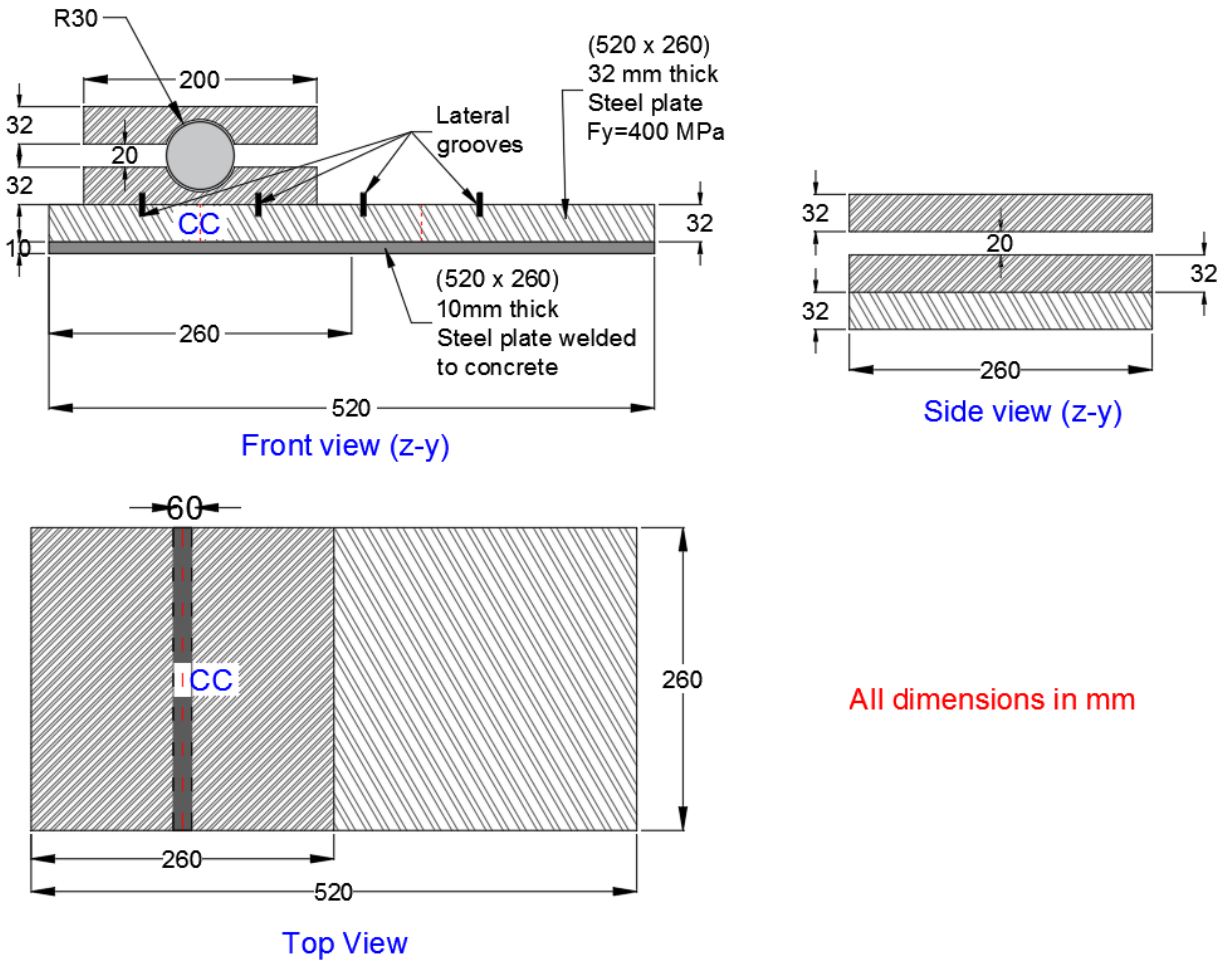

Fig. B.2: Detail of the plates setup for a concentric load application

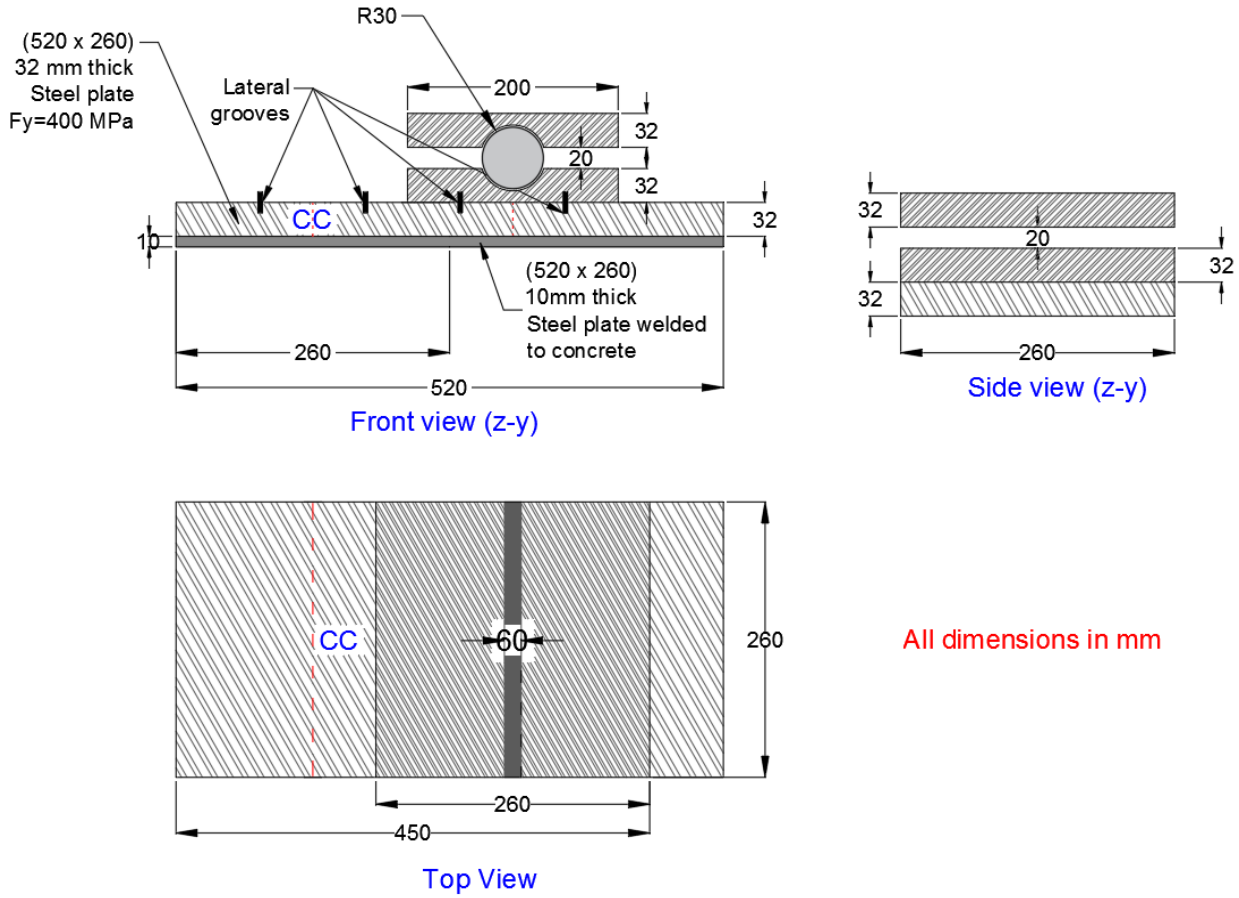

Fig. B.3: Detail of the plates setup for an eccentric load application

B.4. Corbel Design

The top and bottom corbels were design according to ACI 318 (2019).

Design of Bearing Plate:

Assume 260 mm long and 25 mm thick bearing plate Plate width

$$A_{req} = \frac{P_u}{0.6 \times 1.7 f_c} = \frac{747.2 \times 10^3}{0.85 \times 0.65 \times 30 \times 260} = 171.4mm$$

∴ Use 175 mm x 260 mm x 25 mm

Compute Minimum Depth (d):

d = 746.3 × 1000 5.5 × 260 = 520 mm

$$d = \frac{746.3 \times 1000}{5.5 \times 260} = 520mm$$

h = 520 + 30 = 550 mm

Compute Forces on Corbel:

N_{uc}= 0.2 × 746 = 149.2 kN

M_u= 746 × 0.02 + 149.2 (0.55 − 0.52) = 19.7 kN.m

Compute Shear Friction Steel:

$A_{vf} = \frac{747.2\times1000}{0.75\times1.4\times1\times420}$ =1,649mm^2

Compute Flexural Reinforcement (A_f):

$A_{vf} = \frac{19.7\times10^6}{0.75\times420\times0.9\times520}$ =133.7mm^2

$a = \frac{133.7\times420}{0.85\times30\times260}$ =8.5mm

$A_{vf} = \frac{149.2\times1000}{0.75\times420\times0.9\times(520-4.25)}$ =121.3mm^2

Compute Reinforcement of Direct Tension (A_n)

$A_n = \frac{19.7\times10^6}{0.75\times420}$ =133.7mm^2

Compute Area of Tension Tie Reinforcement (A_s)

A$_s$= A_f + A_n = 121.3 + 475 = 596mm^2

$A_s = \frac{2A_v}{3} + A_n = \frac{2\times1,694}{3} + 475$= 1604mm^2

Use A_s = 1,604 mm^2

Use 3-20M (A_s = 900 mm^2) + 2 − M25(A_s= 1,000 mm^2) = 1,900mm^2

$A_{s,min} = \frac{0.03\times30}{420} \times 260 \times 520$=386 mm^2< 1,900mm^2

Compute Area of Horizontal Stirrups

0.5 (A_s – A_n) = (1,900 − 475)/2 = 712.5 mm^2

Use 3-15M double leg stirrups placed within 2/3 d measured for the tension tie.

Establish Anchorage of Tension Tie into Column

$l_{dh-M20} = \frac{0.24\times420\times19.5\times0.7\times0.8}{\sqrt{300}}$=201mm

$l_{dh-M25} = \frac{0.24\times420\times25.2\times0.7\times0.8}{\sqrt{300}}$=260mm